

# ASSEMBLY AND REACTIVITY OF NANOPARTICLES AT LIQUID / LIQUID INTERFACES

THÈSE N° 3535 (2006)

PRÉSENTÉE LE 9 JUIN 2006

À LA FACULTÉ SCIENCES DE BASE

Laboratoire d'électrochimie physique et analytique

SECTION DE CHIMIE ET GÉNIE CHIMIQUE

ÉCOLE POLYTECHNIQUE FÉDÉRALE DE LAUSANNE

POUR L'OBTENTION DU GRADE DE DOCTEUR ÈS SCIENCES

PAR

**Bin SU**

M.Sc. in Chemistry, Chinese Academy of Sciences, Changchun, Chine  
et de nationalité chinoise

acceptée sur proposition du jury:

Prof. P. Vogel, président du jury  
Prof. H. Girault, directeur de thèse  
Prof. M. Grätzel, rapporteur  
Prof. K. Konturi, rapporteur  
Prof. P. Unwin, rapporteur



ÉCOLE POLYTECHNIQUE  
FÉDÉRALE DE LAUSANNE

Lausanne, EPFL

2006



To my wife and my parents...



## Acknowledgements

First and foremost, I would like to thank my supervisor Professor Hubert H. Girault for providing me a chance to study and work in his group. I feel extremely privileged and grateful for his guidance, advice and encouragement he has granted me throughout the past four years.

I would like to give special thanks to Nicolas Eugster for his numerous help in the course of my thesis work and devoting time to read and correct my thesis. Also, I am grateful to David Fermin for his guidance in the first year of my thesis and fruitful discussions with him. Jean-Pierre Abid is acknowledged for his help on electronic microscopic measurements. My sincere gratitude also goes to other past and present members of physical chemistry team, Joseph Kakkassery, Michel Carrara, Christophe Bauer, Mohamad Hojeij, Guillaume Meriquet, Shuxin Tan and Meiqin Zhang, for their help, discussions and encouragement.

I wish to thank Valérie Devaud for her excellent support on techniques and experiments. I am also thankful to Maria Szuman, Claudine Bovey and Sandra Jeanneret, secretaries of LEPA, for their help not only on administrative affairs during my Ph.D study. All my colleagues in LEPA deserve thanks for the innumerable things I have learned from them and the kind help they provided.

I am also indebted to all my friends in Switzerland, especially those in Lausanne, for the joyful time I spent with them and their kind help.

Finally, I wish to express my deepest appreciation to my wife Zhihua Yang for her support, accompanying and patience. Many thanks go to my parents for their unconditional support for so many years. This thesis is dedicated to them.



## Abstract

The interface between two immiscible electrolyte solutions (ITIES), or liquid|liquid interface, provides a defect-free junction for fundamental studies of adsorption phenomena, heterogeneous charge transfer reactions, and phase-formation processes. Recent research interests include the organization and reactivity of metallic and semiconducting nanoparticles (NPs) at ITIES. In a general sense, the present thesis is devoted to addressing this issue, including the voltage-induced assembly of charged NPs, the photoreactivity of semiconducting NPs and the redox properties of alkanethiolate monolayer-protected gold nanoclusters.

The adsorption of ionic species at the liquid|liquid interface was first modeled theoretically. The aim of the simulations was to envisage the effect of the adsorption of charged NPs on the interfacial charge distribution across the liquid|liquid interface. For simplicity, in the calculations the charged NPs were considered as large ions, which were further taken as point charges. Various adsorption isotherms were considered, including potential independent, Langmuir and Frumkin models. The simulation indicates that the ionic adsorption has a strong influence on the potential distribution across the interface. Under certain conditions, it results in a non-monotonous potential profile with a trap at the interface.

The voltage induced assembly of mercaptosuccinic acid (MSA) stabilized gold and cadmium selenide (CdSe) NPs were investigated at the polarizable water|1,2-dichloroethane (DCE) interface. The studies reveal that the surface concentration of NPs at the liquid|liquid boundary is reversibly controlled by the applied bias potential. There was no evidence of irreversible aggregation or deposition of the particles at the interface. Furthermore, the adsorbed CdSe NPs at the water|DCE interface demonstrated the photoreactivity characteristic of a self-assembled ultrathin p-type semiconductor photoelectrode. The surface structure also has significant effect on the optical properties of CdSe NPs.

The redox properties of hexanethiolate monolayer-protected gold nanoclusters (MPCs) were studied in detail at electrochemical interfaces. First, the absolute standard redox potential of MPCs in solutions was theoretically derived from electrostatic considerations. The significant effect of the solvent polarity was verified experimentally by studies in various organic solvents. Second, the redox properties of self-assembled MPCs on a gold electrode were studied in organic electrolytes and room temperature ionic liquids (RTILs). The effect of the electrostatic interaction between MPCs and electrode on the redox properties of MPCs was theoretically considered in terms of the method of images in classical electrostatics and justified experimentally. In RTILs, the rectification of the successive oxidation of self-assembled MPCs by the anionic component of RTILs was observed. Third, MPCs were further used as redox quenchers at the polarizable water|DCE interface. Photocurrent responses originating from the heterogeneous quenching of photoexcited porphyrins by MPCs dissolved in the DCE phase were observed. As MPCs can function as both electron acceptors and electron donors, the photocurrent results from the superposition of two simultaneous processes, which correspond to the oxidation and reduction of MPCs. The magnitude of the net photocurrent is essentially determined by the balance of the kinetics of these two processes, which can be controlled by tuning the Galvani potential difference between the two phases. We show that, within the available potential window, the apparent electron transfer rate constants follow the classical Butler-Volmer dependence on the applied potential difference.

*Keywords:* Nanoparticles; Liquid|liquid interfaces; Electrochemistry; Photocurrent; Assembly



## Résumé

L'interface entre deux solutions d'électrolytes immiscibles (ITIES), ou interface liquide|liquide, constitue un environnement sans défauts structuraux idéal pour l'étude des phénomènes d'adsorption et de transferts de charge hétérogènes, ainsi que des processus de formation de phase. L'organisation et la réactivité de nanoparticules (NP) métalliques ou semi-conductrices aux ITIES ont récemment bénéficié d'un intérêt marqué. D'une manière générale, cette thèse aborde cette problématique par l'étude de l'assemblage de nanoparticules chargées induit par une différence de potentiel, de la photo-réactivité de NP semi-conductrices, ainsi que des propriétés redox de nanoclusters d'or protégés par une monocouche d'alkanethiolates.

L'adsorption d'espèces ioniques à l'interface liquide|liquide est tout d'abord modélisée de façon théorique afin d'analyser l'effet de l'adsorption de NP chargées sur la distribution des charges à l'interface. Afin de simplifier le problème, les NP chargées sont assimilés à des ions de grande dimension, et considérées comme des charges ponctuelles. Plusieurs isothermes d'adsorption sont considérés : adsorption indépendante du potentiel, modèles de Langmuir et de Frumkin. Les simulations montrent que l'adsorption d'ions influence largement la distribution du potentiel. Dans certaines conditions, l'adsorption crée un puit de potentiel à l'interface.

L'assemblage induit par voltage de nanoparticules d'or et de sélénure de cadmium (CdSe) stabilisées par de l'acide mercaptosuccinique (MSA) est étudiée à l'interface eau|1,2-dichloroéthane (DCE). La concentration de surface de NP à l'interface peut être contrôlée de façon réversible par l'application d'un potentiel entre les deux phases. Aucun signe d'une agrégation irréversible ou d'une précipitation des particules à l'interface n'est observé. De plus, les nanoparticules de CdSe à l'interface eau|DCE présentent une photoréactivité caractéristique d'une photo-électrode ultramince auto-assemblée de semi-conducteurs de type p. La structure de la surface a un effet important sur les propriétés optiques des NP de CdSe.

Les propriétés redox de nanoclusters d'or protégés par une monocouche d'héxanethiolate (MPC) aux interfaces électrochimiques sont étudiées en détail. En premier lieu, le potentiel redox absolu standard des MPC en solution est dérivé théoriquement sur la base de considérations électrostatiques. L'effet du solvant est vérifié expérimentalement par des études dans différents solvants organiques. Les propriétés redox de MPC auto-assemblées sur une électrode d'or sont également étudiées en solutions organiques d'électrolytes ainsi que dans des liquides ioniques à température ambiante (RTILS). L'effet des interactions électrostatiques entre les MPC et l'électrode sur les propriétés redox des MPC est non seulement démontrée expérimentalement, mais aussi analysée théoriquement par la méthode des images en électrostatique classique. Dans un RTILS, on observe la rectification des oxydations successives des MPC auto-assemblés par le composé anionique du RTILS.

Finalement, les MPC sont utilisés comme réactifs redox à l'interface eau|DCE polarisée. On observe des photocourants résultant du transfert d'électrons hétérogène entre les porphyrines photo-excitées et les MPC en phase organique. Les MPC pouvant à la fois accepter et donner des électrons, le photocourant résulte de la superposition de deux processus simultanés correspondant à l'oxydation et à la réduction des MPC. L'intensité du photocourant est essentiellement déterminée par la cinétique de ces deux réactions, qui peut être contrôlée en variant la différence de potentiel de Galvani entre les deux phases. Il est montré que, dans la fenêtre de potentiel disponible, les constantes de vitesse apparentes de transfert d'électron suivent une dépendance de type Butler-Volmer classique au potentiel appliqué.

*Mots Clé:* Nanoparticules; Interfaces liquide|liquide; Electrochimie; Photocourant  
Assemblage

# Table of Content

Dedications.....	i
Acknowledgements.....	iii
Abstract.....	v
Résumé.....	vii
Table of Content.....	ix

## Chapter 1 - Introduction to liquid|liquid interfaces and nanoparticles

<b>1.1 Introduction to liquid liquid interfaces.....</b>	<b>1</b>
1.1.1 Relevance and historic background.....	1
1.1.2 Electrochemical double layers.....	3
1.1.2.1 The Galvani potential difference	
1.1.2.2 Modified Verwey-Niessen (MVN) model	
1.1.2.3 Concerning inner layer: solvent mixing and ion interpenetration	
1.1.2.4 Capillary wave model	
1.1.2.5 Microscopic structure	
1.1.3 Electrochemical equilibrium.....	7
1.1.3.1 Ionic partition equilibrium	
1.1.3.2 Redox equilibrium	
1.1.3.3 Interfacial polarization and distribution potential	
1.1.3.4 Potentiostatic polarization	
1.1.4 Thermodynamics of the liquid liquid interface.....	11
1.1.4.1 Fundamental thermodynamics equations	
1.1.4.2 Surface excess concentration and Gibbs adsorption equation	
1.1.4.3 Electrocapillarity	
1.1.5 Adsorption phenomenon.....	13
1.1.6 Ion transfer reactions.....	14
1.1.7 Electron transfer reactions.....	16
1.1.7.1 Background and remaining controversies	

1.1.7.2	Phenomenological expression of electron transfer rate constant	
1.1.7.3	Marcus's expression of rate constant of electron transfer	
1.1.7.4	Photoinduced electron transfer reactions	
<b>1.2</b>	<b>Introduction to nanoparticles (NPs)</b>	<b>21</b>
1.2.1	General introduction	21
1.2.2	Electronic properties	21
1.2.2.1	Metallic NPs	
1.2.2.2	Semiconducting NPs	
1.2.2.3	Surface effect and NP stability	
1.2.3	Optical properties	25
1.2.3.1	Optical absorption of NPs	
1.2.3.2	Size dependent optical properties	
1.2.3.3	Luminescence properties	
<b>1.3</b>	<b>NPs at liquid liquid interfaces</b>	<b>28</b>
1.3.1	Two-phase approach for preparation of NPs	28
1.3.2	Phase transport of NPs	29
1.3.3	Electrodeposition of NPs and their electrocatalysis	31
1.3.4	Potential induced assembly and reactivity of NPs	32
<b>1.4</b>	<b>The scope of the present thesis</b>	<b>34</b>
<b>1.5</b>	<b>References</b>	<b>36</b>

## Chapter 2 - Experimental and Instrumentations

<b>2.1</b>	<b>Electrochemical methods at liquid liquid interfaces</b>	<b>46</b>
2.1.1	The custom four-electrode system	
2.1.2	Preparation of reference electrodes and BTPPATPFB	
2.1.3	Cyclic voltammetry and the potential window	
2.1.4	Differential capacitance measurements	
<b>2.2</b>	<b>Photocurrent transient measurements</b>	<b>50</b>
<b>2.3</b>	<b>Quasi-elastic laser scattering (QELS)</b>	<b>51</b>
2.3.1	Capillary wave theory	

2.3.2	Principle of QELS method and experimental apparatus	
<b>2.4</b>	<b>Other electrochemical techniques</b>	<b>54</b>
2.4.1	Differential pulse voltammetry (DPV)	
2.4.2	Capillary electrophoresis: for measuring the charge of NPs	
<b>2.5</b>	<b>Spectroscopic and microscopic measurements</b>	<b>57</b>
<b>2.6</b>	<b>Synthesis and electrochemical measurements of gold NPs</b>	<b>58</b>
2.6.1	Mercaptosuccinic acid (MSA) stabilized gold NPs	
2.6.2	1-Hexanethiol monolayer protected gold nanoclusters	
2.6.3	Mixed-alkanethiol monolayer protected gold nanoclusters	
2.6.4	Electrochemical measurements of gold NPs	
<b>2.7</b>	<b>Chemical synthesis of CdSe NPs</b>	<b>63</b>
2.7.1	Mercaptosuccinic acid (MSA) stabilized CdSe NPs	
2.7.2	Citrate stabilized CdSe NPs	
<b>2.8</b>	<b>Preparation of room temperature ionic liquids (RTILs)</b>	<b>65</b>
<b>2.9</b>	<b>References</b>	<b>68</b>

## **Chapter 3 - Simulations of the adsorption of ionic species at liquid|liquid interfaces**

<b>3.1</b>	<b>Introduction</b>	<b>71</b>
<b>3.2</b>	<b>Theoretical and mathematical descriptions</b>	<b>72</b>
3.2.1	Microscopic model of the interfacial structure	
3.2.2	Potential distribution	
3.2.3	Charge density and differential capacitance	
3.2.4	Adsorption isotherms	
3.2.5	Simulation parameters	
<b>3.3</b>	<b>In the absence of adsorption</b>	<b>78</b>
<b>3.4</b>	<b>Potential independent isotherm</b>	<b>80</b>
<b>3.5</b>	<b>Langmuir isotherm</b>	<b>83</b>
<b>3.6</b>	<b>Frumkin isotherm</b>	<b>86</b>
<b>3.7</b>	<b>Other adsorption isotherms</b>	<b>89</b>

<b>3.8</b>	<b>Conclusions.....</b>	<b>90</b>
<b>3.9</b>	<b>References.....</b>	<b>91</b>
<b>3.10</b>	<b>Appendix: maple programs.....</b>	<b>92</b>

**Chapter 4 - Voltage induced assembly of gold NPs at the water|DCE interface**

<b>4.1</b>	<b>Introduction.....</b>	<b>103</b>
<b>4.2</b>	<b>Cyclic voltammetry and differential capacitance measurements.....</b>	<b>105</b>
<b>4.3</b>	<b>Assembly of gold NPs at the water DCE interface studied by Quasi-elastic laser scattering measurements.....</b>	<b>107</b>
	4.3.1 QELS measurements	
	4.3.2 Estimation of interfacial charge density and excess concentration	
<b>4.4</b>	<b>Apparent charge number of gold NPs.....</b>	<b>114</b>
<b>4.5</b>	<b>Assembly of gold NPs at the water DCE interface - Simulations.....</b>	<b>116</b>
<b>4.6</b>	<b>Conclusions.....</b>	<b>120</b>
<b>4.7</b>	<b>References.....</b>	<b>121</b>

**Chapter 5 - Assembly and photoreactivity of CdSe NPs at the water|DCE interface**

<b>5.1</b>	<b>Introduction.....</b>	<b>123</b>
<b>5.2</b>	<b>MSA-protected CdSe NPs.....</b>	<b>125</b>
	5.2.1 Spectroscopic characterization	
	5.2.2 Estimation of band edge	
	5.2.3 Voltage induced assembly at water DCE interfaces	
	5.2.4 Photoinduced electron transfer	
	5.2.5 Dynamic aspects of the photoinduced responses	
<b>5.3</b>	<b>Citrate protected CdSe NPs.....</b>	<b>138</b>

5.3.1 Spectroscopic characterization	
5.3.2 Photoreactivity at water DCE interfaces	
<b>5.4 Conclusions</b> .....	141
<b>5.5 References</b> .....	142

## Chapter 6 - Absolute standard redox potential of monolayer-protected gold nanoclusters

<b>6.1 Introduction</b> .....	145
<b>6.2 Absolute standard redox potential of MPCs</b> .....	147
6.2.1 Molecular capacitance model	
6.2.2 Absolute standard redox potential	
6.2.3 Determination of MPC charge	
<b>6.3 Solvent effect on redox properties of MPCs</b> .....	155
6.3.1 Solvents and supporting electrolyte	
6.3.2 Analysis of microelectrode cyclic voltammetric results	
6.3.3 Effect of the solvent dielectric constant	
<b>6.4 Redox properties of self-assembled MPCs</b> .....	165
6.4.1 Electrochemistry of freely diffusing MPCs	
6.4.2 Electrochemistry of self-assembled MPCs	
6.4.3 Effect of the electrostatic interaction between self-assembled MPCs and substrate electrode	
<b>6.5 Redox properties of self-assembled MPCs in RTILs</b> .....	172
6.5.1 In [bmim][PF <sub>6</sub> ]	
6.5.2 In [bmim][Tf <sub>2</sub> N] and [bmim][BF <sub>4</sub> ]	
6.5.3 Analysis of anion rectification effect	
<b>6.6 Conclusions</b> .....	177
<b>6.7 References</b> .....	178

**Chapter 7 - Reactivity of monolayer-protected gold nanoclusters at dye-sensitized water|DCE interfaces**

<b>7.1 Introduction.....</b>	<b>181</b>
<b>7.2 Photocurrent responses involving MPCs.....</b>	<b>182</b>
<b>7.3 Analysis of the photocurrent transient.....</b>	<b>189</b>
<b>7.4 Kinetic analysis of photoinduced electron transfer.....</b>	<b>192</b>
<b>7.5 Conclusions.....</b>	<b>196</b>
<b>7.6 References.....</b>	<b>196</b>
<b>7.7 Appendix to eq 7.16.....</b>	<b>200</b>

**Chapter 8 – Conclusions and outlook.....203**

**Curriculum Vitae.....207**



# Chapter 1

## Introduction to liquid|liquid interfaces and nanoparticles

### 1.1 Introduction to liquid|liquid interfaces

#### 1.1.1 Relevance and historic background

The interface between two immiscible liquids is a unique environment where the dielectric, structural, dynamical and thermodynamic properties are different from those of the bulk liquids. Processes occurring at this interface underlie many important phenomena in chemistry and biology. For example, the transport and exchange of mass across the liquid interface between lipid bilayer membranes and aqueous body fluids play key roles in life activity. All energy conversion processes in living organisms occur by nature at liquid interfaces. These interfaces are also fundamental to a variety of industrial applications including separation and extraction processes, phase transfer catalysis, electrochemical processes, and drug delivery in pharmacology.<sup>1,2</sup>

The study of the liquid|liquid interface dates back to at least the beginning of the last century. In the past 100 years, the experimental and theoretical developments have significantly enriched our knowledge and understanding of the properties of the interface between two immiscible liquids, mainly in two aspects:

- The structure of the interface, including the electrical double layers and potential distribution across the interface between two immiscible electrolyte solutions (ITIES) and the microscopic structure of the interface;
- The electrochemical reactions at the interface, including adsorption at the interface and charge transfer across the interface;

The structure of ITIES remains a rather controversial and interesting topic. Knowledge of the interfacial structure is a prerequisite for understanding chemical reactivity at the interface. Verwey and Niessen<sup>3</sup> proposed the first model describing ITIES as two back-to-back diffuse layers, in between which an inner layer of solvent molecules was later considered to exist. The resulting model, which is called modified Verwey-Niessen model, has been extensively used. Nowadays, microscopic information about the interface is mainly obtained from computer simulations together with up-to-date experimental techniques such as nonlinear optics, neutron and x-ray scattering and infrared spectroscopy.

Electrochemical reactions at the interface include molecular adsorption at the interface and charge transfer across the interface. The first study of a charge transfer process can be traced back to 1902 when Nernst and Riesenfeld observed the transfer of ions across the water|phenol interface using electrochemical methods.<sup>4</sup> However, progress on ITIES research has ever been very slow due to the unknown interfacial structure and potential distribution across the interface and, experimentally, to the large ohmic potential drop in the organic phase. The chemical control of the polarizability of ITIES by Gavach et al.<sup>5</sup> and the invention of the 4-electrode potentiostat with ohmic drop compensation by Samec et al.<sup>6</sup> have motivated a new round of research interest. In the past three decades, there has been a tremendous increase in research in the field of liquid|liquid interface with the emergence of various new techniques such as scanning electrochemical microscopy (SECM), microelectrode, and the combination of electrochemical and surface specific spectroscopic techniques. Various reviews and books have been published, concerning the advances in this field.<sup>7, 8</sup>

## 1.1.2 Electrical double layers

### 1.1.2.1 The Galvani potential difference

In the framework of thermodynamics, the work required to transfer one mole of ions from a vacuum to a liquid phase is defined as the electrochemical potential ( $\tilde{\mu}_i$ ):

$$\tilde{\mu}_i = \mu_i + z_i F \phi \quad (1.1)$$

where  $z_i$ ,  $F$  and  $\phi$  are the valence number of the ion, the Faraday constant and the inner potential or the Galvani potential, respectively.  $z_i F \phi$  is linked to the electrical work required to transfer the charge that the ion carries to the phase. The term  $\mu_i$  includes all the short-distance interactions between the ion and its environment, such as ion-dipole interactions and dispersion forces, and is generally called the chemical contribution of the electrochemical potential. In an ideal solution,  $\mu_i$  is given by:

$$\mu_i = \mu_i^\circ + RT \ln a_i \quad (1.2)$$

where  $\mu_i^\circ$ ,  $a_i$ ,  $R$  and  $T$  are the standard chemical potential, the activity of the ion, the gas constant and the temperature, respectively. Therefore, eq 1.1 is rewritten as:

$$\tilde{\mu}_i = \mu_i^\circ + RT \ln a_i + z_i F \phi \quad (1.3)$$

According to basic electrostatics, the electrical work  $z_i F \phi$  comprise two terms:

- a term associated with crossing the surface layer  $z_i F \chi$ ;
- a term associated with the charge of the phase  $z_i F \psi$ ;

$\chi$  is the surface potential of the liquid phase that originates from the preferred orientation of molecular dipoles at the surface.  $\psi$  is called the outer potential, which denotes the potential difference between the exterior of the surface of a charged object and a vacuum. Thus, the inner potential or Galvani potential of a phase is defined as the sum of the surface and outer potentials:

$$\phi = \chi + \psi \quad (1.4)$$

Therefore, when two immiscible liquids “w” and “o” are brought into contact, a Galvani potential difference happens in the contacting interfacial region:

$$\phi^w - \phi^o = (\chi^w - \chi^o) + (\psi^w - \psi^o) \quad (1.5)$$

or

$$\Delta_o^w \phi = \Delta_o^w \chi + \Delta_o^w \psi \quad (1.6)$$

where  $\Delta_o^w \phi$  expresses the Galvani potential difference between two phases.

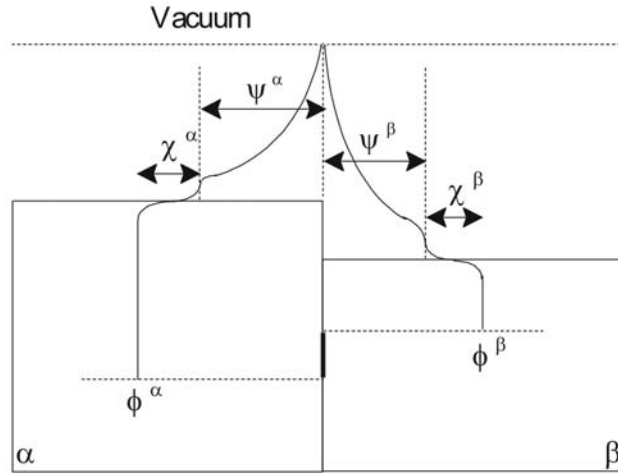


**Figure 1.1** Schematic illustrations of outer potential, surface potential and the Galvani potential for two phases in contact.

At the ITIES, the distribution of ions and dipoles at the interfacial boundary is principally different from that at the respective free surfaces. In the absence of specific adsorption at the interface,  $\Delta_o^w \phi$  can also be written as the sum of the ionic ( $\Delta_o^w \phi(\text{ion})$ ) and dipolar ( $\Delta_o^w \phi(\text{dip})$ ) contributions:

$$\Delta_o^w \phi = \Delta_o^w g(\text{ion}) + \Delta_o^w g(\text{dip}) \quad (1.7)$$

$\Delta_o^w \phi(\text{dip})$  is established as a result of the preferential orientation of solvent molecules at the interfacial region. However, there is a big difference between eqs 1.6 and 1.7 as  $\Delta_o^w \phi(\text{dip})$  is not equal to  $\Delta_o^w \chi$ . Indeed,  $\Delta_o^w \phi(\text{dip})$  is measurable only when the interface is in the zero charge state. Under this condition, the Galvani potential difference is equal to the dipolar term:

$$\Delta_o^w \phi = \Delta_o^w g(\text{dip}) \quad (1.8)$$

The Galvani potential difference at this point is named the potential at the point of zero charge (pzc), which can be changed by the specific adsorption and experimentally can be measured with a streaming electrode.

### 1.1.2.2 Modified Verwey-Niessen (MVN) model

Verwey and Niessen first described the electrical double layer at ITIES as two back-to-back diffuse layers, one of which contains an excess of the positive space charge and the other an equal excess of the negative space charge.<sup>3</sup> The distribution of  $\Delta_o^w \phi$  in the diffuse layers is described in terms of the Gouy-Chapman (GC) theory. Gavach extended this model by introducing an inner layer of oriented solvent molecules in between the two diffuse layers at ITIES.<sup>9</sup> The inner layer can either be free of the ions or accommodate ions as the specifically adsorbed particles. This description is referred to as the modified Verwey-Niessen (MVN) model. MVN model has been widely used although there have been some controversies on the nature of the inner layer.

### 1.1.2.3 Concerning inner layer: solvent mixing and ion interpenetration

*Mixed solvent layer model.* The thickness of the inner layer, as derived from the measurements of the surface excess of water employing a pendant drop method,<sup>10</sup> is dependent on the ionic size and the polarity of the organic solvent. In most cases, the thickness is less than that of a solvent monolayer. These results were rationalized in terms of the mixed solvation of ions and interfacial mixing. It seems unlikely that an ion free layer of either water or polar organic solvent is present, but rather the interface consists of a mixed solvent layer with its composition changing continuously from one media to the other.

*Lattice-gas model.* The mixed solvent layer and the effect of overlapping of the two space charge regions on double layer capacitance have also been considered using lattice-gas model.<sup>11</sup> The system of two immiscible liquids is assumed to be a three-dimensional cubic lattice. Each lattice site is occupied by one of a variety of particles, including solvent molecules and ions. The interactions between particles are restricted to nearest neighbors. Each ion is preferentially solvated by one solvent but badly solvable in the other. The most important result is that the roughness of the interface entails an overlap of the double-layer regions pertaining to the two solvents. This overlap decreases the average distance between the two opposing charges, and hence it decreases the capacity.

---

*Modified Poisson-Boltzmann model.* Studies based on surface tension and capacitance measurements suggested that the potential drop across the inner layer is very small while the inner layer capacitance is very high.<sup>12-14</sup> These results severely questioned the existence of an oriented interfacial dipole contribution. Samec et al. proposed that ions can penetrate into the inner layer over some distance,<sup>13</sup> which is in analogy to the treatment of electron spillover at the electrode|liquid interface with the help of the non-local electrostatic approach. The modified Poisson-Boltzmann (MPB) theory was employed to all three regions of the MVN model to correct the GC theory by accounting for the finite size of the ions and for image effects.<sup>14</sup>

#### **1.1.2.4 Capillary wave model**

Measurements of optical<sup>15</sup> and neutron reflectivity<sup>16</sup> and molecular dynamics simulations<sup>17</sup> show that the interface between two immiscible liquids is not ideally flat but somewhat corrugated with finger-like distortions. The distortion originates from the thermal fluctuations of the interface, which appear in the form of *capillary wave*. Capillary wave theory can give a direct connection between the maximum frequency of the interfacial capillary wave and its surface tension, which experimentally can be determined by quasi-elastic laser scattering (QELS) techniques.<sup>18</sup> The capillary wave theory and QELS technique will be briefly introduced in Chapter 2.

#### **1.1.2.5 Microscopic structure**

There are no experimental methods at the moment giving a proper description of the structure of the interface because of the relatively small size and the buried nature of the interface in comparison with other condensed-phase media. The interfacial image that we have at present mainly comes from the molecular dynamics simulations, which has revealed that the liquid|liquid boundary is molecularly sharp on the picosecond time scale.<sup>19</sup> However, interpenetration of two solvents gives rise to an interfacial roughness extending over about 1 nm, where the monotonic changes in the solvent distribution

occur and therefore the interface consists of a region where the dielectric, solvation and transport properties depend on the position along the normal to the interface.

However, it must be mentioned that the structure of the interface between two liquids relies on the property of the organic liquid, such as the polarity. More polar the organic liquid, more immiscible the two liquids and sharper the interface.<sup>10, 19</sup> Indeed, recently studies using vibrational sum-frequency generation spectroscopy as a probe of the structure, orientation, and bonding of water molecules at the liquid|liquid interface have shown that the water|1,2-dichloroethane (DCE) interface does not have the characteristics of a sharp interface but is molecularly disordered with properties similar to a mixed phase interfacial region,<sup>20</sup> which coincides well with the view of mixed solvent layer model.<sup>10</sup> In contrast, the interface is relatively sharp on a molecular level for nonpolar solvents such as alkanes and tetrachloroform (CCl<sub>4</sub>).<sup>20</sup>

### 1.1.3 Electrochemical equilibrium

#### 1.1.3.1 Ion partition equilibrium

At equilibrium, the distribution of an ionic species  $i$  at the ITIES yields:

$$\Delta G = \tilde{\mu}_i^o - \tilde{\mu}_i^w = 0 \quad (1.9)$$

where o and w refer to the organic and aqueous phases, respectively. And eq 1.9 can be rewritten in terms of eq 1.3 as:

$$\mu_i^{o,w} + RT \ln a_i^w + z_i F \phi^w = \mu_i^{o,o} + RT \ln a_i^o + z_i F \phi^o \quad (1.10)$$

Reorganization of eq 1.10 yields the Galvani potential difference  $\Delta_o^w \phi$ :

$$\Delta_o^w \phi = \phi^w - \phi^o = \Delta_o^w \phi_i^o + \frac{RT}{z_i F} \ln \left( \frac{a_i^o}{a_i^w} \right) \quad (1.11)$$

with  $\Delta_o^w \phi_i^o$  defined as the *standard ion transfer potential*, which is equal to:

$$\Delta_o^w \phi_i^o = \frac{\Delta G_{tr,i}^{o,w \rightarrow o}}{z_i F} = \frac{\mu_i^{o,o} - \mu_i^{o,w}}{z_i F} \quad (1.12)$$

where  $\Delta G_{tr,i}^{o,w \rightarrow o}$  is the *standard Gibbs transfer energy* of the species  $i$ .

### 1.1.3.2 Redox equilibrium

Considering the following heterogeneous electron transfer reaction between an oxidized species  $O_1^w$  in water and a reduced species  $R_2^o$  in an organic phase:



At equilibrium:

$$\Delta G = \left( \tilde{\mu}_{R_1}^w + \tilde{\mu}_{O_2}^o \right) - \left( \tilde{\mu}_{O_1}^w + \tilde{\mu}_{R_2}^o \right) = 0 \quad (1.14)$$

Extending the electrochemical potential terms in eq 1.14 gives:

$$\Delta_o^w \phi = \Delta_o^w \phi_{et}^o - \frac{RT}{nF} \ln \left( \frac{a_{O_1}^w a_{R_2}^o}{a_{R_1}^w a_{O_2}^o} \right) \quad (1.15)$$

where  $\Delta_o^w \phi_{et}^o$  is the *standard electron transfer potential* and is equal to:

$$\Delta_o^w \phi_{et}^o = \frac{\mu_{O_1}^{o,w} + \mu_{R_2}^{o,o} - \mu_{R_1}^{o,w} - \mu_{O_2}^{o,o}}{nF} = E_{O_2/R_2}^{o,o} - E_{O_1/R_1}^{o,w} \quad (1.16)$$

In actual analysis,  $E_{O_2/R_2}^{o,o}$  and  $E_{O_1/R_1}^{o,w}$  are required to be expressed in the same potential scale, for example, the standard hydrogen electrode (SHE) in water. In this case,  $E_{O_2/R_2}^{o,o}$  can be expressed in terms of a thermodynamic cycle involving the transfer of  $O_2$  and  $R_2$  across the interface:

$$E_{O_2/R_2}^{o,o} = E_{O_2/R_2}^{o,w} + \frac{\Delta G_{tr,O_2}^{o,w \rightarrow o} - \Delta G_{tr,R_2}^{o,w \rightarrow o}}{nF} \quad (1.17)$$

where  $\Delta G_{tr,O_2}^{o,w \rightarrow o}$  and  $\Delta G_{tr,R_2}^{o,w \rightarrow o}$  are the standard Gibbs transfer energies of  $O_2$  and  $R_2$  from aqueous to organic phase.

### 1.1.3.3 Interfacial polarization and distribution potential

*Non-polarizable interface.* In the presence of a binary 1:1 electrolyte  $A^+B^-$  in both phases, as illustrated in Figure 1.2, a non-polarizable interface will form. At equilibrium, we have the equality of the electrochemical potentials of both the cation and the anion:

$$\mu_{A^+}^{o,w} + RT \ln a_{A^+}^w + F\phi^w = \mu_{A^+}^{o,o} + RT \ln a_{A^+}^o + F\phi^o \quad (1.18)$$

$$\mu_{B^-}^{o,w} + RT \ln a_{B^-}^w - F\phi^w = \mu_{B^-}^{o,o} + RT \ln a_{B^-}^o - F\phi^o \quad (1.19)$$



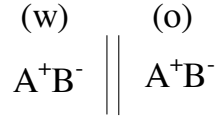


**Figure 1.2** Graphical representation of a non-polarizable liquid|liquid interface.

Therefore, the interfacial potential can be readily derived as:

$$\Delta_o^w \phi = \frac{\Delta_o^w \phi_{A^+}^o + \Delta_o^w \phi_{B^-}^o}{2} + \frac{RT}{2F} \ln \left( \frac{a_{A^+}^o a_{B^-}^w}{a_{A^+}^w a_{B^-}^o} \right) \quad (1.20)$$

Considering the electroneutrality in each phase ( $c_{A^+}^r = c_{B^-}^r$ ), the interfacial potential can be rewritten as:

$$\Delta_o^w \phi = \frac{\Delta_o^w \phi_{A^+}^{o'} + \Delta_o^w \phi_{B^-}^{o'}}{2} + \frac{RT}{2F} \ln \left( \frac{\gamma_{A^+}^o \gamma_{B^-}^w}{\gamma_{A^+}^w \gamma_{B^-}^o} \right) \quad (1.21)$$

Therefore, the interfacial Galvani potential difference is independent on the electrolyte concentration in the presence of equivalent electrolyte in both phases, and is essentially determined by the distribution of the salt. This potential difference is called the *distribution potential*.

*Polarizable interface.* The liquid|liquid interface is polarizable in the presence of very hydrophilic  $A^+B^-$  and very hydrophobic  $C^+D^-$  in phases “w” and “o”, respectively.

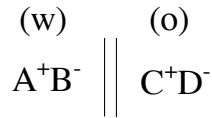


**Figure 1.3** Graphical representation of a polarizable liquid|liquid interface.

Under this condition,  $\Delta_o^w \phi$  is controlled by the electrical charge in the interfacial region, which can be supplied from the external voltage source. In a certain applied potential range, no experimentally observable faradaic current flows through the interface before the noticeable transfer of supporting electrolyte ions. The term "ideally polarizable" refers only to an electrostatic equilibrium where the constituents of each phase have infinite Gibbs energies of transfer, so that no faradaic process occurs at any polarization potential. However, it is clear that real ions have a finite solubility in any solvent. In

practice, the interface can only be polarized within a certain potential window, which is limited by the transfer of the electrolytes.

### 1.1.3.4 Potentiostatic polarization

Experimentally, potentiostatic polarization of the liquid|liquid interface is required to study electrochemical reactions at a certain Galvani potential difference, which simply allows tailoring the driving forces associated with the reactions by changing the Galvani potential difference between two phases.

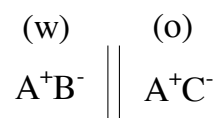


**Figure 1.4** Graphical representation of a polarizable liquid|liquid interface where the Galvani potential difference is controlled by a common ion.

Basically, there are two ways to perform potentiostatic polarization. One is by using a non-polarizable interface, where a single common ion is dissolved in the two phases. Figure 1.4 shows an example cell in which  $\text{A}^+$  functions as the common ion and the counterions  $\text{B}^-$  and  $\text{C}^-$  are hydrophilic and hydrophobic enough respectively to remain in their corresponding phase. Under this condition,  $\Delta_o^w\phi$  is determined by the activities of the common ion  $\text{A}^+$  in both phases:

$$\Delta_o^w\phi = \Delta_o^w\phi_{\text{A}^+}^{\circ} + \frac{RT}{F} \ln \left( \frac{a_{\text{A}^+}^{\circ}}{a_{\text{A}^+}^{\text{w}}} \right) \quad (1.22)$$

This type of polarization has been extensively employed to study the ion and electron transfer reactions using SECM.

Another way to implement potentiostatic polarization is simply using polarizable interface, where  $\Delta_o^w\phi$  can be supplied from the external voltage source by employing a certain reference, for example, the formal transfer potential of tetramethylammonium ( $\text{TMA}^+$ ).

## 1.1.4 Thermodynamics of the liquid|liquid interface

### 1.1.4.1 Fundamental thermodynamics equations

The state of a closed thermodynamic system is determined by a set of state functions, such as temperature ( $T$ ), pressure ( $P$ ) and internal energy ( $U$ ). For a single-phase system, its thermodynamics is described by the following fundamental equation:

$$dU = TdS - PdV + \sum_i \tilde{\mu}_i dn_i \quad (1.23)$$

However, for a two-phase system, there exists an interfacial layer in between two liquids where the thermodynamic properties are different from the bulk values. The changing of the interfacial area ( $A$ ) must involve mechanical work:

$$\delta W = \gamma dA \quad (1.24)$$

where  $\gamma$  is called the surface tension. Therefore, the internal energy of a liquid|liquid system reads:

$$dU = TdS - PdV + \gamma dA + \sum_i \tilde{\mu}_i dn_i \quad (1.25)$$

### 1.1.4.2 Surface excess concentration and Gibbs adsorption equation

The internal energy is a function of extensive variables and is a homogeneous first order state function. According to Euler's theorem for homogeneous functions, eq 1.25 can be presented in an integrated form:

$$U = TS - PV + \gamma A + \sum_i \tilde{\mu}_i n_i \quad (1.26)$$

Differentiating eq 1.26 yields:

$$dU = TdS + SdT - PdV - VdP + \gamma dA + Ad\gamma + \sum_i \tilde{\mu}_i dn_i + \sum_i n_i d\tilde{\mu}_i \quad (1.27)$$

Combining eq 1.25 with eq 1.27, we get the Gibbs-Duhem equation:

$$0 = SdT - VdP + Ad\gamma + \sum_i n_i d\tilde{\mu}_i \quad (1.28)$$

At constant temperature and pressure, eq 1.28 can be transformed to:

$$-d\gamma = \sum_i \frac{n_i}{A} d\tilde{\mu}_i = \sum_i \Gamma_i d\tilde{\mu}_i \quad (1.29)$$

where  $\Gamma_i$  is defined as the *surface excess concentration*. Eq 1.29 for the interface is called the *Gibbs adsorption equation*, which plays an important role in the interfacial thermodynamics.

### 1.1.4.3 Electrocapillarity

We shall consider an interface schematically shown in Figure 1.3 since the work within this thesis was mainly performed at the polarizable liquid|liquid interface. The Gibbs adsorption equation, eq 1.29, for this example can be written as:

$$-d\gamma = \Gamma_{A^+} d\tilde{\mu}_{A^+} + \Gamma_{B^-} d\tilde{\mu}_{B^-} + \Gamma_w d\mu_w + \Gamma_{C^+} d\tilde{\mu}_{C^+} + \Gamma_{D^-} d\tilde{\mu}_{D^-} + \Gamma_o d\mu_o \quad (1.30)$$

The changes of the chemical potentials of the salts,  $A^+B^-$  and  $C^+D^-$ , can be expressed as:

$$d\mu_{AB} = d\tilde{\mu}_{A^+} + d\tilde{\mu}_{B^-} \quad (1.31)$$

$$d\mu_{CD} = d\tilde{\mu}_{C^+} + d\tilde{\mu}_{D^-} \quad (1.32)$$

If neglecting the formation of interfacial ion-pairs for the two salts, we have:

$$\Gamma_{A^+} d\tilde{\mu}_{A^+} + \Gamma_{B^-} d\tilde{\mu}_{B^-} = \Gamma_{A^+} d\mu_{AB} - (\Gamma_{A^+} - \Gamma_{B^-}) d\tilde{\mu}_{B^-} \quad (1.33)$$

$$\Gamma_{C^+} d\tilde{\mu}_{C^+} + \Gamma_{D^-} d\tilde{\mu}_{D^-} = \Gamma_{C^+} d\mu_{CD} - (\Gamma_{C^+} - \Gamma_{D^-}) d\tilde{\mu}_{D^-} \quad (1.34)$$

The charge densities in each phase and the electroneutrality condition give:

$$\sigma^w = (\Gamma_{A^+} - \Gamma_{B^-}) F \quad (1.35)$$

$$\sigma^o = (\Gamma_{C^+} - \Gamma_{D^-}) F \quad (1.36)$$

$$\sigma^w + \sigma^o = 0 \quad (1.37)$$

Thus, eq 1.30 can be reorganized to be:

$$-d\gamma = \Gamma_{A^+} d\mu_{AB} + \Gamma_w d\mu_w + \Gamma_{C^+} d\mu_{CD} + \Gamma_o d\mu_o + \frac{\sigma^w}{F} (d\tilde{\mu}_{D^-} - d\tilde{\mu}_{B^-}) \quad (1.38)$$

The term in brackets in eq 1.38 represents the voltage imposed between the two contacting terminals of the electrochemical cell, which can be further related to the Galvani potential difference across the interface:

$$d\Delta_o^w \phi = (d\tilde{\mu}_{D^-} - d\tilde{\mu}_{B^-}) / F \quad (1.39)$$

Combining eqs 1.38 and 1.39, we get:

$$-d\gamma = \Gamma_{A^+} d\mu_{AB} + \Gamma_w d\mu_w + \Gamma_{C^+} d\mu_{CD} + \Gamma_o d\mu_o + \sigma^w d\Delta_o^w \phi \quad (1.40)$$

Experimentally, for a given system, the interfacial tension can be measured as a function of the Galvani potential difference. As well-known for the mercury|solution interface, the plotting of the interfacial tension versus the potential difference can be called the electrocapillary curve of the ITIES, whose slope indicates the surface excess charge density:

$$\sigma^w = - \left( \frac{d\gamma}{d\Delta_o^w \phi} \right)_{T,P,\mu_i} \quad (1.41)$$

This equation is the same in form as the well-known *Lippmann equation* at the metal|electrolyte interface. The interfacial charge density is in fact related to the surface excess of the ionic components. Experimentally, at a certain Galvani potential difference the surface tension can be measured as a function of the concentration of an ionic component, for example  $A^+$ . Then the *surface excess concentration* of  $A^+$  at this Galvani potential difference can be determined:

$$\Gamma_{A^+} = - \left( \frac{d\gamma}{d\mu_{AB}} \right)_{\Gamma_w, \Gamma_o, \Gamma_{c^+}, \Delta_o^w \phi} \quad (1.42)$$

### 1.1.5 Adsorption phenomenon

The liquid|liquid interface is a heterogeneous system involving two solvents of different solvation characteristics, which provides an interesting environment for the study of adsorption phenomenon. The study of the adsorption phenomenon at liquid|liquid interface has focused mainly on the following several aspects:

- Adsorption of compounds of biological importance
- Adsorption of surfactant and dye molecules
- Adsorption effect on the electrical double structure

Adsorption of biological molecules at the ITIES is helpful to understand the biological membrane phenomena, as primarily pointed out by Koryta *et al.*<sup>21</sup> The potential dependent formation of a monolayer or the aggregation of a series of phospholipids compounds,<sup>22-26</sup> has been observed at the polarized water|DCE or water|nitrobenzene (NB) interface by employing different experimental techniques, such as surface tension measurement<sup>27</sup> and Langmuir trough method.<sup>28</sup>

-----

Adsorption of surfactant and dye molecules at ITIES has been initially extensively studied employing electrocapillary and capacitance measurement and later by using surface sensitive optical and spectroscopic techniques. The adsorption of ionic surfactants and dyes, such as hexadecyltrimethylammonium (HTMA<sup>+</sup>),<sup>9</sup> demonstrate a pronounced dependence on the potential drop across the ITIES. However, the adsorption of nonionic surfactants, for example tetra-, hexa- and octaethylene glycol monododecyl ethers,<sup>29-32</sup> can take place over the entire range of the potential window.

It has been experimentally observed that the specific adsorption of HTMA<sup>+</sup> at the ITIES results in a significant change in the structure of the electrical double layer, probably the inversion of the inner potential from a negative to positive value.<sup>33</sup> Theoretical consideration of this phenomenon using the lattice gas model has shown that the specific adsorption affects the potential distribution markedly.<sup>34</sup> In some cases an overshoot of the potential can be observed, similarly to that observed for specific adsorption at metal electrodes. We shall introduce our recent theoretical work on the adsorption of ionic species at the ITIES using the classical Gouy-Chapmann theory in Chapter 3. It can be seen clearly that the adsorption has a strong influence on the potential profile across the interface, resulting in a non-monotonous potential distribution with a potential trap at the interface under certain conditions.

### 1.1.6 Ion transfer reactions

Ion transfer reaction at ITIES has been an area of active research for more than two decades.<sup>35, 36</sup> Various experimental approaches, which can be classified mainly into four types, have been employed to this area so far. The first type includes classical electrochemical galvanostatic or potentiostatic techniques<sup>6, 37-42</sup>, which were used in early studies and were applied mostly to ITIES with a macroscopic area (typically 0.1 cm<sup>2</sup>). The second type refers to the micro-ITIES supported at the tip of a glass micropipette<sup>43, 44</sup> or a polymer micro-hole.<sup>45</sup> Using a micro-ITIES can effectively reduce of resistive effect of the organic phase and enhance the mass transfer. The third type includes a series of techniques based on the combination of electrochemical and spectroscopic methods, such

as chronofluorometry,<sup>46</sup> chronoabsorptometry,<sup>47</sup> potential modulated reflectance<sup>48, 49</sup> and potential modulated fluorescence<sup>50, 51</sup> measurements. This type of methods features an advantage of being less sensitive to non-faradaic processes. The fourth type refers to the three-phase electrode, a simple system for the determination of formal ion transfer potentials,<sup>52, 53</sup> which can be obtained by immersion an electrode modified by a droplet or thin film of organic liquid containing electrochemically active molecules into an aqueous electrolyte solution. In this system, ion transfer is driven by electrochemically generating charged species in the droplet or thin film.

However, reliable kinetic data are difficult to obtain for ion transfer reactions due to the high solution resistance (typically 200-300  $\Omega$ ) compared with the kinetic resistance (typically  $< 10 \Omega$ ). The obtained kinetic data are rather scattered with standard rate constants ranging from  $10^{-4}$  to  $10 \text{ cm s}^{-1}$ ,<sup>6, 12, 41, 48, 49, 54-61</sup> dependent on the experimental methodology. The theoretical description of ion transfer reactions still remains controversial owing to uncertainties concerning the interfacial structure and potential distribution across the ITIES. There have been a number of theories put forward using different approaches, classical,<sup>37, 62</sup> diffusion<sup>57, 63</sup> and stochastic,<sup>64, 65</sup> as well as those provided by computer simulations.<sup>66-72</sup> The main question at present is whether to describe the ion transfer reaction as a chemical reaction or simply as a transport process.

Earlier experimentally obtained kinetic data for ion transfer reactions appeared to follow a Butler-Volmer relationship,<sup>37, 40, 63, 73-75</sup> which supports the idea that the ion transfer reaction involves an activated state. The kinetic barrier has been considered to be most probably associated with the existence of the compact solvent layer at the interface.<sup>63</sup> The difficulty of this model resides in the description of the potential profile across the interface. Furthermore, impedance measurements at micro-interface concluded that ion transfer is very fast with a rate constant as high as  $32 \text{ cm s}^{-1}$ ,<sup>61</sup> which questioned the kinetic control of the ion transfer process.

The idea of ion transfer across a liquid|liquid interface being more similar to the migration and diffusion transport in a distinct medium than a chemical reaction was first proposed by Girault and Shiffrin,<sup>73</sup> although they still considered the ion transfer process as an activated jump based on the Stearn and Eyring model of ionic transport in liquids.<sup>76</sup>

Another controversial point is the dependence of the bimolecular rate constant on the Galvani potential difference. Most experimental results support the assumption that the electron transfer is driven by the Galvani potential difference across the interface.<sup>82-84, 92-94, 106-109</sup> Accordingly, the potential dependence of the rate constant obeys the Butler-Volmer equation and levels off at much higher overpotentials in terms of the Marcus theory.<sup>110-112</sup> However, few experimental works have reported the potential independence of the electron transfer rate constants.<sup>95, 98, 113</sup> This deviation was supposed to arise from the concentration polarization, which is also supported by the computer simulations using a lattice-gas model. All these facts suggest that the potential and ionic distributions are far more complex than what is described by current modeling.

### 1.1.7.2 Phenomenological expression of electron transfer rate constant

The theory of outer-sphere electron transfer has been well developed and generally gives an expression in the form:

$$k_{\text{et}} = Z \exp\left(-\frac{\Delta G_{\text{act}}}{RT}\right) \quad (1.43)$$

where  $\Delta G_{\text{act}}$  is the Gibbs free energy of activation and  $Z$  is a pre-exponential factor. The physical compositions of both parameters are dependent on the microscopic model considered.

Phenomenologically, the obtained electron transfer rate constants for reactions under low driving forces were found to follow Butler-Volmer relationship. The activation energy associated with the heterogeneous electron transfer is affected by a fraction,  $\alpha$ , of the Galvani potential difference:

$$\Delta G_{\text{act}} = \Delta G_{\text{act}}^{\circ} - \alpha n F (\Delta_o^{\text{w}} \phi - \Delta_o^{\text{w}} \phi_{\text{et}}^{\circ}) \quad (1.44)$$

where  $\Delta G_{\text{act}}^{\circ}$  and  $\Delta_o^{\text{w}} \phi_{\text{et}}^{\circ}$  correspond to the Gibbs activation energy at equilibrium state and the standard electron transfer Galvani potential difference, respectively. Thus, the forward electron transfer rate constant can be described as:

$$k_{\text{et}} = k_{\text{et}}^{\circ} \exp\left[\frac{\alpha n F}{RT} (\Delta_o^{\text{w}} \phi - \Delta_o^{\text{w}} \phi_{\text{et}}^{\circ})\right] \quad (1.45)$$

with



-----

This idea was later developed by several groups using the Nernst-Planck equation,<sup>77-80</sup> which has shown that ionic motion across the interface is more likely similar to that in the bulk solution. This model is also supported by molecular dynamic simulations.<sup>66</sup> Ion transfer kinetics has been well documented in two recent reviews.<sup>35, 36</sup>

## 1.1.7 Electron transfer reactions

### 1.1.7.1 Background and remaining controversies

Since the pioneering work of Samec et al.,<sup>81</sup> electron transfer reactions at the ITIES have been extensively studied. Various experimental techniques primarily developed for kinetic measurements of ion transfer reactions have also been applied to electron transfer.<sup>42, 82-89</sup> However, only few works employing these techniques reported kinetic data for electron transfer reactions, because of lacking information on the interfacial structure and the potential distribution across the ITIES. Since the mid-1990s, the application of spectroelectrochemical techniques,<sup>90-92</sup> scanning electrochemical microscopy (SECM)<sup>93-96</sup>, thin-layer solvent methods<sup>97-99</sup> and dynamic photoelectrochemical techniques<sup>100-102</sup> has greatly enriched our knowledge of the correlation between structure and reactivity at this molecular interface. These heterogeneous processes have been considered to be significant not only in regard to life-sustaining redox biological processes<sup>103</sup> but also to the important applications in energy conversion area.<sup>104</sup>

The first controversial point is that the location where the electron transfer reaction takes place. Samec et al. supposed that the electron transfer step occurs across the ion-free layer composed of oriented solvent molecules.<sup>105</sup> In contrast, Girault and Schiffrin considered that it happens across a mixed solvent region where electrochemical potentials are dependent on the position of the reactants at the interface.<sup>73</sup> This difference is translated in the physical meaning of the pre-exponential term of the phenomenological rate constant expression.

$$\alpha = \frac{RT}{nF} \left[ \frac{\partial \ln k_{\text{et}}}{\partial (\Delta_o^w \phi)} \right] \quad (1.46)$$

where  $k_{\text{et}}^\circ$  is called the standard rate constant. It should be noted that this simple derivation only represents a macroscopic theory, in which the reaction rate was expressed in terms of two phenomenological parameters,  $\alpha$  and  $k_{\text{et}}^\circ$ . This approach cannot predict how the kinetics is affected by microscopic parameters such as the distance separating the redox species, the nature and structure of the redox species and the solvent.

### 1.1.7.3 Marcus expression of the rate constant of electron transfer

In a series of papers, Marcus developed the electron transfer theory from a microscopic point of view,<sup>110-112</sup> yielding an expression for  $k_{\text{et}}$  at a molecularly sharp interface:

$$k_{\text{et}} = 2\pi (a_1 + a_2) (\Delta R)^3 \nu_n \kappa_{\text{el}} \exp\left(-\frac{\Delta G_{\text{act}}}{RT}\right) \quad (1.47)$$

where  $\nu_n$  is the nuclear frequency factor ( $\text{s}^{-1}$ ), which represents the frequency of attempts on the energy barrier (associated with the nuclear vibrations and solvent motion).  $\kappa_{\text{el}}$  is the electronic transmission coefficient (or Landau-Zener factor), which indicates the probability of the electron transfer. This probability obviously depends on the interaction or electronic coupling of the reactants. In the presence of a strong interaction, the electron transfer proceeds with a nearly unit probability and the reaction is said to be adiabatic. If the interaction is weak, the electron transfer reaction occurs with a smaller likelihood and is said to be nonadiabatic. The parameters  $a_1$  and  $a_2$  in eq 1.47 refer to the radii of the two reactants  $\text{O}_1^w$  and  $\text{R}_2^o$ , respectively.  $\Delta R$  is defined as the region beyond the core-to-core distance ( $R$ ) of the two reactants, over which the contribution to the electron transfer is significant.

Correspondingly, the Gibbs free energy of activation,  $\Delta G_{\text{act}}$ , is derived as:

$$\Delta G_{\text{act}} = \frac{\lambda}{4} \left( 1 + \frac{\Delta G_{\text{et}}^{\circ'} - w_{\text{O}} + w_{\text{R}}}{\lambda} \right) \quad (1.48)$$

where  $w_O$  and  $w_R$  represent the work terms associated with bringing the reactants and removing the products to and from the interface.  $\Delta G_{et}^{\circ}$  is the formal Gibbs free energy, for an electron transfer reaction, which corresponds to the so-called driving force and is dependent on the Galvani potential difference with the following expression:

$$\Delta G_{et}^{\circ} = -nF(\Delta_o^w\phi - \Delta_o^w\phi_{et}^{\circ}) \quad (1.49)$$

The total reorganization energy,  $\lambda$  in eq 1.48, represents the energy necessary to transform the nuclear configurations in the reactants as well as the surrounding solvation spheres to a certain configuration where electron transfer occurs.

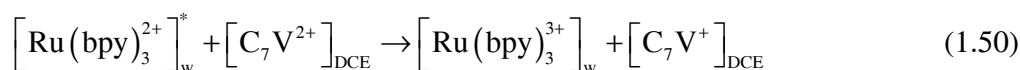
#### 1.1.7.4 Photoinduced electron transfer reactions

Photoinduced electron transfer reactions at the interface between two immiscible liquids have been widely recognized as a model system for natural photosynthesis and heterogeneous photocatalysis.<sup>1, 2, 114-116</sup> In 1960s when Rabinowitch *et al.*<sup>117, 118</sup> studied the photochemical reactions at the interface between immiscible liquids, they pointed out that the higher energy conversion of artificial photosynthesis could be achieved by dividing the photoproducts between two phases in a heterogeneous system. In 1970s, Volkov *et al.* found that the chlorophyll adsorbed at the interface of two immiscible liquids could photocatalyze the electron transfer between a hydrophilic donor and a hydrophobic acceptor.<sup>119, 120</sup> This work presented the possibility of converting solar energy into electrochemical energy at ITIES and encouraged very intensive research in the field of photochemistry at liquid|liquid interfaces.

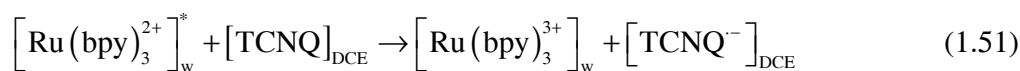
A series of papers by Volkov *et al.* have demonstrated that the oligomers of chlorophyll *a* immobilized at the hydrocarbon|water interface could catalyze oxygen evolution during the photooxidation of water.<sup>121-128</sup> This work threw many concerns on the biological perspective of the system. Soon afterwards, the different effects associated with photoinduced processes at the polarized liquid|liquid interface were investigated by Girault and coworkers,<sup>129, 130</sup> De Armond and coworkers,<sup>131-133</sup> and Kotov and Kuzmin.<sup>134-137</sup> Most of these works were concerned with photoelectrochemical effects at the polarizable liquid|liquid junction, including the generation of photocurrent or photopotential. The system studied mostly featured the homogeneous generation of

charged photoproducts, followed by the transfer of these species across the liquid|liquid interface. These fundamental studies have been reviewed recently.<sup>138</sup>

The photocurrent response associated with heterogeneous electron transfer across the water|DCE interface was first reported by Girault *et al.*<sup>139</sup> The photoreduction of 1,1'-diheptyl-4,4'-bipyridinium ( $C_7V^{2+}$ ) in the organic phase by photoactive tri(2,2'-bipyridine)ruthenium(II) ( $Ru(bpy)_3^{2+}$ ) located in the aqueous phase was studied:



The photocurrent responses were measured under chopped illumination and lock-in detection. However, the observed photocurrent responses may suffer from the effects of ion transfer, photopotential and quenching of  $Ru(bpy)_3^{2+}$  by TPB.<sup>140</sup> Later they modified the system as follows:<sup>140</sup>



7,7',8,8'-tetracyanoquinodimethane (TCNQ) was used as the organic quencher. The water|DCE interface was polarized with a four-electrode potentiostat and a more inert organic supporting electrolyte was employed. All these conditions ensured that the photocurrent responses were related to heterogeneous electron transfer across the water|DCE interface.

Recently, a series of papers were published on photocurrent responses involving porphyrin species and semiconducting nanoparticles, as well as various aspects involved in the kinetics of photoinduced electron transfer at ITIES.<sup>91, 92, 102, 104, 108, 109, 141-146</sup> These studies threw new light on the possible way of conducting photoelectric energy conversion. Indeed, the analysis of the output power of a porphyrin-sensitized water|DCE interface has been reported.<sup>104</sup> Although the conversion efficiency was estimated to be rather low, from 0.01% to 0.1%, it remains to be very promising and worthy of further studying. On the other hand, in comparison to electron transfer responses observed electrochemically, the photocurrent is initiated by light excitation of reactive dyes. Therefore, not only concentration polarization phenomenon can be effectively avoided, but also large driving forces can be attained.<sup>108, 109</sup> This allows a detailed analysis of electron transfer reactions at the ITIES.

## 1.2 Introduction to nanoparticles (NPs)

### 1.2.1 General introduction

Nanoparticles (NPs) have fascinated scientists for a long time because of their brilliant colorful colloidal solutions. Gold NPs were used as ruby-colored pigment by the Chinese in coloring vases and other ornaments and throughout Europe in stained glass windows of cathedrals. Nowadays, NPs refer to a class of materials with relevant physical dimensions on the length scale of 1-100 nm. They serve as bridges from molecules to condensed matter, and therefore belong to a new realm of matter that lies between chemistry and solid-state physics. The scientific research dealing with the chemical, optical, electronic, and magnetic properties of NPs is growing fast worldwide and remains one of the most dynamic fields in nanoscience and nanotechnology. The interest stems from the fact that these properties are very different from those of the bulk materials and isolated atoms or molecules with the same chemical composition and, equally important, that these properties are often strongly dependent on the particle size, shape and surface modification. Furthermore, the interest has been sparked by their potential applications, ranging from microelectronics to nonlinear optics, optoelectronics, catalysis, photography and electrochemistry.<sup>147</sup>

### 1.2.2 Electronic properties

The size-dependent properties of NPs can be attributed to two main factors: their small size and extremely large surface-to-volume ( $S/V$ ) ratio. These two are interrelated since the  $S/V$  ratio increases as the size decrease, for example,  $S/V = 3/r$  for a spherical particle. In general, the density of electronic states (DOS) decreases and the energy level spacing increases as a consequence of reducing the dimensionality, which means that a charge carrier in NPs is no longer solvated in an effectively infinite medium. From a quantum mechanical point of view, it is due to the spatial confinement of the wave function of charge carriers, which is termed quantum size confinement and result in the quantization of energy states. With this property, NPs are sometimes called quantum dots or artificial molecules.

### 1.2.2.1 Metallic NPs

The energetic band structures in a metallic atom, a metallic NP and a bulk metal are compared in Figure 1.5. The bulk metal has a band structure that consists of a large number of electronic levels with very similar energy. In a metallic atom, the electronic structure features a series of discrete energetic levels with a highest occupied molecular orbital (HOMO) and a lowest unoccupied molecular orbital (LUMO). However, in a NP consisting of a few tens or hundreds of atoms, the structured *s*- and *d*-bands are beginning to be split and disappear and discrete energy levels are appearing but not truly forming. There is no sharp borderline between these two fundamental situations, but this transition is continuous. The description of bulk metals is made in terms of the laws of classical physics. And quantum mechanics is a well-established theory for describing the electronic situation in molecules and atoms. So far, there is nothing new, however, in relation to NPs. The model of the “electron in a box”, normally used for atoms, helps to describe simply the situation in small metal particles when size restriction begin to influence electronic behavior.

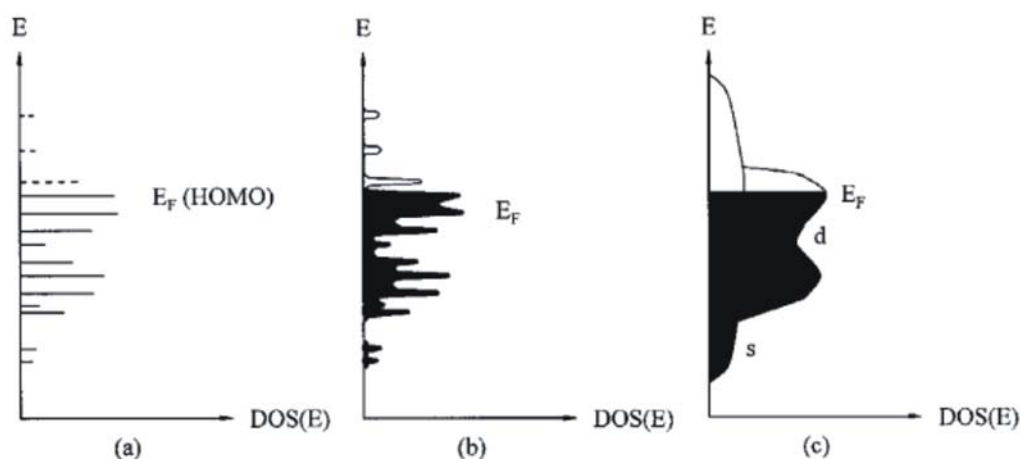


**Figure 1.5** Comparison of the electronic band structure of a metallic atom (a), a metallic NP (b) and a bulk metal (c).  $E_F$  = Fermi energy; DOS = density of states.

The most important property of a metal is its conductivity. For example, in  $d^{10}$  elements such as palladium, platinum, or gold, the *s*-bands can function as unoccupied bands for transfer of electrons located in the fully occupied *d*-bands. The conductivity in the bulk metal follows the classic Ohm's law. However, as a metal particle becomes small

enough, discrete energy levels finally dominate and, as a consequence, ohms law is no longer valid. Indeed, small gold NPs consisting of less than 200 gold atoms do not show a linear current response with respect to the potential but a successive single electron transfer behavior even at room temperature.<sup>148</sup> We shall consider this behavior from an electrostatic point of view in Chapter 7.

### 1.2.2.2 Semiconducting NPs

According to the theory of energy levels in solid-state physics, the electronic properties of a bulk semiconductor are determined by the energy band gap ( $E_g$ ) between valence band (VB) and conduction band (CB):

$$E_g = E_{CB} - E_{VB} \quad (1.52)$$

As particles become smaller, their electronic structure changes, and eventually the charge carriers produces discrete energy states in the valence and conduction bands due to local confinement: there is no sufficient space for electron-hole pairs to form. The electronic and optical properties of such small particles are hence more like those of a molecule than an extended solid. Size dependent effects are expected to occur when the particle size become smaller than the Bohr radius of the first exciton in the bulk semiconductor. The Bohr radius is defined as:

$$r_B = \frac{h^2 \epsilon_0 \epsilon_r}{\pi e^2 m^* m_0} \quad (1.53)$$

where  $h$  is the Plank constant.  $\epsilon_0$  and  $\epsilon_r$  are the dielectric constants of the vacuum and the semiconducting material, respectively.  $e$ ,  $m^*$  and  $m_0$  are the elementary charge, the effective mass of the charge carriers and the electron mass, respectively. In general, semiconducting NPs with physical dimensions smaller than  $r_B$  are termed quantum dots. In quantum dots, the band gap energy becomes size-dependent:<sup>149</sup>

$$E_g(\text{QDs}) = E_g(\text{bulk}) + \frac{h^2}{8r^2} \left( \frac{1}{m_e^* m_0} + \frac{1}{m_h^* m_0} \right) - \frac{1.8e^2}{4\pi\epsilon_0 \epsilon_r r} - \frac{0.124e^4}{h^2 (4\pi\epsilon_0 \epsilon_r)^2} \left( \frac{1}{m_e^* m_0} + \frac{1}{m_h^* m_0} \right)^{-1} \quad (1.54)$$

The first term is the band gap energy of the bulk semiconductor,  $r$  is the particle radius,  $m_e^*$  and  $m_h^*$  are the effective mass of the electron and hole, respectively. The third term

---

shifts  $E_g$  (QDs) to smaller energy as  $r$ , while the second term shifts  $E_g$  (QDs) to higher energy as  $r^2$ . The fourth term is generally very small. Thus the apparent band gap energy will always increase for small enough  $r$ .

### 1.2.2.3 Surface effect and NP stability

With decreasing the size of metal particles, the percentage of surface atoms increases. This is an important point to be considered when one discusses NP properties. The influence of surface atoms becomes more important the smaller the particle is. Strictly speaking, only the inner-core atoms represent a minute piece of the bulk with strong quantum size effects. Physical measurements that give averaged information on the total particle are therefore always to be considered in this light. Another surface effect is equally important: NPs in general are provided with a protective shell of ligand molecules. Otherwise, we would not be able to prepare them by chemical methods and especially to isolate and to investigate them as individual particles.

NPs can be stabilized electrostatically in solutions. Basically, the repulsive interactions of diffuse layers around NPs offsets the van der Waals interactions. The sum of these two energies determines the particle stability. High diffuse layer potentials and low electrolyte concentrations, which increase the range of repulsion, are necessary for NP stability. A typical example is the stabilization of gold NPs prepared by citrate reduction following the Turkevich method.<sup>150</sup> In this case, gold NPs are stabilized by an electric double layer composed of bulky citrate ions, chloride ions and the cations attached to them.

In contrast to the charge-stabilization of NPs, the stabilization of NPs by ligands which form chemical bonds with or chemisorb onto the particle surface are an effective method, which also enable NPs use for a variety of purposes. A typical example is the stabilization of gold NPs by molecules with mercaptan groups, which have a very strong affinity for gold surfaces and ensure the formation of a dense monolayer on the surface. The merit of this approach is that the stabilized NPs can be repeatedly isolated from and dissolved in the dispersing solvent without irreversible aggregation or decomposition. Importantly, further functionalization is possible by ligand-exchange reactions.



## 1.2.3 Optical properties

### 1.2.3.1 Optical absorption of NPs

According to Lambert-Beer law, for a dilute colloidal solution, if the particles are much smaller than the incident light wavelength, the electric dipole absorption is predominant:

$$A = \lg\left(\frac{I_0}{I}\right) = \frac{N\sigma l}{2.303} \quad (1.55)$$

where  $l$  in cm is the light path in a spectrophotometer,  $N$  in  $\text{cm}^{-3}$  is the number density of the particle and  $\sigma$  is the extinction cross-section of a single particle in  $\text{cm}^2$ .

For a metallic NP,  $\sigma$  is given by:

$$\sigma = \frac{24\pi^2 r^3 \varepsilon_m^{3/2} \varepsilon_2}{\lambda(\varepsilon_1 + 2\varepsilon_m)^2 + \varepsilon_2^2} \quad (1.56)$$

where  $\lambda$  is the wavelength of the incident light,  $r$  is the particle radius,  $\varepsilon_m$  is the dielectric function of the medium,  $\varepsilon_1$  and  $\varepsilon_2$  are the real and imaginary parts of the complex dielectric function of the particle ( $\varepsilon = \varepsilon_1 + i\varepsilon_2$ ). Considering the motions of electrons in a spherical metal NP under the effect of an electric field vector of the light, it is possible to get:

$$\varepsilon_1 = \varepsilon^\infty - \frac{\omega_p^2}{\omega^2 + \omega_d^2} \quad (1.57)$$

$$\varepsilon_2 = \frac{\omega_p^2 \omega_d}{\omega(\omega^2 + \omega_d^2)} \quad (1.58)$$

where  $\omega$  is the frequency of the incident light,  $\varepsilon^\infty$  is the high-frequency dielectric constant,  $\omega_d$  is the relaxation or damping frequency and  $\omega_p$  is the bulk plasma frequency.

For a semiconductor NP, if the optical transitions far from the strong resonance and far from the band edges where the density of states could be approximated as a continuum, its extinction cross-section can be formalized to the sum of the absorption ( $\sigma_{\text{abs}}$ ) and scattering ( $\sigma_{\text{scat}}$ ) cross sections:<sup>151</sup>

$$\sigma_{\text{ex}} = \sigma_{\text{abs}} + \sigma_{\text{scat}} \quad (1.59)$$

For particles with radii much smaller than the light wavelength,  $\sigma_{\text{abs}}$  is much larger than  $\sigma_{\text{scat}}$ . Therefore, the latter can be neglected. Then for the absorbing particles with isotropic polarizability,  $\sigma_{\text{abs}}$  can be evaluated from:

$$\sigma = 4\pi k \operatorname{Re}(i\alpha) = \frac{8\pi^2 m_2}{\lambda} \operatorname{Re}(i\alpha) \quad (1.60)$$

where  $k$  is the wave vector and  $\lambda$  the light wavelength.  $\alpha$  is the polarizability of the dielectric sphere:

$$\alpha = \frac{m_1^2 - m_2^2}{m_1^2 + 2m_2^2} a^3 \quad (1.61)$$

where  $a$  is the radius of the particle,  $m_1 = n_1 - ik_1$  and  $m_2 = n_2 - ik_2$  are the complex refractive indices of the particle and the solvent. Thus,  $\sigma_{\text{abs}}$  is given by:

$$\begin{aligned} \sigma_{\text{abs}} = & \frac{8\pi^2 m_2}{\lambda} \\ & \times \frac{(2n_1 k_1 - 2n_2 k_2)(n_1^2 - k_1^2 + 2n_2^2 - 2k_2^2) - (n_1^2 - k_1^2 - n_2^2 + k_2^2)(2n_1 k_1 + 4n_2 k_2)}{(n_1^2 - k_1^2 + 2n_2^2 - 2k_2^2)^2 + (2n_1 k_1 + 4n_2 k_2)^2} \end{aligned} \quad (1.62)$$

### 1.2.3.2 Size dependent optical properties

For a bulk metal, there is:

$$\omega_d = \frac{v_F}{r_\infty} \quad (1.63)$$

where  $v_F$  is the electron velocity at Fermi level and  $r_\infty$  the mean free path of the electron in the bulk metal. When the particle radius,  $r$ , is smaller than  $r_\infty$ , the mean free path,  $R$ , becomes size-dependent with:

$$\frac{1}{R} = \frac{1}{r} + \frac{1}{r_\infty} \quad (1.64)$$

It can be seen that a decrease in the particle size leads to an increase in  $\omega_d$ , causing the band to broaden and the maximum intensity to decrease. The peak position is virtually unaffected by small changes of  $\omega_d$ , but for large damping frequencies a slow shift to

lower energies occurs. For rather small particles (< 1-2 nm), quantization of the energy levels within the conduction band takes place as the metal character of the particles begins to disappear, and the plasmon band characteristic of the delocalized electrons breaks up into discrete bands due to single electron optical transitions.

For semiconducting NPs, the fundamental absorption edge is related to the band gap energy via:

$$\lambda_g \text{ (nm)} = \frac{1240}{E_g \text{ (eV)}} \quad (1.65)$$

Since in quantum dots the effective band gap increases with decreasing size of the particles, accordingly, a blue shift in the band edge absorption will be observed.

### 1.2.3.3 Luminescence properties

For a  $d^{10}$  metallic NP, absorption of light by the  $d$ -band electrons leads to interband transitions of these electrons to the empty  $sp$ -conduction band above the Fermi level. Both electrons and holes can relax by scattering with phonons then recombine radiatively to give rise to the visible luminescence.<sup>152</sup>

Light excitation of a semiconducting NP with an energy higher than that of the band gap leads to an electron-hole pair in the NP. The recombination lifetime of this excitation is usually small (in the picosecond to microsecond range) depending on the recombination pathway. Ideally, the luminescence of semiconducting NPs should be size dependent as that of the excitation. But it is not the case. First, the nature of the NP surface strongly influences the luminescence through the surface trap states, which may result from a lot of factors, such as structural defects, atomic vacancies, dangling bonds, and adsorbates at the interface. For well-passivated surfaces, the luminescence of the NPs is indeed very strong and is blue-shifted when the NP size is decreased. The luminescence is attributed to the radiative band-gap or near-band-gap (shallow trap states) recombination. However, if the electrons and/or holes are able to crossover into traps of various energy levels, the possibility of radiative recombination is decreased. A weak, broad, and substantially red-shifted luminescence band is usually observed, indicating the loss of the radiationless recombination.<sup>153, 154</sup> Second, if the holes or electrons are preferentially scavenged by a

reducing or oxidizing species, the NP is left with electrons (or holes) solely. As electrons and holes are separated into two different phases, the lifetime of the charge carriers in the NP can be relatively long.<sup>155</sup> Third, electrons can be injected into semiconducting NPs using strong reducing species. The oxidized species form then the positive countercharge, compensating the charge of the electrons in the NPs.<sup>156, 157</sup>

### **1.3 NPs at liquid|liquid interfaces**

#### **1.3.1 Two-phase approach for preparation of NPs**

The two-phase method proposed by Brust and Schiffrin<sup>158</sup> is a great contribution to the field of chemical preparation of metallic NPs. In fact, the two-phase approach was initially introduced by Faraday,<sup>159</sup> who prepared a ruby colored aqueous solution of dispersed gold particles by reducing an aqueous gold salt with phosphorus in carbon disulfide. Combining Faraday's method with the concept of self-assembled monolayer of alkanethiol on planar gold electrode surface, Brust and Schiffrin designed a new strategy to prepare derivatized gold NPs.

The reaction occurs in a water|toluene two-phase system, which is expected to be able to well separate the nucleation and growth processes in the presence of surface stabilization. Briefly, the aqueous metal salt,  $\text{AuCl}_4^-$ , is first transferred into toluene using tetraoctylammonium bromide as the phase transfer agent. The reduction is carried out by adding sodium borohydride aqueous solution in the presence of dodecanethiol ( $\text{C}_{12}\text{H}_{25}\text{SH}$ ). The initial ratio between capping molecule and metal salt can be adjusted to control the relative rates of particle nucleation and growth, and finally determine the particle size. The Au NPs prepared with this approach have high stability and can be repeatedly precipitated and redispersed. Most importantly, they allow further functionalization and other manipulations. The two-phase approach has been extended to prepare other noble metallic NPs, such as Ag, Pt and Pd. Although many new routes have

been proposed afterwards, this two-phase approach still remains the most effective and efficient way to prepare hydrophobic metallic NPs.

On the other hand, material scientists have attempted to synthesize NPs in-situ at the liquid|liquid interface (Note that this technique differs from the electrodeposition described in Section 1.3.3). This method has been named the liquid|liquid interface reaction technique (LLIRT). Different types of NPs but mainly semiconducting NPs, including CdSe, CdS, ZnS, CuInS<sub>2</sub>, ZnO and Fe<sub>2</sub>O<sub>3</sub>, have been reported.<sup>160-166</sup> Principally, LLIRT involves the precipitation reactions at the interface by contacting the organic solution of nonmetallic precursors (S, Se) with the aqueous solution of metallic precursors (Cd, Zn, Cu or In), with one exception in which the situation is completely reverse.<sup>167</sup> The advantage of this technique is that no stabilizing/capping agents are used. Therefore, eventually the NPs will grow into two-dimensional nanocrystalline particulate thin film, which can be transferred onto the suitable substrate to be further characterized.

### 1.3.2 Phase transport of NPs

The compatibility of NPs with the physicochemical environment is a critical point for different applications. For example, water-soluble NPs are needed for biomedical applications, while a compatibility of NPs with common organic solvents, monomers, and polymers is desired for their applications in the optoelectronic field. Therefore, the chemical synthesis and proper surface modification of NPs become more and more significant. Nevertheless, in most cases the NPs are prepared only in either the aqueous phase or the organic phase. Both routes have their own advantages and drawbacks. The ideal condition would be to somehow find a way to switch the compatibility of NPs. Towards this purpose, much research efforts have been invested to develop simple and sufficiently effective protocols allowing the transport of NPs synthesized in one medium (water/organic solvent) to another medium (organic solvent/water).<sup>168</sup>

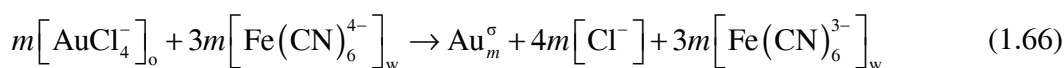
The transport of a wide variety of metallic and semiconducting NPs has been achieved by using various methods. Essentially, transport of NPs between water and organic solvent requires hydrophobization or hydrophilization of the NPs. A majority of

hydrophobization methods are based on the direct covalent coordination of alkanethiols or alkylamines to the NP surface. The transport of NPs stabilized by a monolayer of molecules containing cyclodextrin groups has been reported on the basis of the formation or loss of host-guest inclusion complexes between cyclodextrin groups and specific molecules present in the organic solvents.<sup>169, 170</sup> Initially hydrophilic Ag NPs protected by oleate anions can be transported into organic solvent through the change in conformation of the surface-bound oleate ions, from one in which carboxylic groups are exposed to water to one in which the hydrocarbon tails are exposed towards the organic solvent.<sup>171</sup> In addition, electrostatic interactions, which can be either pure electrostatic interactions between the charged NP core surface and the oppositely charged organic surfactant<sup>172</sup> or attractive electrostatic interactions via the formation of acid-base pairs between charged capping agents and oppositely charged surfactants,<sup>173-176</sup> can also spark the transport NPs from water to organic solvents.

Procedures for the transport of NPs from an organic solvent to water have also been developed. Most approaches involve ligand exchange reactions, replacing part or all of the hydrophobic groups bound to the NP surface with polar and hydrophilic groups and thus making the NPs water-soluble. For example, alkanethiol protected gold NPs can be transported into water through the exchange of the alkanethiol by hydrophilic  $\omega$ -thiol carboxylic acid molecules.<sup>177</sup> More directly, gold and palladium NPs synthesized in toluene by the Brust and Schiffrin reaction and stabilized by tetraoctylammonium bromide (TOABr) can be rapidly and completely transported into water by a hydrophilic compound, 4-dimethylaminopyridine (DMAP).<sup>178</sup> The DMAP molecules can expel TOABr molecules away from the NP surface and form a labile donor-acceptor complex with the surface gold atoms through the endocyclic nitrogen atoms. The transport of NPs from organic solvents has also been reported on the basis of the interdigitation of the hydrocarbon tails of water-soluble surfactant molecules with those of the protecting ligands coordinated to the NP surface.<sup>179</sup> Finally, the transport of NPs from an organic solvent to water can also be achieved on the basis of cyclodextrin host-guest chemistry, that is, the inclusion between the surfactant molecules bound to the surfaces of NPs and the hydrophilic cyclodextrins.<sup>180</sup>

### 1.3.3 Electrodeposition of NPs and their electrocatalysis

The article entitled “Electrochemical Metallization at the Liquid-Liquid Interfaces of Non-miscible Electrolytic Solution”, published by Guainazzi et al., was perhaps the first report on deposition of metals at ITIES.<sup>181</sup> Sometimes, this paper was also regarded as the first experiment demonstrating heterogeneous electron transfer at the liquid|liquid interface. In this work, it was found that the passage of electric current across the interface led to deposition of copper metallic layers at the water|DCE and the water|dichloromethane interfaces. This initial experiment was continued in 1996 when Cheng and Schiffrin reported the electrodeposition of gold NPs at ITIES via a heterogeneous electron transfer reaction:<sup>182</sup>



Strong in-situ spectroscopic evidence supported that the gold NPs have been synthesized at the water|DCE interface by applying a suitable potential.

Some other systems leading to the electrodeposition of metallic NPs at ITIES have been reported later, including the deposition of palladium particles at the water|DCE interface by heterogeneous reduction of aqueous ammonium tetrachloropalladate ( $\text{NH}_4\text{PdCl}_4$ ) by ferrocene derivatives present in the organic phase.<sup>183-186</sup> Additionally, Efrima *et al.* have also demonstrated the electrodeposition of silver metal liquid-like films grown from an electrode tip in contact with a liquid|liquid interface.<sup>187, 188</sup> Electrodeposition at the molecular liquid|liquid interface differs from that occurs at solid electrodes as the interaction between the substrate and the newly formed phase is absent or very weak in the former case. In addition, the liquid|liquid interface is free from preferential nucleation sites and thus provides a simple system to study the nucleation and growth kinetics.<sup>184-186</sup>

It should be noted that all these works describe the electrodeposition of metallic NPs at the ITIES in the absence of stabilizing/capping agents. In this situation, the NPs formed tend to aggregate, which hampers the mechanism analysis.<sup>186</sup> One method to get rid of this problem is to modify the interface with a porous template,<sup>189-193</sup> which can localize the electrodeposition process in the micron or sub-micron pores on the template and thus well separate the formed NPs from each other. The deposition of Pt, Pd and co-deposition of Pt and Pd NPs have been reported employing hydrophilic  $\gamma$ -alumina membranes.

Another method is to synthesize polymer-coated NPs or NPs in a polymer matrix by taking advantage of the simultaneous nucleation of metallic NPs and polymerization reactions.<sup>194, 195</sup> This method probably follows an EC mechanism. Typically, the transfer of metallic ions from one phase to another is followed by a homogeneous electron transfer from a polymer to the metallic ion. Therefore, electropolymerization proceeds simultaneously with the electrodeposition of metallic NPs. The newly formed NPs act as nucleation sites for the deposition of the polymer (and possibly vice versa).

Efrima et al. have predicted that the electrodeposited metal particles may exhibit catalytic and photocatalytic activities<sup>187</sup>, since colloidal particles have been extensively used as catalysts in a wide range of chemical reactions and photocatalysis. Indeed, as-deposited Pd particles have been proved to catalyze heterogeneous electron transfer at liquid|liquid interface. In an international seminar, Schiffrin and Cheng have reported the dehalogenation of 2-bromoacetophenone to acetophenone in the presence of electrogenerated Pd NPs at the water|DCE interface.<sup>196</sup> In this respect, NPs at liquid|liquid junctions can be regarded as “surface states”, employing a terminology familiar from surface science. This kind of surface state might be able to enhance electron transfer by improving adsorption or coadsorption of redox species. Additionally, in a recent report Lahtinen et al.<sup>183</sup> have demonstrated that the in-situ electrodeposited Pd NPs can act as electron mediators in the heterogeneous photoreduction of 7,7,8,8-tetracyanoquinone in DCE by a hydrophilic dye species.<sup>183</sup>

### 1.3.4 Potential induced assembly and reactivity of NPs

In a broad sense, liquid|liquid interfaces are ubiquitous in nature and can be used as an ideal framework for the self-assembly of NPs.<sup>197</sup> However, we shall only discuss the voltage induced assembly of NPs at ITIES from an electrochemical point of view. Additionally, NPs discussed here refer to those post-prepared to distinguish with the in-situ electrodeposited NPs mentioned in Section 1.3.3. Recently, there are several publications on fundamental aspects of potential induced assembly and reactivity NPs at the liquid|liquid interface, which will be addressed below.



The voltage induced accumulation of charged  $\text{TiO}_2$  and dye-sensitized  $\text{TiO}_2$  NPs at the water|DCE interface have been reported recently.<sup>142, 145</sup> The interfacial concentration of NPs can be tuned by varying the Galvani potential difference across the interface and the pH of the aqueous phase. Excitation of the  $\text{TiO}_2$  accumulated at the interface can lead to photocurrent responses in the presence of redox quenchers in the organic phase. These responses are associated with the heterogeneous electron transfer reaction between  $\text{TiO}_2$  and the redox couples in DCE. Recently, the adsorption of Au and Au core-Ag shell (Au@Ag) NPs at ITIES has been studied by second harmonic generation, a well-established surface sensitive technique to investigate the interface between two centrosymmetric materials. Interestingly, the results indicates that the adsorption and desorption of Au@Ag NPs at the interface can be controlled by the Galvani potential difference across ITIES.<sup>198</sup> The surface enhanced Raman scattering (SERS) spectra from oleate-stabilized Ag NPs adsorbed at the toluene|water interface have also been reported.<sup>199</sup> The oleate ions were found to adsorb on the silver NP surface in two different conformations. On the NP surface contacting with water, the ethylene group of the oleate was adsorbed, while on the rest surface in organic phase side, the carboxylate group of the oleate was adsorbed. In addition, the toluene molecules were also found to adsorb on the NP surface with a weak interaction.

Liquid|liquid interfaces provide a unique environment to study the optical and electronic properties of NPs, with the advantage of minimizing the mechanical constraints on the NPs. Furthermore, the strong electronic interaction usually observed with solid substrates is removed effectively. The nonlinear optical responses from Au@Ag NPs at a liquid|liquid interface have been studied and compared to their linear optical responses.<sup>198</sup> In the spectral range where the second harmonic (SH) generation frequency is resonant with the surface plasmon (SP) resonance excitation of NPs, the observed SH response is dominated by the SP resonance enhancement with negligible contributions from the interband transitions, which however delicately interplay in the linear optical absorption response. While the linear optical absorption spectrum exhibits only one broad feature, the SH spectrum exhibits two clear SP resonance bands attributed to the two SP resonances of Au@Ag NPs.

Another aspect of the reactivity of NPs at the liquid|liquid interface is associated with their propensity to act as electron donors and/or electron acceptors. This allows NPs to be

involved in heterogeneous electron transfer reactions at ITIES. For instance, Pd or Au NPs prepared by classical citrate reduction can accept electrons from decamethylferrocene (DMFc) present in the organic phase through heterogeneous electron transfer reactions.<sup>200</sup> The charged NPs can be subsequently used as catalysts for dehalogenation reactions. In addition, alkanethiolate monolayer-protected gold nanocluster (MPCs) can also function as multivalent redox species at ITIES. The interfacial electron transfer reaction between Au<sub>140</sub> MPCs dissolved in DCE and aqueous redox species was first reported by Quinn *et al.* using SECM.<sup>201</sup> They found that that electron transfer reaction was surprisingly slow, which was rationalized in terms of the large size and hydrophobicity of the MPCs resulting in a large separation between the reactants. However, in a later work, the electron transfer reaction between organic soluble Au<sub>38</sub> MPCs and aqueous redox species was found to be faster than similar electron transfer reactions between conventional aqueous and organic redox species at the liquid|liquid interface.<sup>202</sup> The dependences of the effective heterogeneous rate constant on the concentration of the aqueous redox mediator and reaction driving force were found to be in agreement with theoretical expectations.

## 1.4 The scope of the present thesis

This thesis work is within the long-term project of photoinduced charge transfer and separation at molecular interfaces at the Laboratory of Physical and Analytical Electrochemistry (LEPA) in Ecole Polytechnique Federale de Lausanne (EPFL). The project is dedicated to explore the fundamental aspects concerning the organization and reactivity of photoactive species at interfaces between two immiscible electrolyte solutions (ITIES). In these systems, the light excitation of photoactive species leads to a charge transfer process in the presence of a redox couple located in the adjacent liquid phase. In a general sense, the present thesis is concerned with the assembly and reactivity of NPs at liquid|liquid interfaces.

In Chapter 1, the electrochemistry at liquid|liquid interfaces, including the interfacial structure, potential distribution, adsorption phenomenon and charge transfer reactions is reviewed. The research interest on NPs, as well as their electronic and optical properties is also briefly introduced. The reactivity of NPs at the liquid|liquid interface is described with an overview about the synthesis, deposition, transport and voltage-induced assembly. Chapter 2 is dedicated to the experimental techniques and the instrumentation, as well as to the synthesis and characterization of NPs.

Chapter 3 describes the simulation of adsorption of ionic species at the liquid|liquid interface. Various adsorption isotherms are considered, including potential independence, Langmuir and Frumkin models. The simulation indicates that the ionic adsorption has a strong influence on the potential distribution across the interface. Under certain conditions, it results in a non-monotonous potential profile with a trap at the interface.

Chapter 4 and Chapter 5 deal with the assembly and reactivity of water soluble mercaptosuccinic acid (MSA) stabilized gold and cadmium selenide (CdSe) NPs, respectively, at the liquid|liquid interface. It is shown that the accumulation of NPs at the interfacial boundary can be reversibly controlled by the Galvani potential difference across the interface. Additionally, the photoexcitation of CdSe NPs assembled at the interface can lead to heterogeneous electron transfer to electron acceptors located in the organic phase.

Chapter 6 and Chapter 7 describe the redox properties of hexanethiolate monolayer-protected gold nanoclusters (MPCs) in different electrochemical environments. More specifically, Chapter 6 deals with the absolute standard redox property of MPCs freely diffusing in solutions and self-assembled on electrode surface. Chapter 7 illustrates the study using MPCs as redox quenchers in photoinduced electron transfer reactions at porphyrin-sensitized liquid|liquid interfaces.

---

## 1.5 References

- (1) Volkov, A. G.; Deamer, D. W.; Editors *Liquid-Liquid Interfaces: Theory and Methods*, 1996.
- (2) Volkov, A. G.; Deamer, D. W.; Tanelian, D. L.; Markin, V. a. S. *Liquid Interfaces in Chemistry and Biology*, 1998.
- (3) Verwey, E. J. W.; Niessen, K. F. *Philosophi. Mag.* **1939**, 28, 435.
- (4) Nernst, W.; Riesenfeld, E. H. *Annal. Phys.* **1902**, 8, 600.
- (5) Gavach, C.; Mlodnicka, T.; Guastalla, J. *Comp. Rend. Acad. Sci. Ser. C* **1968**, 266, 1196.
- (6) Samec, Z.; Marecek, V.; Weber, J. *J. Electroanal. Chem.* **1979**, 100, 841.
- (7) Girault, H. H. In *Modern Aspects of Electrochemistry*, 1993; Vol. 25, pp 1.
- (8) Reymond, F.; Fermin, D.; Lee, H. J.; Girault, H. H. *Electrochim. Acta* **2000**, 45, 2647.
- (9) Gavach, C.; Seta, P.; D'Epenoux, B. *J. Electroanal. Chem.* **1977**, 83, 225.
- (10) Girault, H. H.; Schiffrin, D. J. *J. Electroanal. Chem.* **1983**, 150, 43.
- (11) Schmickler, W. *Surfactant Science Series* **2001**, 95, 153.
- (12) Samec, Z.; Marecek, V.; Homolka, D. *J. Electroanal. Chem.* **1981**, 126, 121.
- (13) Samec, Z.; Marecek, V.; Homolka, D. *Faraday Discuss. Chem. Soc.* **1984**, 197.
- (14) Samec, Z.; Marecek, V.; Homolka, D. *J. Electroanal. Chem.* **1985**, 187, 31.
- (15) Beaglehole, D. *Phys. Rev. Lett.* **1987**, 58, 1434.
- (16) Lee, L. T.; Langevin, D.; Farnoux, B. *Phys. Rev. Lett.* **1991**, 67, 2678.
- (17) Schweighofer, K. J.; Benjamin, I. *J. Electroanal. Chem.* **1995**, 391, 1.
- (18) Schiffrin, D. *J. Electroanal. Chem.* **2001**, 514, 133.
- (19) Benjamin, I. *Annul. Rev. Phys. Chem.* **1997**, 48, 407.
- (20) Walker, D. S.; Brown, M. G.; McFearin, C. L.; Richmond, G. L. *J. Phys. Chem B* **2004**, 108, 2111.
- (21) Koryta, J.; Hung, L. Q.; Hofmanova, A. *Studia Biophys.* **1982**, 90, 25.
- (22) Girault, H. H. J.; Schiffrin, D. J. *J. Electroanal. Chem.* **1984**, 179, 277.
- (23) Kakiuchi, T.; Kobayashi, M.; Senda, M. *Bull. Chem. Sod. Jpn.* **1988**, 61, 1545.
- (24) Kakiuchi, T.; Nakanishi, M.; Senda, M. *Bull. Chem. Sod. Jpn.* **1989**, 62, 403.
- (25) Kakiuchi, T.; Kondo, T.; Senda, M. *Bull. Chem. Sod. Jpn.* **1990**, 63, 3270.

- (26) Grandell, D.; Murtomaki, L.; Kontturi, K.; Sundholm, G. *J. Electroanal. Chem.* **1999**, *463*, 242.
- (27) Kakiuchi, T. *Surfactant Science Series* **2001**, *95*, 105.
- (28) Murtomaki, L.; Manzanares, J. A.; Mafe, S.; Kontturi, K. *Surfactant Science Series* **2001**, *95*, 533.
- (29) Kakiuchi, T.; Usui, T.; Senda, M. *Bull. Chem. Sod. Jpn.* **1990**, *63*, 2044.
- (30) Kakiuchi, T.; Usui, T.; Senda, M. *Bull. Chem. Sod. Jpn.* **1990**, *63*, 3264.
- (31) Kakiuchi, T. *J. Electroanal. Chem.* **1993**, *345*, 191.
- (32) Kakiuchi, T. *J. Colloid Interf. Sci.* **1993**, *156*, 406.
- (33) Kakiuchi, T.; Kobayashi, M.; Senda, M. *Bull. Chem. Sod. Jpn.* **1987**, *60*, 3109.
- (34) Frank, S.; Schmickler, W. *J. Electroanal. Chem.* **2001**, *500*, 491.
- (35) Samec, Z.; Kakiuchi, T. *Charge transfer kinetics at water-organic solvent phase boundaries*, 1995.
- (36) Fermin, D. J.; Jensen, H.; Girault, H. H. In *Encyclopedia of Electrochemistry*, 2003; Vol. 2, pp 360.
- (37) Gavach, C.; D'Epenoux, B.; Henry, F. *J. Electroanal. Chem.* **1975**, *64*, 107.
- (38) Gavach, C.; D'Epenoux, B. *J. Electroanal. Chem.* **1974**, *55*, 59.
- (39) Gavach, C.; Henry, F. *J. Electroanal. Chem.* **1974**, *54*, 361.
- (40) Kakiuchi, T.; Noguchi, J.; Kotani, M.; Senda, M. *J. Electroanal. Chem.* **1990**, *296*, 517.
- (41) Shao, Y.; Girault, H. H. *J. Electroanal. Chem.* **1990**, *282*, 59.
- (42) Samec, Z.; Marecek, V.; Weber, J.; Homolka, D. *J. Electroanal. Chem.* **1981**, *126*, 105.
- (43) Taylor, G.; Girault, H. H. *J. Electroanal. Chem.* **1986**, *208*, 179.
- (44) Stewart, A. A.; Shao, Y.; Pereira, C. M.; Girault, H. H. *J. Electroanal. Chem.* **1991**, *305*, 135.
- (45) Osborne, M. C.; Shao, Y.; Pereira, C. M.; Girault, H. H. *J. Electroanal. Chem.* **1994**, *364*, 155.
- (46) Kakiuchi, T.; Takasu, Y. *Anal. Chem.* **1994**, *66*, 1853.
- (47) Ding, Z.; Wellington, R. G.; Brevet, P.-F.; Girault, H. H. *J. Electroanal. Chem.* **1997**, *420*, 35.
- (48) Fermin, D. J.; Ding, Z.; Brevet, P. F.; Girault, H. H. *J. Electroanal. Chem.* **1998**, *447*, 125.

- (49) Ding, Z.; Reymond, F.; Baumgartner, P.; Fermin, D. J.; Brevet, P.-F.; Carrupt, P.-A.; Girault, H. H. *Electrochim. Acta* **1998**, *44*, 3.
- (50) Nagatani, H.; Iglesias, R. A.; Fermin, D. J.; Brevet, P.-F.; Girault, H. H. *J. Phys. Chem. B* **2000**, *104*, 6869.
- (51) Nakatani, K.; Nagatani, H.; Fermin, D. J.; Girault, H. H. *J. Electroanal. Chem.* **2002**, *518*, 1.
- (52) Marken, F.; Webster, R. D.; Bull, S. D.; Davies, S. G. *J. Electroanal. Chem.* **1997**, *437*, 209.
- (53) Banks, C. E.; Davies, T. J.; Evans, R. G.; Hignett, G.; Wain, A. J.; Lawrence, N. S.; Wadhawan, J. D.; Marken, F.; Compton, R. G. *Phys. Chem. Chem. Phys.* **2003**, *5*, 4053.
- (54) Samec, Z.; Marecek, V.; Koryta, J.; Khalil, M. W. *J. Electroanal. Chem.* **1977**, *83*, 393.
- (55) Bronner, W. E.; Melroy, O. R.; Buck, R. P. *J. Electroanal. Chem.* **1984**, *162*, 263.
- (56) Buck, R. P.; Bronner, W. E. *J. Electroanal. Chem.* **1986**, *197*, 179.
- (57) Samec, Z.; Marecek, V. *J. Electroanal. Chem.* **1986**, *200*, 17.
- (58) Shao, Y.; Osborne, M. D.; Girault, H. H. *J. Electroanal. Chem.* **1991**, *318*, 101.
- (59) Osakai, T.; Kakutani, T.; Senda, M. *Bull. Chem. Sod. Jpn.* **1985**, *58*, 2626.
- (60) Osakai, T.; Kakutani, T.; Senda, M. *Bull. Chem. Sod. Jpn.* **1984**, *57*, 370.
- (61) Beattie, P. D.; Delay, A.; Girault, H. H. *Electrochim. Acta* **1995**, *40*, 2961.
- (62) Koryta, J. *Electrochim. Acta* **1988**, *33*, 189.
- (63) Wandlowski, T.; Marecek, V.; Holub, K.; Samec, Z. *J. Phys. Chem.* **1989**, *93*, 8204.
- (64) Samec, Z.; Kharkats, Y. I.; Gurevich, Y. Y. *J. Electroanal. Chem.* **1986**, *204*, 257.
- (65) Gurevich, Y. Y.; Kharkats, Y. I. *J. Electroanal. Chem.* **1986**, *200*, 3.
- (66) Benjamin, I. *J. Chem. Phys.* **1992**, *96*, 577.
- (67) Benjamin, I. *Science* **1993**, *261*, 1558.
- (68) Dang, L. X. *J. Phys. Chem. B* **1999**, *103*, 8195.
- (69) Dang, L. X. *J. Phys. Chem. B* **2001**, *105*, 804.
- (70) Fernandes, P. A.; Cordeiro, M. N. D. S.; Gomes, J. A. N. F. *J. Phys. Chem. B* **1999**, *103*, 8930.
- (71) Fernandes, P. A.; Cordeiro, M. N. D. S.; Gomes, J. A. N. F. *J. Phys. Chem. B* **2000**, *104*, 2278.
- (72) Marcus, R. A. *J. Chem. Phys.* **2000**, *113*, 1618.

- (73) Girault, H. H. J.; Schiffrin, D. J. *J. Electroanal. Chem.* **1985**, *195*, 213.
- (74) Girault, H. H. *J. Electroanal. Chem.* **1988**, *257*, 47.
- (75) Shao, Y.; Campbell, J. A.; Girault, H. H. *J. Electroanal. Chem.* **1991**, *300*, 415.
- (76) Stearn, A. E.; Eyring, H. *J. Phys. Chem.* **1940**, *44*, 955.
- (77) Kakiuchi, T. *J. Electroanal. Chem.* **1992**, *322*, 55.
- (78) Kontturi, K.; Manzanares, J. A.; Murtomaeki, L. *Electrochim. Acta* **1995**, *40*, 2979.
- (79) Senda, M. *Electrochim. Acta* **1995**, *40*, 2993.
- (80) Kontturi, K.; Manzanares, J. A.; Murtomaeki, L.; Schiffrin, D. J. *J. Phys. Chem. B* **1997**, *101*, 10801.
- (81) Samec, Z.; Marecek, V.; Weber, J. *J. Electroanal. Chem.* **1979**, *103*, 11.
- (82) Geblewicz, G.; Schiffrin, D. J. *J. Electroanal. Chem.* **1988**, *244*, 27.
- (83) Cunnane, V. J.; Schiffrin, D. J.; Beltran, C.; Geblewicz, G.; Solomon, T. *J. Electroanal. Chem.* **1988**, *247*, 203.
- (84) Cheng, Y.; Schiffrin, D. J. *J. Electroanal. Chem.* **1991**, *314*, 153.
- (85) Cheng, Y.; Schiffrin, D. J. *J. Chem. Soc. Faraday Trans.* **1993**, *89*, 199.
- (86) Cheng, Y.; Schiffrin, D. J. *J. Chem. Soc. Faraday Trans.* **1994**, *90*, 2517.
- (87) Cunnane, V. J.; Geblewicz, G.; Schiffrin, D. J. *Electrochim. Acta* **1995**, *40*, 3005.
- (88) Kihara, S.; Suzuki, M.; Maeda, K.; Ogura, K.; Matsui, M.; Yoshida, Z. *J. Electroanal. Chem.* **1989**, *271*, 107.
- (89) Maeda, K.; Kihara, S.; Suzuki, M.; Matsui, M. *J. Electroanal. Chem.* **1991**, *303*, 171.
- (90) Ding, Z.; Fermin, D. J.; Brevet, P.-F.; Girault, H. H. *J. Electroanal. Chem.* **1998**, *458*, 139.
- (91) Fermin, D. J.; Ding, Z.; Duong, H. D.; Brevet, P. F.; Girault, H. H. *Chem. Commun.* **1998**, 1125.
- (92) Fermin, D. J.; Ding, Z.; Duong, H. D.; Brevet, P.-F.; Girault, H. H. *J. Phys. Chem. B* **1998**, *102*, 10334.
- (93) Wei, C.; Bard, A. J.; Mirkin, M. V. *J. Phys. Chem.* **1995**, *99*, 16033.
- (94) Tsionsky, M.; Bard, A. J.; Mirkin, M. V. *J. Phys. Chem.* **1996**, *100*, 17881.
- (95) Liu, B.; Mirkin, M. V. *J. Am. Chem. Soc.* **1999**, *121*, 8352.
- (96) Liu, B.; Mirkin, M. V. *J. Phys. Chem. B* **2002**, *106*, 3933.
- (97) Shi, C.; Anson, F. C. *J. Phys. Chem. B* **1998**, *102*, 9850.

- (98) Shi, C.; Anson, F. C. *J. Phys. Chem. B* **1999**, *103*, 6283.
- (99) Shi, C.; Anson, F. C. *J. Phys. Chem. B* **2001**, *105*, 1047.
- (100) Dryfe, R. A. W.; Ding, Z.; Wellington, R. G.; Brevet, P. F.; Kuznetsov, A. M.; Girault, H. H. *J. Phys. Chem. A* **1997**, *101*, 2519.
- (101) Duong, H. D.; Brevet, P. F.; Girault, H. H. *J. Photochem. Photobio. A* **1998**, *117*, 27.
- (102) Fermin, D. J.; Dung Duong, H.; Ding, Z.; Brevet, P. F.; Girault, H. H. *Phys. Chem. Chem. Phys.* **1999**, *1*, 1461.
- (103) Volkov, A. G. *Liquid Interfaces in Chemical, Biological, and Pharmaceutical Applications*, 2001.
- (104) Fermin, D. J.; Duong, H. D.; Ding, Z.; Brevet, P. F.; Girault, H. H. *Electrochem. Commun.* **1999**, *1*, 29.
- (105) Samec, Z. *J. Electroanal. Chem.* **1979**, *99*, 197.
- (106) Tsionsky, M.; Bard, A. J.; Mirkin, M. V. *J. Am. Chem. Soc.* **1997**, *119*, 10785.
- (107) Zhang, Z.; Yuan, Y.; Sun, P.; Su, B.; Guo, J.; Shao, Y.; Girault, H. H. *J. Phys. Chem. B* **2002**, *106*, 6713.
- (108) Eugster, N.; Fermin, D. J.; Girault, H. H. *J. Phys. Chem. B* **2002**, *106*, 3428.
- (109) Eugster, N.; Fermin, D. J.; Girault, H. H. *J. Am. Chem. Soc.* **2003**, *125*, 4862.
- (110) Marcus, R. A. *J. Phys. Chem.* **1991**, *95*, 2010.
- (111) Marcus, R. A. *J. Phys. Chem.* **1990**, *94*, 1050.
- (112) Marcus, R. A. *J. Phys. Chem.* **1990**, *94*, 4152.
- (113) Sherburn, A.; Platt, M.; Arrigan, D. W. M.; Boag, N. M.; Dryfe, R. A. W. *Analyst* **2003**, *128*, 1187.
- (114) Volkov, A. G. *Electrochim. Acta* **1998**, *44*, 139.
- (115) Volkov, A. G.; Gugeshashvili, M. I.; Deamer, D. W. *Electrochim. Acta* **1995**, *40*, 2849.
- (116) Volkov, A. G. *Interfacial Catalysis* **2003**, 1.
- (117) Mathai, K. G.; Rabinowitch, E. *J. Phys. Chem.* **1962**, *66*, 663.
- (118) Frackowiak, D.; Rabinowitch, E. *J. Phys. Chem.* **1966**, *70*, 3012.
- (119) Boguslavskii, L. I.; Volkov, A. G.; Kandelaki, M. D. *Bioelectrochem. Bioenerg.* **1977**, *4*, 68.
- (120) Boguslavskii, L. I.; Volkov, A. G.; Kandelaki, M. D. *FEBS Lett.* **1976**, *65*, 155.
- (121) Kandelaki, M. D.; Volkov, A. G.; Shubin, V. V.; Levin, A. L.; Boguslavskii, L. I. *Elektrokhimiya* **1988**, *24*, 288.



- (122) Kandelaki, M. D.; Volkov, A. G.; Shubin, V. V.; Boguslavskii, L. I. *Biochim. et Biophys. Acta* **1987**, *893*, 170.
- (123) Kandelaki, M. D.; Volkov, A. G.; Levin, A. L.; Boguslavskii, L. I. *Bioelectrochem. Bioenerg.* **1983**, *11*, 167.
- (124) Volkov, A. G. *Elektrokhimiya* **1985**, *21*, 91.
- (125) Volkov, A. G. *Bioelectrochem. Bioenerg.* **1984**, *12*, 15.
- (126) Volkov, A. G. *Bioelectrochem. Bioenerg.* **1989**, *21*, 3.
- (127) Volkov, A. G.; Kolev, V. D.; Levin, A. L.; Boguslavskii, L. I. *Elektrokhimiya* **1986**, *22*, 1303.
- (128) Volkov, A. G.; Kolev, V. D.; Levin, A. L.; Boguslavskii, L. I. *Photobiochem. Photobiophys.* **1985**, *10*, 105.
- (129) Samec, Z.; Brown, A. R.; Yellowlees, L. J.; Girault, H. H. *J. Electroanal. Chem.* **1990**, *288*, 245.
- (130) Samec, Z.; Brown, A. R.; Yellowlees, L. J.; Girault, H. H.; Base, K. J. *J. Electroanal. Chem.* **1989**, *259*, 309.
- (131) Marecek, V.; De Armond, A. H.; De Armond, M. K. *J. Electroanal. Chem.* **1989**, *261*, 287.
- (132) Dvorak, O.; De Armond, A. H.; De Armond, M. K. *Langmuir* **1992**, *8*, 955.
- (133) Dvorak, O.; De Armond, A. H.; De Armond, M. K. *Langmuir* **1992**, *8*, 508.
- (134) Kotov, N. A.; Kuz'min, M. G. *J. Electroanal. Chem.* **1990**, *285*, 223.
- (135) Kotov, N. A.; Kuz'min, M. G. *J. Electroanal. Chem.* **1992**, *338*, 99.
- (136) Kotov, N. A.; Kuzmin, M. G. *J. Electroanal. Chem.* **1992**, *327*, 47.
- (137) Kotov, N. A.; Kuzmin, M. G. *J. Electroanal. Chem.* **1992**, *341*, 47.
- (138) Kuzmin, M. G.; Soboleva, I. V.; Kotov, N. A. *Anal. Sci.* **1999**, *15*, 3.
- (139) Thomson, F. L.; Yellowlees, L. J.; Girault, H. H. *J. Chem. Soc. Chem. Commun.* **1988**, 1547.
- (140) Brown, A. R.; Yellowlees, L. J.; Girault, H. H. *J. Chem. Soc. Faraday Trans.* **1993**, *89*, 207.
- (141) Fermin, D. J.; Duong, H. D.; Ding, Z.; Brevet, P.-F.; Girault, H. H. *J. Am. Chem. Soc.* **1999**, *121*, 10203.
- (142) Fermin, D. J.; Jensen, H.; Moser, J. E.; Girault, H. H. *ChemPhysChem* **2003**, *4*, 85.
- (143) Eugster, N.; Jensen, H.; Fermin, D. J.; Girault, H. H. *J. Electroanal. Chem.* **2003**, *560*, 143.

- (144) Jensen, H.; Fermin, D. J.; Girault, H. H. *Phys. Chem. Chem. Phys.* **2001**, *3*, 2503.
- (145) Jensen, H.; Fermin, D. J.; Moser, J. E.; Girault, H. H. *J. Phys. Chem. B* **2002**, *106*, 10908.
- (146) Jensen, H.; Kakkassery, J. J.; Nagatani, H.; Fermin, D. J.; Girault, H. H. *J. Am. Chem. Soc.* **2000**, *122*, 10943.
- (147) Klabunde, K. J.; Editor *Nanoscale Materials in Chemistry*, 2001.
- (148) Chen, S.; Ingrma, R. S.; Hostetler, M. J.; Pietron, J. J.; Murray, R. W.; Schaaff, T. G.; Khoury, J. T.; Alvarez, M. M.; Whetten, R. L. *Science* **1998**, *280*, 2098.
- (149) Brus, L. E. *J. Chem. Phys.* **1984**, *80*, 4403.
- (150) Enustun, B. V.; Turkevich, J. *J. Am. Chem. Soc.* **1963**, *85*, 3317.
- (151) Van de Hulst, H. C. *Light Scattering by Small Particles*, 1982.
- (152) Huang, T.; Murray, R. W. *Journal of Physical Chemistry B* **2001**, *105*, 12498.
- (153) Rogach, A. L.; Kornowski, A.; Gao, M.; Eychmueller, A.; Weller, H. *J. Phys. Chem. B* **1999**, *103*, 3065.
- (154) Gao, M.; Richter, B.; Kirstein, S.; Moehwald, H. *J. Phys. Chem. B* **1998**, *102*, 4096.
- (155) Germeau, A.; Roest, A. L.; Vanmaekelbergh, D.; Allan, G.; Delerue, C.; Meulenkamp, E. A. *Phys. Rev. Lett.* **2003**, *90*, 097401/1.
- (156) Wang, C.; Shim, M.; Guyot-Sionnest, P. *Science* **2001**, *291*, 2390.
- (157) Shim, M.; Guyot-Sionnest, P. *Nature* **2000**, *407*, 981.
- (158) Brust, M.; Walker, M.; Bethell, D.; Schiffrin, D. J.; Whyman, R. *J. Chem. Soc. Chem. Commun.* **1994**, 801.
- (159) Faraday, M. *Philos. Trans. R. Soc. London* **1857**, *147*, 145.
- (160) Godbole, P. D.; Mitra, A.; Pasricha, R.; Mandale, A. B.; Patil, K. R. *Mater. Lett.* **2005**, *59*, 1958.
- (161) Pawaskar, N. R.; Sathaye, S. D.; Bhadbhade, M. M.; Patil, K. R. *Mater. Res. Bull.* **2002**, *37*, 1539.
- (162) Mandale, A. B.; Sathaye, S. D.; Patil, K. R. *Mater. Lett.* **2002**, *55*, 30.
- (163) Sathaye, S. D.; Patil, K. R.; Paranjape, D. V.; Padalkar, S. R. *Mater. Res. Bull.* **2001**, *36*, 1149.
- (164) Patil, K. R.; Paranjape, D. V.; Sathaye, S. D.; Mitra, A.; Padalkar, S. R.; Mandale, A. B. *Mater. Lett.* **2000**, *46*, 81.
- (165) Sathaye, S. D.; Patil, K. R.; Paranjape, D. V.; Mitra, A.; Awate, S. V.; Mandale, A. B. *Langmuir* **2000**, *16*, 3487.

- (166) Wu, P. W.; Gao, L.; Guo, J. K. *Thin Solid Films* **2002**, *408*, 132.
- (167) Gautam, U. K.; Ghosh, M.; Rao, C. N. R. *Chem. Phys. Lett.* **2003**, *381*, 1.
- (168) Sastry, M. *Chemistry of Nanomaterials* **2004**, *1*, 31.
- (169) Liu, J.; Alvarez, J.; Ong, W.; Roman, E.; Kaifer, A. E. *J. Am. Chem. Soc.* **2001**, *123*, 11148.
- (170) Lala, N.; Lalbegi, S. P.; Adyanthaya, S. D.; Sastry, M. *Langmuir* **2001**, *17*, 3766.
- (171) Wang, W.; Efrima, S.; Regev, O. *Langmuir* **1998**, *14*, 602.
- (172) Cheng, W.; Wang, E. *J. Phys. Chem. B* **2004**, *108*, 24.
- (173) Yao, H.; Momozawa, O.; Hamatani, T.; Kimura, K. *Bull. Chem. Soc. Jpn.* **2000**, *73*, 2675.
- (174) Yao, H.; Momozawa, O.; Hamatani, T.; Kimura, K. *Chem. Mater.* **2001**, *13*, 4692.
- (175) Chen, S.; Yao, H.; Kimura, K. *Langmuir* **2001**, *17*, 733.
- (176) Devarajan, S.; Vimalan, B.; Sampath, S. *J. Colloid Interf. Sci.* **2004**, *278*, 126.
- (177) Templeton, A. C.; Hostetler, M. J.; Warmoth, E. K.; Chen, S.; Hartshorn, C. M.; Krishnamurthy, V. M.; Forbes, M. D. E.; Murray, R. W. *J. Am. Chem. Soc.* **1998**, *120*, 4845.
- (178) Gittins, D. I.; Caruso, F. *Angew. Chem. Int. Ed.* **2001**, *40*, 3001.
- (179) Swami, A.; Kumar, A.; Sastry, M. *Langmuir* **2003**, *19*, 1168.
- (180) Wang, Y.; Wong, J. F.; Teng, X.; Lin, X. Z.; Yang, H. *Nano Letters* **2003**, *3*, 1555.
- (181) Guainazzi, M.; Silvestri, G.; Serravalle, G. *J. Chem. Soc. Chem. Commun.* **1975**, 200.
- (182) Cheng, Y.; Schiffrin, D. J. *J. Chem. Soc. Faraday Trans.* **1996**, *92*, 3865.
- (183) Lahtinen, R. M.; Fermin, D. J.; Jensen, H.; Kontturi, K.; Girault, H. H. *Electrochem. Commun.* **2000**, *2*, 230.
- (184) Johans, C.; Lahtinen, R.; Kontturi, K.; Schiffrin, D. J. *J. Electroanal. Chem.* **2000**, *488*, 99.
- (185) Johans, C.; Kontturi, K.; Schiffrin, D. J. *J. Electroanal. Chem.* **2002**, *526*, 29.
- (186) Johans, C.; Liljeroth, P.; Kontturi, K. *Phys. Chem. Chem. Phys.* **2002**, *4*, 1067.
- (187) Yogeve, D.; Efrima, S. *J. Phys. Chem.* **1988**, *92*, 5754.
- (188) Zeiri, L.; Younes, O.; Efrima, S.; Deutsch, M. *J. Phys. Chem. B* **1997**, *101*, 9299.
- (189) Platt, M.; Dryfe, R. A. W.; Roberts, E. P. L. *Chem. Commun.* **2002**, 2324.
- (190) Platt, M.; Dryfe, R. A. W.; Roberts, E. P. L. *Electrochim. Acta* **2003**, *48*, 3037.
- (191) Platt, M.; Dryfe, R. A. W.; Roberts, E. P. L. *Electrochim. Acta* **2004**, *49*, 3937.

- (192) Platt, M.; Dryfe, R. A. W. *Phys. Chem. Chem. Phys.* **2005**, *7*, 1807.
- (193) Dryfe, R. A. W.; Simm, A. O.; Kralj, B. *J. Am. Chem. Soc.* **2003**, *125*, 13014.
- (194) Johans, C.; Clohessy, J.; Fantini, S.; Kontturi, K.; Cunnane, V. J. *Electrochem. Commun.* **2002**, *4*, 227.
- (195) Knake, R.; Fahmi, A. W.; Tofail, S. A. M.; Clohessy, J.; Mihov, M.; Cunnane, V. *J. Langmuir* **2005**, *21*, 1001.
- (196) Schiffrin, D. J.; Cheng, Y. *International Seminar on Charge Transfer at Liquid|Liquid and Liquid|Membrane Interfaces*, Kyoto.
- (197) Binder, W. H. *Angew. Chem.* **2005**, *44*, 5172.
- (198) Abid, J.-P.; Nappa, J.; Girault, H. H.; Brevet, P.-F. *J. Chem. Phys.* **2004**, *121*, 12577.
- (199) Yamamoto, S.; Fujiwara, K.; Watarai, H. *Anal. Sci.* **2004**, *20*, 1347.
- (200) Lahtinen, R.; Johans, C.; Hakkarainen, S.; Coleman, D.; Kontturi, K. *Electrochem. Commun.* **2002**, *4*, 479.
- (201) Quinn, B. M.; Liljeroth, P.; Kontturi, K. *J. Am. Chem. Soc.* **2002**, *124*, 12915.
- (202) Georganopoulou, D. G.; Mirkin, M. V.; Murray, R. W. *Nano Lett.* **2004**, *4*, 1763.

## Chapter 2

### Experimental and instrumentation

In the present chapter, we shall provide details about the experimental procedures and techniques employed in this thesis. First of all, the instrumentation related to electrochemical and photoelectrochemical measurements at liquid|liquid interfaces, including home made four-electrode potentiostat, cyclic voltammetry, difference capacitance, and photocurrent transient measurements will be described. The interfacial tension measurements based on quasi-elastic laser scattering technique and its working principle, capillary wave theory, will be sketched out. Other electrochemical techniques employed to study and characterize NPs, including differential pulse voltammetry and capillary electrophoresis, will be introduced. The synthesis of metallic and semiconductor NPs will be also outlined, including a little basic about electronic and optical properties, spectroscopic and microscopic characterization. Finally, we shall briefly describe the synthesis of several types of room temperature ionic liquids used in the present thesis.

## 2.1 Electrochemical methods at liquid|liquid interfaces

### 2.1.1 The four-electrode potentiostat

The invention of the four electrode potentiostat was an important advance in the field of electrochemistry at liquid|liquid interfaces,<sup>1, 2</sup> as it enabled external control of the polarization of the interface. Indeed, most experimental results on the electric double layer and heterogeneous charge transfer reactions at the liquid|liquid interface are collected by means of the four-electrode system introduced by Samec et al.,<sup>1, 2</sup> which includes a feedback circuit employed to compensate the ohmic potential drop ( $iR$ ).

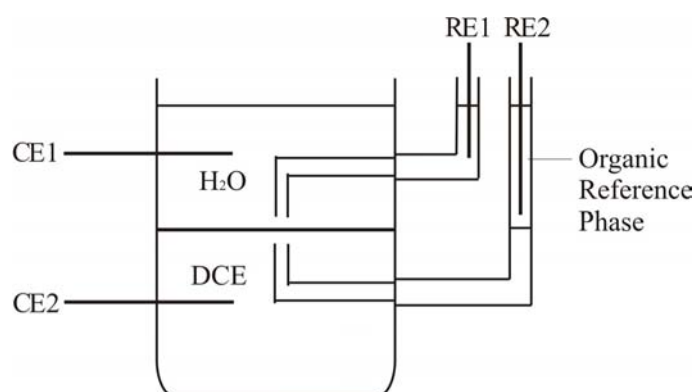


**Figure 2.1** Schematic representation of the four-electrode glass cell.

In practical electrochemical measurements at liquid|liquid interfaces, a homemade glass cell that features a cylindrical vessel with a geometric area of 1.53 cm<sup>2</sup> and two Luggin capillary arms is used, as depicted in Figure 2.1. The interface between the upper aqueous phase and the bottom organic phase is formed between the two Luggin capillaries. In each phase, a platinum counter electrode is positioned, which supplies the current flow. The interface is polarized by means of the two reference electrodes RE<sub>1</sub> and RE<sub>2</sub>, which are usually silver|silver chloride (Ag|AgCl) or silver|silver sulfate (Ag|Ag<sub>2</sub>SO<sub>4</sub>) depending on the supporting electrolyte employed. It should be mentioned that RE<sub>2</sub> functions as the reference electrode in the organic phase together with a nonpolarizable water|DCE interface formed in the capillary.

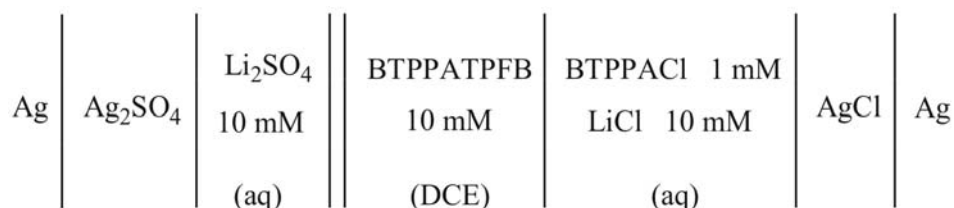


**Figure 2.2** Schematic composition of the blank electrochemical cell.

Externally polarizable liquid|liquid interfaces are formed in the presence of a hydrophilic electrolyte in the aqueous phase and a hydrophobic salt in the organic phase. A schematic composition of an electrochemical cell is displayed in Figure 2.2, where lithium sulfate (Li<sub>2</sub>SO<sub>4</sub>) and bis(triphenylphosphoranylidene) ammonium tetrakis(pentafluorophenyl)borate (BTTPATPFB) are used as the supporting electrolytes in water and DCE, respectively.

### 2.1.2 Preparation of reference electrodes and BTTPATPFB

Reference electrodes Ag|AgCl and Ag|Ag<sub>2</sub>SO<sub>4</sub> were prepared by connecting a newly polished silver wire and a platinum wire to the positive and negative terminals, respectively, of a battery with a voltage output of 1.5 V. An aqueous solution of NaCl plus a small amount of HCl or Li<sub>2</sub>SO<sub>4</sub> plus a small amount of H<sub>2</sub>SO<sub>4</sub> were employed as the electrolytic solution, respectively. The passage of current in the circuit produced a layer of the insoluble silver salt on the silver wire, which is accompanied by the electrolytic reduction of proton at the platinum wire.

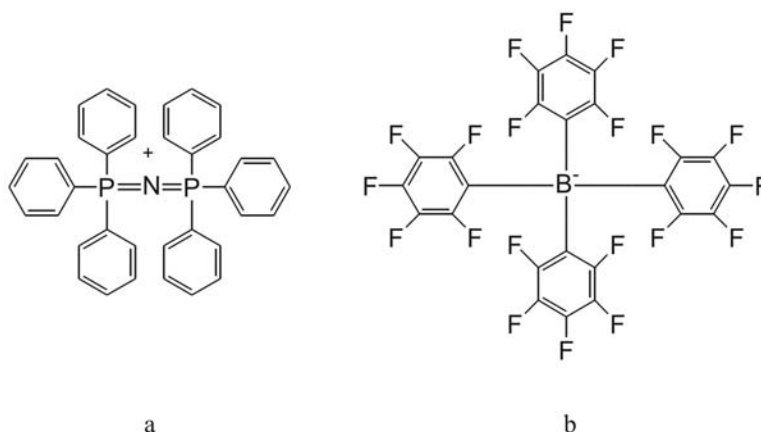


**Figure 2.3** Structures of the organic ions: (a) BTTPA<sup>+</sup> and (b) TPFB<sup>-</sup>.

In this thesis, unless specified otherwise, BTPPATPFB is used as the supporting electrolyte in the organic phase for electrochemical measurements at liquid|liquid interfaces.<sup>3</sup> It was prepared by metathesis of bis(triphenylphosphoranylidene)ammonium chloride (BTPPACl) and lithium tetrakis(pentafluorophenyl)borate diethyl etherate (LiTPFB) in a molar ratio of 1:1 in 2:1 methanol/water mixture. The resulting precipitate was washed with copious amount of water, followed by recrystallization in acetone. The white crystals obtained were then dried under vacuum before use. The molecular structures of these two ions are illustrated in Figure 2.3.

### 2.1.3 Cyclic voltammetry and the potential window

Cyclic voltammetry is a widely used technique in electrochemistry. The solid line in Figure 2.4a corresponds to the cyclic voltammogram obtained with the electrochemical cell displayed in Figure 2.2. The current rises observed at the extremes of the potential window are associated with the transfer of  $\text{Li}^+$  at positive potentials and  $\text{SO}_4^{2-}$  at negative potentials. The potential window provides a 700 mV potential range in which electrochemical reactions can be studied.

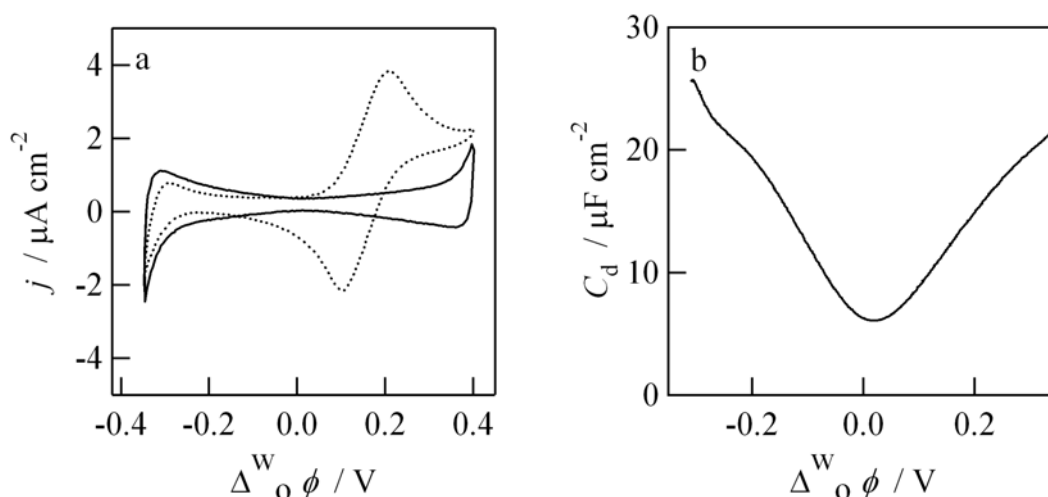


**Figure 2.4** (a) Cyclic voltammograms in the absence (solid line) and presence (dotted line) of  $0.5 \text{ mM TMA}^+$  in the aqueous phase; (b) The differential capacitance-potential curve for a cell composition illustrated in Figure 2.2.



The potential scale displayed in Figure 2.4 is the Galvani potential difference across the water|DCE interface, which is estimated by referring the cell potential applied between two reference electrodes to an internal reference based on a certain extrathermodynamic assumption. The commonly used ‘‘TATB’’ assumption states that tetraphenylarsonium (TPAs<sup>+</sup>) and tetraphenylborate (TPB<sup>-</sup>) have an identical standard transfer energy at the water|DCE interface.<sup>4</sup> On the basis of this assumption, the formal ion transfer potential of tetramethylammonium cation (TMA<sup>+</sup>) at the water|DCE interface is estimated as 0.160 V.<sup>5</sup> This value has been used extensively as the internal reference. Also shown in dotted line in Figure 2.4a is the cyclic voltammogram in the presence of 0.5 mM TMA<sup>+</sup> in water. Accordingly, the potential where the faradaic current wave centered is 0.160 V. Therefore, the cell potential in the whole range can be related to the Galvani potential difference.

### 2.1.4 Differential capacitance measurements

The interfacial capacitance was calculated from admittance measurements by imposing an a.c potential at a certain frequency to the homemade four-electrode system. In the absence of any faradaic process, we assume that the liquid|liquid interface can be modeled as a solution resistance ( $R_s$ ) and an interfacial capacitance ( $C_{dl}$ ) in series, as shown in Figure 2.5.



**Figure 2.5** Equivalent circuit for the liquid|liquid interface in the absence of Faradaic process.

Under perturbation by a small sine signal at a given frequency:

$$e = E \sin(\omega t) \quad (2.1)$$

where  $E$  is the amplitude of the potential modulation and  $\omega$  the frequency, the admittance of this circuit is:

$$Y = \frac{1}{R_s + \frac{1}{i\omega C_{dl}}} = \frac{R_s (\omega C_{dl})^2 - i\omega C_{dl}}{1 + (\omega R_s C_{dl})^2} \quad (2.2)$$

And the current magnitude is:

$$I = E \cdot \frac{R_s (\omega C_{dl})^2 + i\omega C_{dl}}{1 + (\omega R_s C_{dl})^2} \quad (2.3)$$

with the real and imaginary parts:

$$I_{re} = E \cdot \frac{R_s (\omega C_{dl})^2}{1 + (\omega R_s C_{dl})^2} \quad (2.4)$$

$$I_{im} = E \cdot \frac{\omega C_{dl}}{1 + (\omega R_s C_{dl})^2} \quad (2.5)$$

Hence the interfacial capacitance can be calculated as:

$$C_{dl} = \frac{I_{re}^2 + I_{im}^2}{\omega E I_{im}} \quad (2.6)$$

A typical differential capacitance-potential curve is shown in Figure 2.4b. Capacitance measurements can provide a qualitative evidence of the adsorption of charged species at the liquid|liquid interface.

## 2.2 Photocurrent transient measurements

The setup for photocurrent transient measurement is illustrated in Figure 2.6.

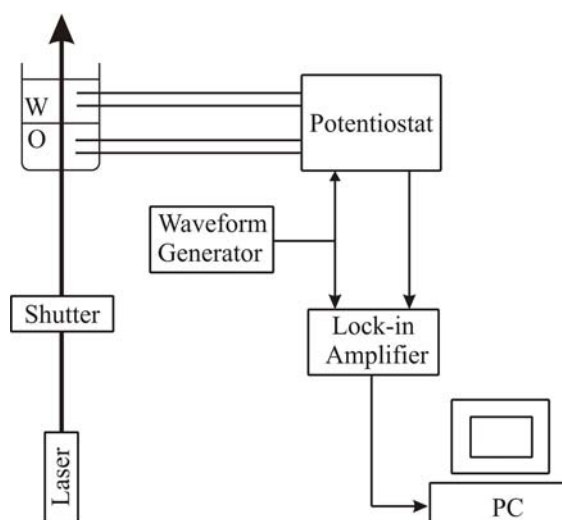


**Figure 2.6** Setup for photocurrent transient measurements.

The photocurrent transients were measured under potentiostatic conditions, where the four-electrode potentiostat was connected a Hi-Tek waveform generator (Hi-Tek Instruments PP-R1). The illumination was carried out with 442 nm light of a He-Cd laser (Omnichrome S74) or 454 nm light of a tunable Ar-ion laser (Omnichrome S43) under transmission mode. The incident photon flux was quantitatively determined by measuring the incident light intensity with a photomultiplier (Model 70316, Thermo Oriel Instruments). An optical shutter with an aperture time in the range of few microseconds was used to control the illumination time. The photoinduced electrical current was recorded via the auxiliary channel of a lock-in amplifier (Stanford Research System SR830).

## 2.3 Quasi-elastic laser scattering (QELS)

### 2.3.1 Capillary wave theory

Thermal fluctuations roughen the interface between two liquids. Experiments based on optical<sup>6</sup> and neutron<sup>7, 8</sup> reflectivity and molecular dynamics simulations have show that the liquid|liquid interface is never flat but highly corrugated. The corrugation appears in the form of *capillary waves*.<sup>9</sup> The displacement of the interface  $\zeta(\vec{r}, t)$  with respect to its equilibrium plane ( $\zeta = 0$ ) can be written as a sum of Fourier components, each of which can be described by:<sup>10</sup>

$$\zeta(\vec{r}, t) = \zeta_0 \exp\left[i(\vec{k} \cdot \vec{r} + \omega t)\right] \quad (2.7)$$

where  $\vec{k}$  represents the wave vector of the selected wave and  $\omega$  is its complex frequency ( $\omega = \omega_0 + i(\Delta\omega)$ ). The thermally excited capillary waves tend to disappear under the influence of restoring forces (surface tension and gravity) and damping forces due to the viscosities of bulk liquids. The motion of the capillary wave at a liquid|liquid interface can be described by the hydrodynamic equations (Lamb's equations).<sup>11, 12</sup> Neglecting the gravitational contribution to the motion for short-length capillary waves, the following relationship can be derived using the first order approximation:

$$\omega_0 = \sqrt{\frac{\gamma k^3}{\rho^w + \rho^o}} \quad (2.8)$$

where  $k$  is the wave number of the capillary wave,  $\gamma$  is the surface tension,  $\rho^r$  ( $r = w, o$ ) represents the density of the corresponding liquid,  $\omega_0$  is the peak frequency of the capillary wave. Experimentally, quasi-elastic laser scattering (QELS) technique allows us to measure the power spectrum of the capillary wave for a selected wave number.<sup>13-15</sup> The spectrum after being Fourier transformed is approximately Lorentzian in form, characterized by a peak frequency that can be identified with  $\omega_0$ . According to eq 2.8, we can estimate the surface tension from  $\omega_0$ , which can be used further to estimate the surface excess concentration.

### 2.3.2 Principle of QELS method and experimental apparatus

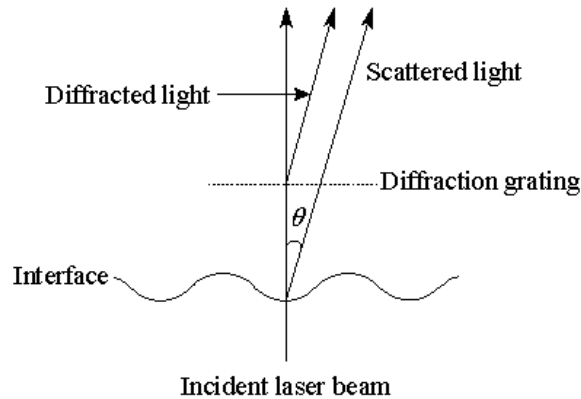


**Figure 2.7** Principle of QELS method.

As illustrated in Figure 2.7, when an incident laser beam vertically irradiates the interface, some photons are quasi-elastically scattered by the capillary wave at the interface with a small angle to the normal determined by the momentum conservation:

$$K \tan \theta = k \quad (2.9)$$

where  $\theta$  is the scattering angle.  $K$  and  $k$  are the wave numbers of the incident beam and the capillary wave, respectively. In this process, the incident light frequency  $\omega$  is modulated by the capillary wave with a frequency of  $\omega_0$ . The scattered light has a frequency of  $\omega \pm \omega_0$ . A diffraction grating positioned after the scattering process and

perpendicular to the incident laser beam acts as the local oscillator, which generates the diffracted beams in one or more space directions with a frequency of  $\omega$  equal to that of the incident beam. The scattered light from the interface will mix with a certain order of the diffracted beam in the same direction. The mixing beam can be selected with a pinhole in front of a photomultiplier (PMT). Therefore, the light scattered by the capillary wave with a frequency of  $\omega \pm \omega_0$  is received by the PMT, where it interferes with light of frequency  $\omega$  that is diffracted by the optical grating. The PMT gives an output current containing components at the frequency of the capillary wave frequency  $\omega_0$ .

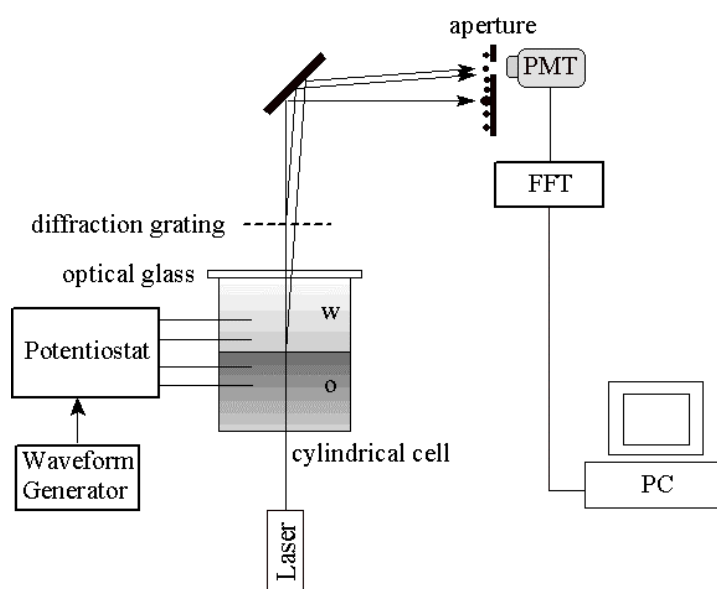


**Figure 2.8** Schematic diagram of the experimental QELS setup.

Figure 2.8 shows the diagram of the experimental setup. The liquid|liquid interface is constructed in a cylindrical quartz glass cell with a cross section of  $15.9 \text{ cm}^2$ . The water and organic solvent are saturated each other before use. The surface of the aqueous phase is covered with an optical glass window to minimize the light scattering from the air|water interface. The light beam from a 4 mW He-Ne laser at 632.8 nm (Uniphase Model 1101) passes through the bottom of the cylindrical quartz cell and illuminates the interface perpendicularly. A diffraction grating consisting of dark lines with 0.285 mm spacing on a photographic glass plate was placed after the optical cell. The third-order diffraction spot was selected with an aperture, monitored by a PMT tube, and analyzed by a fast-Fourier transform analyzer (FFT, Stanford Research Systems SR 770).

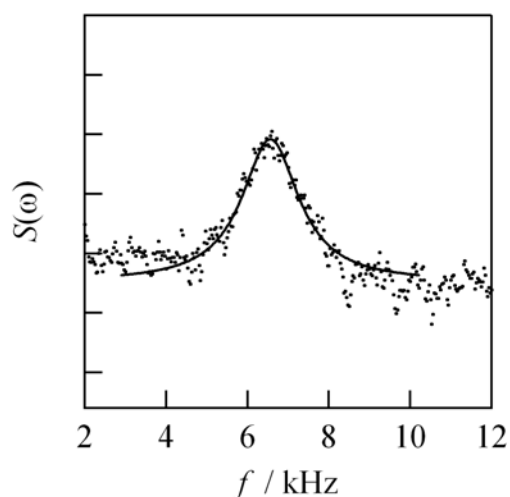


**Figure 2.9** Power spectrum corresponding to the third-order spot of QELS at a neat water|DCE interface.

A typical power spectrum of the light scattered by the neat water|DCE interface (without supporting electrolytes in both phases) is displayed in Figure 2.9, in which the line represents the fitting with a Lorentzian function. The spectrum features a peak at frequency of 6550.1 Hz, which can be related to the surface tension  $\gamma$  in terms of eq 2.8. The wave number,  $k$ , can be determined with eq 2.9 by considering the instrumental configuration. For the one we employed,  $k = 510.4 \text{ cm}^{-1}$  can be estimated by taking the interfacial tension of the neat water|DCE interface as  $28.5 \text{ mN m}^{-1}$ .<sup>16</sup>

## 2.4 Other electrochemical techniques

### 2.4.1 Differential pulse voltammetry (DPV)

The potential waveform of DPV involves the imposition of a potential pulse of constant height and width to a staircase increased base potential, as illustrated in Figure 2.10. It can be characterized by four parameters: pulse period ( $\tau$ ), pulse width ( $\tau'$ ), pulse height ( $\Delta E_{\text{ph}}$ ), and potential increment ( $\Delta E_{\text{b}}$ ). Recommended values are  $\Delta E_{\text{b}} = 1 \sim 10 \text{ mV}$ ,  $\Delta E_{\text{ph}} = 10 \sim 100 \text{ mV}$ ,  $\tau' = 5 \sim 100 \text{ ms}$ , and  $\tau = 0.5 \sim 4 \text{ s}$ . The effective scan rate,  $\nu = \Delta E_{\text{b}}/\tau$ , is generally about  $1 \sim 20 \text{ mV s}^{-1}$ . Each pulse function comprises a base

potential and a pulse potential. The application of the base potential creates the surface concentrations according to the Nernst equation, which can be considered as the “apparent bulk concentrations” when the potential pulse comes to operate. This is reasonable when the base potential period ( $\tau - \tau'$ ) is typically 10 or more times longer than the pulse width ( $\tau'$ ). In this condition, the potential pulse only negligibly modifies the bulk concentrations enforced by the prior base potential.

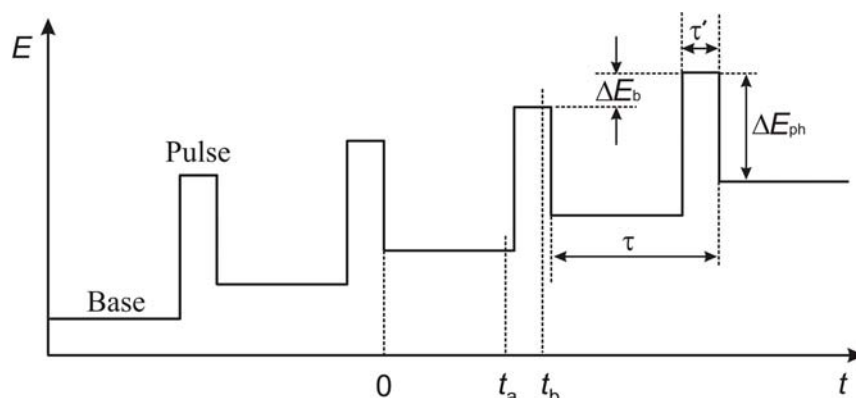


**Figure 2.10** Potential waveform of differential pulse voltammetry.

The difference between two sampled currents at times  $t_b$  and  $t_a$  ( $I(t_b) - I(t_a)$ ) is measured, registered just before the end of the pulse and just before pulse application. This subtractive method reduces the contribution from the background current, enhancing the sensitivity. The current difference is plotted against the base potential and leads to a peak-shaped current-potential curve when the potential fulfills:

$$E_p = E^{\circ'} + \frac{RT}{nF} \ln \sqrt{\frac{D_R}{D_O}} - \frac{\Delta E_{ph}}{2} \quad (2.10)$$

where  $E^{\circ'}$  is the formal redox potential,  $D_O$  and  $D_R$  are the diffusion coefficients of the oxidized and reduced species, respectively. Assuming  $D_O = D_R$  for usual electrochemical reactions, the peak potential for an oxidation process anticipates the formal redox potential by  $\Delta E_{ph}/2$ :

$$E_p = E^{\circ'} - \frac{\Delta E_{ph}}{2} \quad (2.11)$$

Therefore, DPV is very convenient to determine  $E^{\circ'}$ .

### 2.4.2 Capillary electrophoresis applied to the measurement of the charge of NPs

We shall describe how to use capillary electrophoresis to measure the charge of small particles since in Chapter 4 we measure the apparent surface charge of gold NPs. Figure 2.11 depicts the motion of a spherical and charged object of radius  $a$  with a rate of  $v$  under an electric field  $E$ .  $\kappa^{-1}$  is often called Debye length, which is a property of the electrolyte solution and represents the screening effect of electrolyte ions to the charged object. In a dilute solution,  $\kappa^{-1}$  is much larger than  $a$  and its effect can be neglected. The movement of the charged sphere undergoes two forces: the driving force ( $F_E = zeE$ ) imparted by the electric field and the retarding frictional force ( $F_f = fv$ ).

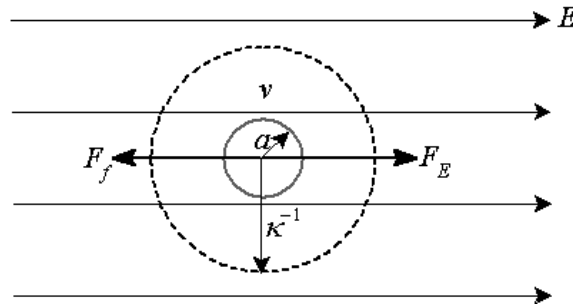


**Figure 2.11** Electrophoretic motion of a charged particle in a viscous medium under an electric field.

When the movement reaches a steady state velocity, the driving force balances with the frictional force:

$$zeE = fv \quad (2.12)$$

where  $ze$  represents the effective charge of the particle,  $E$  the electric field strength, and  $v$  the velocity of the movement.  $f$  is the frictional coefficient, which is given by the hydrodynamics for a spherical particle:

$$f = 6\pi\eta r \quad (2.13)$$

where  $\eta$  is the viscosity of the solvent and  $r$  the hydrodynamic radius of the particle sphere. Therefore, rearranging eq 2.12 yields:

$$v = \frac{zeE}{6\pi\eta r} \quad (2.14)$$

This equation gives the electrophoretic mobility:



$$\mu_{\text{ep}} = \frac{v}{E} = \frac{ze}{6\pi\eta r} \quad (2.15)$$

In practical measurements, the observed electrophoretic mobility ( $\mu_{\text{app}}$ ) may not be directly related to the electrophoretic mobility of the solute. Instead, it corresponds to a combination of the electrophoretic mobility of the solute ( $\mu_{\text{ep}}$ ) and the electro-osmotic mobility of the solvent ( $\mu_{\text{eof}}$ ):

$$\mu_{\text{app}} = \mu_{\text{ep}} + \mu_{\text{eof}} \quad (2.16)$$

$\mu_{\text{eof}}$  can be measured using a neutral marker in the same solution.

Experimental measurements in Chapter 4 were performed on a P/ACE<sup>TM</sup> Capillary Electrophoresis System (Beckman Coulter) with a 60 cm long capillary tube, an applied voltage of 30 kV, and a UV diode array detector set at 198 nm. The sample was dissolved in a four times dilute of a buffer at pH 7 (~0.029 M NaOH + ~0.050 KH<sub>2</sub>PO<sub>4</sub>) and ethanol was used as the neutral marker.

## 2.5 Spectroscopic and microscopic measurements

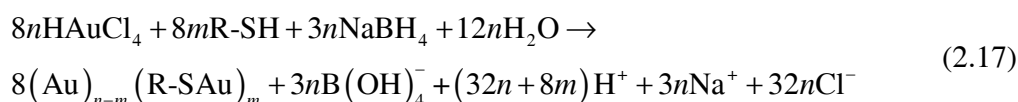
Ultraviolet-visible (UV-Vis) absorption spectroscopy, fluorescence spectroscopy and transmission electron microscopy (TEM) have been extensively employed to characterize the chemically prepared NPs.

UV-Vis absorption spectra were collected on an Ocean Optics CHEM2000-UV-Vis spectrometer using standard 1 cm path cuvettes. Fluorescence spectra were obtained from a Perkin Elmer LS50B Luminescence Spectrometer using a four-wall transparent cubic quartz cell. The fluorescence was detected in the direction normal to the excitation beam. TEM measurements were performed on a Philips CM 20 operating at 200 kV. For very small NPs, measurements were also carried out on a Philips CM 300, a high-resolution TEM (HRTEM) with an accelerating voltage of 300 kV. The specimen were generally prepared by deposition of small volumes of sample solutions on copper mesh grids and dried under nitrogen atmosphere.

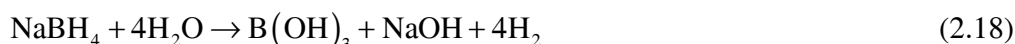
## 2.6 Synthesis and electrochemical measurements of gold NPs

### 2.6.1 Mercaptosuccinic acid (MSA) stabilized gold NPs

Aqueous suspensions of gold NPs protected by mercaptosuccinic acid (MSA) were synthesized at room temperatures by reduction of  $\text{AuCl}_4^-$  with sodium borohydride ( $\text{NaBH}_4$ ) in a mixture of water and methanol. The synthesis follows the protocol reported by Chen and Kimura.<sup>17</sup> In a typical synthesis, an aqueous solution of  $\text{HAuCl}_4$  (0.05 M) was mixed with 100 mL of ethanol containing MSA (0.0125 M) for 10 minutes. 25 mL of fresh  $\text{NaBH}_4$  (0.20 M) aqueous solution was added at a rate of 5 mL/min under vigorous stirring. The solution turned dark-brown immediately and was further stirred continuously for one hour. The overall reaction can be expressed as:



which is also accompanied by the hydrolysis of excess  $\text{NaBH}_4$ :



In a second stage, the nanoparticles were separated and purified in order to remove unreacted molecules and contaminants. The solution was centrifuged at 5500 rpm for 15 minutes. The sediment was washed five times with a water/methanol mixture ( $V:V = 1:5$ ), followed by washing with pure methanol to remove unbounded MSA molecules. After the purification, the dark brown precipitate is dried at temperatures below 40 °C and pressure below  $5 \times 10^{-3}$  torr for 24 hours.

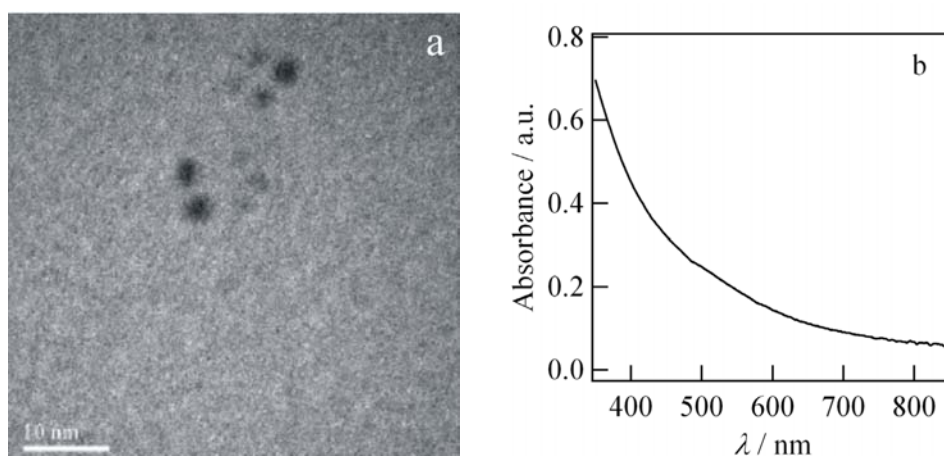


**Figure 2.12** HRTEM graph (a) and UV-Vis spectrum for MSA stabilized Au NPs.

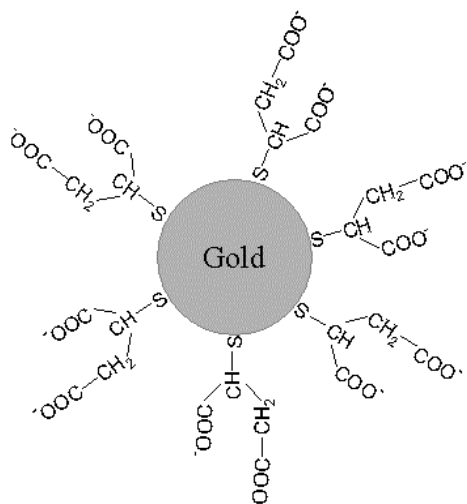
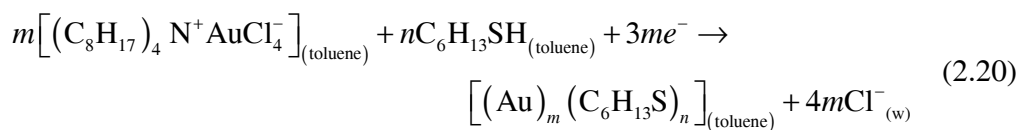
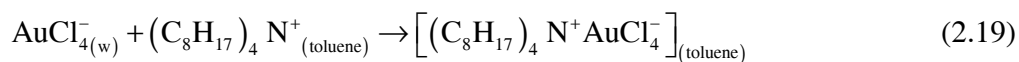


**Figure 2.13** Surface Structure of an MSA stabilized Au NP.

The HRTEM image, as shown in Figure 2.12a, gives an average size of  $(1.5 \pm 0.4)$  nm in diameter. The UV-visible absorption spectrum of MSA stabilized gold NPs dispersed in water is displayed in Figure 2.12b. A highly damped plasmon resonance is observed due to the small size of the NPs. Figure 2.13 schematically shows the surface structure of a Au NP protected by MSA. The thiol group is binding at the surface of the particle and the carboxylic groups are left outside. The presence of a high density of carboxylic groups on the surface makes the NPs highly water dispersible. Certainly, there exists extensive hydrogen bond formation between  $\text{H}_2\text{O}$  and the carbonyl groups.<sup>17</sup>

### 2.6.2 1-Hexanethiol monolayer protected gold nanoclusters

The 1-hexanethiol Monolayer Protected Gold Clusters (MPCs) were prepared by the Brust two-phase reaction<sup>18, 19</sup> followed by extraction and annealing processes to harvest a population of MPCs with relatively uniform metallic cores.<sup>20</sup> Briefly, 1.55 g of  $\text{HAuCl}_4 \cdot 3\text{H}_2\text{O}$  in water was mixed with 1.12 g of TOABr in toluene under vigorous stirring. After  $\text{AuCl}_4^-$  was completely extracted into toluene, 1.8 mL 1-hexanethiol corresponding to a 3:1 molar ratio (S: Au) was added. The mixture was further stirred for 20 minutes, followed by the addition of 1.90 g of  $\text{NaBH}_4$  all at once at  $0^\circ\text{C}$ , which resulted in an immediate, pronounced darkening of the mixture. The general reaction can be summarized as follows:



The reduction was allowed to proceed for 45 minutes, after which the water layer was removed with a separating funnel and the toluene removed by rotary evaporation at 40 °C. The black slurry remaining in the round-bottom flask includes all fractions of MPCs, byproducts and unreacted residues.

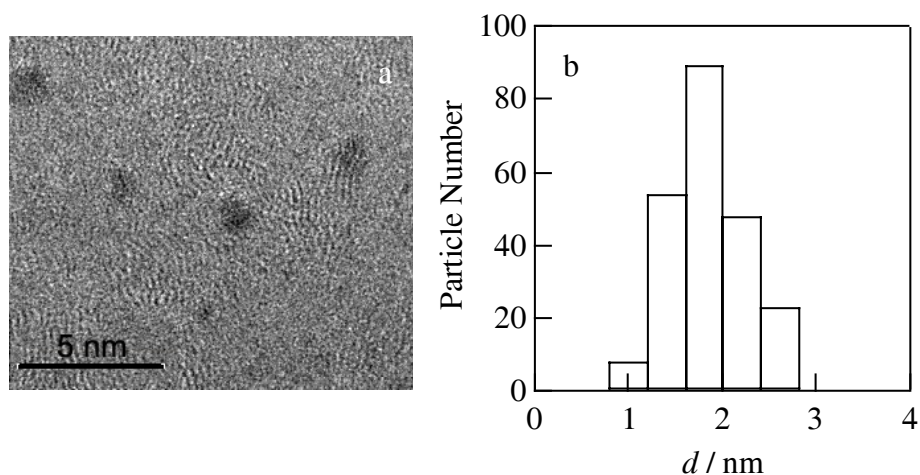


**Figure 2.14** HRTEM image (a) and the corresponding size distribution (b) of the final MPC product.

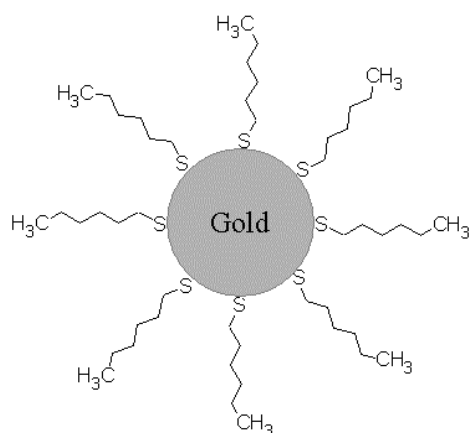


**Figure 2.15** Cartoon structure of a C<sub>6</sub>Au-MPC.

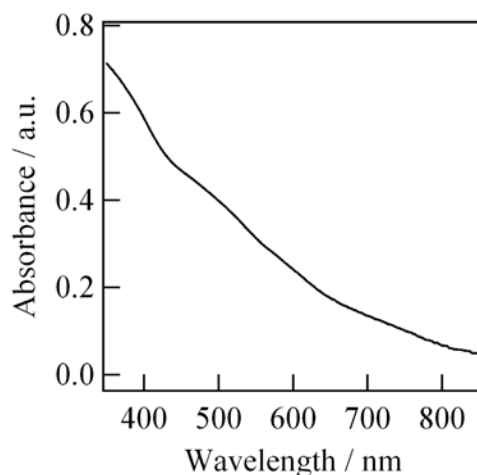


**Figure 2.16** UV-Vis absorption spectrum of C<sub>6</sub>Au-MPCs in DCE.

The extraction was then carried out as follows: 100 mL ethanol was added to the flask, which was covered to stand overnight and then filtered. The filtrate was evaporated to dryness to obtain a fraction of MPCs called ethanol-soluble MPCs, to which then 100 mL CH<sub>3</sub>CN was added. After 24 h, the MPC product was collected on a frit where it was washed with copious amounts of CH<sub>3</sub>CN. The extraction treatment not only removed the byproducts and unreacted residues but also some fractions of smaller core size MPCs.<sup>21</sup>

The obtained MPCs with above treatment were further annealed in dichloromethane in which a 500-fold excess of 1-hexanethiol was dissolved. After stirring for 4 days, dichloromethane was removed by rotary evaporation. The remaining product in the flask was sonicated in CH<sub>3</sub>CN and collected through several cycles of centrifugation and washing. The final product has a dominant population with an average core mass of 28 kDa, which corresponds to ca. 140 Au atoms protected with ca. 53 1hexanethiol ligands.<sup>20</sup> The population has a mean diameter of  $1.6 \pm 0.4$  nm in the metallic core determined by HRTEM, as shown in Figure 2.14. Figure 2.15 is the cartoon structure of a MPC, in which the metallic core is covered by a monolayer of 1-hexanethiol. A highly damped plasmon resonance due to the small size of the NPs is also observed as shown in Figure 2.16.

### 2.6.3 Mixed-alkanethiol monolayer protected gold nanoclusters

1,9-nonanedithiol can be incorporated into 1-hexanethiol monolayer protected gold nanoclusters by ligand-place exchange reaction.<sup>22</sup> Typically, 60 mg of MPCs prepared as described above and 4  $\mu$ L 1,9-nonanedithiol were co-dissolved in 10 mL of hexane in a round-bottom flask, and the mixture was stirred for about 36 h. During this period, some 1-hexanethiol ligands on the particle surface were displaced by 1,9-nonanedithiol. Some precipitates were also found to stick on the flask wall due to the intercalation and cross-linking by the 1,9-nonanedithiol. The hexane solution was repeatedly extracted with methane to remove excessive and displaced thiol ligands. The resulting solution contains MPCs protected by a mixed monolayer of 1-hexanethiol and 1,9-nonanedithiol, where the free mercapto groups of 1,9-nonanedithiol on the surface of MPC sphere served as anchor sites for self-assembling on a gold electrode.

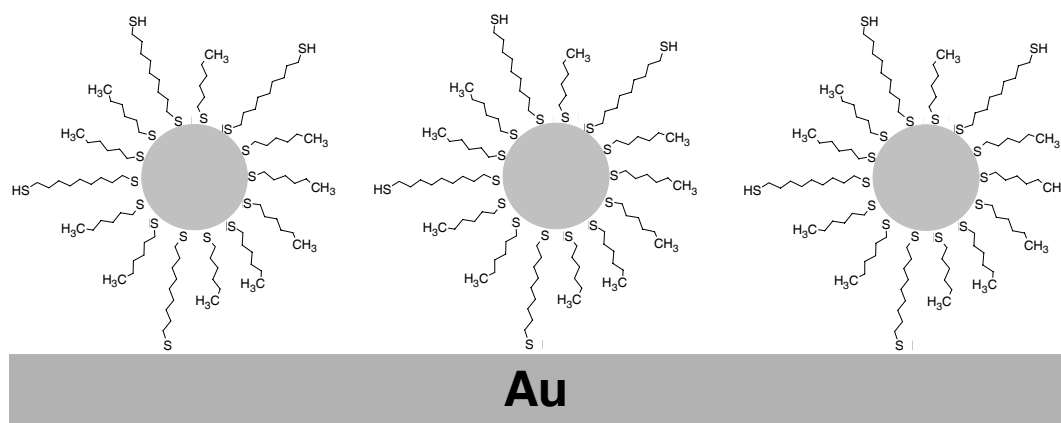


**Figure 2.17** Schematic illustration of MPCs self assembled on the gold electrode surface.

The self-assembling of MPCs on a gold electrode was simply performed by immersing the gold electrode into the above mentioned hexane solution for typically 36 h. The electrode was then rinsed with copious hexane to remove loosely bound particles, dried in an Argon stream and transferred to an electrolyte solution for electrochemical measurements. The architecture of MPC self-assembled on the electrode surface is schematically shown in Figure 2.17.

## 2.6.4 Electrochemical characterization of gold NPs

In Chapter 6, the redox properties of MPCs in solutions and self-assembled on gold electrodes were studied by cyclic voltammetry (CV) and differential pulse voltammetry (DPV), which were performed on a CHI-900 electrochemical workstation (CH-Instruments, TX). For freely diffusing MPCs in solutions, the measurements were carried out in a two-electrode arrangement, in which a 25- $\mu\text{m}$  diameter disk-shaped platinum microelectrode (CH-Instruments, TX) was used as the working electrode and a silver wire was used both as quasi-reference electrode (QRE) and counter electrode. The potential was either corrected to the ferrocenium/ferrocene ( $\text{Fc}^+/\text{Fc}$ ) scale by adding Fc to the cell at the end of the measurement or referred to the apparent potential reference (AgQRE). For MPCs self-assembled on the electrode surface, the CV and DPV measurements were performed in a three-electrode cell, in which a gold electrode functions as the working electrode (WE) and a platinum wire and a silver wire as the counter electrode (CE) and quasi-reference electrode (QRE), respectively.

## 2.7 Chemical synthesis of CdSe NPs

### 2.7.1 MSA stabilized CdSe NPs

Water dispersible MSA protected CdSe NPs were prepared using a published protocol,<sup>23</sup> however  $\text{Na}_2\text{Se}$  was used instead of  $\text{NaHSe}$ . In a typical synthesis, 513.3 mg (2.35 mmol) of  $\text{CdCl}_2 \cdot 2\text{H}_2\text{O}$  was dissolved in 125 mL of water, and 866.4 mg (5.77 mmol) MSA was added under stirring, followed by adjusting the pH to 11.2 by droplet addition of 1 M solution of NaOH. After bubbling the solution with  $\text{N}_2$  for 40 min, newly prepared solution of 1.1 mmol  $\text{Na}_2\text{Se}$  in 22 mL water was introduced under stirring. The resulting mixture was then subjected to a reflux at 100°C under air condition. During the reflux, aliquots were taken out of the flask at different times to measure the absorption spectra to monitor the growth of the NPs. The transparent solution with bright-orange color was first concentrated on a rotary evaporator. Then acetone was added to precipitate the NPs inside the solution. The resulted mixture was stirred for 30 min, and the precipitate and

supernatant were separated through centrifugation. The precipitate was washed 5 times with water/acetone mixture and then dried.

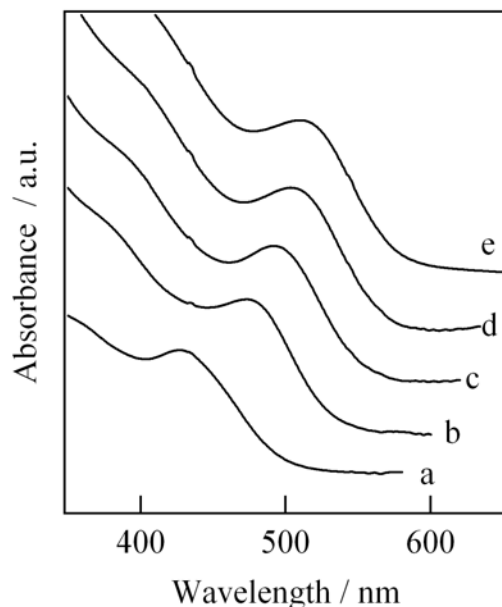


**Figure 2.18** (a) Temporal evolution of the absorption spectra of the reaction solution refluxed at 100 °C: (a) 20, (b) 40, (c) 60, (d) 80, and (e) 120 min.

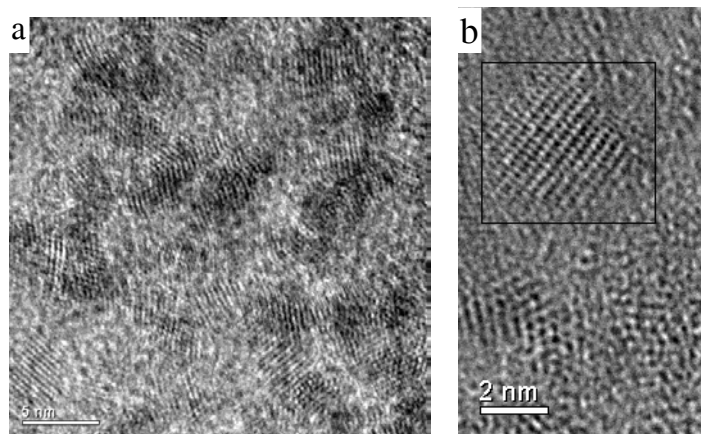


**Figure 2.19** (a) Representative HRTEM image of CdSe NPs; (b) HRTEM image of a single CdSe NP (in the black pane).

Figure 2.18 illustrates the temporal evolution of the absorption spectrum of the colloidal suspension of CdSe NPs under reflux at 100 °C. The growth of the particles is clearly evidenced by the shifts of the exciton peak and the absorption onset to longer wavelengths, which is due to the well-known quantum size effect in terms of eq 1.57 in Chapter 1. A typical HRTEM image of CdSe NPs obtained after 120 minutes of reflux is



shown in Figure 2.19a. The particles tend to form agglomerates due to the strong interaction of the carboxylic groups, leading to a possible overestimation of the mean size and size distribution. The analysis of the micrographs showed CdSe NPs with sizes ranging from 2 to 3.8 nm and resulting on an average size of 2.8 nm. Figure 2.19b shows the HRTEM image of a single CdSe NP, which is well crystallized with clearly resolved lattice planes. The surface structure of MSA stabilized CdSe NPs is expected to be the same as that of MSA stabilized gold NPs as shown in Figure 2.13.

### **2.7.2 Citrate stabilized CdSe NPs**

Citrate-stabilized CdSe NPs were prepared according to the procedure previously reported.<sup>24</sup> In a typical synthesis, 0.05 g trisodium citrate and 2 mL of 0.04 M cadmium perchlorate ( $\text{Cd}(\text{ClO}_4)_2 \cdot \text{H}_2\text{O}$ ) were added to 45 mL water, and the pH was then adjusted to 9.0 with 0.1 M sodium hydroxide (NaOH). The solution was further bubbled with nitrogen for 10 min and 2 mL of 0.01 M *N,N*-dimethylselenourea was added, which corresponds to a Cd:Se molar ratio of 4:1. The mixture was heated in a microwave oven at 900 W for 50 s. The resulting solution has a transparent orange color, containing CdSe NPs stabilized electrostatically by anions in the solution.

## **2.8 Preparation of room temperature ionic liquids (RTILs)**

RTILs form a novel class of liquids, which are entirely composed of ions that melt at ambient temperatures due to the overwhelmingly coulombic forces. They have been used in diverse fields of chemistry including synthesis, catalysis, separations, and electrochemistry.<sup>25</sup> Interest stems from their unique chemical and physical properties and from the ability of tuning their properties by varying in the structure and nature of the ionic components. RTILs are non-volatile and non-flammable. They are attractive to electrochemists mainly because they provide large potential windows and can act as both solvent and electrolyte.<sup>26</sup>

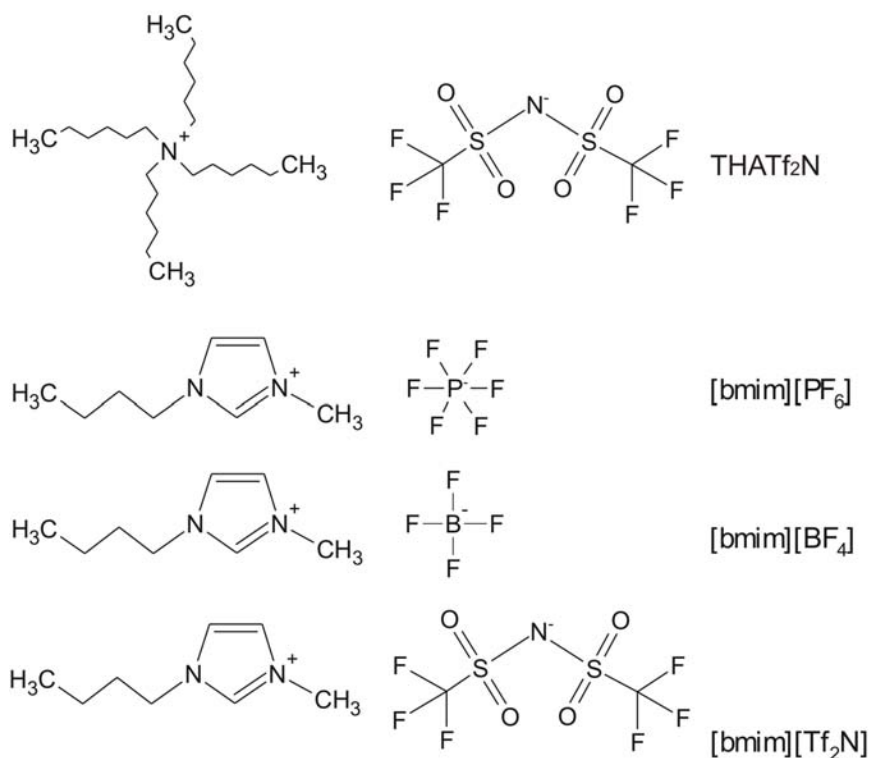


**Figure 2.20** The structures of various RTILs.

**Table 2.1** Physicochemical properties of RTILs.

RTILs	m.p.(K)	$d$ (g cm <sup>-3</sup> )	$\eta$ (mPa s)	$\Lambda$ (S m <sup>-1</sup> )	$\epsilon$
THATf <sub>2</sub> N <sup>a</sup>	266	1.11	435	0.011	-----
[bmim][PF <sub>6</sub> ]	212 <sup>b</sup>	1.43 <sup>c</sup>	52 <sup>c</sup>	0.146 <sup>d</sup>	11.4 ± 0.6 <sup>e</sup>
[bmim][Tf <sub>2</sub> N] <sup>f</sup>	269	1.37	312	0.39	-----
[bmim][BF <sub>4</sub> ]	192 <sup>b</sup>	1.17 <sup>c</sup>	233 <sup>g</sup>	0.173 <sup>d</sup>	11.7 ± 0.6 <sup>e</sup>

a: at 298 K;<sup>27</sup> b: cited from ref. 28;<sup>28</sup> c: at 303 K;<sup>29</sup> d: at 298.5 K;<sup>29</sup> e: at 298.15 K;<sup>30</sup> f: at 293 K;<sup>27</sup> g: at 303 K.<sup>31</sup>

In Chapter 6, four types of RTILs were employed as supporting electrolyte and/or solvent to study the redox properties of MPCs. They are tetrahexylammonium bis(trifluoromethylsulfonyl)imide (THATf<sub>2</sub>N), 1-*n*-butyl-3-methylimidazolium hexafluorophosphate ([bmim][PF<sub>6</sub>]), 1-*n*-butyl-3-methylimidazolium tetrafluoroborate ([bmim][BF<sub>4</sub>]) and 1-*n*-butyl-3-methylimidazolium bis(trifluoromethylsulfonyl)imide ([bmim][Tf<sub>2</sub>N]). Their structures are illustrated in Figure 2.20, and their physicochemical properties are compared in Table 2.1. THATf<sub>2</sub>N was prepared in the LEPA and the other

three were kindly provided by Laboratory of Organometallic and Medicinal Chemistry (LCOM, Prof. Paul Dyson), EPFL. The detailed preparations of four RTILs are described as below:

**THATf<sub>2</sub>N**<sup>27</sup> was prepared by metathesis of tetrahexylammonium chloride (THACl) and lithium bis(trifluoromethylsulfonyl)imide (LiTf<sub>2</sub>N) in a molar ratio of 1:1 in water under vigorous stirring. The resulting turbid mixture was extracted with dichloromethane, followed by evaporation of dichloromethane on a rotary evaporator. The liquid left in the flask was washed with a large amount of water, and then dried at 100°C under vacuum. The final product is transparent and viscous.

**[bmim][PF<sub>6</sub>]** and **[bmim][Tf<sub>2</sub>N]** were prepared by mixing 1-*n*-butyl-3-methylimidazolium chloride ([bmin][Cl]) with potassium hexafluorophosphate (KPF<sub>6</sub>) and LiTf<sub>2</sub>N, respectively, in a molar ratio of 1:1 in water. The mixture was stirred at room temperatures overnight, leading to the formation of ionic liquids as a separate phase. The crude product was washed repeatedly with water and then dried at 100°C under vacuum.

**[bmim][BF<sub>4</sub>]**. [bmin][Cl] was reacted with an excess of ammonium tetrafluoroborate in a dichloromethane solution overnight, and the ionic liquid [bmim][BF<sub>4</sub>] was formed. Product ammonium halide and any residual ammonium tetrafluoroborate were removed from the ionic liquid by washing with water. The resulting [bmim][BF<sub>4</sub>] was dried 100°C under vacuum for use.

---

## 2.9 References

- (1) Samec, Z.; Marecek, V.; Weber, J. *J. Electroanal. Chem.* **1978**, *96*, 245-247.
- (2) Samec, Z.; Marecek, V.; Weber, J. *J. Electroanal. Chem.* **1979**, *100*, 841-852.
- (3) Su, B.; Abid, J.-P.; Fermin, D. J.; Girault, H. H.; Hoffmannova, H.; Krtil, P.; Samec, Z. *J. Am. Chem. Soc.* **2004**, *126*, 915-919.
- (4) Parker, A. J. *Electrochim. Acta* **1976**, *21*, 671-679.
- (5) Abraham, M. H.; De Namor, A. F. D. *J. Chem. Soc. Faraday Trans. 1* **1976**, *72*, 955-962.
- (6) Beaglehole, D. *Phys. Rev. Lett.* **1987**, *58*, 1434-1436.
- (7) Lee, L. T.; Langevin, D.; Meunier, J.; Wong, K.; Cabane, B. *Prog. in Colloid & Polymer Sci.* **1990**, *81*, 209-214.
- (8) Lee, L. T.; Langevin, D.; Farnoux, B. *Phys. Rev. Lett.* **1991**, *67*, 2678-2681.
- (9) Daikhin, L. I.; Kornyshev, A. A.; Urbakh, M. *J. Electroanal. Chem.* **2000**, *483*, 68-80.
- (10) Langevin, D. *Light Scattering by Liquid Surfaces and Complementary Techniques*; Marcel Dekker: New York, 1992.
- (11) Lamb, H. *Hydrodynamics*; Dover, New York, 1945.
- (12) Levich, V. G. *Physicochemical Hydrodynamics*; Prentice hall, Englewood Cliffs, NJ, 1962.
- (13) Zhang, Z.; Tsuyumoto, I.; Takahashi, S.; Kitamori, T.; Sawada, T. *J. Phys. Chem. A* **1997**, *101*, 4163-4166.
- (14) Trojanek, A.; Krtil, P.; Samec, Z. *J. Electroanal. Chem.* **2001**, *517*, 77-84.
- (15) Trojanek, A.; Krtil, P.; Samec, Z. *Electrochem. Commun.* **2001**, *3*, 613-618.
- (16) Nagatani, H.; Samec, Z.; Brevet, P.-F.; Fermin, D. J.; Girault, H. H. *J. Phys. Chem. B* **2003**, *107*, 786-790.
- (17) Chen, S.; Kimura, K. *Langmuir* **1999**, *15*, 1075-1082.
- (18) Brust, M.; Fink, J.; Bethell, D.; Schiffrin, D. J.; Kiely, C. *J. Chem. Soc. Chem. Commun.* **1995**, 1655-1656.
- (19) Brust, M.; Walker, M.; Bethell, D.; Schiffrin, D. J.; Whyman, R. *J. Chem. Soc. Chem. Commun.* **1994**, 801-802.
- (20) Hicks, J. F.; Miles, D. T.; Murray, R. W. *J. Am. Chem. Soc.* **2002**, *124*, 13322-13328.

- (21) Hicks, J. F.; Templeton, A. C.; Chen, S.; Sheran, K. M.; Jasti, R.; Murray, R. W.; Debord, J.; Schaaff, T. G.; Whetten, R. L. *Anal. Chem.* **1999**, *71*, 3703-3711.
- (22) Chen, S. *J. Phys. Chem. B* **2000**, *104*, 663-667.
- (23) Rogach, A. L.; Kornowski, A.; Gao, M.; Eychmueller, A.; Weller, H. *J. Phys. Chem. B* **1999**, *103*, 3065-3069.
- (24) Rogach, A. L.; Koktysh, D. S.; Harrison, M.; Kotov, N. A. *Chem. Mater.* **2000**, *12*, 1526-1528.
- (25) Wasserscheid, P.; Welton, T. *Multiphasic catalysis with ionic liquids in combination with compressed CO<sub>2</sub>*; Wiley-VCH: Weinheim, Germany, 2003.
- (26) Bonhote, P.; Dias, A.-P.; Papageorgiou, N.; Kalyanasundaram, K.; Graetzel, M. *Inorg. Chem.* **1996**, *35*, 1168-1178.
- (27) Matsumoto, H.; Kageyama, H.; Miyazaki, Y. *Chem. Lett.* **2001**, 182-183.
- (28) Suarez, P. A. Z.; Dullius, J. E. L.; Einloft, S.; De Souza, R. F.; Dupont, J. *Polyhedron* **1996**, *15*, 1217-1219.
- (29) Suarez, P. A. Z.; Einloft, S.; Dullius, J. E. L.; De Souza, R. F.; Dupont, J. *J. Chim. Phys. Phys.-Chim. Bio.* **1998**, *95*, 1626-1639.
- (30) Wakai, C.; Oleinikova, A.; Ott, M.; Weingaertner, H. *J. Phys. Chem. B* **2005**, *109*, 17028-17030.
- (31) Earle, M. J.; McCormac, P. B.; Seddon, K. R. *Chem. Commun.* **1998**, 2245-2246.



## **Chapter 3**

# **Simulations of the adsorption of ionic species at liquid|liquid interfaces**

### **3.1 Introduction**

As mentioned in Chapter 1, the present thesis is largely concerned with the assembly and reactivity of metallic and semiconducting NPs at the polarized liquid|liquid interface. In the following Chapter 4 and 5, we shall describe the adsorption of negatively charged mercaptosuccinic acid protected gold and CdSe NPs at the liquid|liquid interface. The adsorption of these NPs at the interface increases the charge density in the interfacial region and was found to be potential dependent. Phenomenologically, these NPs can be considered as big anions owing to the carboxylic groups of the surface-protecting agents. It is well known that ionic adsorption at the liquid|liquid interface is primarily controlled by the molecular structure of the interface, which in turn determines the potential profile across the interface. However, many analyses do not take into account the change of the electrical potential profile. Theoretical developments allowing the unambiguous

interpretation of the effect of ionic adsorption on the interfacial structure has not been reported yet.

Given this fact, we shall consider the adsorption of charged NPs at the liquid|liquid interface from a theoretical point of view. For simplicity, the charged NPs are considered as ions. The effect of their adsorption on the charge distribution at the ITIES will be simulated based on the classical description of the interface employing the Gouy-Chapman model. In the simulation, the inner layer is considered as a charged plane, where the ionic adsorption takes place. The potential at this plane is determined by the electro-neutrality condition. Various adsorption isotherms are considered, including potential dependent isotherms based on the Langmuir and Frumkin adsorption models. The potential distribution and the charge density profile are derived by numerically solving the Poisson-Boltzmann equation. We shall show here that the interfacial composition is significantly altered by the adsorption of ionic species, resulting in a substantial change in the potential distribution across the interface. Under certain conditions, the adsorption results in a non-monotonous potential distribution with a potential trap at the interface.

## 3.2 Theoretical and mathematical descriptions

### 3.2.1 Microscopic model of the interfacial structure

The microscopic model of the interfacial composition is schematically depicted in Figure 3.1. An inner layer separates two diffuse layers, which are classically described by the Gouy-Chapman (GC) theory. The total potential difference splits into three parts:

$$\Delta_o^w \phi = (\phi^w - \phi^2) + (\phi^2 - \phi^1) + (\phi^1 - \phi^o) = \Delta_2^w \phi + \Delta_1^2 \phi + \Delta_o^1 \phi \quad (3.1)$$

where  $\Delta_1^2 \phi$  is the potential drop across the inner layer and  $\Delta_2^w \phi$  and  $\Delta_o^1 \phi$  are the potential drops across the diffuse layers in the aqueous and organic phases, respectively. For the sake of simplicity, we make three assumptions:



- the potential drop across the inner layer is negligible, that is,  $\Delta_1^2\phi = \phi^2 - \phi^1 = 0$ .

The inner layer is reduced to a charged plane. This assumption is compatible with the GC model that considers ions as point charges. Therefore, the total potential drop takes place over two diffuse layers:

$$\Delta_o^w\phi = \Delta_2^w\phi + \Delta_o^2\phi \quad (3.2)$$

- we only consider the adsorption from the aqueous phase, which is supposed to take place at the charged plane. Furthermore, we assume that the adsorption of ionic species does not change the dielectric environment of the interface and the GC theory is still considered to be valid in the presence of adsorption. Given that the supporting electrolyte is in large excess of the adsorbate, the charge density due to the adsorption of ionic species and that due to the electrolytes in the diffuse layer are additive;
- in actual calculations, it is taken that  $\phi^w = 0$ , and  $x_1 = x_2 = 0$ . The adsorption takes place on the geometric surface dividing the two phases.

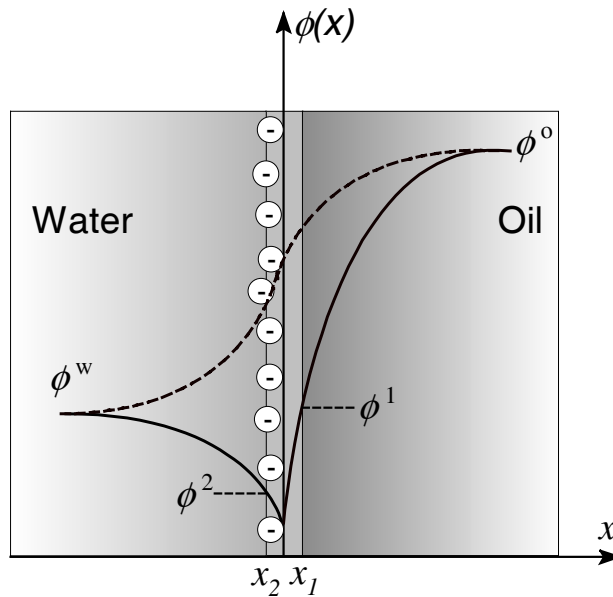


**Figure 3.1** Illustration of the potential profiles across the ITIES in the absence (dash line) and presence (solid line) of the adsorption of anionic species from the aqueous phase to the interface.

### 3.2.2 Potential Distribution

For clarity, we shall present here the classical GC theory<sup>1</sup> and its application to ITIES. Assuming the distribution of ions is uniform in a volume element parallel to the interface and follows Boltzmann's statistics, the spatial distribution of ionic charges can be defined as:

$$c_i(x) = c_i^r \exp\left\{-\frac{z_i F [\phi(x) - \phi^r]}{RT}\right\} \quad (3.3)$$

where  $c_i(x)$  is the concentration of ionic species  $i$  at a distance  $x$  from the interface ( $x=0$ ),  $c_i^r$  ( $r = w$  or  $o$ ) the corresponding bulk concentration, and  $z_i$  the valence of the ionic species. And  $F$ ,  $R$ ,  $T$  are, respectively, the Faraday constant, the gas constant and the temperature.

For the volume element defined by the planes of abscissae  $x$  and  $x+dx$ , the Laplacian of the potential is a function of the volumic charge density  $\rho(x)$  as given by Poisson's equation :

$$\frac{\partial^2 \phi(x)}{\partial x^2} = -\frac{\rho(x)}{\epsilon_0 \epsilon_r} \quad (3.4)$$

where  $\epsilon_0$  and  $\epsilon^r$  are the vacuum permittivity and the relative permittivity of the appropriate phase ( $r = w$  or  $o$ ), respectively.

The spatial charge density in solution can be simply expressed as:

$$\rho(x) = \sum_i z_i F c_i(x) \quad (3.5)$$

By substituting eq 3.5 into eq 3.4, we have:

$$\frac{\partial^2 \phi(x)}{\partial x^2} = -\frac{1}{\epsilon_0 \epsilon_r} \sum_i z_i F c_i^r \exp\left\{-\frac{z_i F [\phi(x) - \phi^r]}{RT}\right\} \quad (3.6)$$

This equation is known as the Poisson-Boltzmann equation describing the relation between the potential gradient and the charge density. In the case of 1:1 univalent supporting electrolyte, this relation becomes:

$$\frac{\partial^2 \phi(x)}{\partial x^2} = \frac{2Fc^r}{\varepsilon_0 \varepsilon^r} \sinh \left\{ \frac{F[\phi(x) - \phi^r]}{RT} \right\} \quad (3.7)$$

Integrating eq 3.7 with the following boundary conditions

$$x \rightarrow -\infty, \phi(x) \rightarrow \phi^w \text{ and } \frac{\partial \phi(x)}{\partial x} \rightarrow 0$$

$$x \rightarrow \infty, \phi(x) \rightarrow \phi^o \text{ and } \frac{\partial \phi(x)}{\partial x} \rightarrow 0$$

we obtain the potential gradients in the two diffuse layers:

$$\frac{\partial \phi(x)}{\partial x} \Big|_{-\infty < x \leq x_2} = \sqrt{\frac{8RTc^w}{\varepsilon_0 \varepsilon^w}} \sinh \left[ f(\phi(x) - \phi^w) \right] \quad (3.8a)$$

$$\frac{\partial \phi(x)}{\partial x} \Big|_{x_1 \leq x < \infty} = -\sqrt{\frac{8RTc^o}{\varepsilon_0 \varepsilon^o}} \sinh \left[ f(\phi(x) - \phi^o) \right] \quad (3.8b)$$

where  $f$  is equal to  $F/2RT$ .

Further integration of eqs 3.8a and 3.8b with the additional boundary condition

$$x = x_1 = x_2, \phi(x) = \phi^2$$

gives the potential distributions in two diffuse layers:

$$\phi(x) \Big|_{-\infty < x \leq x_2} = \phi^w + \frac{2}{f} \operatorname{arctanh} \left\{ \exp[\kappa^w(x - x_2)] \tanh \left[ \frac{f}{2}(\phi^2 - \phi^w) \right] \right\} \quad (3.9a)$$

$$\phi(x) \Big|_{x_1 < x \leq \infty} = \phi^o + \frac{2}{f} \operatorname{arctanh} \left\{ \exp[\kappa^o(x - x_1)] \tanh \left[ \frac{f}{2}(\phi^2 - \phi^o) \right] \right\} \quad (3.9b)$$

where  $\kappa^w = F(2c^w/RT\varepsilon_0\varepsilon^w)^{1/2}$  and  $\kappa^o = F(2c^o/RT\varepsilon_0\varepsilon^o)^{1/2}$ . The potential  $\phi^2$  is defined by the electro-neutrality condition for the entire interfacial region:

$$\sigma^w + \sigma^o + \sigma^{\text{ads}} = 0 \quad (3.10)$$

where  $\sigma^{\text{ads}}$  is the surface charge density due to the adsorption of ionic species from the aqueous phase to the interface and will be specified in the different adsorption models.

$\sigma^w$  and  $\sigma^o$  are the surface charge densities in the diffuse layers of the aqueous and organic phases, respectively. They are classically given by:

$$\sigma^w = -\varepsilon_0 \varepsilon^w \frac{\partial \phi(x)}{\partial x} \Big|_{x=x_2} = -a \sinh \left[ f(\phi^2 - \phi^w) \right] \quad (3.11a)$$

$$\sigma^o = -\varepsilon_0 \varepsilon^o \frac{\partial \phi(x)}{\partial x} \Big|_{x=x_1} = -b \sinh \left[ f(\phi^2 - \phi^o) \right] \quad (3.11b)$$

where  $a = \sqrt{8RT\varepsilon_0\varepsilon^w c^w}$  and  $b = \sqrt{8RT\varepsilon_0\varepsilon^o c^o}$ .

### 3.2.3. Charge density and differential capacitance

According to eq 3.10, we define the interfacial charge density as:

$$\sigma = \sigma^w + \sigma^{\text{ads}} = -\sigma^o \quad (3.12)$$

The interfacial capacitance is given as the derivative of the charge density with respect to the Galvani potential difference:<sup>2</sup>

$$\frac{1}{C_d} = \frac{d\Delta_o^w \phi}{d\sigma} = \frac{d\Delta_2^w \phi}{d\sigma} + \frac{d\Delta_o^2 \phi}{d\sigma} = \frac{1}{C^w} + \frac{1}{C^o} \quad (3.13)$$

The total capacitance can be represented as two capacitances in series. The individual capacitances are given as follows:

$$C^w = \frac{d\sigma}{d\Delta_2^w \phi} = \frac{d(\sigma^w + \sigma^{\text{ads}})}{d(\phi^w - \phi^2)} = -\frac{d(\sigma^w + \sigma^{\text{ads}})}{d(\phi^2 - \phi^w)} \quad (3.14a)$$

$$C^o = \frac{d\sigma}{d\Delta_o^2 \phi} = -\frac{d\sigma^o}{d(\phi^2 - \phi^o)} \quad (3.14b)$$

### 3.2.4 Adsorption isotherms

The adsorption isotherm establishes a functional relationship between the adsorbed amount of a species (interfacial concentration) and its amount in the bulk phase (bulk concentration). It usually has the following form:

$$f(\theta) = \frac{c^r}{c^o} \exp\left(-\frac{\Delta G_a}{RT}\right) \quad (3.15)$$

where  $f(\theta)$  and  $c^r$  represent the interfacial fugacity and the bulk concentration of the adsorbate.  $\Delta G_a$  is the adsorption Gibbs free energy, which includes two parts:

$$\Delta G_a = \Delta G_a^o + zF\Delta\phi \quad (3.16)$$

where  $\Delta G_a^\circ$  is the standard adsorption Gibbs energy and  $\Delta\phi$  represent the potential difference externally imposed on the adsorption process. In our simulations,  $\Delta\phi = \phi^s - \phi^w$  is considered for ionic adsorption from the aqueous phase to the interface. The most frequently used isotherms are the Langmuir isotherm:

$$f(\theta) = \frac{\theta}{1-\theta} \quad (3.17)$$

and the Frumkin isotherm:

$$f(\theta) = \frac{\theta}{1-\theta} \cdot \exp(-2x\theta) \quad (3.18)$$

where  $\theta$  is the relative surface coverage, and  $x$  in eq 3.18 is the interaction factor between the adsorbates.

Taking into account other parameters such as the size difference between solvent and adsorbate, more elaborate models can be obtained. For example, the amphiphilic isotherm developed by Markin and Vokov takes the following form:<sup>3,4</sup>

$$f(\theta) = \frac{\theta [p - (p-1)\theta]^{p-1}}{p^p (1-\theta)^p} \cdot \exp(-2x\theta) \quad (3.19)$$

where  $p$  is the number of solvent molecules replaced by one surfactant molecule.

$\Delta G_a^\circ$  and other parameters may be determined, provided that a proper adsorption isotherm is identified and is fitted to experimental data. However, it is usually difficult to unequivocally choose an appropriate isotherm; an experimental isotherm may well be fitted to a multitude of theoretical isotherms having several adjustable parameters.

### 3.2.5 Simulation parameters

All the results presented in this chapter were obtained using Maple 9.0 (Maplesoft, Waterloo Maple Inc.) program. In all simulations, the concentrations of supporting electrolytes in each phase were  $c^w = c^o = 10 \text{ mol m}^{-3}$ , and the relative dielectric constants were  $\epsilon^w = 70$  and  $\epsilon^o = 10$ . The absolute temperature was taken as 298 K. The Maple programs for different adsorption isotherms can be found in the Appendix.

### 3.3 In the absence of adsorption

To allow further comparison, we present first the classical way to calculate the Gouy-Chapman capacitance. In the absence of adsorption, that is,  $\sigma^{\text{ads}} = 0$ , the expression of  $\phi^2$  is obtained from eqs 3.10, 3.11a, and 3.11b:

$$\phi^2 = \phi^w - \frac{1}{2} \Delta_o^w \phi + \frac{1}{2f} \ln \left\{ \frac{a \exp(f \Delta_o^w \phi) + b}{a + b \exp(f \Delta_o^w \phi)} \right\} \quad (3.20)$$

By substituting eq 3.20 into eqs 3.9a and 3.9b separately, the potential distributions in the aqueous and organic diffuse layers become:

$$\begin{aligned} \phi(x) \Big|_{-\infty < x \leq x_2} &= \phi^w \\ &+ \frac{2}{f} \operatorname{arctanh} \left\{ \exp[\kappa^w (x - x_2)] \tanh \left\{ \frac{1}{4} \ln \left[ \frac{a \exp(f \Delta_o^w \phi) + b}{a + b \exp(f \Delta_o^w \phi)} \right] - \frac{f}{4} \Delta_o^w \phi \right\} \right\} \end{aligned} \quad (3.21a)$$

$$\begin{aligned} \phi(x) \Big|_{x_1 \leq x < \infty} &= \phi^o \\ &+ \frac{2}{f} \operatorname{arctanh} \left\{ \exp[\kappa^o (x - x_1)] \tanh \left\{ \frac{1}{4} \ln \left[ \frac{a \exp(f \Delta_o^w \phi) + b}{a + b \exp(f \Delta_o^w \phi)} \right] + \frac{f}{4} \Delta_o^w \phi \right\} \right\} \end{aligned} \quad (3.21b)$$

Inserting eq 3.20 into eq 3.12, we obtain the charge density at the interface:

$$\sigma = \frac{ab \left\{ -1 + \left[ \exp(2f \Delta_o^w \phi) \right] \right\}}{2 \sqrt{\exp(f \Delta_o^w \phi) \left[ a + b \exp(f \Delta_o^w \phi) \right] \left[ a \exp(f \Delta_o^w \phi) + b \right]}} \quad (3.22)$$

Then, from eqs 3.14a, 3.14b, and 3.22, we have:

$$C^w = af \cosh \left\{ \frac{1}{2} \ln \left[ \frac{a + b \exp(-f \Delta_o^w \phi)}{a + b \exp(f \Delta_o^w \phi)} \right] \right\} \quad (3.23a)$$

$$C^o = bf \cosh \left\{ \frac{1}{2} \ln \left[ \frac{a \exp(f \Delta_o^w \phi) + b}{a \exp(-f \Delta_o^w \phi) + b} \right] \right\} \quad (3.23b)$$

From eqs 3.23a and 3.23b we can calculate the total differential capacitance,  $C_d$ , according to eq 3.13.

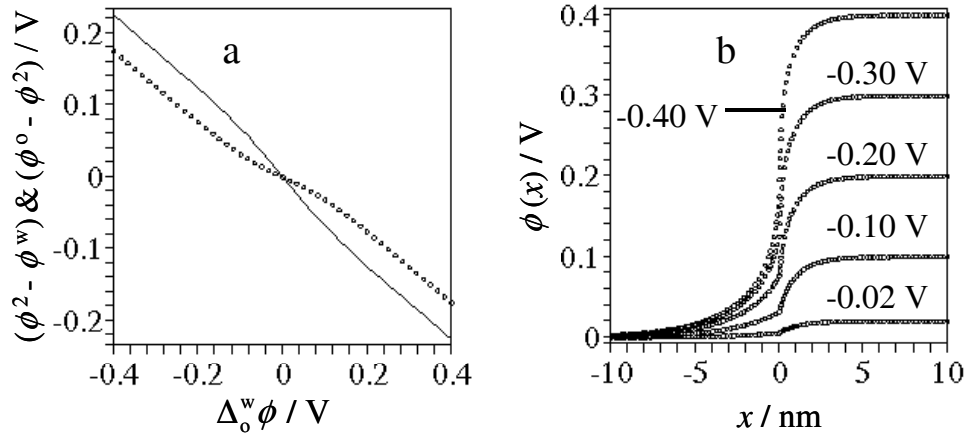


**Figure 3.2** (a) The magnitudes of the aqueous (point) and organic (line) diffuse layer potential drops as functions of  $\Delta_0^w \phi$ ; (b) Potential profiles at various  $\Delta_0^w \phi$  in the absence of adsorption.

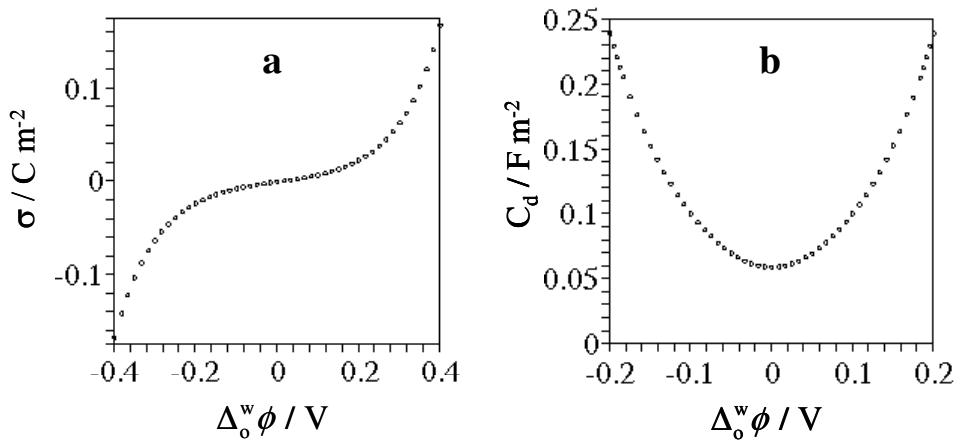


**Figure 3.3** Charge density (a) and differential capacitance (b) as functions of  $\Delta_0^w \phi$  in the absence of adsorption.

The potential at  $x = 0$  is  $\phi^2$ , which under the present definition has a sign opposite to  $\Delta_0^w \phi$  in the absence of adsorption. The dotted line in Figure 3.2a shows the evolution of  $\phi^2$  as a function of  $\Delta_0^w \phi$  ( $\phi^2 - \phi^w = \phi^2$  as  $\phi^w = 0$ ), as calculated from eq 3.20. The parameter  $\phi^2$  determines the magnitude of the potential drops in the two diffuse layers,  $\phi^2 - \phi^w$  and  $\phi^0 - \phi^2$ . They are also compared in Figure 3.2a. The larger magnitude of the potential drop in the organic phase is related to the smaller dielectric constant.

Figure 3.2b shows the potential profiles at various potential differences. Under the conditions employed, the potential extends within 10 to 20 nm on both sides of the interface. Figure 3.3 displays the charge density and differential capacitance in the absence of adsorption at the interface. The features observed are associated with the distribution of the supporting electrolytes in the diffuse layers.

### 3.4 Potential independent isotherm

We start with a simple example, potential independent isotherm, to see how the adsorption affects the potential distribution across the interface. Under this approximation, the adsorption process is potential independent and the extent of the adsorption is only controlled by the standard adsorption Gibbs energy ( $\Delta G_a^0$ ). This means that the interfacial concentration of the adsorbate remains constant over the whole potential window and the adsorbed charge  $\sigma^{\text{ads}}$  can be defined as:

$$\sigma^{\text{ads}} = z_b F \Gamma^* \theta \quad (3.24)$$

where  $z_b$  and  $\Gamma^*$  are the charge number and the maximum surface concentration of the adsorbed species, respectively.  $\theta$  is the relative surface coverage, indicating the percentage of the occupied sites in all available adsorbed sites at the interface. From eqs 3.15, 3.16 and 3.17,  $\theta$  can be obtained for potential independent adsorption isotherm:

$$\theta = \frac{\frac{c_z}{c_{\text{H}_2\text{O}}} \exp\left(-\frac{\Delta G_a^0}{RT}\right)}{1 + \frac{c_z}{c_{\text{H}_2\text{O}}} \exp\left(-\frac{\Delta G_a^0}{RT}\right)} \quad (3.25)$$

where  $c_z$  and  $c_{\text{H}_2\text{O}}$  are the concentrations of the adsorbed species and water molecules in the aqueous phase, respectively. Eq 3.24 is introduced in the electroneutrality equation (eq 3.10) to derive  $\phi^2$ .



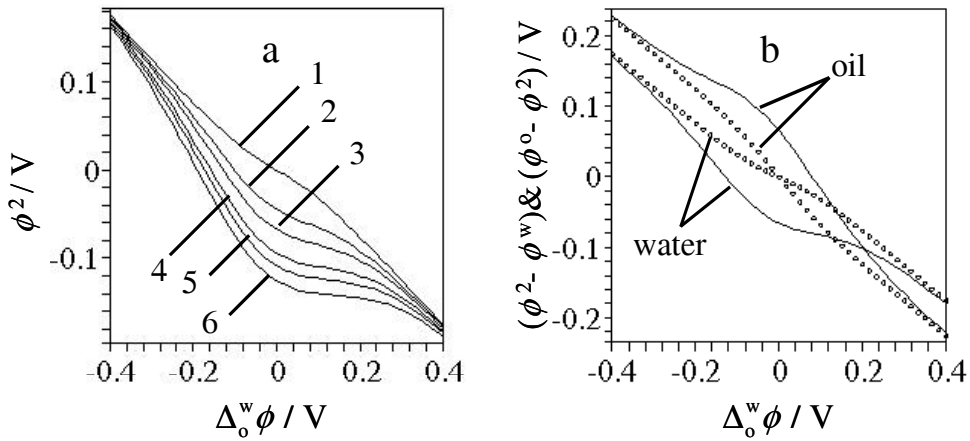


**Figure 3.4** (a)  $\phi^2$  as a function of  $\Delta_o^w \phi$  at various values of  $c_z$ ;  $z_b = -1$ ,  $\Gamma^* = 1 \times 10^{-6} \text{ mol m}^{-2}$ ,  $\Delta G_a^0 = -40 \text{ kJ mol}^{-1}$ , and  $c_z = 0$  (1), 0.001 (2), 0.002 (3), 0.005 (4), 0.010 (5), and  $0.050 \text{ mol m}^{-3}$  (6); (b) The magnitudes of the diffuse layer potential drops in the absence (point) and presence (line) of adsorption when  $c_z = 0.002 \text{ mol m}^{-3}$ .

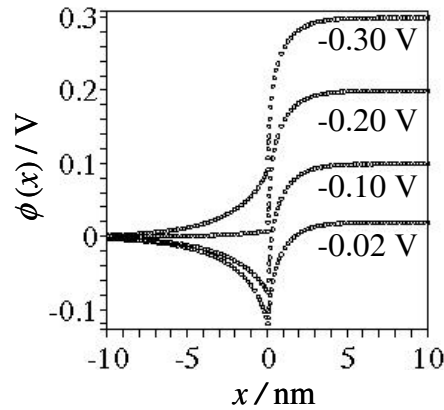


**Figure 3.5** Potential profiles at various  $\Delta_o^w \phi$ :  $z_b = -1$ ,  $\Gamma^* = 1 \times 10^{-6} \text{ mol m}^{-2}$ ,  $\Delta G_a^0 = -40 \text{ kJ mol}^{-1}$ , and  $c_z = 0.050 \text{ mol m}^{-3}$ .

Figure 3.4a illustrates the effect of the adsorption of ionic species on  $\phi^2$  for various bulk concentrations of the adsorbate. The change of  $\phi^2$  is negligible at large potential differences, whilst much more pronounced at potential difference close to 0 V. For example, in the case of mono-anionic species with a bulk concentration of  $10^{-2} \text{ mol m}^{-3}$  ( $\sigma^{\text{ads}} = 6 \text{ } \mu\text{C cm}^{-2}$  with the parameters used in the simulation, as indicated in the figure caption), the decrease of  $\phi^2$  induced by the adsorption is very clear in a potential range from -0.2 V to 0.2 V. As the parameter  $\phi^2$  determines the magnitudes of the potential

drops in the two diffuse layers, the changes in  $\phi^2$  indicate the variations in the potential drops. As shown in Figure 3.4b, the magnitudes of the potential drops in the two diffuse layers are significantly altered in the low potential range. For instance, negative potential drops in the aqueous diffuse layer ( $\phi^2 - \phi^w < 0$ ) are observed in a range of negative values of  $\Delta_0^w \phi$ . Under these conditions, the potential distribution is inverted as exemplified in Figure 3.5 in the case of potentials -0.10 V and -0.02 V. This kind of potential profile has been inferred from the qualitative analysis of experimental results on the adsorption of surfactant ions at the ITIES.<sup>5</sup> The electric double layer composition of the interface is significantly altered under conditions where the charge density due to the adsorption exceeds that related to the supporting electrolytes in the diffuse layers.

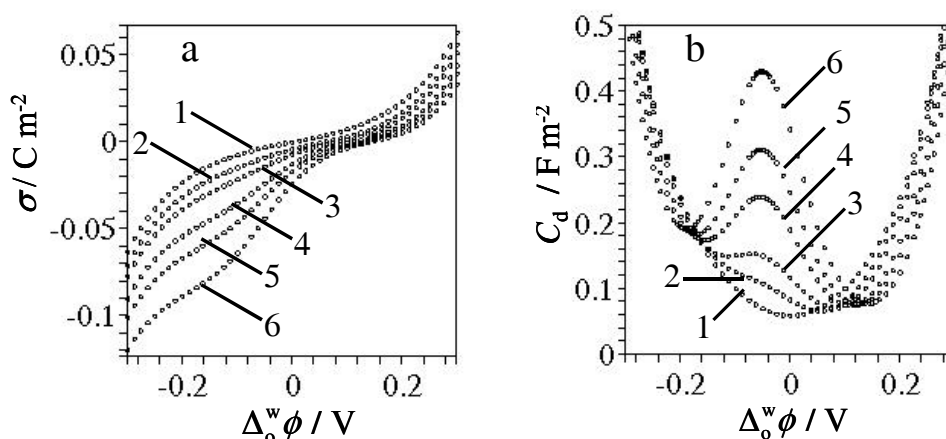


**Figure 3.6** Charge density (a) and differential capacitance (b) at various concentrations for the potential independent model. The parameters are the same as in Figure 3.4a.

Mathematically, eqs 3.10, 3.11a and 3.11b tell us that  $\phi^2$  changes with  $\sigma^{\text{ads}}$ , meaning that the potential profile changes upon adsorption even though the quantity of adsorbed species remains constant. Hence, the dependence of both the interfacial charge density and differential capacitance on the potential difference is affected by the adsorption of ions, as illustrated by Figure 3.6. The adsorption of anionic species manifests itself as an increase of the charge density and differential capacitance, especially at negative potentials. Furthermore, the minimum of the capacitance shifts to positive values of  $\Delta_0^w \phi$ . These features are consistent with the experimental data on the adsorption of ionic species at the ITIES.<sup>5,6</sup>

### 3.5 Langmuir isotherm

Previous studies have suggested that the adsorption of ionic species at the ITIES is generally potential dependent.<sup>7</sup> The Langmuir and Frumkin isotherms are most frequently used to analyze experimental data.<sup>7-9</sup> In the case of Langmuir isotherm, the relative surface coverage  $\theta$  is given by:<sup>10</sup>

$$\theta = \frac{c_z}{c_{\text{H}_2\text{O}}} \frac{\exp\left(-\frac{\Delta G_a^0}{RT}\right) \exp\left[-\frac{z_b F}{RT}(\phi^2 - \phi^w)\right]}{1 + \frac{c_z}{c_{\text{H}_2\text{O}}} \exp\left(-\frac{\Delta G_a^0}{RT}\right) \exp\left[-\frac{z_b F}{RT}(\phi^2 - \phi^w)\right]} \quad (3.26)$$

All the parameters have the same meanings as in section 3.2. The adsorbed charge  $\sigma^{\text{ads}}$  can be calculated by inserting eq 3.26 into eq 3.24, which is further introduced in eq 3.10 to derive  $\phi^2$ . Although no analytical solution is obtained in this case, the symbolic expression can be evaluated numerically. This kind of treatment is extended to the computation of the potential distribution, the relative surface coverage, charge density and differential capacitance.

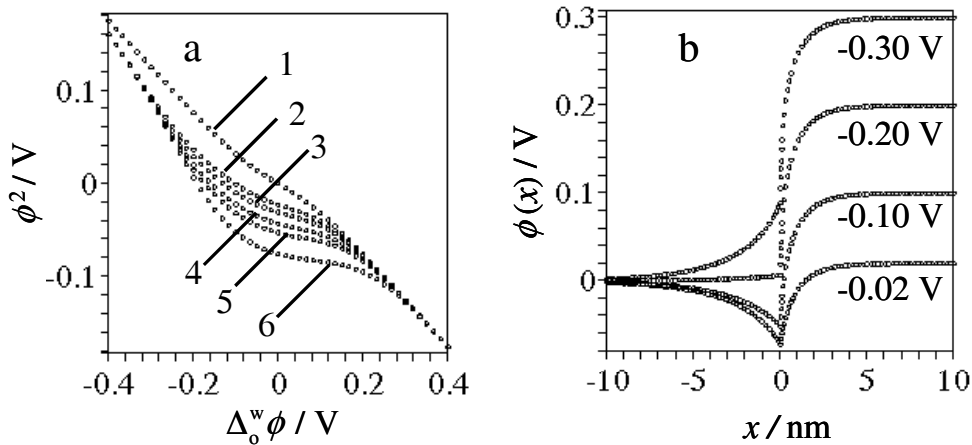


**Figure 3.7** (a)  $\phi^2$  as a function of  $\Delta_0^w \phi$  at various values of  $c_z$ . The parameters are the same as in Figure 3.4a; (b) Potential profiles at various potential differences for the Langmuir model. The parameters are the same as in Figure 3.5.

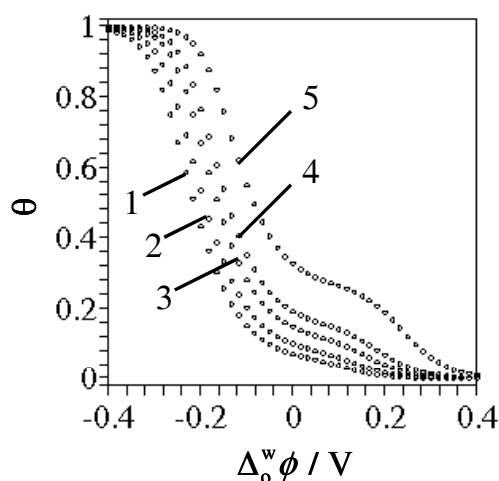


**Figure 3.8** The effect of  $c_z$  on the relative surface coverage for the Langmuir model. The parameters are the same as in Figure 3.4a.

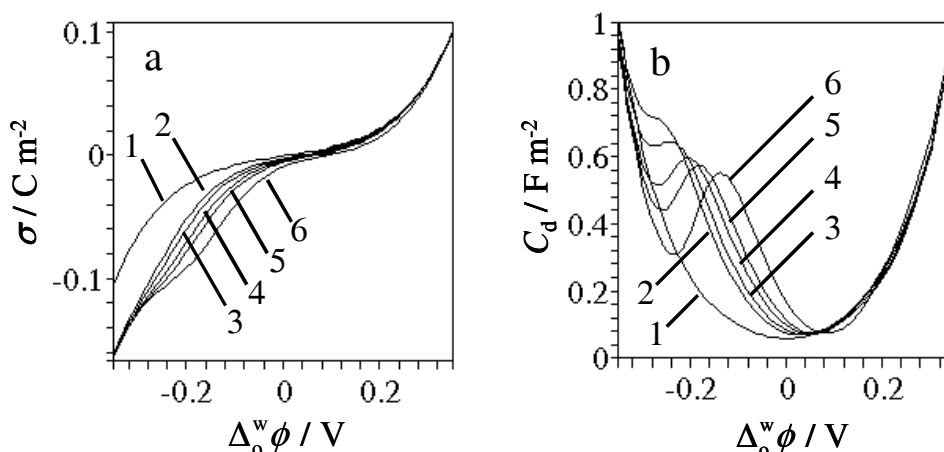
As from eqs 3.24 and 3.26, the adsorption behaviour is controlled by several variables including  $z_b$ ,  $\Gamma^*$ ,  $c_z$ , and  $\Delta G_a^0$ . The parameters  $z_b$  and  $\Delta G_a^0$  are constant for a given species.  $\Gamma^*$  is mainly determined by the dimension of the species itself, although it may possibly be potential dependent.<sup>9</sup> Hence, we shall not consider the variations of the parameters  $z_b$ ,  $\Gamma^*$ , and  $\Delta G_a^0$ , but rather focus on the effect of  $c_z$ , which is experimentally controllable.

Figure 3.7a shows  $\phi^2$  as a function of the applied potential difference in the presence of various concentrations of the surface-active species in the aqueous phase. It is evident that  $\phi^2$  is strongly affected by the adsorption over a large potential range. The inversion of  $\phi^2$  from positive to negative is also observed, indicating a redistribution of the potential drop in the two diffuse layers. The corresponding potential profiles across the interface are plotted in Figure 3.7b. The results presented in Figures 3.5 and 3.7b should be compared with the curves in Figure 3.2b. It is clear that the presence of adsorbed ions affects the potential distribution on both sides of the interface. This behaviour should be taken into account when reactions involving adsorbed species at liquid|liquid interfaces are studied. Comparison of Figures 3.4a and 3.7a shows that at  $\Delta_0^w \phi = 0$  the potential  $\phi^2$  in the potential independent model is more negative than that in the Langmuir model.

This indicates that in the potential independent model a larger potential drop will be developed in the aqueous phase.

According to eq 3.26, the relative surface coverage associated with a specific bulk concentration of the adsorbate is determined by two different exponential terms. The first term is related to the potential independent adsorption, which is a function of the standard Gibbs energy of adsorption. The second term is responsible for the potential dependence of the surface concentration. The respective contribution of these terms to the relative coverage is controlled by the potential difference. Figure 3.8 displays the relative coverage in the presence of the adsorption of an ion of charge  $z_b = -1$  at the interface. The relative coverage is very low at rather positive potentials, where  $\phi^2 - \phi^w > 0$  and the potential independent adsorption is dominant. The coverage slowly increases as the potential difference becomes negative, as manifested by the appearance of a hump in the potential range of 0 to 0.2 V. In this region, the coverage is controlled by the convolution of two types of adsorption. At more negative potential differences, the potential dependent adsorption becomes dominant and the coverage steeply increases before reaching saturation.

The interfacial charge density and differential capacitance, as calculated with the isotherm in eq 3.26, are plotted in Figure 3.9. Again, the minimum of the differential capacitance curve shifts to positive values of  $\Delta_0^w \phi$  with increasing bulk concentration of the adsorbate. However, the charge density and differential capacitance curves coincide well at positive potential differences regardless of the concentration of adsorbate, indicating complete desorption of the species at the interface. These features are commonly observed experimentally on the adsorption of anionic species from the aqueous phase to the interface.<sup>5, 6</sup> The overlap of the charge density curves, as well as of the differential capacitance curves, at negative potential differences is associated with the saturation of the adsorption at the interface. When the adsorbate reaches full coverage at a certain concentration or potential, no more species will be accepted at the interface. The present model does not account for multilayer assemblies with variations of the Gibbs energy of adsorption.



**Figure 3.9** Charge density (a) and differential capacitance (b) for Langmuir model at various values of  $c_z$ . The parameters are the same as in Figure 3.4a.

The results in Figure 3.9b should be compared with the capacitance curves obtained with the potential independent isotherm (Figure 3.6b). An important point is that, for equivalent concentrations, the increase in capacitance occurs at more negative potentials in the case of the Langmuir isotherm. At  $\Delta_0^w \phi = 0$  the capacitance is lower than that in the potential independent model. In both cases, although the inner potential is the same in each phase, the potential  $\phi^2$  at the interface is negative due to the adsorption of negatively charged species. Hence, the second exponential term in eq 3.26 takes values between 0 and 1 and the surface coverage is decreased. This emphasizes the importance of evaluating the potential profiles at the interface before interpreting capacitance data, as the modification in the electric structure of the interface significantly affects the shape of capacitance-potential curve.

### 3.6 Frumkin isotherm

The Langmuir isotherm represents an ideal case where the intermolecular interactions between adsorbed species are neglected. However, these interactions are expected to play an important role in the adsorption process, especially at high surface coverage. Higgins

and Corn have shown that in some cases, the adsorbed species can enhance the incoming adsorption with increasing interfacial coverage.<sup>10</sup> In other cases, repulsion between adsorbates can hinder the adsorption.<sup>7</sup> These phenomena can be conveniently rationalized in terms of the Frumkin isotherm, in which an intermolecular interaction factor is taken into account. The expression for this model is written in the general form:

$$\ln\left(\frac{\theta}{1-\theta}\right) = \ln\left(\frac{a_z}{a_{\text{H}_2\text{O}}}\right) - \frac{\Delta G_a^0}{RT} - \frac{zF}{RT}(\phi^2 - \phi^w) - \frac{x\theta}{RT} \quad (3.27)$$

where  $x$  is the interaction factor (with units of  $\text{kJ mol}^{-1}$ ), which represents the intermolecular interaction between the adsorbed species and is negative in the case of attraction and positive in the case of repulsion. The physical meaning of parameter  $x$  is equivalent to that of  $g'$  in ref. 11,<sup>11</sup> and usually takes values between  $-5$  and  $5 \text{ kJ mol}^{-1}$ .

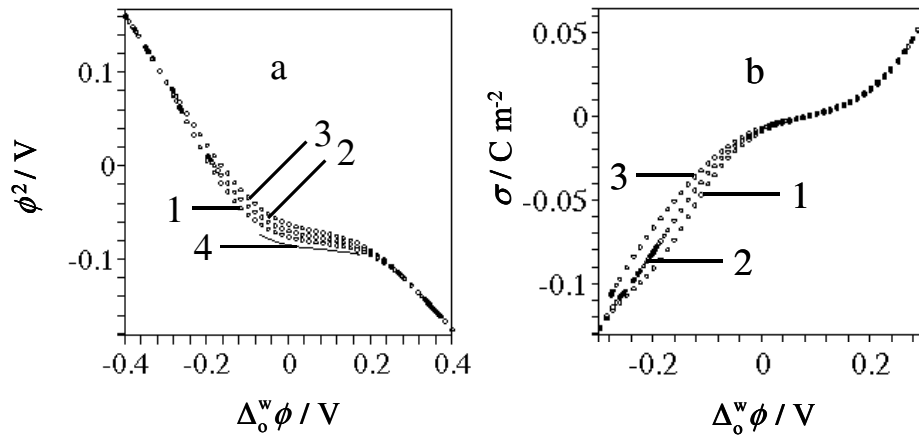


**Figure 3.10**  $\phi^2$  (a) and charge density (b) for the Frumkin model at various values of  $x$ : 0 (1), 4 (2), 10 (3), and  $-4 \text{ kJ mol}^{-1}$  (4) and  $z_b = -1$ ,  $\Gamma^* = 1 \times 10^{-6} \text{ mol m}^{-2}$ ,  $c_z = 0.050 \text{ mol m}^{-3}$ ,  $\Delta G_a^0 = -40 \text{ kJ mol}^{-1}$ .

Although we can work out the symbolic function of  $\phi^2$  as a function of the applied potential difference, we fail to evaluate it numerically over all values of  $x$  and  $\Delta_o^w \phi$ . As shown in Figure 3.10a, a complete evaluation is only possible with positive values of  $x$ . In the case of  $x = -4 \text{ kJ mol}^{-1}$ , we merely get a discontinuous curve (Figure 3.10a, curve 4). Figure 3.10b illustrates the charge density with three assigned value of  $x$ . We can observe that the charge density decreases due to the repulsive interaction between the adsorbed species.

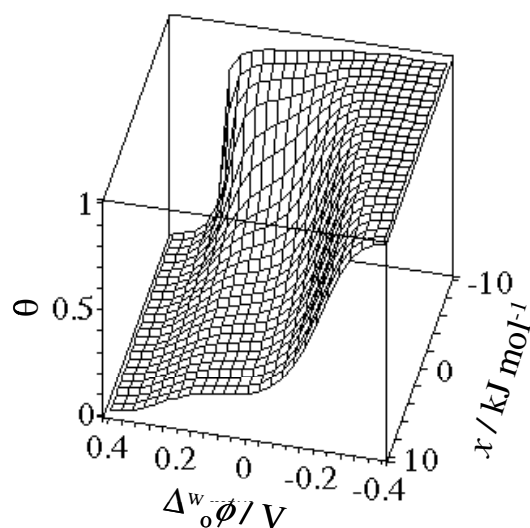


**Figure 3.11** Three dimensional graph of the relative surface coverage as a function of  $\Delta_0^w \phi$  and  $x$ .

Owing to the discontinuities in Figure 3.10a, it is difficult to make a complete evaluation of the effect of  $x$  on the surface coverage. However, the interfacial coverage can be plotted as a function of the interaction factor and potential difference by taking as an approximation that the variations in  $\phi^2$  introduced by the interaction between adsorbates can be neglected. Hence,  $\phi^2$  can be computed using the Langmuir isotherm (eq 3.26) and then introduced into eq 3.26 to evaluate the surface coverage. This simplification is reasonable because  $x$  does not induce a big change in  $\phi^2$  as shown in Figure 3.10a. Figure 3.11 is a three-dimensional graph displaying the relative coverage as a function of  $x$  and  $\Delta_0^w \phi$ . In the presence of attractive interactions ( $x < 0$ ), the adsorption is enhanced and the saturation is reached at relatively low potential differences. On the other hand, repulsive interactions decrease the surface concentration and shift the saturation potential to more negative values. The intermolecular interaction plays an important role on the extent of the adsorption, which in turn affects the electric structure of the interface.



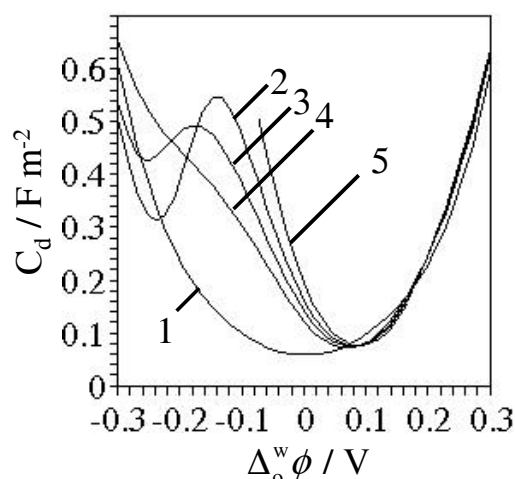


**Figure 3.12** Differential capacitance for the Frumkin model at  $x = 0$  (2), 4 (3), 10 (4), and  $-4 \text{ kJ mol}^{-1}$  (5). Curve 1 is that in the absence of adsorption. Other parameters are the same as in Figure 3.5.

The capacitance curves obtained for different values of the interaction parameter  $x$  are displayed in Figure 3.12. The repulsive interaction results in a decrease of the capacitance at negative potentials, as expected from the evolution of the surface coverage in Figure 3.11.

### 3.7 Other adsorption isotherms

As explained in Section 3.6, the numerical evaluation of the interfacial potential using the Frumkin isotherm was already difficult. In comparison to the Frumkin isotherm, the amphiphilic isotherm is more precise to describe the adsorption process at the liquid interface since the size difference and replacement between solvent and adsorbate are taken into account. However, it has a more complicated expression than the Frumkin isotherm, as seen from eq 3.19. Therefore, the numerical evaluation of this model will be even more difficult and will not be considered.

---

### 3.8 Conclusions

The electric double layer structure of the ITIES is significantly altered by the adsorption of ionic species. On the basis of the common assumptions of the Gouy-Chapman theory, the ionic species are considered as point charges and the inner layer is reduced to a charged plane. The potential at this plane,  $\phi^2$ , which is resolved using the electro-neutrality condition of the system, determines the magnitudes of the potential drops in the two diffuse layers,  $\phi^2 - \phi^w$  and  $\phi^o - \phi^2$ . Computation of the potential profile across the interface using numerical methods allows estimating the charge density and double layer capacity for various adsorption models.

The results clearly show that the potential profile across the interface is affected markedly by the adsorption of ionic species. At a certain potential range, the sign of  $\phi^2$  is inverted once the adsorbed charge exceeds the excess charge in the diffuse layer regardless of the adsorption model, resulting in a non-monotonous potential distribution with a potential trap at the interface. Obviously, the redistribution of the potential will increase the interfacial charge density and capacity, as well as shift the potential of zero charge. A fundamental question is how this modified potential profile affects charge transfer reactions at the interface. In terms of the model introduced by Girault and Schiffrin on electron transfer at the ITIES,<sup>12</sup> the driving force for the electron transfer includes two work terms associated with the formation of the precursor and successor complexes. The change in the potential distribution alters the local potential drop sensed by the precursor according to eqs 10, 17, and 18 in ref. 50. Hence, the electron transfer rate constant and the transfer coefficient will change in response to the potential redistribution.

On the other hand, the primary idea of the present simulations was to see the effect of the adsorption of charged NPs on the interfacial charge distribution across the liquid|liquid interface. For simplicity, in the calculation the charged NPs were considered as large ions, which were further taken as point charges. It should be mentioned that the size of a NP is larger than those of conventional ions and solvent molecules. There is no doubt that the adsorption of charged NPs at the interface strongly affects the interfacial structure, however, the results of the present simulations should be considered with caution.

### 3.9 References

- (1) Girault, H. H. *Analytical and Physical Electrochemistry*; EPFL Press, 2004.
- (2) Cheng, Y.; Cunnane, V. J.; Schiffrin, D. J.; Murtomaki, L.; Kontturi, K. *J. Chem. Soc. Faraday Trans.* **1991**, *87*, 1665.
- (3) Volkov, A. G.; Deamer, D. W.; Tanelian, D. L.; Markin, V. a. S. *Liquid Interfaces in Chemistry and Biology*, 1998.
- (4) Volkov, A. G.; Deamer, D. W.; Editors *Liquid-Liquid Interfaces: Theory and Methods*, 1996.
- (5) Kakiuchi, T.; Kobayashi, M.; Senda, M. *Bull. Chem. Soc. Jpn.* **1987**, *60*, 3109-3115.
- (6) Fermin, D. J.; Ding, Z.; Duong, H. D.; Brevet, P.-F.; Girault, H. H. *J. Phys. Chem. B* **1998**, *102*, 10334-10341.
- (7) Kakiuchi, T. *Surfactant Science Series* **2001**, *95*, 105-121.
- (8) Murtomaki, L.; Manzanares, J. A.; Mafe, S.; Kontturi, K. *Surfactant Science Series* **2001**, *95*, 533-551.
- (9) Kakiuchi, T. *J. Electroanal. Chem.* **2002**, *536*, 63-69.
- (10) Higgins, D. A.; Corn, R. M. *J. Phys. Chem.* **1993**, *97*, 489-493.
- (11) Bard, A. J.; Faulkner, L. R. *Electrochemical Methods: Fundamentals and Applications, second Edition*; John Wiley & Sons, Inc., 2001.
- (12) Girault, H. H. J.; Schiffrin, D. J. *J. Electroanal. Chem.* **1988**, *244*, 15-26.

### 3.10 Appendix - maple programs

The Maple programs are listed below, in which the fonts in the normal style represent the Maple inputs and the italic fonts are the text explanation.

#### 3.10.1 In the Absence of Adsorption

```
[> restart;
```

##### *Part 1: $\phi^2$*

```
[> eqn:=a*sinh(f*(phi[2]-phi[w]))+b*sinh(f*(phi[2]-phi[o]))=0;
[> a:=- (8*RT*epsilon[0]*epsilon[w]*c[w])^(1/2);
[> b:=- (8*RT*epsilon[0]*epsilon[o]*c[o])^(1/2);
[> f:=F/2/RT;
```

```
[> phi[2]:=solve(eqn,phi[2]);
```

```
[> para1:=F=96487,RT=8.314*298,epsilon[0]=8.85e-12,epsilon[w]=70,epsilon[o]=10,
      c[w]=10,c[o]=10;
[> para2:=phi[w]=0,phi[o]=-Delta;
[> para3:=Delta=-0.1;
```

##### *(1) $\phi^2$ as a function of the Galvani potential difference*

```
[> dphi[2]:=eval(phi[2],[para1,para2]);
[> plot(dphi[2],Delta=-0.4..0.4,style=point,color=red);
```

##### *(2) Potential drop in aqueous phase: $\phi^2 - \phi^w = f(\Delta)$ ;*

```
[> Pdw:=eval(phi[2]-phi[w],[para1,para2]);
```

##### *(3) Potential drop in organic phase: $\phi^o - \phi^2 = f(\Delta)$ ;*

```
[> Pdo:=eval(phi[o]-phi[2],[para1,para2]);
```

##### *(4) The ration of the potential drops in two phases: $[\phi^2 - \phi^w] / [\phi^o - \phi^2] = f(\Delta)$ ;*

```
[> Pdr:=eval(Pdw/Pdo,[para1,para2]);
[> plot([Pdw,Pdo],Delta=-0.4..0.4,style=point,color=[blue,red]);
[> plot(Pdr,Delta=-0.4..0.4,style=point,color=gold);
```

##### *Part 2: Potential profile across the interface*

##### *(1) Poisson equations:*

```
[> eqnw:=diff(xi(x),x)=(8*RT*c[w]/epsilon[0]/epsilon[w])^(1/2)*sinh(f*(xi(x)-phi[w]));
[> eqno:=diff(zeta(x),x)=(8*RT*c[o]/epsilon[0]/epsilon[o])^(1/2)*sinh(f*(phi[o]-zeta(x)));
```

##### *(2) Potential profile in aqueous phase:*

```
[> ppw:=dsolve({eqnw,xi(0)=phi2},xi(x));
```

*(3) Potential profile in organic phase:*

```
[> ppo:=dsolve({eqno,zeta(0)=phi2},zeta(x));
```

*(4) Plots:*

```
[> phi2:=eval(phi[2],[para1,para2]);
```

```
[> xi(x):=eval(eval(subs(ppw[2],xi(x)),[para1,para2,para3]),para3);
```

```
[> zeta(x):=eval(eval(subs(ppo[2],zeta(x)),[para1,para2,para3]),para3);
```

```
[> with(plots):
```

```
[> Pfw:=plot(xi(x),x=-1e-8..0,style=point,color=blue):
```

```
[> Pfo:=plot(zeta(x),x=0..1e-8,style=point,color=red):
```

```
[> display({Pfw,Pfo});
```

**Part 3: Charge density and differential capacitance**

```
[> sigma[w]:=a*sinh(f*(chi[w]));
```

```
[> sigma[o]:=b*sinh(f*(chi[o]));
```

```
[> C[w]:=diff(sigma[w],chi[w]);
```

```
[> C[o]:=diff(sigma[o],chi[o]);
```

```
[> C[t]:=-C[w]*C[o]/(C[w]+C[o]);
```

```
[> chi[w]:=eval(phi[2]-phi[w],[para1,para2]);
```

```
[> chi[o]:=eval(phi[2]-phi[o],[para1,para2]);
```

```
[> with(plots):
```

```
[> sigmaw:=plot(eval(sigma[w],[para1,para2]),Delta=-0.4..0.4,style=[point],color=[black]):
```

```
[> sigmao:=plot(eval(sigma[o],[para1,para2]),Delta=-0.4..0.4,style=[point],color=[red]):
```

```
[> display({sigmaw,sigmao});
```

```
[> plot(eval(C[t],[para1,para2]),Delta=-0.2..0.2,style=point,color=green);
```

### 3.10.2 Potential Independent Isotherm

```
[> restart;
```

**Part 1:  $\phi^2$**

```
[> eqn:=a*sinh(f*(phi[2]-phi[w]))+b*sinh(f*(phi[2]-phi[o]))+sigma[ads]=0;
```

```
[> a:=-(8*RT*epsilon[0]*epsilon[w]*c[w])^(1/2);
```

```
[> b:=-(8*RT*epsilon[0]*epsilon[o]*c[o])^(1/2);
```

```
[> f:=F/2/RT;
```

```
[> sigma[ads]:=z[S]*F*Gamma*theta;
```

```
[> theta:=(c[z]/c[0])*(exp(-G/RT))/(1+(c[z]/c[0])*(exp(-G/RT)));
```

```
[> phi[2]:=solve(eqn,phi[2]);
```

```
[> para1:=F=96487,RT=8.314*298,epsilon[0]=8.85e-12,epsilon[w]=70,epsilon[o]=10,  
c[w]=10,c[o]=10,c[0]=1000000/18,G=-40000,Gamma=1e-06;
```

```
[> para2:=phi[w]=0,phi[o]=-Delta;
[> para3:=Delta=-0.1;
[> para4:=z[S]=-1;
```

(1)  $\phi^2 = f(\Delta, c[z])$  :

```
[> three[phi[2]]:=eval(phi[2][1],[para1,para2,para4]);
[> plot3d(three[phi[2]],Delta=-0.4..0.4,c[z]=0..0.1,axes=boxed);
```

(2)  $\phi^2 = f(\Delta)$  at various  $c[z]$ :

```
[> dphi2[1]:=eval(phi[2][1],[para1,para2,para4,c[z]=0]);
    dphi2[2]:=eval(phi[2][1],[para1,para2,para4,c[z]=0.001]);
    dphi2[3]:=eval(phi[2][1],[para1,para2,para4,c[z]=0.002]);
    dphi2[4]:=eval(phi[2][1],[para1,para2,para4,c[z]=0.005]);
    dphi2[5]:=eval(phi[2][1],[para1,para2,para4,c[z]=0.01]);
    dphi2[6]:=eval(phi[2][1],[para1,para2,para4,c[z]=0.05]);
[> plot([dphi2[1],dphi2[2],dphi2[3],dphi2[4],dphi2[5],dphi2[6]],Delta=-0.4..0.4,style=point);
[> dphi2o[1]:=eval(phi[o]-phi[2][1],[para1,para2,para4,c[z]=0]);
    dphi2o[3]:=eval(phi[o]-phi[2][1],[para1,para2,para4,c[z]=0.002]);
[> plot([dphi2[1],dphi2o[1],dphi2[3],dphi2o[3]],Delta=-0.4..0.4,style=[point,point,line,line]);
```

## Part 2: Potential profile across the interface

(1) Poisson equations:

```
[> eqnw:=diff(xi(x),x)=(8*RT*c[w]/epsilon[0]/epsilon[w])^(1/2)*sinh(f*(xi(x)-phi[w]));
    eqno:=diff(zeta(x),x)=(8*RT*c[o]/epsilon[0]/epsilon[o])^(1/2)*sinh(f*(phi[o]-zeta(x)));
```

(2) Potential profile in aqueous phase:

```
[> ppw:=dsolve({ eqnw,xi(0)=phi2 },xi(x));
```

(3) Potential profile in organic phase:

```
[> ppo:=dsolve({ eqno,zeta(0)=phi2 },zeta(x));
```

Evaluation:  $\Delta = -0.02$  V;

```
[> xi0(x):=eval(eval(subs(ppw[2],xi(x)),[para1,para2,Delta=-0.02]),[Delta=-0.02,phi2=
    eval(eval(phi[2][1],[para1,para2,para4,c[z]=0]),Delta=-0.02]));
    zeta0(x):=eval(eval(subs(ppo[1],zeta(x)),[para1,para2,Delta=-0.02]),[Delta=-0.02,phi2=
    eval(eval(phi[2][1],[para1,para2,para4,c[z]=0]),Delta=-0.02]));
    xi1(x):=eval(eval(subs(ppw[2],xi(x)),[para1,para2,Delta=-0.02]),[Delta=-0.02,phi2=
    eval(eval(phi[2][1],[para1,para2,para4,c[z]=0.05]),Delta=-0.02]));
    zeta1(x):=eval(eval(subs(ppo[1],zeta(x)),[para1,para2,Delta=-0.02]),[Delta=-0.02,phi2=
    eval(eval(phi[2][1],[para1,para2,para4,c[z]=0.05]),Delta=-0.02]));
```

Evaluation:  $\Delta = -0.05$ ;

```
[> xi2(x):=eval(eval(subs(ppw[2],xi(x)),[para1,para2,Delta=-0.05]),[Delta=-0.05,phi2=
    eval(eval(phi[2][1],[para1,para2,para4,c[z]=0.05]),Delta=-0.05]));
    zeta2(x):=eval(eval(subs(ppo[1],zeta(x)),[para1,para2,Delta=-0.05]),[Delta=-0.05,phi2=
    eval(eval(phi[2][1],[para1,para2,para4,c[z]=0.05]),Delta=-0.05]));
```

Evaluation:  $\Delta = -0.10$ ;

```
[> xi3(x):=eval(eval(subs(ppw[2],xi(x)),[para1,para2,Delta=-0.10]),[Delta=-0.10,phi2=
    eval(eval(phi[2][1],[para1,para2,para4,c[z]=0.05]),Delta=-0.10));
    zeta3(x):=eval(eval(subs(ppo[1],zeta(x)),[para1,para2,Delta=-0.10]),[Delta=-0.10,phi2=
    eval(eval(phi[2][1],[para1,para2,para4,c[z]=0.05]),Delta=-0.10));
```

*Evaluation: Delta = -0.20;*

```
[> xi4(x):=eval(eval(subs(ppw[2],xi(x)),[para1,para2,Delta=-0.20]),[Delta=-0.20,phi2=
    eval(eval(phi[2][1],[para1,para2,para4,c[z]=0.05]),Delta=-0.20));
    zeta4(x):=eval(eval(subs(ppo[1],zeta(x)),[para1,para2,Delta=-0.20]),[Delta=-0.20,phi2=
    eval(eval(phi[2][1],[para1,para2,para4,c[z]=0.05]),Delta=-0.20));
```

*Evaluation: Delta = -0.30;*

```
[> xi5(x):=eval(eval(subs(ppw[2],xi(x)),[para1,para2,Delta=-0.30]),[Delta=-0.30,phi2=
    eval(eval(phi[2][1],[para1,para2,para4,c[z]=0.05]),Delta=-0.30));
    zeta5(x):=eval(eval(subs(ppo[1],zeta(x)),[para1,para2,Delta=-0.30]),[Delta=-0.30,phi2=
    eval(eval(phi[2][1],[para1,para2,para4,c[z]=0.05]),Delta=-0.30));
```

[> with(plots):

```
xi1:=plot(xi1(x),x=-1e-08..0,style=point,color=black):
zeta1:=plot(zeta1(x),x=0..1e-08,style=point,color=black):
xi3:=plot(xi3(x),x=-1e-08..0,style=point,color=red):
zeta3:=plot(zeta3(x),x=0..1e-08,style=point,color=red):
xi4:=plot(xi4(x),x=-1e-08..0,style=point,color=blue):
zeta4:=plot(zeta4(x),x=0..1e-08,style=point,color=blue):
xi5:=plot(xi5(x),x=-1e-08..0,style=point,color=green):
zeta5:=plot(zeta5(x),x=0..1e-08,style=point,color=green):
display({xi1,zeta1,xi3,zeta3,xi4,zeta4,xi5,zeta5});
```

### ***Part 3: Charge density and differential capacitance***

```
[> sigma[w]:=a*sinh(f*(chi[w]))+sigma[ads];
```

```
sigma[o]:=b*sinh(f*(chi[o]));
```

```
[> C[w]:=diff(sigma[w],chi[w]);
```

```
C[o]:=diff(sigma[o],chi[o]);
```

```
[> C[t]:=-C[w]*C[o]/(C[w]+C[o]);
```

```
[> chi01:=eval(phi[2][1]-phi[w],[para1,para2,para4,c[z]=0]):
```

```
chi02:=eval(phi[2][1]-phi[o],[para1,para2,para4,c[z]=0]):
```

```
chi11:=eval(phi[2][1]-phi[w],[para1,para2,para4,c[z]=0.001]):
```

```
chi12:=eval(phi[2][1]-phi[o],[para1,para2,para4,c[z]=0.001]):
```

```
chi21:=eval(phi[2][1]-phi[w],[para1,para2,para4,c[z]=0.002]):
```

```
chi22:=eval(phi[2][1]-phi[o],[para1,para2,para4,c[z]=0.002]):
```

```
chi31:=eval(phi[2][1]-phi[w],[para1,para2,para4,c[z]=0.005]):
```

```
chi32:=eval(phi[2][1]-phi[o],[para1,para2,para4,c[z]=0.005]):
```

```
chi41:=eval(phi[2][1]-phi[w],[para1,para2,para4,c[z]=0.01]):
```

```
chi42:=eval(phi[2][1]-phi[o],[para1,para2,para4,c[z]=0.01]):
```

```
chi51:=eval(phi[2][1]-phi[w],[para1,para2,para4,c[z]=0.05]):
```

```
chi52:=eval(phi[2][1]-phi[o],[para1,para2,para4,c[z]=0.05]):
```

```
[> P1:=plot(eval(sigma[w],[para1,para2,para4,c[z]=0,chi[w]=chi01]),Delta=-0.4..0.4):
```

```
P3:=plot(eval(sigma[w],[para1,para2,para4,c[z]=0.001,chi[w]=chi11]),Delta=-0.4..0.4):
```

```
P5:=plot(eval(sigma[w],[para1,para2,para4,c[z]=0.002,chi[w]=chi21]),Delta=-0.4..0.4):
```

```
P7:=plot(eval(sigma[w],[para1,para2,para4,c[z]=0.005,chi[w]=chi31]),Delta=-0.4..0.4):
```

```
P9:=plot(eval(sigma[w],[para1,para2,para4,c[z]=0.01,chi[w]=chi41]),Delta=-0.4..0.4):
```

```
P11:=plot(eval(sigma[w],[para1,para2,para4,c[z]=0.05,chi[w]=chi51]),Delta=-0.4..0.4):
```

```
[> display({P1,P3,P5,P7,P9,P11});
```

```
[> C0:=plot(eval(C[t],[para1,para2,para4,c[z]=0,chi[w]=chi01,chi[o]=chi02]),Delta=-
0.3..0.3,style=point,color=black):
```

```

C1:=plot(eval(C[t],[para1,para2,para4,c[z]=0.001,chi[w]=chi11,chi[o]=chi12]),Delta=-
0.3..0.3,style=point,color=red):
C2:=plot(eval(C[t],[para1,para2,para4,c[z]=0.002,chi[w]=chi21,chi[o]=chi22]),Delta=-
0.3..0.3,style=point,color=blue):
C3:=plot(eval(C[t],[para1,para2,para4,c[z]=0.005,chi[w]=chi31,chi[o]=chi32]),Delta=-
0.3..0.3,style=point,color=green):
C4:=plot(eval(C[t],[para1,para2,para4,c[z]=0.01,chi[w]=chi41,chi[o]=chi42]),Delta=-
0.3..0.3,style=point,color=yellow):
C5:=plot(eval(C[t],[para1,para2,para4,c[z]=0.05,chi[w]=chi51,chi[o]=chi52]),Delta=-
0.3..0.3,style=point,color=brown):
[> display({C0,C1,C2,C3,C4,C5});

```

### 3.10.3 Langmuir Isotherm

```
[> restart;
```

#### *Part 1: $\phi^2$*

```

[> eqnb:=a*sinh(f*(phi[2]-phi[w]))+b*sinh(f*(phi[2]-phi[o]))=0;
eqn:=a*sinh(f*(phi[2]-phi[w]))+b*sinh(f*(phi[2]-phi[o]))+sigma[ads]=0;
[> a:=- (8*RT*epsilon[0]*epsilon[w]*c[w])^(1/2);
b:=- (8*RT*epsilon[0]*epsilon[o]*c[o])^(1/2);
f:=F/2/RT;

```

```

[> sigma[ads]:=z[S]*F*Gamma*theta;
[> theta:=beta*c[z]/(1+beta*c[z]);
[> beta:=exp(-G/RT)*exp(z[S]*F/RT*(phi[w]-phi[2]))/c[0];

```

```

[> phi[b2]:=solve(eqnb,phi[2]);
[> phi[2]:=solve(eqn,phi[2]);

```

```

[> para1:=F=96500,RT=8.314*298,epsilon[0]=8.85e-12,epsilon[w]=70,epsilon[o]=10,
c[w]=10,c[o]=10;
[> para2:=phi[w]=0,phi[o]=-Delta;
[> para3:=Delta=-0.1;
[> para4:=z[S]=-1,c[0]=1000000/18,G=-40000,Gamma=1e-06;
[> para5:=c[z]=0.05;

```

```

[> P0:=eval(phi[b2],[para1,para2]);
P1:=eval(phi[2],[para1,para2,para4,c[z]=0.001]);
P2:=eval(phi[2],[para1,para2,para4,c[z]=0.002]);
P3:=eval(phi[2],[para1,para2,para4,c[z]=0.005]);
P4:=eval(phi[2],[para1,para2,para4,c[z]=0.01]);
P5:=eval(phi[2],[para1,para2,para4,c[z]=0.05]);
[> plot([P0,P1,P2,P3,P4,P5],Delta=-0.4..0.4);

```

#### *Part 2: Potential profile across the interface*

##### *(1) Poisson equations:*

```

[> eqnw:=diff(xi(x),x)=(8*RT*c[w]/epsilon[0]/epsilon[w])^(1/2)*sinh(f*(xi(x)-phi[w]));
eqno:=diff(zeta(x),x)=(8*RT*c[o]/epsilon[0]/epsilon[o])^(1/2)*sinh(f*(phi[o]-zeta(x)));

```



(2) *Potential profile in aqueous phase:*

```
[> ppw:=dsolve({eqnw,xi(0)=phi2},xi(x));
```

(3) *Potential profile in organic phase:*

```
[> ppo:=dsolve({eqno,zeta(0)=phi2},zeta(x));
```

*Evaluation: Delta = -0.02 V;*

```
[> xi1(x):=eval(eval(subs(ppw[2],xi(x)),[para1,para2,Delta=-0.02]),[Delta=-0.02,phi2=
    eval(eval(phi[2],[para1,para2,para4,para5],Delta=-0.02)]));
    zeta1(x):=eval(eval(subs(ppo[1],zeta(x)),[para1,para2,Delta=-0.02]),[Delta=-0.02,phi2=
    eval(eval(phi[2],[para1,para2,para4,para5],Delta=-0.02)]));
```

*Evaluation: Delta = -0.10;*

```
[> xi2(x):=eval(eval(subs(ppw[2],xi(x)),[para1,para2,Delta=-0.10]),[Delta=-0.10,phi2=
    eval(eval(phi[2],[para1,para2,para4,para5],Delta=-0.10)]));
    zeta2(x):=eval(eval(subs(ppo[1],zeta(x)),[para1,para2,Delta=-0.10]),[Delta=-0.10,phi2=
    eval(eval(phi[2],[para1,para2,para4,para5],Delta=-0.10)]));
```

*Evaluation: Delta = -0.20;*

```
[> xi3(x):=eval(eval(subs(ppw[2],xi(x)),[para1,para2,Delta=-0.20]),[Delta=-0.20,phi2=
    eval(eval(phi[2],[para1,para2,para4,para5],Delta=-0.20)]));
    zeta3(x):=eval(eval(subs(ppo[1],zeta(x)),[para1,para2,Delta=-0.20]),[Delta=-0.20,phi2=
    eval(eval(phi[2],[para1,para2,para4,para5],Delta=-0.20)]));
```

*Evaluation: Delta = -0.30;*

```
[> xi4(x):=eval(eval(subs(ppw[2],xi(x)),[para1,para2,Delta=-0.30]),[Delta=-0.30,phi2=
    eval(eval(phi[2],[para1,para2,para4,para5],Delta=-0.30)]));
    zeta4(x):=eval(eval(subs(ppo[1],zeta(x)),[para1,para2,Delta=-0.30]),[Delta=-0.30,phi2=
    eval(eval(phi[2],[para1,para2,para4,para5],Delta=-0.30)]));
```

```
[> with(plots):
```

```
    xi1:=plot(xi1(x),x=-1e-08..0,style=point,color=black):
    zeta1:=plot(zeta1(x),x=0..1e-08,style=point,color=black):
    xi2:=plot(xi2(x),x=-1e-08..0,style=point,color=red):
    zeta2:=plot(zeta2(x),x=0..1e-08,style=point,color=red):
    xi3:=plot(xi3(x),x=-1e-08..0,style=point,color=blue):
    zeta3:=plot(zeta3(x),x=0..1e-08,style=point,color=blue):
    xi4:=plot(xi4(x),x=-1e-08..0,style=point,color=green):
    zeta4:=plot(zeta4(x),x=0..1e-08,style=point,color=green):
    display({xi1,zeta1,xi2,zeta2,xi3,zeta3,xi4,zeta4});
```

### **Part 3: $\theta$**

```
[> theta[1]:=eval(theta,[para1,para2,para4,c[z]=0.001]);
    theta[2]:=eval(theta,[para1,para2,para4,c[z]=0.002]);
    theta[3]:=eval(theta,[para1,para2,para4,c[z]=0.005]);
    theta[4]:=eval(theta,[para1,para2,para4,c[z]=0.01]);
    theta[5]:=eval(theta,[para1,para2,para4,c[z]=0.05]);
[> plot([the1,the2,the3,the4,the5],Delta=-0.4..0.4);
```

### **Part 4: Charge density and differential capacitance**

```
[> sigma[w]:=a*sinh(f*(chi[w]))+z[S]*F*Gamma*exp(-G/RT)*exp(z[S]*F*(-chi[w])/RT)
    *c[z]/(c[0]*(1+exp(-G/RT)*exp(z[S]*F*(-chi[w])/RT)*c[z]/c[0]));
```

```
[> sigma[o]:=b*sinh(f*(chi[o]));
[> C[o]:=diff(sigma[o],chi[o]);
[> C[w]:=diff(sigma[w],chi[w]);
```

```

[> C[t]:=-C[w]*C[o]/(C[w]+C[o]):

[> chi0[w]:=eval(phi[b2]-phi[w],[para1,para2]);
[> chi0[o]:=eval(phi[b2]-phi[o],[para1,para2]);

[> chi1[w]:=eval(phi[2]-phi[w],[para1,para2,para4,c[z]=0.001]):
  chi1[o]:=eval(phi[2]-phi[o],[para1,para2,para4,c[z]=0.001]):
  chi2[w]:=eval(phi[2]-phi[w],[para1,para2,para4,c[z]=0.002]):
  chi2[o]:=eval(phi[2]-phi[o],[para1,para2,para4,c[z]=0.002]):
  chi3[w]:=eval(phi[2]-phi[w],[para1,para2,para4,c[z]=0.005]):
  chi3[o]:=eval(phi[2]-phi[o],[para1,para2,para4,c[z]=0.005]):
  chi4[w]:=eval(phi[2]-phi[w],[para1,para2,para4,c[z]=0.01]):
  chi4[o]:=eval(phi[2]-phi[o],[para1,para2,para4,c[z]=0.01]):
  chi5[w]:=eval(phi[2]-phi[w],[para1,para2,para4,c[z]=0.05]):
  chi5[o]:=eval(phi[2]-phi[o],[para1,para2,para4,c[z]=0.05]):

[> sigw0:=eval(sigma[w],[para1,para2,para4,c[z]=0,chi[w]=chi0[w]]):
  sigw1:=eval(sigma[w],[para1,para2,para4,c[z]=0.001,chi[w]=chi1[w]]):
  sigw2:=eval(sigma[w],[para1,para2,para4,c[z]=0.002,chi[w]=chi2[w]]):
  sigw3:=eval(sigma[w],[para1,para2,para4,c[z]=0.005,chi[w]=chi3[w]]):
  sigw4:=eval(sigma[w],[para1,para2,para4,c[z]=0.01,chi[w]=chi4[w]]):
  sigw5:=eval(sigma[w],[para1,para2,para4,c[z]=0.05,chi[w]=chi5[w]]):

[> plot([sigw0,sigw1,sigw2,sigw3,sigw4,sigw5],Delta=-0.3..0.3,style=point);

[> with(plots):
  cap0:=plot(eval(C[t],[para1,para2,para4,c[z]=0,chi[w]=chi0[w],chi[o]=chi0[o]]),
    Delt a=-0.3..0.3,style=point,color=black):
  cap1:=plot(eval(C[t],[para1,para2,para4,c[z]=0.001,chi[w]=chi1[w],chi[o]=chi1[o]]),
    Delta=-0.3..0.3,style=point,color=red):
  cap2:=plot(eval(C[t],[para1,para2,para4,c[z]=0.002,chi[w]=chi2[w],chi[o]=chi2[o]]),
    Delta=-0.3..0.3,style=point,color=blue):
  cap3:=plot(eval(C[t],[para1,para2,para4,c[z]=0.005,chi[w]=chi3[w],chi[o]=chi3[o]]),
    Delta=-0.3..0.3,style=point,color=green):
  cap4:=plot(eval(C[t],[para1,para2,para4,c[z]=0.01,chi[w]=chi4[w],chi[o]=chi4[o]]),
    Delta=-0.3..0.3,style=point,color=yellow):
  cap5:=plot(eval(C[t],[para1,para2,para4,c[z]=0.05,chi[w]=chi5[w],chi[o]=chi5[o]]),
    Delta=-0.3..0.3,style=point,color=brown):
display({ cap0,cap1,cap2,cap3,cap4,cap5 });

```

### 3.10.4 Frumkin Isotherm

```

[> restart;
[> with(plots):

```

**Part 1:**  $\phi^2$

```

[> eqn1:=a*sinh(f*(phi[2]-phi[w]))+b*sinh(f*(phi[2]-phi[o]))=0;
[> eqn2:=a*sinh(f*(phi[2]-phi[w]))+b*sinh(f*(phi[2]-phi[o]))-sigma[ads]=0;
[> a:=(8*R*T*epsilon[0]*epsilon[w]*c[w])^(1/2);
  b:=(8*R*T*epsilon[0]*epsilon[o]*c[o])^(1/2);

```

```
f:=F/2/R/T;

[> sigma[ads]:=z[S]*F*Gamma*theta1;
[> eqn3:=ln(theta/(1-theta))=ln(c[z]/c[0])-G/R/T+z[S]*F*(phi[w]-phi[2])/R/T-c*theta/R/T;
[> theta1:=solve(eqn3,theta);

[> phi[a2]:=solve(eqn1,phi[2]):
[> phi[b2]:=solve(eqn2,phi[2]):

[> para1:=phi[w]=0,phi[o]=-Delta;
[> para2:=F=96487,R=8.314,T=298,epsilon[0]=8.85e-12,epsilon[w]=70,epsilon[o]=10,
      c[w]=10,c[o]=10;
[> para3:=Delta=-0.15;
[> para4:=z[S]=-1,G=-40000,Gamma=1e-6,c[0]=1000000/18;
[> points:=[seq(i/20*0.6-0.3,i=0..20)];

[> P1:=eval(phi[a2],[para1,para2,para4,c[z]=0]);
[> P2:=eval(phi[b2],[param1,param2,param4,c[z]=0.05,c=0]);
[> P3:=eval(phi[b2],[param1,param2,param4,c[z]=0.05,c=4000]);
[> P4:=eval(phi[b2],[param1,param2,param4,c[z]=0.05,c=10000]);
[> P5:=eval(phi[b2],[param1,param2,param4,c[z]=0.05,c=-4000]);
[> plot([P1,P2,P3,P4,P5],Delta=-0.3..0.3,adaptive=false,sample=points);
```

## ***Part 2: Potential profile across the interface***

### *(1) Poisson equations:*

```
[> eqnw:=diff(xi(x),x)=(8*R*T*c[w]/epsilon[0]/epsilon[w])^(1/2)*sinh(F*(xi(x)-
      phi[w])/2/R/T);
[> eqno:=diff(zeta(x),x)=(8*R*T*c[o]/epsilon[0]/epsilon[o])^(1/2)*sinh(F*(phi[o]-
      zeta(x))/2/R/T);
```

### *(2) Potential profiles*

```
[> ppw:=dsolve({eqnw,xi(0)=phi2},xi(x));
[> ppo:=dsolve({eqno,zeta(0)=phi2},zeta(x));

[> points2:=seq(-i/20*1e-8,i=0..20);
[> points3:=seq(i/20*1e-8,i=0..20);
```

### *(3) Evaluation for various c:*

```
[> xi0(x):=eval(eval(subs(ppw[2],xi(x)),[para1,para2,para3]),[para3,phi2=
      eval(eval(phi[a2],[para1,para2]),para3)]);
[> zeta0(x):=eval(eval(subs(ppo[1],zeta(x)),[para1,para2,para3]),[para3,phi2=
      eval(eval(phi[a2],[para1,para2]),para3)]);

[> xi1(x):=eval(eval(subs(ppw[2],xi(x)),[para1,para2,para3]),[para3,phi2=
      eval(eval(phi[b2],[para1,para2,para4,c[z]=0.05,c=0]),para3)]);
[> zeta1(x):=eval(eval(subs(ppo[1],zeta(x)),[para1,para2,para3]),[para3,phi2=
      eval(eval(phi[b2],[para1,para2,para4,c[z]=0.05,c=0]),para3)]);

[> xi2(x):=eval(eval(subs(ppw[2],xi(x)),[para1,para2,para3]),[para3,phi2=
      eval(eval(phi[b2],[para1,para2,para4,c[z]=0.05,c=4000]),para3)]);
[> zeta2(x):=eval(eval(subs(ppo[1],zeta(x)),[para1,para2,para3]),[para3,phi2=
      eval(eval(phi[b2],[para1,para2,para4,c[z]=0.05,c=4000]),para3)]);
```

---

```
[> xi3(x):=eval(eval(subs(ppw[2],xi(x)),[para1,para2,para3]),[para3,phi2=
eval(eval(phi[b2],[para1,para2,para4,c[z]=0.05,c=10000]),para3))]:
[> zeta3(x):=eval(eval(subs(ppo[1],zeta(x)),[para1,para2,para3]),[para3,phi2=
eval(eval(phi[b2],[para1,para2,para4,c[z]=0.05,c=10000]),para3))]:

[> xi4(x):=eval(eval(subs(ppw[2],xi(x)),[para1,para2,para3]),[para3,phi2=
eval(eval(phi[b2],[para1,para2,para4,c[z]=0.05,c=-4000]),para3))]:
[> zeta4(x):=eval(eval(subs(ppo[1],zeta(x)),[para1,para2,para3]),[param,phi2=
eval(eval(phi[b2],[para1,para2,para4,c[z]=0.05,c=-4000]),para3))]:

[> P1:=plot(xi0(x),x=-1e-8..0,color=black,adaptive=false,sample=points2):
[> P2:=plot(zeta0(x),x=0..1e-8,color=black,adaptive=false,sample=points3):
[> P3:=plot(xi1(x),x=-1e-8..0,color=blue,adaptive=false,sample=points2):
[> P4:=plot(zeta1(x),x=0..1e-8,color=blue,adaptive=false,sample=points3):
[> P5:=plot(xi2(x),x=-1e-8..0,color=red,adaptive=false,sample=points2):
[> P6:=plot(zeta2(x),x=0..1e-8,color=red,adaptive=false,sample=points3):
[> P7:=plot(xi3(x),x=-1e-8..0,color=green,adaptive=false,sample=points2):
[> P8:=plot(zeta3(x),x=0..1e-8,color=green,adaptive=false,sample=points3):

[> display({P1,P2,P3,P4,P5,P6,P7,P8});
```

### ***Part 3: $\theta = f(c, \Delta)$***

```
[> eqn4:=eval(eqn3,[(phi[w]-phi[2])=chi[w]]);
[> theta2:=solve(eqn4,theta);
plot3d(theta2,Delta=-0.4..0.4,c=-10..10,axes=boxed);
```

### ***Part 4: Charge density and differential capacitance***

```
[> sigma2[ads]:=z[S]*F*Gamma*theta2;
[> sigma[aw]:=-a*sinh(f*(-chi[w]));
[> sigma[bw]:=-a*sinh(f*(-chi[w]))+sigma2[ads];
[> sigma[o]:=-b*sinh(f*(chi[o]));

[> C[aw]:=diff(sigma[aw],chi[w]);
[> C[bw]:=diff(sigma[bw],chi[w]);
[> C[o]:=-diff(sigma[o],chi[o]);

[> C[at]:=C[aw]*C[o]/(C[aw]+C[o]);
[> C[bt]:=C[bw]*C[o]/(C[bw]+C[o]);

[> chi0[w]:=eval(phi[w]-phi[a2],[para1,para2]);
[> chi0[o]:=eval(phi[a2]-phi[o],[para1,para2]);
[> chi1[w]:=eval(phi[w]-phi[b2],[para1,para2,para4,c[z]=0.05,c=0]):
[> chi1[o]:=eval(phi[b2]-phi[o],[para1,para2,para4,c[z]=0.05,c=0]):
[> chi2[w]:=eval(phi[w]-phi[b2],[para1,para2,para4,c[z]=0.05,c=4000]):
[> chi2[o]:=eval(phi[b2]-phi[o],[para1,para2,para4,c[z]=0.05,c=4000]):
[> chi3[w]:=eval(phi[w]-phi[b2],[para1,para2,para4,c[z]=0.05,c=10000]):
[> chi3[o]:=eval(phi[b2]-phi[o],[para1,para2,para4,c[z]=0.05,c=10000]):
[> chi4[w]:=eval(phi[w]-phi[b2],[para1,para2,para4,c[z]=0.05,c=-4000]):
[> chi4[o]:=eval(phi[b2]-phi[o],[para1,para2,para4,c[z]=0.05,c=-4000]):
[> P1:=plot(eval(sigma[aw],[para1,para2,para4,chi[w]=chi0[w]]),
Delta=-0.3..0.3,color=[black],adaptive=false,sample=points):
[> P2:=plot(eval(sigma[o],[para1,para2,para4,c[z]=0,chi[o]=chi0[o]]),
```

```

Delta=-0.3..0.3,color=[black],adaptive=false,sample=points):
[> P3:=plot(eval(sigma[bw],[para1,para2,para4,c[z]=0.05,c=0,chi[w]=chi1[w]]),
Delta=-0.3..0.3,color=[blue],adaptive=false,sample=points):
[> P4:=plot(eval(sigma[o],[para1,para2,para4,c[z]=0.05,c=0,chi[o]=chi1[o]]),
Delta=-0.3..0.3,color=[blue],adaptive=false,sample=points):
[> P5:=plot(eval(sigma[bw],[para1,para2,para4,c[z]=0.05,c=4000,chi[w]=chi2[w]]),
Delta=-0.3..0.3,color=[red],adaptive=false,sample=points):
[> P6:=plot(eval(sigma[o],[para1,para2,para4,c[z]=0.05,c=4000,chi[o]=chi2[o]]),
Delta=-0.3..0.3,color=[red],adaptive=false,sample=points):
[> P7:=plot(eval(sigma[bw],[para1,para2,para4,c[S]=0.05,c=10000,chi[w]=chi3[w]]),
Delta=-0.3..0.3,color=[green],adaptive=false,sample=points):
[> P8:=plot(eval(sigma[o],[para1,para2,para4,c[z]=0.05,c=10000,chi[o]=chi3[o]]),
Delta=-0.3..0.3,color=[green],adaptive=false,sample=points):
[> P9:=plot(eval(sigma[bw],[para1,para2,para4,c[z]=0.05,c=-4000,chi[w]=chi4[w]]),
Delta=-0.3..0.3,color=[gold],adaptive=false,sample=points):
[> P10:=plot(eval(sigma[o],[para1,para2,para4,c[z]=0.05,c=-4000,chi[o]=chi4[o]]),
Delta=-0.3..0.3,color=[gold], adaptive=false,sample=points):
[> display({P1,P2,P3,P4,P5,P6,P7,P8,P9,P10});
[> Cap1:=plot(eval(C[at],[para1,para2,para4,chi[w]=chi0[w],
chi[o]=chi0[o]]),Delta=-0.3..0.3,adaptive=false,sample=points):
[> Cap2:=plot(eval(C[bt],[para1,para2,para4,c[z]=0.05,c=0,chi[w]=chi1[w],
chi[o]=chi1[o]]),Delta=-0.3..0.3,adaptive=false,sample=points):
[> Cap3:=plot(eval(C[bt],[para1,para2,para4,c[z]=0.05,c=4000,chi[w]=chi2[w],
chi[o]=chi2[o]]),Delta=-0.3..0.3,adaptive=false,sample=points):
[> Cap4:=plot(eval(C[bt],[para1,para2,para4,c[z]=0.05,c=10000,chi[w]=chi3[w],
chi[o]=chi3[o]]),Delta=-0.3..0.3,adaptive=false,sample=points):
[> Cap5:=plot(eval(C[bt],[para1,para2,para4,c[z]=0.05,c=-4000,chi[w]=chi4[w],
chi[o]=chi4[o]]),Delta=-0.3..0.3,adaptive=false,sample=points):
[> display({Cap1,Cap2,Cap3,Cap4,Cap5});

```



## Chapter 4

# Voltage-induced assembly of gold NPs at liquid|liquid interfaces

### 4.1 Introduction

Current trends in nanosciences and nanotechnology are pointing towards the fabrication of 2D and 3D assemblies of monodispersed nanostructures at surfaces.<sup>1-3</sup> A variety of protocols has been developed in the past few years for the assembly of functionalised metal and semiconducting NPs at electrode surfaces.<sup>4-14</sup> The optical and electronic properties of the ensemble are determined not only by the properties of individual nanostructures but also by the particle-particle and particle-substrate interactions.<sup>7, 11, 15</sup> A rather challenging issue is to address the effect of these interactions on the reactivity of individual particles. In order to assess this information, assembling protocols should be developed in which the interparticle and particle-substrate couplings can be effectively deconvoluted. Recent publications by Dinsmore and co-workers show that interparticle interactions can be uniquely studied at liquid|liquid interfaces.<sup>16, 17</sup>

Liquid|liquid interfaces are ubiquitous in nature and can be utilized for the organization of nanometer-sized objects.<sup>18</sup> For example, interfacial ordering effects can be used for the self-assembly of NPs.<sup>16, 19, 20</sup> Of key importance is the assembly of NPs at a liquid|liquid interface where the interfacial energy is high. The assembly of NPs at the interface can effectively decrease the high interfacial energy. This decrease in the surface energy in turn favours the formation of a monolayer of NPs located at the interface. As a matter of fact, at the macroscopic level, such processes have been known for a long time as “Pickering emulsions”,<sup>21, 22</sup> in which large particles stabilize emulsions efficiently by adsorbing onto the liquid|liquid interface.

Interfaces between two immiscible electrolyte solutions (ITIES) provide a defect free junction for studying adsorption phenomena, charge transfer reactions and phase formation processes.<sup>23-25</sup> In the presence of hydrophilic and hydrophobic electrolytes, the Galvani potential difference between the two liquid phases can be biased potentiostatically. In a recent work, it has been demonstrated that titanium dioxide (TiO<sub>2</sub>) NPs can be electrostatically assembled at the polarizable water|1,2-dichloroethane (DCE) interface.<sup>26, 27</sup> Assembling TiO<sub>2</sub> NPs at the interface effectively increases the surface excess charge, which is found to be dependent on the Galvani potential difference across the water|DCE interface.

In the present chapter, we shall describe the voltage induced assembly of mercaptosuccinic acid (MSA) stabilized gold NPs of  $1.5 \pm 0.4$  nm in diameter at the polarizable water|DCE interface. The gold NPs are negatively charged due to the deprotonation of carboxylic groups of MSA molecules attached on the particle surfaces. Admittance measurements and quasi-elastic laser scattering (QELS) studies reveal that the surface concentration of the gold NPs at the water|DCE interface is reversibly controlled by the applied potential. The electrochemical and optical measurements provide no evidence of irreversible aggregation or deposition of the particles at the interface. The assembly of gold NPs at the interface induces changes in the surface tension as estimated from QELS measurements. The measurements of the average charges of gold NPs by capillary electrophoresis also confirmed that the changes in the surface tension are related to the interfacial assembly of negatively charged gold NPs.



## 4.2 Cyclic voltammetry and differential capacitance measurements

This section will provide electrochemical evidence that the assembly of MSA stabilized gold NPs at the water|DCE interface can be tuned by the Galvani potential difference across the interface. The electrochemical cell employed for the measurements in the present chapter are schematically illustrated in Figure 4.1.



**Figure 4.1** Schematic representation of the electrochemical cell employed for the measurements in Chapter 4.

Cyclic voltammograms at a scan rate of  $100 \text{ mV s}^{-1}$  and various concentrations of the gold NPs are illustrated in Figure 4.2a. The voltammograms feature a peak at negative potentials, the position and width of which are slightly dependent on the concentration of gold NPs in the aqueous phase. The magnitude of the peak current slightly increases with increasing the concentration of gold NPs in the aqueous phase. The peak current also exhibits a linear dependence on the potential scan rate, as shown in Figure 4.3. These facts suggest that the process is associated with the specific adsorption of the gold NPs.

However, the current peak is broad in comparison to that of conventional molecules at the metal electrode|solution interface. In addition to the uncompensated resistance effects, the width of adsorption peaks in cyclic voltammograms at the polarizable liquid|liquid interfaces is determined by the charge of the adsorbing species and the effective potential drop in the aqueous side of the junction. The relatively broad adsorption features in Figure 4.2a and Figure 4.3a provide at least two indications. First, it may indicate that only a small portion of the applied potential is developed in the aqueous side of the interface. Second, it possibly suggests that the effective charge per particle is significantly smaller than the charge expected if all the MSA groups were fully ionised. This aspect will be discussed further below.

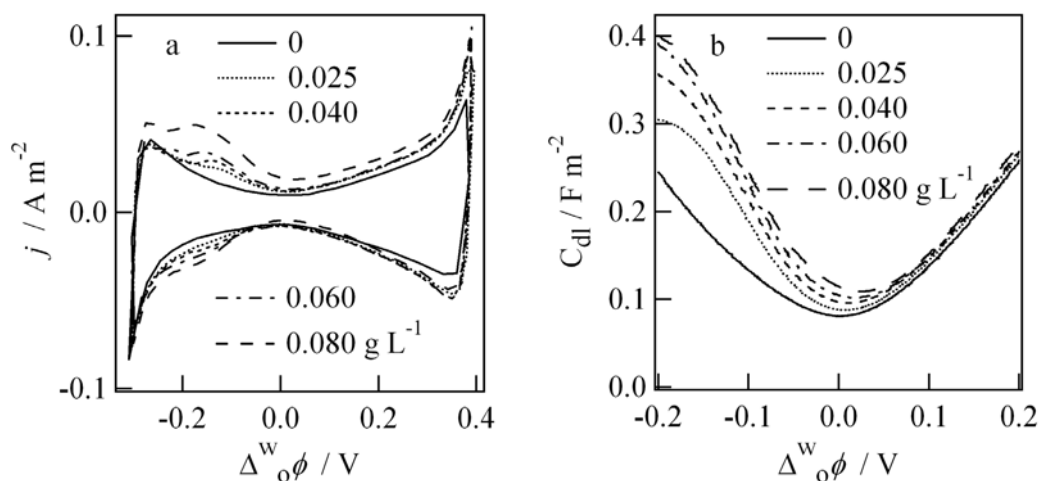


**Figure 4.2** CVs at scan rates of  $100 \text{ mV s}^{-1}$  (a) and differential capacitance curves (b) for various concentrations of gold NPs in the aqueous phase. The Galvani potential difference is referred to the potential at the minimum of the capacitance in the absence of the NPs (this reference is employed in this chapter).

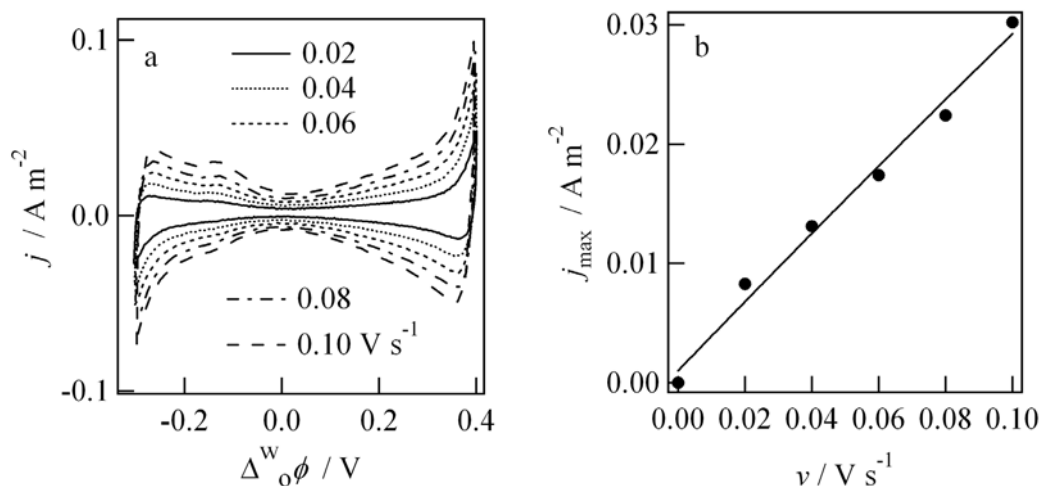


**Figure 4.3** (a) CVs at various scan rates in the presence of  $0.04 \text{ g L}^{-1}$  gold NPs in the aqueous phase; (b) The dependence of the peak current on the scan rate.

Evidence for the adsorption nature of the voltammetric responses can be also obtained from the differential capacitance ( $C_{dl}$ ) curves shown in Figure 4.2b. These curves were estimated from admittance measurements assuming that the impedance of the cell can be

expressed in terms of a double layer capacitance and an uncompensated resistance between the reference electrodes. The value of  $C_{dl}$  can be rationalized as the derivative of the excess charge in the electric double layer with respect to the applied potential. From Figure 4.2b, it can be clearly observed that the excess charge in the negative potential range increases with respect to the background differential capacitances. Furthermore, with increasing particle concentration up to values close to  $0.1 \text{ g dm}^{-3}$ , a continuous increase of the negative excess charge associated with the assembly of gold NPs is observed, as well as the shift of the minimum of the differential capacitance curves to more positive potentials. These features further suggest that the excess charge at negative potentials is originating from the voltage induced assembly of the gold NPs at the liquid|liquid interface.

### 4.3 Assembly of gold NPs at the water|DCE interface studied by quasi-elastic laser scattering measurements

This section is aimed at exploring the changes in the interfacial tension due to the assembly of gold NP at the water|DCE boundary by quasi-elastic laser scattering (QELS) measurements. The surface coverage of gold NPs will be also estimated.

#### 4.3.1 QELS measurements

It is well known that the specific adsorption of species at the liquid|liquid interface manifests itself by changes in the surface tension of the interface. As shown in section 2.3 of Chapter 2, the surface tension ( $\gamma$ ) of the liquid|liquid interface can be estimated from the characteristic frequency ( $f_0$ ) of the thermally excited capillary waves at the interface, which can be experimentally measured by QELS technique. Rearranging eq 2.8, the relation between these two parameters can be rewritten as:

$$f_0 = \frac{1}{2\pi} \sqrt{\frac{\gamma k^3}{\rho^w + \rho^{\text{DCE}}}} \quad (4.1)$$

where  $\rho^w$  and  $\rho^{\text{DCE}}$  are the densities of water and DCE, respectively. The capillary wavenumber  $k = 510.4 \text{ cm}^{-1}$  was estimated assuming that the interfacial tension of the neat water|DCE junction is  $28.5 \text{ mN m}^{-1}$ .<sup>28</sup>

Figure 4.4 displays the evolution of the QELS power spectrum corresponding to the third order diffracted spot with increasing concentration of the NPs at  $\Delta_0^w \phi = -0.16 \text{ V}$ . The displacement of the maximum towards lower frequencies with increasing the concentration of gold NPs in the aqueous phase indicates a decrease in the frequency of the capillary waves, which corresponds to the decrease of the surface tension of the water|DCE interface. The evolution of the QELS power spectrum with negative polarization of the interface is illustrated in Figure 4.5. It is apparent that the characteristic frequency of the capillary waves continuously shifts to a lower value with increasing the magnitude of the Galvani potential difference across the interface, indicating the continuous decrease of the surface tension.

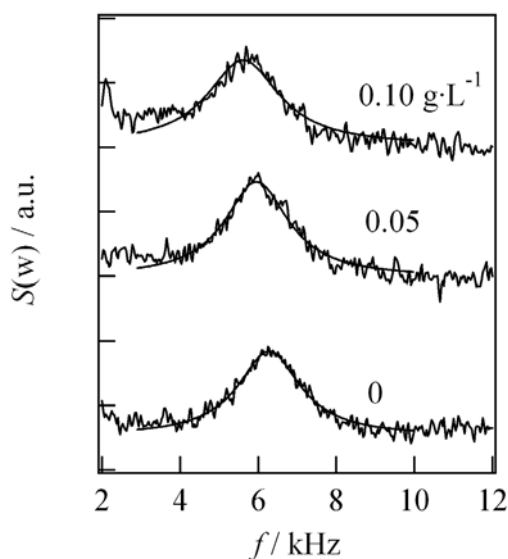


**Figure 4.4** Evolution of QELS power spectra of the third order diffraction spot with the concentration of gold NPs at  $\Delta_0^w \phi = -0.16 \text{ V}$ . The experimental curves were fitted with Lorentzian function.

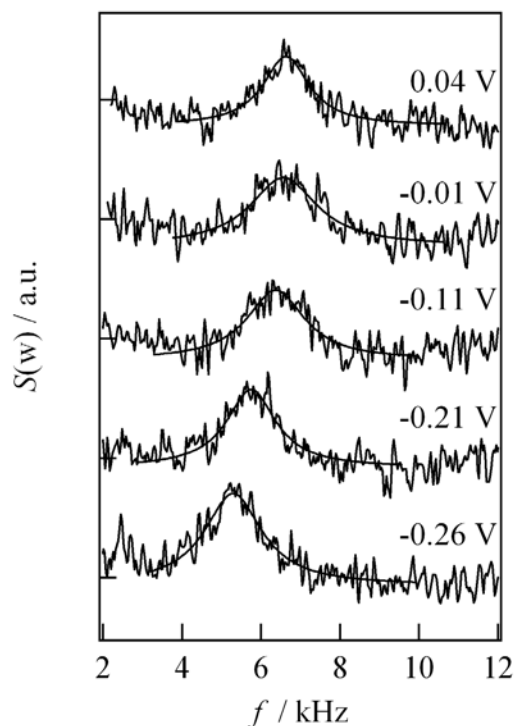


**Figure 4.5** QELS power spectra of the third order diffraction spot as a function of the Galvani potential difference. The concentration of gold NPs is  $0.10 \text{ g L}^{-1}$ . The smooth curves are corresponding Lorentzian fittings.

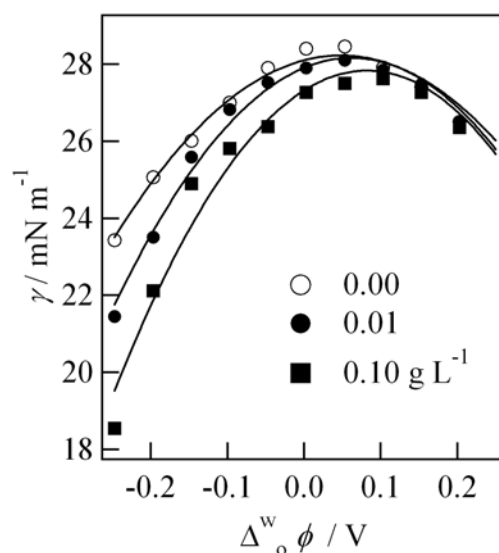


**Figure 4.6** Electrocapillary curves at various gold NP concentrations.

The dependence of  $f_0$  on the concentration of the gold NPs as well as the potential bias across the interface allows constructing electrocapillary curves, the surface tension as a function of the potential, as shown in Figure 4.6. In the absence of NPs, the maximum of

the electrocapillary curves is located at potentials close to the minimum of the differential capacitance. As the concentration of the gold NPs increases, the interfacial tension decreases at negative Galvani potential differences due to the assembly of the gold NPs at the interface. Comparing the results displayed in Figures 4.2b and Figure 4.6, one can see that the onset potential for the formation of the NP assembly is close to the potential at the minimum of the differential capacitance curve or the maximum of the electrocapillary curves.

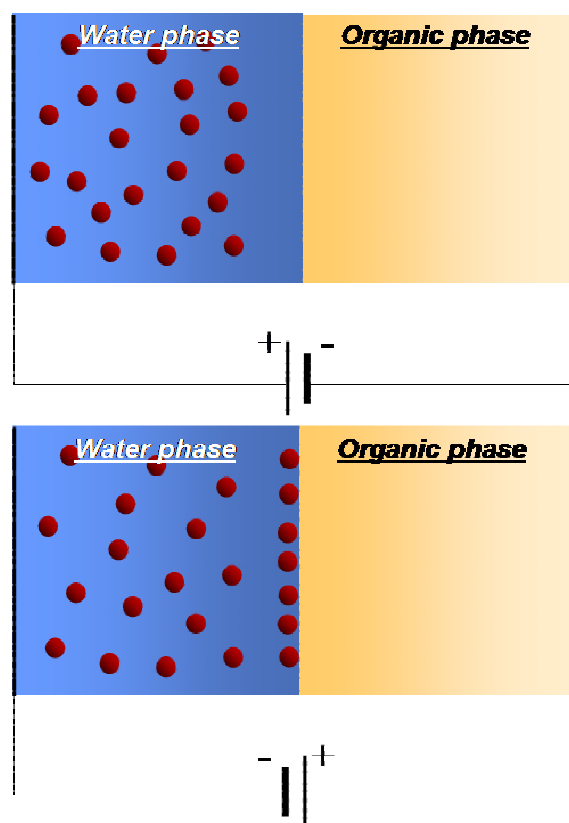


**Figure 4.7** *Cartoon of the voltage induced assembly of NPs at the interface.*

The dependence of  $\gamma$  and  $C_{dl}$  on the applied bias remains unaffected after several potential cycles over the whole polarizable window. These results indicate that the formation of the NP assembly can be reversibly controlled by the applied voltage, and that no irreversible processes such as aggregation or gold nucleation take place at the liquid|liquid interface. This situation can be simply described by the cartoon shown in Figure 4.7. In the negative potential region, the inner potential of the aqueous phase is biased negatively with respect to the organic phase, inducing the accumulation of negatively charged gold NPs in the diffuse layer of the aqueous side of the interface and

therefore the excess negative charge. In contrast, in the positive potential regime, the gold NPs are pushed away from the interfacial boundary.

### 4.3.2 Estimation of interfacial charge density and excess concentration

In order to further rationalize the changes in the surface tension, it is considered that the charged species distributed in the electrical double layer comprise the ions of the aqueous supporting electrolyte  $\text{Na}^+$  and  $\text{Cl}^-$ , the gold NPs  $\text{Au}^{z-}$  ( $z > 0$ ), and the ions of the organic supporting electrolyte  $\text{BTPPA}^+$  and  $\text{TPFB}^-$ . As the charges of the gold NPs are counterbalanced by  $\text{Na}^+$ , changes in the concentration of the particles do not affect the pH significantly. Consequently, the Gibbs adsorption equation at constant temperature ( $T$ ) and pressure ( $P$ ) can be expressed as:

$$\begin{aligned}
 -d\gamma_{T,P} = & \Gamma_{\text{H}_2\text{O}}d\mu_{\text{H}_2\text{O}} + \Gamma_{\text{Au}^{z-}}d\tilde{\mu}_{\text{Au}^{z-}} + \Gamma_{\text{Na}^+}d\tilde{\mu}_{\text{Na}^+} + \Gamma_{\text{Cl}^-}d\tilde{\mu}_{\text{Cl}^-} \\
 & + \Gamma_{\text{DCE}}d\mu_{\text{DCE}} + \Gamma_{\text{BTPPA}^+}d\tilde{\mu}_{\text{BTPPA}^+} + \Gamma_{\text{TPFB}^-}d\tilde{\mu}_{\text{TPFB}^-}
 \end{aligned} \quad (4.2)$$

where  $\gamma$  is the interfacial tension and  $\Gamma$  represents the surface excess concentration, respectively.

Upon expressing the changes in the chemical potentials of the electrolytes  $\text{NaCl}$ ,  $\text{Na}_z\text{Au}$  and  $\text{BTPPATPFB}$  as:

$$d\mu_{\text{Na}_z\text{Au}} = z d\tilde{\mu}_{\text{Na}^+} + d\tilde{\mu}_{\text{Au}^{z-}} \quad (4.3)$$

$$d\mu_{\text{NaCl}} = d\tilde{\mu}_{\text{Na}^+} + d\tilde{\mu}_{\text{Cl}^-} \quad (4.4)$$

$$d\mu_{\text{BTPPATPFB}} = d\tilde{\mu}_{\text{BTPPA}^+} + d\tilde{\mu}_{\text{TPFB}^-} \quad (4.5)$$

the following relations are obtained:

$$\begin{aligned}
 \Gamma_{\text{Au}^{z-}}d\tilde{\mu}_{\text{Au}^{z-}} + \Gamma_{\text{Na}^+}d\tilde{\mu}_{\text{Na}^+} + \Gamma_{\text{Cl}^-}d\tilde{\mu}_{\text{Cl}^-} = \\
 \Gamma_{\text{Au}^{z-}}d\mu_{\text{Na}_z\text{Au}} + \Gamma_{\text{Cl}^-}d\mu_{\text{NaCl}} + \left( \Gamma_{\text{Na}^+} - z\Gamma_{\text{Au}^{z-}} - \Gamma_{\text{Cl}^-} \right) d\tilde{\mu}_{\text{Na}^+}
 \end{aligned} \quad (4.6)$$

$$\begin{aligned}
 \Gamma_{\text{BTPPA}^+}d\tilde{\mu}_{\text{BTPPA}^+} + \Gamma_{\text{TPFB}^-}d\tilde{\mu}_{\text{TPFB}^-} = \\
 \Gamma_{\text{TPFB}^-}d\mu_{\text{BTPPATPFB}} + \left( \Gamma_{\text{BTPPA}^+} - \Gamma_{\text{TPFB}^-} \right) d\tilde{\mu}_{\text{BTPPA}^+}
 \end{aligned} \quad (4.7)$$

And the excess charge densities in each phase together with the electroneutrality condition give:

$$\sigma^w = \left( \Gamma_{\text{Na}^+} - z\Gamma_{\text{Au}^{z-}} - \Gamma_{\text{Cl}^-} \right) F \quad (4.8)$$

$$\sigma^o = \left( \Gamma_{\text{BTPPA}^+} - \Gamma_{\text{TPFB}^-} \right) F \quad (4.9)$$

$$\sigma^w + \sigma^o = 0 \quad (4.10)$$

Thus, the electrocapillary equation, eq 4.2, can be rewritten as:

$$\begin{aligned} -d\gamma_{T,P} = & \Gamma_{\text{H}_2\text{O}} d\mu_{\text{H}_2\text{O}} + \Gamma_{\text{Au}^{z-}} d\mu_{\text{Na}_z\text{Au}} + \Gamma_{\text{Cl}^-} d\mu_{\text{NaCl}} \\ & + \Gamma_{\text{DCE}} d\mu_{\text{DCE}} + \Gamma_{\text{TPFB}^-} d\mu_{\text{BTPPATPFB}} \\ & + \frac{\sigma^w}{F} \left( d\tilde{\mu}_{\text{Na}^+} - d\tilde{\mu}_{\text{BTPPA}^+} \right) \end{aligned} \quad (4.11)$$

The bracket term in eq 4.11 can be related to the Galvani potential difference across the interface:

$$\left( d\tilde{\mu}_{\text{Na}^+} - d\tilde{\mu}_{\text{BTPPA}^+} \right) = F d\Delta_o^w \phi \quad (4.12)$$

Consequently, according to eqs 4.11 and 4.12,  $\sigma^w$  and  $\Gamma_{\text{Au}^{z-}}$  are given by:

$$\sigma^w = - \left( \frac{\partial \gamma}{\partial \Delta_o^w \phi} \right)_{T,P,\mu_i} \quad (4.13)$$

and

$$\Gamma_{\text{Au}^{z-}} = - \left( \frac{\partial \gamma}{\partial \mu_{\text{Na}_z\text{Au}}} \right)_{T,P,\Delta_o^w \phi, \mu_i \neq \mu_{\text{Na}_z\text{Au}}} \quad (4.14)$$

Finally, assuming that the most important contribution to  $\sigma^w$  arises from the gold NPs, eq 4.14 can also be approximated to:

$$\Gamma_{\text{Au}^{z-}} \approx - \left( \frac{\partial \gamma}{\partial \tilde{\mu}_{\text{Au}^{z-}}} \right)_{T,P,\Delta_o^w \phi, \mu_i \neq \mu_{\text{Na}_z\text{Au}}} \quad (4.15)$$

Considering the definition of the electrochemical potential, we get:

$$\Gamma_{\text{Au}^{z-}} \approx - \frac{1}{RT} \left( \frac{\partial \gamma}{\partial \ln c_{\text{Au}^{z-}}} \right)_{T,P,\Delta_o^w \phi, \mu_i \neq \mu_{\text{Na}_z\text{Au}}} \quad (4.16)$$

where  $c_{\text{Au}^{z-}}$  is the bulk concentration of gold NPs in the aqueous phase. Eq 4.16 sets up a relationship between the surface coverage and the bulk concentration. Therefore, analysis of the electrocapillary curves on the basis of eqs 4.13 and 4.16 can provide information on the particle charge number  $z$ .



The dependencies of  $\sigma^w$  and  $\Gamma_{\text{Au}^{z-}}$  on the concentration of the gold NPs in the aqueous phase as derived from eqs 4.13 and 4.16 are illustrated in Figure 4.8a and 4.8b, respectively. The derivatives were calculated by interpolating the surface tension values employing a polynomial expression. It can be observed that both interfacial parameters increase as the concentration of the particles increases and as the interface is biased to negative potentials. Considering that:

$$\sigma^w \approx \sigma^{\text{Au}^{z-}} = -ze\Gamma_{\text{Au}^{z-}} \quad (4.17)$$

the effective average value of  $z$  obtained from the data illustrated in Figure 4.8 corresponds to  $5.1 \pm 0.7$ .

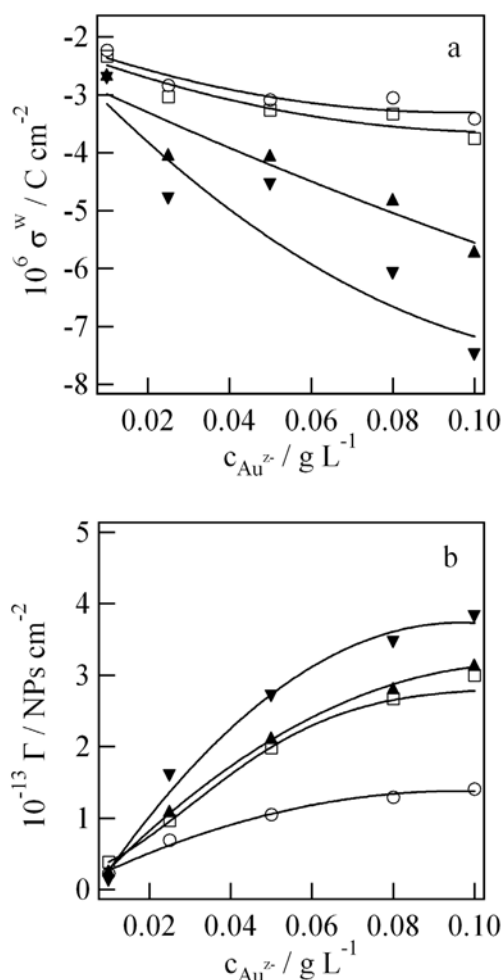


**Figure 4.8** Interfacial charge density (a) and interfacial excess concentration of gold NPs as a function of the bulk concentration of gold NPs for various Galvani potential differences:  $-0.11 \text{ V}$  ( $\circ$ ),  $-0.16 \text{ V}$  ( $\square$ ),  $-0.21 \text{ V}$  ( $\blacktriangle$ ) and  $-0.24 \text{ V}$  ( $\blacktriangledown$ ).

The maximum value of  $\Gamma_{\text{Au}^{2-}}$  estimated from the electrocapillary curves is  $3.8 \times 10^{13} \text{ cm}^{-2}$ , corresponding to approximately 67% of a square closed-pack arrangement of spherical NPs of 1.5 nm diameter in a pseudo 2D assembly. In principle, the NP assembly can be visualized as a concentration polarization phenomenon, i.e. the gold NPs are distributed in the space charge region at the aqueous side of the interface. However, it should be also taken into account that the diameter of the NPs is comparable to the characteristic Debye length at the aqueous side of the interface, i.e. 5 nm for the electrolyte composition described in Figure 4.1. Consequently, although the experimental results do not provide unambiguous evidences of the formation of a 2D assembly upon potential polarization, the intrinsic structure of the interface determines that the charged gold NPs are confined to a narrow region within few nanometers from the liquid|liquid boundary.

#### 4.4 Apparent charge number of gold NPs

Each MSA molecule contains two carboxylic groups with  $\text{p}K_1 = 3.30$  and  $\text{p}K_2 = 4.94$ .<sup>29</sup> The degree of electrolytic dissociation of MSA molecules can be estimated to vary with solution pH using the following equation:<sup>30</sup>

$$\alpha = \frac{2K_1K_2 + (K_1 + K_2)x}{2(K_1 + x)(K_2 + x)} \quad (4.18)$$

where  $x = [\text{H}^+]$ . The degree of electrolytic dissociation of MSA molecules can be calculated to be 99.56% in a solution of pH around 7. Considering a packing density of MSA on the gold NP surface of  $0.214 \text{ nm}^{-2}$ ,<sup>31</sup> the surface of a 1.5 nm in diameter gold NP is covered by about 33 MSA molecules. Therefore, if neglecting the variations of  $\text{p}K_1$  and  $\text{p}K_2$  of MSA molecules when attaching them to a particle surface, an MSA-derivatized gold NP is highly charged due to the nearly complete deprotonation of carboxylic groups attached to the particle surface. However, the charge number estimated from electrocapillary curves is much smaller than that expected. In order to verify the estimation, the charge state of MSA-derivatized gold NPs is also studied by capillary electrophoresis.

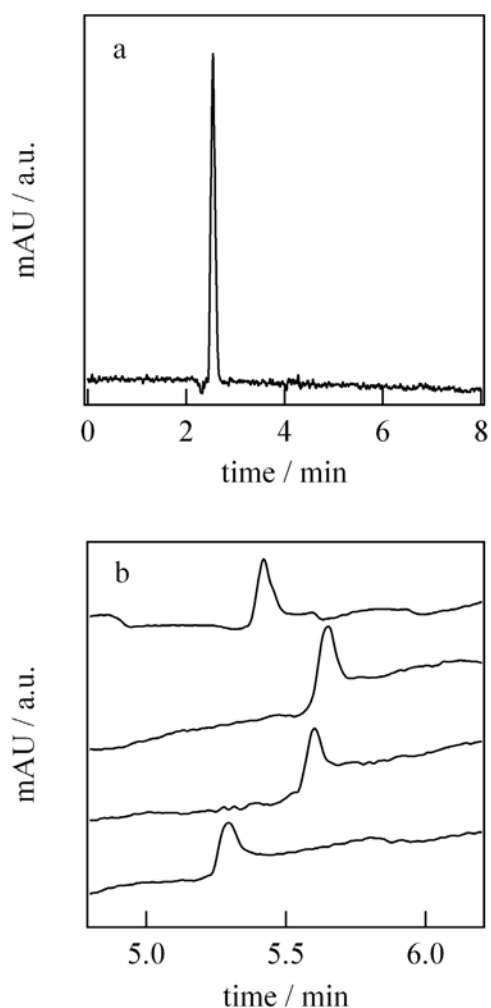


**Figure 4.9** Capillary electropherograms of the neutral marker ethanol (a) and the gold NPs with four times measurements (b). The sample was dissolved in a four times dilute of a pH 7.0 buffer ( $\sim 0.029\text{ M NaOH} + \sim 0.050\text{ KH}_2\text{PO}_4$ ) and detected with a UV diode array set at 198 nm.

Figure 4.9 shows the capillary electropherograms of solutions containing 1.5 nm MSA stabilized gold NPs with ethanol as the neutral marker. From the peak displayed in Figure 4.9a, the electrophoretic mobility of solvent,  $\mu_{\text{eof}}$ , was calculated to be  $8.0 \times 10^{-8}\text{ m}^2\text{ V}^{-1}\text{ s}^{-1}$ . As shown in Figure 4.9b, the peaks around 5.5 minutes, which are associated with 1.5 nm gold NPs inside the solutions, yield an average apparent electrophoretic mobility ( $\mu_{\text{app}}$ ) of  $3.6 \times 10^{-8}\text{ m}^2\text{ V}^{-1}\text{ s}^{-1}$ . Therefore, the real electrophoretic mobility of gold NPs can be estimated as  $-4.4 \times 10^{-8}\text{ m}^2\text{ V}^{-1}\text{ s}^{-1}$ . The negative value shows that the net charge on the NP surface is negative. According to eq 2.15 in Chapter 2, the average NP charge number is  $-4.3$  assuming spherical NPs with an average diameter of 2.6 nm including the

MSA protecting layer. This number is far less than the total deprotonated carboxylic groups present on the NP surface. However, this  $z$  value is consistent with the previous estimations based on the electrocapillary curves, confirming that the changes in the surface tension are related to the interfacial assembly of the gold NPs.

It should be noted that the experimentally derived charge from electrophoretic mobility does not reflect the real surface charge of NPs due to the screening effect from the surrounding ionic charges. Indeed, Templeton et al. obtained similar average charges for gold NPs of the same dimensions stabilized by Tiorponin.<sup>32</sup> A quantitative calculation of the surface potential of a colloidal particle is difficult because of the lack of knowledge regarding the accurate surface structure of the particle. The determination of the surface charge of NPs and its theoretical derivation is still a challenging goal in colloidal chemistry.

#### 4.5 Assembly of gold NPs at the water|DCE interface - Simulations

In Chapter 3, we have demonstrated that on the basis of simulations using the classical Gouy-Chapman theory the adsorption of charged species at the liquid|liquid interface has a strong effect on the interfacial structure. This section will be dedicated to theoretical consideration on the effect of assembly of MSA gold NPs on the interfacial structure using the Langmuir isotherm exemplified in Chapter 3. The interfacial charge density and differential capacitance will be calculated and compared to the experimental curves.

According to the Langmuir isotherm, the relative surface coverage  $\theta$  is given by:<sup>33</sup>

$$\theta = \frac{c_z}{c_{\text{H}_2\text{O}}} \frac{\exp\left(-\frac{\Delta G_a^0}{RT}\right) \exp\left[-\frac{z_b F}{RT}(\phi^2 - \phi^w)\right]}{1 + \frac{c_z}{c_{\text{H}_2\text{O}}} \exp\left(-\frac{\Delta G_a^0}{RT}\right) \exp\left[-\frac{z_b F}{RT}(\phi^2 - \phi^w)\right]} \quad (4.19)$$

All the parameters have been defined in Chapter 3 and will be assigned as follows. The molar concentration,  $c_z$ , can be roughly estimated by considering the molar mass of 1.5

nm gold NPs as  $25000 \text{ g mol}^{-1}$ . This value is taken as the sum of the gold core mass and 33 MSA ligands on the particle surface. The gold core mass was calculated from  $\rho V$ , where  $\rho$  and  $V$  represent the density of bulk gold and the volume of a 1.5 nm gold NPs. Thus  $0.080 \text{ g L}^{-1}$  corresponds to a molar concentration of  $0.0032 \text{ mol m}^{-3}$ . The charge number of gold NPs is taken as  $-4$ , as determined above by surface tension and electrophoresis measurements. The maximum surface coverage  $\Gamma^* = 3.12 \times 10^{-7} \text{ mol m}^{-2}$  is estimated by assuming a square closed-pack coverage of gold NPs at the interface. The electrolyte concentrations  $c^w = 5 \text{ mol m}^{-3}$  and  $c^o = 10 \text{ mol m}^{-3}$  are used in order to be consistent with the experimental conditions.  $\Delta G_a^0$  is a parameter difficult to estimate, and thus will be considered as a variable. All the other parameters are the same as those used in Chapter 3.

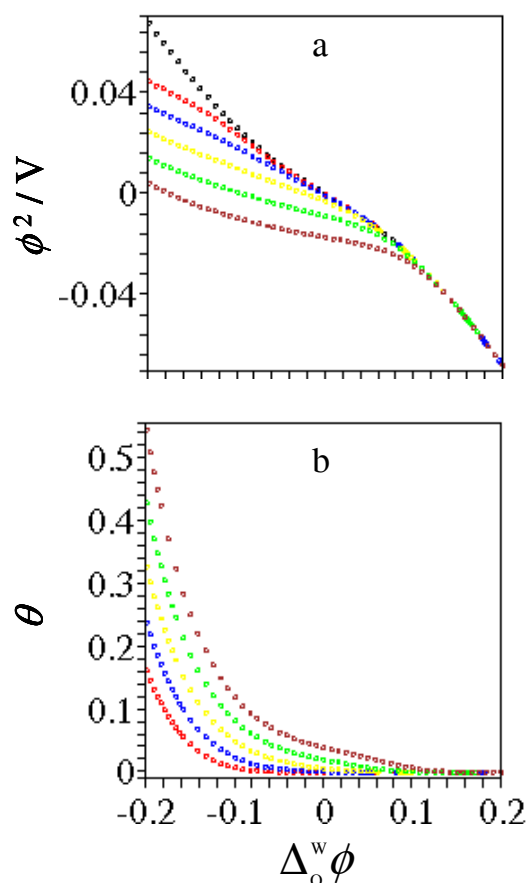


**Figure 4.10**  $\phi^2$  (a) and the relative surface coverage  $\theta$  (b) as a function of  $\Delta_o^w \phi$  at various  $\Delta G_a^0$ : -20 (red), -25 (blue), -30 (yellow), -35 (green) and -40  $\text{kJ mol}^{-1}$  (brown). The black curve in (a) corresponds to the absence of NPs.

Figure 4.10a illustrates the evolution of  $\phi^2$  as a function of the Galvani potential difference across the interface at various values of  $\Delta G_a^0$ .  $\phi^2$  represents the potential at the charged plane where the adsorption is assumed to take place. This potential varies significantly in the presence of adsorption of charged gold NPs at the interface. When  $\Delta G_a^0 > -25 \text{ kJ mol}^{-1}$ , the inversion of  $\phi^2$  occurs over a certain range of Galvani potential differences, resulting in a potential trap at the interface. Figure 4.10b illustrates the relative surface coverage as a function of the Galvani potential difference. Two adsorption stages are clearly observed. In the middle of the potential window, the adsorption is dominantly determined by the magnitude of  $\Delta G_a^0$  and the surface coverage slowly increases. In the potential range of more negative than  $-0.1 \text{ V}$ , the adsorption becomes potential dependent and the coverage steeply increases.

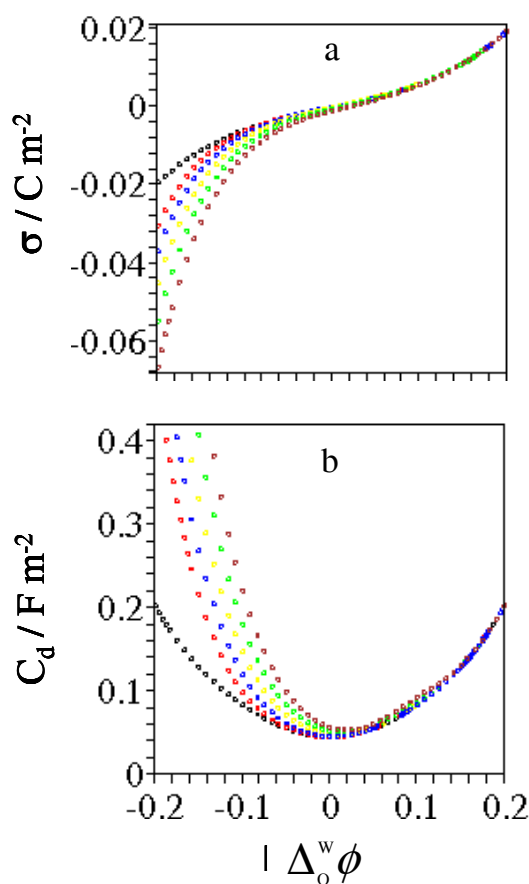


**Figure 4.11** Charge density (a) and differential capacitance (b) as a function of  $\Delta_0^w \phi$  at various  $\Delta G_a^0$ :  $-20$  (red),  $-25$  (blue),  $-30$  (yellow),  $-35$  (green) and  $-40 \text{ kJ mol}^{-1}$  (brown). The black curves correspond to the absence of NPs.

Figure 4.11a and 4.11b illustrate the charge density and differential capacitance as a function of the Galvani potential difference across the interface. The charge density and differential capacitance strongly increase at negative potential differences but remain unchanged in the positive potential range. This feature is consistent with the experimental observation on adsorption of negatively charged species from the aqueous phase to the interface. The calculated differential capacitance curves displayed in Figure 4.11b should be compared with the experimental traces shown in Figure 4.2b. These two figures are displayed in the same unit and scale for comparison. In a potential range of more positive than  $-0.1$  V, the brown curve in Figure 4.11 with  $\Delta G_a^0$  being assigned as  $-40$  kJ mol $^{-1}$  is apparently in a good agreement with the experimental curve displayed in Figure 4.2b, both in the magnitude of the differential capacitance and the shift of the minimum point of the curve. A large value of  $\Delta G_a^0$  indicates that the MSA protected gold NPs have a strong affinity for the water|DCE interface.

However, at more negative Galvani potential differences ( $> -0.1$  V), the simulated differential capacitance increases much more deeply and is larger than that experimentally observed. The discrepancy between theoretical simulation and experimental observation can be ascribed to the limitation of Gouy-Chapman model and the complexity of the present system. The diffuse layer capacitance is only dominant at low concentrations near the potential of zero charge, whereas, at a potential far from the potential of zero charge the surface charge density is large and the contribution from the inner layer, called as the Helmholtz capacitance, has to be taken into account.<sup>34</sup> On the other hand, the gold NPs were considered as point charges in the simulations. In fact, the size of gold NPs is larger than a conventional ion. Moreover, the interactions between charged NPs were also neglected, which should affect the surface coverage of gold NPs at the interface. The gold NPs in the surface assembly are expected to feel the coulombic repulsive interaction between NPs due to the existence of a surrounding electric double layer, as well as the classical van der Waal's attractive interaction.<sup>35</sup> The counterbalance of these two interactions determines the interparticle energies, which is a key parameter in the colloidal chemistry.<sup>36, 37</sup> If taking these interactions into account and using the Frumkin isotherm, better agreement between simulation and experiment may be obtained, as we have discussed in Chapter 3. Based on these points, the above simulations should

---

be considered from a qualitative point of view. It is obvious that the assembly of charged gold NPs at the interface has a strong effect on its electrical structure.

## 4.6 Conclusions

We have provided evidences that reversible assembly of mercaptosuccinic acids stabilized gold NPs of  $1.5 \pm 0.4$  nm in diameter can be onset at the water|1, 2-dichloroethane interface upon applying a potential bias. Cyclic voltammograms, admittance measurements and quasi-elastic laser scattering (QELS) studies reveal that the surface concentration of the gold NPs at the liquid|liquid boundary is reversibly controlled by the applied bias potential. The electrochemical and optical measurements provide no evidence of irreversible aggregation or deposition of the gold NPs at the interface. Analysis of the electrocapillary curves constructed from the dependence of the frequency of the capillary waves on the applied potential and bulk particle concentration indicated that the maximum particle surface density is  $3.8 \times 10^{13} \text{ cm}^{-2}$ , which corresponds to 67% of a square closed-pack arrangement.

The voltage-induced assembly of NPs at the liquid|liquid interface has also been theoretically considered using the Langmuir adsorption model exemplified in Chapter 3. Although the theoretical prediction does not coincide well with the experimental observation due to the complexity of present system, it is clearly demonstrated that the assembly of charged gold NPs at the interface strongly affects the interfacial structure.

The voltage-induced assembly of NPs at a liquid|liquid interface has a unique advantage in that the number of particles at the interface can be effectively controlled by tuning the Galvani potential difference. In conjunction with surface spectroscopic techniques, this method allows studying single vs. collective properties of metal and semiconductor NPs.



## 4.7 References

- (1) Gudiksen, M. S.; Lauhon, U. J.; Wang, J.; Smith, D. C.; Lieber, C. M. *Nature* **2002**, *415*, 617.
- (2) Kovtyukhova, N. I.; Mallouk, T. E. *Chem. A Euro. J* **2002**, *8*, 4354.
- (3) Maruyama, N.; Koito, T.; Nishida, J.; Sawadaishi, T.; Cieren, X.; Ijiro, K.; Karthaus, O.; Shimomura, M. *Thin Solid Films* **1998**, *327-329*, 854.
- (4) Grabar, K. C.; Freeman, R. G.; Hommer, M. B.; Natan, M. J. *Anal. Chem.* **1995**, *67*, 735.
- (5) Grabar, K. C.; Allison, K. J.; Baker, B. E.; Bright, R. M.; Brown, K. R.; Freeman, R. G.; Fox, A. P.; Keating, C. D.; Musick, M. D.; Natan, M. J. *Langmuir* **1996**, *12*, 2353.
- (6) Grabar, K. C.; Smith, P. C.; Musick, M. D.; Davis, J. A.; Walter, D. G.; Jackson, M. A.; Guthrie, A. P.; Natan, M. J. *J. Am. Chem. Soc.* **1996**, *118*, 1148.
- (7) Baum, T.; Bethell, D.; Brust, M.; Schiffrin, D. J. *Langmuir* **1999**, *15*, 866.
- (8) Chen, S. *J. Phys. Chem. B* **2000**, *104*, 663.
- (9) Hicks, J. F.; Zamborini, F. P.; Murray, R. W. *J. Phys. Chem. B* **2002**, *106*, 7751.
- (10) Kotov, N. A.; Dekany, I.; Fendler, J. H. *J. Phys. Chem.* **1995**, *99*, 13065.
- (11) Bakkers, E. P. A. M.; Vanmaekelbergh, D. *Phys. Rev. B* **2000**, *62*, R7743.
- (12) Bakkers, E. P. A. M.; Marsman, A. W.; Jenneskens, L. W.; Vanmaekelbergh, D. *Angew. Chem. Int. Ed.* **2000**, *39*, 2297.
- (13) Bakkers, E. P. A. M.; Roest, A. L.; Marsman, A. W.; Jenneskens, L. W.; De Jong-Van Steensel, L. I.; Kelly, J. J.; Vanmaekelbergh, D. *J. Phys. Chem. B* **2000**, *104*, 7266.
- (14) Liu, Y.; Wang, Y.; Claus, R. O. *Chem. Phys. Lett.* **1998**, *298*, 315.
- (15) Kakkassery, J. J.; Abid, J.-P.; Carrara, M.; Fermin, D. J. *Faraday Discuss.* **2003**, *125*, 157.
- (16) Lin, Y.; Skaff, H.; Emrick, T.; Dinsmore, A. D.; Russell, T. P. *Science* **2003**, *299*, 226.
- (17) Nikolaidis, M. G.; Bausch, A. R.; Hsu, M. F.; Dinsmore, A. D.; Brenner, M. P.; Gay, C.; Weitz, D. A. *Nature* **2002**, *420*, 299.
- (18) Binder, W. H. *Angew. Chem. Int. Ed.* **2005**, *44*, 5172.

- 
- (19) Reincke, F.; Hickey, S. G.; Kegel, W. K.; Vanmaekelbergh, D. *Angew. Chem. Int. Ed.* **2004**, *43*, 458.
- (20) Duan, H.; Wang, D.; Kurth, D. G.; Moehwald, H. *Angew. Chem. Int. Ed.* **2004**, *43*, 5639.
- (21) Kralchevsky, P. A.; Ivanov, I. B.; Ananthapadmanabhan, K. P.; Lips, A. *Langmuir* **2005**, *21*, 50.
- (22) Aveyard, R.; Binks, B. P.; Clint, J. H. *Advances in Colloid and Interface Science* **2003**, *100-102*, 503.
- (23) Fermin, D. J.; Jensen, H.; Girault, H. H. *Encyclopedia of Electrochemistry* **2003**, *2*, 360.
- (24) Fermin, D. J.; Lahtinen, R. *Surfactant Science Series* **2001**, *95*, 179.
- (25) Kakiuchi, T. *Surfactant Science Series* **2001**, *95*, 105.
- (26) Jensen, H.; Fermin, D. J.; Moser, J. E.; Girault, H. H. *J. Phys. Chem. B* **2002**, *106*, 10908.
- (27) Fermin, D. J.; Jensen, H.; Moser, J. E.; Girault, H. H. *ChemPhysChem* **2003**, *4*, 85.
- (28) Nagatani, H.; Samec, Z.; Brevet, P.-F.; Fermin, D. J.; Girault, H. H. *J. Phys. Chem. B* **2003**, *107*, 786.
- (29) Cheney, G. E.; Fernando, Q.; Freiser, H. *J. Phys. Chem.* **1959**, *63*, 2055.
- (30) Kimura, K.; Takashima, S.; Ohshima, H. *J. Phys. Chem. B* **2002**, *106*, 7260.
- (31) Chen, S.; Kimura, K. *Langmuir* **1999**, *15*, 1075.
- (32) Templeton, A. C.; Cliffler, D. E.; Murray, R. W. *J. Am. Chem. Soc.* **1999**, *121*, 7081.
- (33) Higgins, D. A.; Corn, R. M. *Journal of Physical Chemistry* **1993**, *97*, 489.
- (34) Girault, H. H. *Analytical and Physical Electrochemistry*; EPFL Press: Lausanne, 2004.
- (35) Mulvaney, P. In *Nanoscale Materials in Chemistry*, 2001, pp 121.
- (36) Hunter, R. J. *Foundations of Colloid Science, Vol. I*, 1986.
- (37) Israelachvili, J. N. *Intermolecular and Surface Forces*, 1991.

## Chapter 5

### Assembly and photoreactivity of CdSe NPs at liquid|liquid interfaces

#### 5.1 Introduction

Photoinduced heterogeneous electron transfer reactions at the liquid|liquid interface have proved to be a valuable approach to artificial photosynthetic and photocatalytic processes.<sup>1-3</sup> At this molecular junction, photocurrent responses originating from the heterogeneous quenching of photoexcited water-soluble dyes by hydrophobic redox species have been studied in detail.<sup>4-12</sup> It has been observed that the Galvani potential difference across the liquid|liquid interface can affect the surface coverage of the photoactive species as well as the dynamics of photoinduced electron transfer and back electron transfer. Water-soluble porphyrins, chlorines and phthalocyanines have been employed as photo-active dyes at the interface between water and 1, 2-dichloroethane (DCE).<sup>5, 7-13</sup> Recently, it has been demonstrated that titanium dioxide (TiO<sub>2</sub>) NPs can be assembled at the polarized interface between water and DCE electrolyte solutions upon

applying a potential bias.<sup>13, 14</sup> Illumination of the interface led to the interfacial transfer of holes or electrons to redox species located in the organic phase. The charge transfer reactions can be monitored by photocurrent measurements phenomenologically similar to those observed on solid photoelectrodes.<sup>15-17</sup>

Semiconductor quantum dots have all three dimensions in the nanometer range and possess unique electronic and optical properties that are strongly size dependent.<sup>18, 19</sup> Not only are they interesting from a theoretical viewpoint, but a variety of applications have also been considered. For example, luminescent semiconductor quantum dots are a promising alternative to organic dyes for fluorescence applications since they are more stable against photobleaching and have a narrow and size-tunable multicolor emission as well as functional advantages.<sup>20, 21</sup> Some of the most exciting applications involve new generation of opto-electronic<sup>22-25</sup> and photovoltaic devices<sup>26</sup> and exploratory biotechnology research using quantum dots as ultra-sensitive biological fluorescent tags.<sup>21, 27-30</sup>

In the present chapter, we shall describe the reversible adsorption of mercaptosuccinic acid (MSA) stabilized CdSe NPs at the water|DCE interface. In the presence of electron acceptors in the organic phase, heterogeneous photocurrent responses arising from the adsorbed CdSe NPs can be recorded upon illumination of the interfacial region. Analysis of the photocurrent responses as a function of the applied potential difference and the formal redox potential of the organic phase quencher suggests that the heterogeneous electron transfer takes place from occupied trap states in the CdSe NPs. However, no photocurrents were observed in the presence of electron donors in the organic phase, indicating that the holes are swiftly removed by fast reactions in the aqueous phase. This situation can be compared to the photoelectrochemical behavior of citrate anion stabilized CdSe NPs at the water|DCE interface. In this case, photocurrent responses were observed in the presence of electron donors or electron acceptors, indicating that both photoexcited electrons and holes are available for heterogeneous electron transfer reactions. These results suggest that the surface has significant influence on the optical and electronic properties of NPs.

## 5.2 MSA-protected CdSe NPs

### 5.2.1 Spectroscopic characterization of CdSe NPs

The synthesis of MSA protected CdSe NPs is described in Chapter 2. For thiol-stabilized CdSe NPs prepared at a low temperature, the cubic zinc blende phase is preferentially obtained.<sup>31</sup> Figure 5.1 demonstrates the absorption and photoluminescence (PL) spectra of the CdSe NP suspension that was used in the following experiments. An exciton peak is clearly observed at 520 nm in the absorption spectrum, which is indicative of a narrow size distribution of CdSe NPs in the sample. If the size distribution is broad, there would be a number of exciton peaks appearing at different energies corresponding to different sized NPs and overlapping with each other and hence on sharp excitonic peaks will be observed in the absorption spectrum, but only a broad and featureless absorption edge. However, the sample exhibits a broad PL band significantly red-shifted with respect to the exciton peak. The size distribution, even it is narrow, maybe account for slightly to the spectral broadening. However, the main features of the PL band reveal a wide distribution of energy states that spread in the band gap acting as trap sites. The luminescence efficiency for these NPs is below 0.1%, indicating that the relaxation processes are dominated by “non-radiative” recombination at trap levels.<sup>31, 32</sup> This type of optical behavior has been extensively observed for thiol-stabilized CdSe NPs.<sup>31-35</sup>

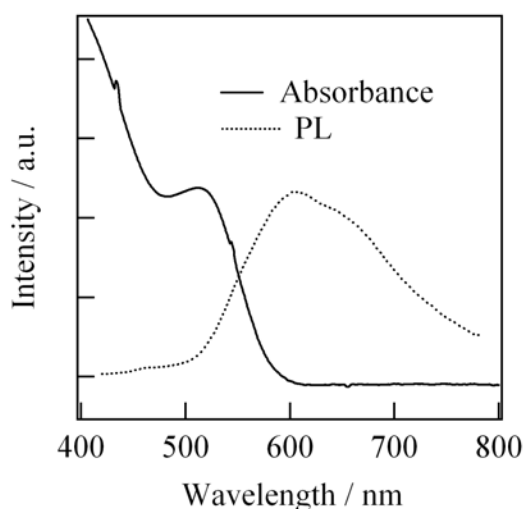


**Figure 5.1** The UV-vis spectrum (solid) and photoluminescence spectrum upon excitation at 400 nm (dashed) of MSA protected CdSe NPs.

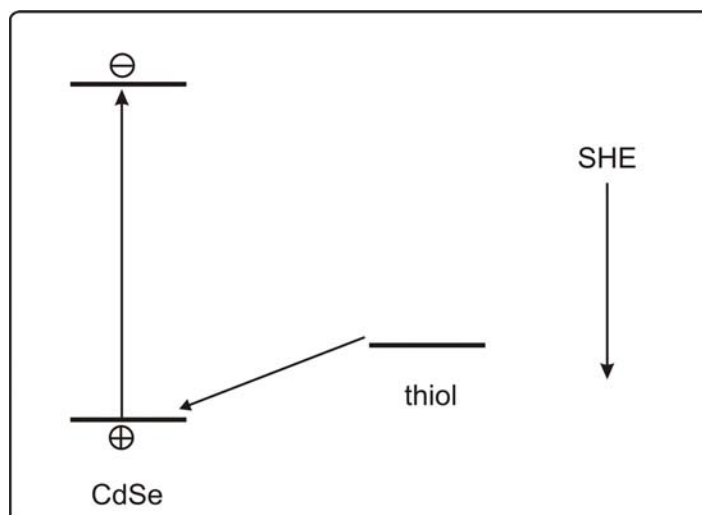


**Figure 5.2** Schematic representation of positions of CdSe band edges with respect to the redox energy level of a thiol.

An explanation for the quenched luminescence can be found in Figure 5.2. Since the energetic position of the valence band edge of a CdSe NP is lower than the redox energy level of a thiol, hole trapping from the photoexcited CdSe NP on the thiol is energetically favorable. This process is probably a photocatalysis reaction, which reduces the thiols into disulfides on the CdSe NP surface. The first step of this process involves trapping of the photogenerated hole on a thiol molecule, resulting in the generation of a thyl radical. Two thyl radicals can then be converted into a disulfide.<sup>36</sup> As reported previously, this process is very efficient observed not only for CdSe electrode<sup>37</sup> but also CdSe NPs.<sup>38, 39</sup> On the other hand, for radiative recombination both the hole and electron are needed. If the hole is trapped on a thiol molecule, the radiative recombination of the exciton is hindered and therefore decreases remarkably the quantum yield of the fluorescence.

### 5.2.2 Absorption cross-section

For optical transitions far from the strong resonance and far from the band edge, the absorption cross section of a semiconducting NP can be calculated according to eq 1.65, as introduced in Section 1.2.3 of Chapter 1. Since the imaginary part of the complex refractive index of the water medium,  $k_2$ , is very small and negligible,  $m_2$  simply can be considered equal to  $n_2=1.33$ . The complex refractive index of the bulk CdSe are  $n_1 = 2.7$

and  $k_1 = 0.7^{40}$ , respectively. Therefore, the absorption cross-section of a 2.8 nm (in diameter) CdSe particle is estimated to be about  $1.05 \times 10^{-15} \text{ cm}^2$  at 454 nm, at which the photocurrent measurements involving CdSe NPs shall be measured.

### 5.2.3 Estimation of the band edge energies

After absorption of a photon with the energy larger than the band gap, an electron-hole pair is generated in the semiconductor particle. The redox photoreactivity of the semiconductor particles is determined by the position of the quasi-Fermi level of the electrons ( ${}_n\mathcal{E}_f^*$ ) and holes ( ${}_h\mathcal{E}_f^*$ ). For single crystalline materials,  ${}_n\mathcal{E}_f^*$  lies very close to the conduction band edge which in the case of CdSe is associated with a redox potential ( $E_{\text{CB}}$ ) of -0.20 V vs SHE.<sup>41</sup> However,  $E_{\text{CB}}$  can be substantially shifted to more negative potentials in nanometer-sized particles. This shift can be estimated following the calculation reported by Burda et al:<sup>41</sup>

$$E_{\text{CB}} = E_{\text{CB}}^{\text{b}} - (E_{\text{g}} - E_{\text{g}}^{\text{b}}) \times \frac{m_{\text{e}}^*}{m_{\text{e}}^* + m_{\text{h}}^*} \quad (5.1)$$

where  $E_{\text{CB}}^{\text{b}}$  is the redox potential of the band edge of bulk CdSe ( $E_{\text{CB}}^{\text{b}} = -0.2 \text{ V}$ ).  $E_{\text{g}}$  and  $E_{\text{g}}^{\text{b}}$  are the band gap energies of CdSe NPs and bulk CdSe, respectively.  $m_{\text{e}}^*$  and  $m_{\text{h}}^*$  are the effective masses of electron and hole, respectively. Taking the effective masses of electrons and holes as 0.11 and 0.44,<sup>31</sup> and  $E_{\text{g}} = 2.50 \text{ eV}$ <sup>31</sup> as estimated from the absorption spectra for 2.8 nm CdSe NPs,  $E_{\text{CB}}$  can be estimated as -0.84 V. Furthermore, the redox potential of holes in the valence band edge ( $E_{\text{VB}}$ ) can be calculated to be 1.66 V. It should be mentioned that the estimated values of  $E_{\text{CB}}$  and  $E_{\text{VB}}$  do not necessarily reflect the real energetic levels of populated electrons and holes. Indeed, as shown in Figure 5.1, there is possibly a wide distribution of defect sites that can capture electrons or holes in the mid-band gap region. Furthermore, the effect of the capping ligands, which of course influence the electronic properties of CdSe NPs,<sup>42</sup> was not taken into account either.

### 5.2.4 Voltage induced assembly at the water|DCE interface

Figure 5.3 displays the electrochemical cell employed for studying the assembly and photoreactivity of MSA protected CdSe NPs at the water|DCE interface. The CdSe NPs are dispersed in the aqueous phase at various concentrations.



**Figure 5.3** Schematic composition of the electrochemical cell.

The MSA stabilizes the CdSe NPs with the thiol group binding at the surface of the particle and leaving the carboxylic groups outside. As a result, the CdSe NPs have high density of negative charges on the surface and are highly water dispersible. Cyclic voltammograms of the water|DCE interface for various concentrations of the CdSe NPs in the aqueous phase are illustrated in Figure 5.4a. The broad peak observed at negative Galvani potential differences is dependent on the concentration of CdSe NPs and varies linearly with the scan rate, suggesting that it is associated with the adsorption of CdSe NPs at the interfacial boundary.

The adsorption of CdSe NPs at the water|DCE interface is further confirmed by differential capacitance ( $C_{dl}$ ) measurements, as displayed in Figure 5.4b. The differential capacitance data were extracted from admittance measurements at a frequency of 6 Hz and amplitude of 10 mV rms. It can be observed that the excess charge at the interfacial boundary increases at negative biases and with increasing concentration of CdSe NPs. At positive potentials, the excess charge in the presence and absence of the NPs is identical. Furthermore, the dependence of  $C_{dl}$  on the Galvani potential difference remains unaffected upon potential cycling, confirming that no irreversible aggregation or phase formation takes place at the liquid|liquid interface. All these facts indicate that the adsorption of CdSe NPs is not only voltage induced but also reversibly controlled.



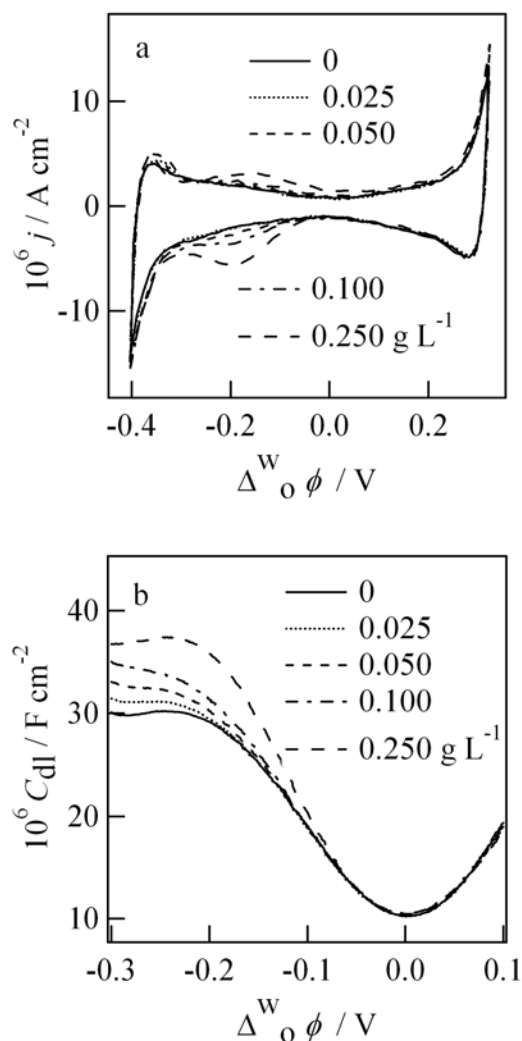


**Figure 5.4** CVs at scan rates of  $50 \text{ mV s}^{-1}$  (a) and differential capacitance curves (b) for various concentrations of CdSe NPs.

On the other hand, Figure 5.4b clearly illustrates that the minimum of the differential capacitance curves does not shift significantly in the presence of CdSe NPs in the aqueous phase. This indicates that the CdSe NPs have a smaller Gibbs energy of absorption according to the theoretical simulations in Chapter 4 for the adsorption of Au NPs at the water|DCE interface. However, if taking the thickness of MSA protecting layer ( $\sim 0.6 \text{ nm}$ ) into account, the size of CdSe NPs is about  $4 \text{ nm}$  in diameter, which is comparable to the Debye length at the aqueous side of the interface ( $5 \text{ nm}$ ). Therefore, the theoretical simulations illustrated in Chapter 3 should be considered with caution to analyze the absorption of CdSe NPs at the liquid|liquid interface.

### 5.2.5 Photoinduced electron transfer

We demonstrated above that CdSe NPs can be adsorbed at the water|DCE interface. On a thermodynamic ground, in the presence of redox quenchers in the organic phase, photoexcitation of the adsorbed CdSe NPs can lead to heterogeneous charge when the energy level of the redox quencher is lower than the energy level of the electron or higher than the energy level of the hole. This behavior has been observed for TiO<sub>2</sub> NPs assembled at the water|DCE interface.<sup>14</sup>

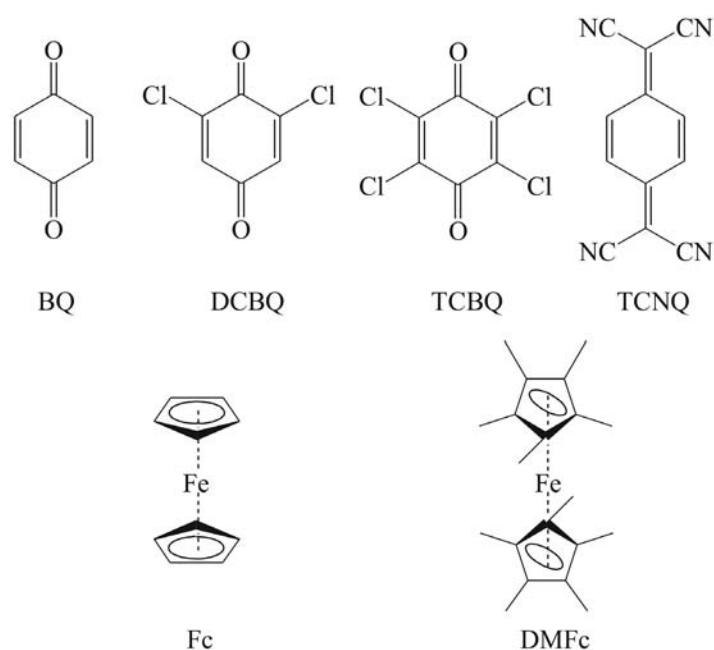


**Figure 5.5** Molecular structures of various redox quenchers.

**Table 5.1** The Formal Redox Potentials of Various Redox Species in bulk DCE.<sup>4,6</sup>

Redox couple	$E^{0'}$ , V (vs. SHE)
7,7',8,8'-tetracyanoquinodimethane (TCNQ/TCNQ <sup>-</sup> )	0.29 V
2,3,5,6-tetrachloro-1,4-benzoquinone (TCBQ/TCBQ <sup>-</sup> )	0.17 V
2,6-dichloro-1,4-benzoquinone (DCBQ/DCBQ <sup>-</sup> )	-0.02 V
benzoquinone (BQ/BQ <sup>-</sup> )	-0.34 V
ferrocene (Fc <sup>+</sup> /Fc)	0.64 V
decamethylferrocene (DMFc <sup>+</sup> /DMFc)	0.02 V

Several redox quenchers are studied, including quinones and ferrocene derivatives. Their molecular structures are schematically illustrated in Figure 5.5, and their formal redox potentials<sup>4,6</sup> versus standard hydrogen electrode (SHE) are summarized in Table 5.1.

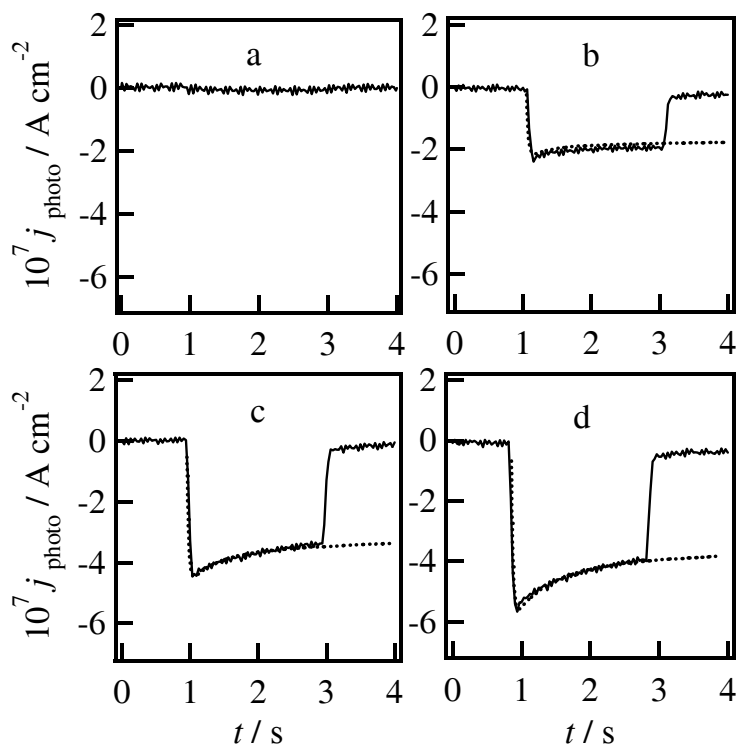


**Figure 5.6** Photocurrent transients arising from the photoinduced electron transfer from CdSe NPs to TCNQ at various potential differences: (a)  $-0.07$ , (b)  $-0.12$ , (c)  $-0.17$ , and (d)  $-0.22$  V. The dotted curves in (b), (c), and (d) are simulations with the parameters  $I_0 = 1.10 \times 10^{17} \text{ cm}^{-2} \text{ s}^{-1}$ ,  $D_Q^0 = 1.05 \times 10^{-5} \text{ cm}^2 \text{ s}^{-1}$  and  $RC_{dl} = 0.025 \text{ s}^{-1}$ . The fits provide values of  $g$  of  $2.30 \times 10^{-12}$ ,  $4.80 \times 10^{-12}$  and  $6.30 \times 10^{-12} \text{ mol cm}^{-2} \text{ s}^{-1}$  at  $-0.12$ ,  $-0.17$  and  $-0.22$  V respectively. Typical values obtained for  $k_b$  was  $0.40 \text{ s}^{-1}$  at these three potentials while  $k_{ps}$  were  $2.60$ ,  $2.00$ , and  $1.25 \text{ s}^{-1}$ , respectively.

Photoinduced heterogeneous electron transfer processes involving CdSe NPs and redox species in the organic phase were investigated under potentiostatic conditions. The photocurrent transient responses at various Galvani potential differences in the presence of the electron acceptor 7,7',8,8'-tetracyanoquinodimethane (TCNQ) in DCE are illustrated in Figure 5.6. The negative photocurrent indicates the transfer of a negative charge from the aqueous to the organic phase. Similarly to the behavior observed at dye-sensitized water|DCE interfaces, no significant photoresponses are observed in the absence of CdSe NPs or TCNQ. Taking into account the difference in redox potential between the electrons in the conduction band edge and TCNQ, it would be expected that

photoinduced electron transfer occurs over the whole potential range. However, the photocurrent magnitude in Figure 5.6 shows a strong dependence on the Galvani potential difference. This potential dependence of the photocurrent can be rationalized in terms of (i) changes in the particle density in the interfacial region and (ii) changes in the driving force for the heterogeneous electron transfer. A comparison between the potential dependence of the photocurrent and capacitance values in the presence of TCNQ suggests that voltage induced changes in the particle coverage do affect the photocurrent conversion efficiency. Indeed, the onset of the photocurrent responses is close to 0 V, which coincides with the onset potential for the adsorption of CdSe NPs at the interface.

It has to be mentioned that the observed photoinduced electron transfer stems from a heterogeneous photooxidation process, perhaps leading to the corrosion of CdSe NPs that has been previously reported to occur in aqueous solutions with photoexcited electrons removed by electron acceptors and surface selenium anion oxidized by the remaining holes.<sup>43</sup> Certainly, this can also occur homogeneously, for example, with dissolved O<sub>2</sub>.<sup>44</sup> However, this homogeneous process does not involve any charge transfer across the liquid|liquid interface and therefore not contribute to the observed photocurrent.

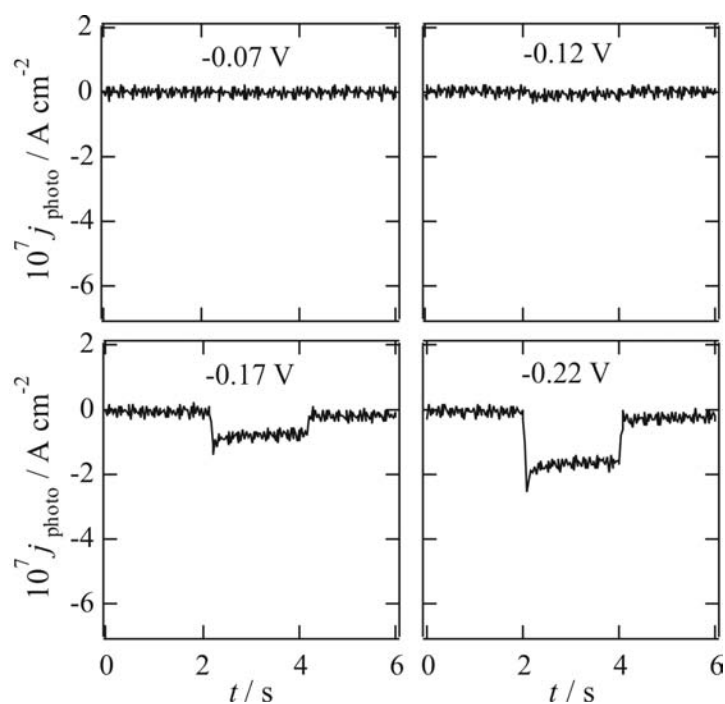


**Figure 5.7** Photocurrent transients arising from the photoinduced electron transfer from CdSe NPs to TCNQ at various Galvani potential differences.

The photocurrent transient responses in the presence of 2,3,5,6-tetrachloro-1,4-benzoquinone (TCBQ) and 2,6-dichloro-1,4-benzoquinone (DCBQ) in the organic phase are displayed in Figures 5.7 and 5.8, respectively. Similarly to the case of TCNQ, the photocurrent transient in the presence of TCBQ as redox quenchers is observed only at potentials more negative than  $-0.1$  V. However, in the case of DCBQ, the photocurrent signal is significant only at potentials more negative than  $-0.3$  V, i.e. at the edge of the polarizable window. This change in the photocurrent onset corresponds to the difference in redox potential between the two quenchers. In addition, no photocurrent responses were observed in the presence of benzoquinone (BQ), which has a formal redox potential of  $-0.34$  V versus SHE in bulk DCE. These results clearly show that the photocurrent magnitude decreases as the redox potential of the acceptor is more negative, indicating the dependence of the photocurrent on the redox potential of the electron acceptor.

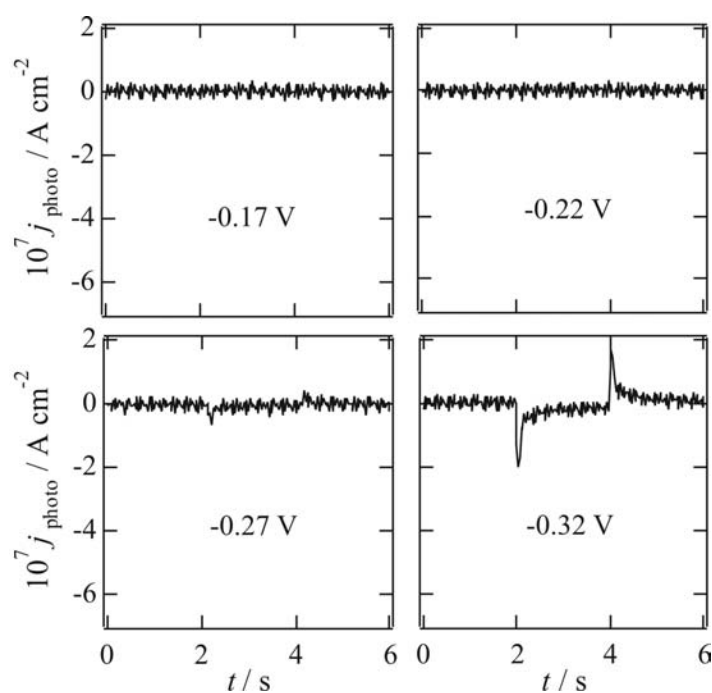


**Figure 5.8** Photocurrent transients arising from the photoinduced electron transfer from CdSe NPs to DCBQ at various Galvani potential differences.

The dependence of the photocurrent on the redox potential of the electron acceptor can be clearly seen by comparing the photocurrent transient responses in the presence of TCNQ, TCBQ and DCBQ at the same Galvani potential difference, as shown in Figure 5.9. The dependence of the photocurrent on the redox potential of the electron acceptor indicates that the photoinduced electron transfer reaction is kinetically controlled.

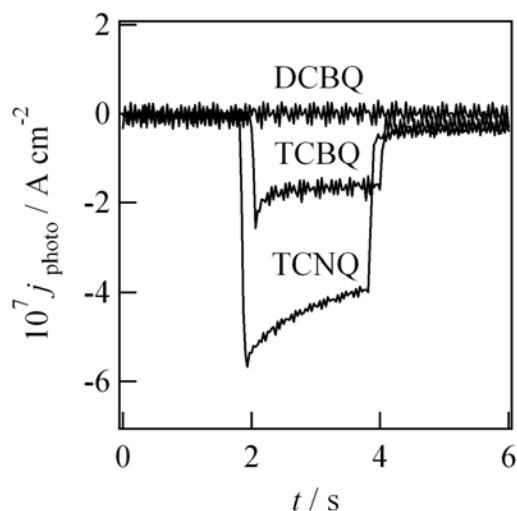


**Figure 5.9** Photocurrent transients at  $-0.22$  V in the presence of various electron acceptors. The concentration of the nanoparticles and electron acceptor were  $0.25$  g  $L^{-1}$  and  $1 \times 10^{-3}$  M, respectively. The incident photon flux was  $1.10 \times 10^{17}$   $cm^{-2} s^{-1}$ .

A strategy to uncouple the potential dependences of the particle interfacial density and electron transfer rate involves the study of the photocurrent responses associated with the transfer of photogenerated holes. For instance, the redox potentials of ferrocene (Fc) and decamethylferrocene (DMFc) are  $0.64$  V and  $0.02$  V vs. SHE, respectively, which are well above the valence band of the CdSe NP. This should enable them to act as effective scavengers for photogenerated holes. However, no photocurrents were observed in the presence of electron donors in DCE over the whole potential range. These results indicate that the photogenerated holes are swiftly captured by fast homogeneous processes. One possibility is the one that is illustrated in Figure 5.2.

### 5.2.6 Dynamic aspects of the photoinduced responses

Based on the discussion in last section, the photoreactivity of CdSe NPs at the water|DCE interface can be schematically described as that in Figure 5.10. The photoexcitation generates electrons and holes in the conduction and valence bands, respectively. However, the fast homogeneous hole quenching process hampers the direct recombination of photogenerated electron and hole, which may result in a long-lived electron in the CB or populated electron trap states. It is well known in literatures that trap charge carriers in localized surface states can exhibit remarkably slow depopulation

time constants ( $> 1$  ms).<sup>45</sup> The results displayed in Figures 5.6, 5.7, 5.8 and 5.9 also clearly show that photoinduced heterogeneous electron transfer only occurs to redox species featuring potential significantly more positive than  $E_{CB}$ . Further considering that the electron transfer reaction across the water|DCE interface most probably takes place in the microsecond time scale due to the weak electronic coupling between donors and acceptors,<sup>4</sup> we suggest that the electron injection occurs via deep trap states at the particle surface. The dynamics of population/depopulation of trap states are beyond the scope of this paper. In the subsequent discussion, we shall describe the overall relaxation of photogenerated electrons by a phenomenological rate constant  $k_d$  ( $s^{-1}$ ). This parameter represents the electron trapping rate constant integrated over the energy range of depopulated states in the band gap.

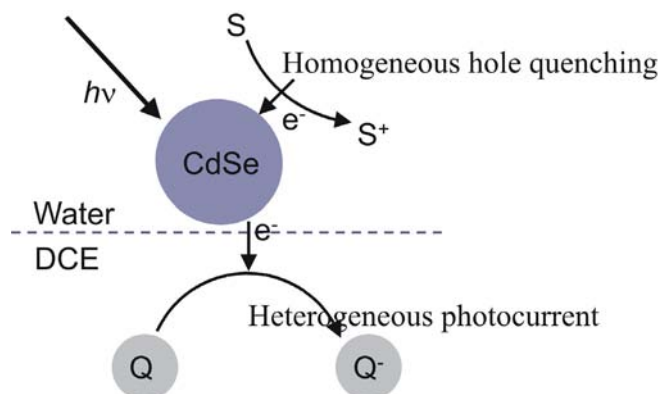


**Figure 5.10** Schematic illustration of photoreactivity of CdSe NPs at the water|DCE interface.

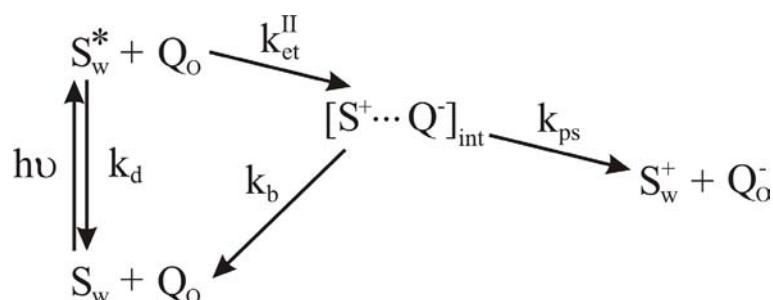


**Figure 5.11** Scheme of heterogeneous photoinduced electron transfer reaction between a photoactive electron acceptor in water ( $S_w$ ) and an electron donor in organic phase ( $Q_o$ ).  $h\nu$  represents the photoexcitation process.  $k_d$  is the rate constant associated with the decay of the excited state,  $k_{et}^{II}$  is the bimolecular rate constant of electron transfer,  $k_b$  and  $k_{ps}$  are associated with back electron transfer and product separation steps.

Previous models developed for dye-sensitized liquid|liquid interfaces describe the photocurrent responses as a result of a series of competing reactions,<sup>4, 6, 8, 9</sup> as illustrated in Figure 5.11. The first competition upon illumination involves the relaxation of the photogenerated electron ( $k_d$ ) and the photoinduced heterogeneous electron transfer ( $k_{et}$ ). The electron transfer process is followed by the competition between the back electron transfer reaction ( $k_b$ ) regenerating the initial reactants and the product separation process ( $k_{ps}$ ) leading to the final products in their respective electrolyte phases.

We shall apply this model to extract kinetic information on heterogeneous electron transfer from CdSe NPs to quinone species at the water|DCE interface. Assuming that the interfacial concentration of the particles is time independent, the photocurrent responses can be expressed in the Laplace plane as:<sup>46</sup>

$$\overline{\Delta j_{ph}} = \frac{Fg}{1 + sRC_{dl}} \frac{k_{ps} + s}{(s + k_b + k_{ps}) + (s + k_{ps})\lambda_{et}s^{\frac{1}{2}}} \quad (5.2)$$

where

$$g = \frac{k_{et}^{II} c_Q^0}{k_{et}^{II} c_Q^0 + k_d} \sigma I_0 \Gamma \quad (5.3)$$

$$\lambda_{et} = \frac{g}{(D_Q^0)^{\frac{1}{2}} c_Q^0} \quad (5.4)$$

$k_{et}^{II}$  is the second order rate constant with respect to the populated density states in the particle and unoccupied density states in the redox species,  $c_Q^0$  is the initial concentration of electron acceptors,  $I_0$  is the photon flux and  $\Gamma$  the interfacial concentration of particle at the liquid|liquid boundary. The second term in eq 5.2 not only describes the competition between product separation and back electron transfer, but also the diffusion of the acceptor to the interface upon continuous illumination (represented by the diffusion coefficient  $D_Q^0$ ). The parameter  $RC_{dl}$  relates to the attenuation of the photoresponses at short time determined by the uncompensated resistance  $R$  and the double layer capacitance  $C_{dl}$ .



The dotted lines in Figure 5.6 correspond to numerical solutions of eqs 5.2, 5.3 and 5.4 employing  $g$ ,  $k_b$  and  $k_{ps}$  as adjustable parameters.  $D_Q^0$  was set to  $1.05 \times 10^{-5} \text{ cm}^2 \text{ s}^{-1}$  according to previous reports,<sup>47, 48</sup> and  $RC_{dl}$  was estimated as  $0.025 \text{ s}^{-1}$  from the admittance measurements. The rising portion of the photocurrent are determined by the  $RC_{dl}$  component, while the response decay is sensitive to  $D_Q^0$  and the rate constants  $k_b$  and  $k_{ps}$ . On the other hand, the initial magnitude of the photocurrent is determined by the parameter  $g$  (eq 5.3). As illustrated in Figure 5.6, consistent fits were obtained for values of  $g$  of  $2.30 \times 10^{-12} \text{ mol cm}^{-2} \text{ s}^{-1}$  at  $-0.12 \text{ V}$ ,  $4.80 \times 10^{-12} \text{ mol cm}^{-2} \text{ s}^{-1}$  at  $-0.17 \text{ V}$  and  $6.30 \times 10^{-12} \text{ mol cm}^{-2} \text{ s}^{-1}$  at  $-0.22 \text{ V}$ . As discussed in the previous section, the dependence of  $g$  on the Galvani potential difference is determined not only by changes in  $\Gamma$  but also in the rate of electron transfer  $k_{ct}^{\text{II}}$ . Independent analysis of the interfacial concentration of the particles as a function of the applied potential would be required to further rationalize these results. Taking into account the values obtained at  $-0.22 \text{ V}$  in the presence of TCNQ, the photocurrent conversion efficiency given by the ratio between  $g$  and the photon flux  $I_0$  can be estimated as  $0.35 \%$ .

The analysis of the photocurrent decay shows that the most important contribution arises from the diffusion of the electron acceptor to the interfacial region. However, at high photocurrent densities it appears that back electron transfer also contributes to the decay of the photocurrent. This behavior may arise from the fact that the model considers the back electron transfer as a first order reaction with respect to intermediate charge transfer complex formed after the heterogeneous electron transfer step.<sup>46</sup> Although this approximation is validated by experimental results in the case of porphyrin sensitized liquid|liquid interfaces, it may not be applicable to the CdSe system. However, the key result is that the photocurrent decay is mostly determined by the diffusion of the acceptor in the organic phase. In phenomenological terms, the photoelectrochemical responses resemble those observed for p-type semiconductor in the depletion potential range. Obviously, there is no such depletion layer in the CdSe NPs inducing the migration of majority carriers. In this case, the fast quenching of holes by species in the aqueous phase is the physical phenomena behind the depletion of holes at the liquid|liquid boundary.

## 5.3 Citrate protected CdSe NPs

### 5.3.1 Spectroscopic characterization

The synthesis of citrate protected CdSe NPs has been described in Chapter 2. The absorption and photoluminescence spectra of citrate protected CdSe NPs are compared in Figure 4.12. A well-defined 1s-1s electronic transition is observed in the absorption spectrum. The photoluminescence spectrum reveals an excitonic emission band that is very narrow in comparison to that of MSA protected CdSe NPs, where a broad photoluminescence band significantly red-shifted with respect to the exciton peak is observed. This indicates that the surface has a strong influence on the optical properties of NPs, although both types of CdSe particles produce a very weak luminescence efficiency of 0.1-0.15 %.

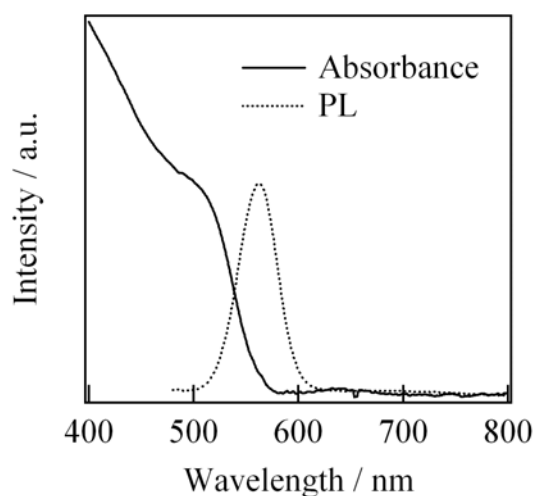


**Figure 5.12** The UV-vis spectrum (solid) and photoluminescence spectrum with excitation at 442 nm (dashed) of citrate protected CdSe NPs.

### 5.3.2 Photoreactivity at the water|DCE interface

The electrochemical cell displayed in Figure 5.13 was employed for studying the photoreactivity of citrate protected CdSe NPs at the water|DCE interface. The as-

prepared colloidal solution containing negatively charged CdSe NPs is used as the aqueous phase without purification. Because the CdSe NPs are stabilized by an electric double layer composed of citrate or other anions and cations attached to them, purification may change the ionic strength and result in irreversible precipitation or aggregation. According to the synthetic recipe, the as-prepared CdSe colloidal solution contains  $\text{Na}^+$ ,  $\text{ClO}_4^-$ , citrate anions, and unreacted  $\text{Cd}^{2+}$  and  $\text{Se}^{2-}$ . However, these ions are not expected to participate in photoinduced reactions within the potential range employed.



**Figure 5.13** Schematic composition of the electrochemical cell.

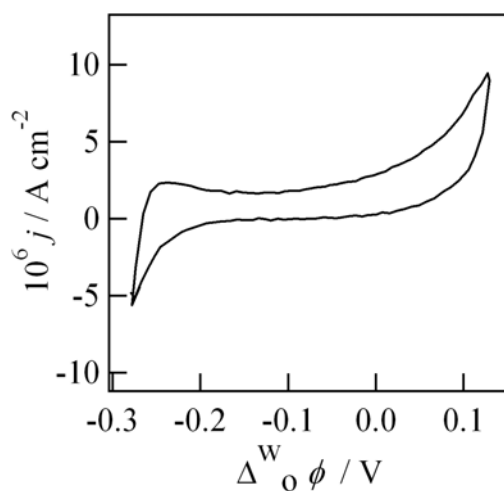


**Figure 4.14** CV at a scan rate of  $50 \text{ mV s}^{-1}$  in the absence (dotted line) and presence (solid line) of citrate protected CdSe NPs in the aqueous phase.

Figure 5.14 shows the corresponding CV. A smaller potential window of around 250 mV is observed, which is possibly limited by the transfer of ions present in the aqueous solution as above mentioned. The Galvani potential difference will be constrained in this potential window in the subsequent photocurrent measurements. Contrary to the case of MSA protected NPs, no adsorption of citrate stabilized CdSe NPs was observed in the negative potential range.

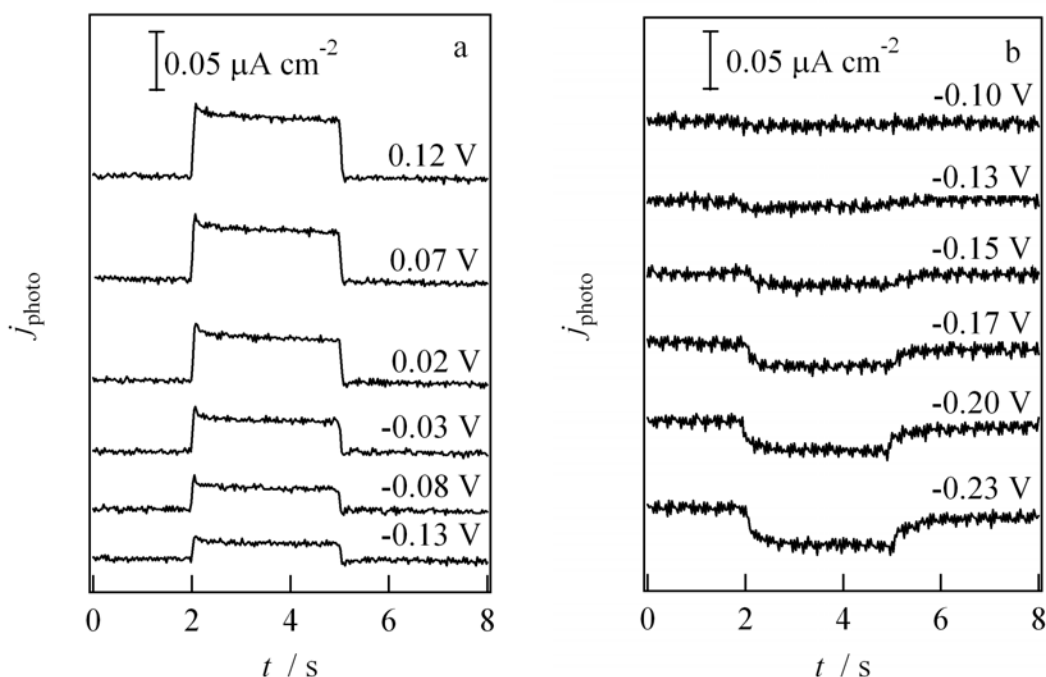


**Figure 5.15** Photocurrent transients arising from photoinduced charge transfer between CdSe NPs and DMFc (a) and TCNQ (b) at various  $\Delta\phi^{\text{w}}$ . The concentration of DMFc and TCNQ in DCE is 1 mM.

Photocurrent responses at various Galvani potential differences in the presence of DMFc or TCNQ in DCE are displayed in Figure 5.15a and 5.15b, respectively. Unlike the MSA protected CdSe NPs studied in the previous section, photocurrent can be observed in both directions. This behavior is similar to that of TiO<sub>2</sub> NPs at the water|DCE interface, where both photoexcited electrons and holes are available for heterogeneous electron transfer reactions. The photocurrent magnitude also shows a strong dependence on the Galvani potential difference, which may result from changes in the particle density in the interfacial region and changes in the driving force for the heterogeneous electron transfer. Since the photocurrent magnitude is small, we did not perform further studies. Nevertheless, the different photoelectrochemical behavior observed with MSA and citrate protected CdSe NPs suggests that the surface has significant influence on the optical and electronic properties of NPs, as well as the adsorption behavior. Since citrate stabilized CdSe NPs do not show affinity for the water|DCE interface, there are less CdSe NPs available at the interface upon illumination. This explains the small photocurrents observed with citrate CdSe NPs in comparison with that of MSA-stabilized CdSe NPs.

## 5.4 Conclusions

Water-soluble MSA protected CdSe NPs can be reversibly adsorbed at the water|DCE interface by tuning the Galvani potential difference. In the potential range where the NPs are adsorbed, band-gap illumination leads to heterogeneous electron transfer from CdSe NPs to electron scavengers located in the organic phase. However, no photocurrents were observed in the presence of electron donors, indicating that valence band holes are swiftly removed. These facts indicate that only photoexcited electrons are kinetically allowed to be transferred heterogeneously across the liquid|liquid interface. The photocurrent efficiency strongly depends on the applied Galvani potential difference and the formal redox potential of the electron acceptor. These results not only reflect the role of the Galvani potential difference on the number density of NPs at the interface, but also on the dynamics of heterogeneous electron transfer. It is concluded that trapped electrons are involved as intermediates in the heterogeneous photoreaction. Analysis of the photocurrent transients reveals that the initial photocurrent magnitude is determined by the competition between electron relaxation and heterogeneous electron transfer, while the photocurrent decay upon constant illumination is mostly determined by the diffusion of the acceptor to the interfacial region.

Unlike the behavior of MSA protected CdSe NPs, photocurrent responses can be observed in both directions with citrate protected CdSe NPs at the water|DCE interface. That is, both photoexcited electrons and holes are available for heterogeneous electron transfer reactions. This suggests that the surface has significant influence on the electronic properties of NPs. The surface also markedly affects the adsorption behavior of particles. The weaker affinity of citrate stabilized NPs for the water|DCE interface means that fewer particles are available for heterogeneous electron transfer upon illumination, which explains the smaller photocurrent observed in this case.

---

## 5.5 References

- (1) Reymond, F.; Fermin, D.; Lee, H. J.; Girault, H. H. *Electrochim. Acta* **2000**, *45*, 2647.
- (2) Fermin, D. J.; Lahtinen, R. *Surfactant Science Series* **2001**, *95*, 179.
- (3) Lahtinen, R.; Jensen, H.; Fermin, D. J. *Interfacial Catalysis* **2003**, 611.
- (4) Eugster, N.; Fermin, D. J.; Girault, H. H. *J. Phys. Chem. B* **2002**, *106*, 3428.
- (5) Eugster, N.; Jensen, H.; Fermin, D. J.; Girault, H. H. *J. Electroanal. Chem.* **2003**, *560*, 143.
- (6) Eugster, N.; Fermin, D. J.; Girault, H. H. *J. Am. Chem. Soc.* **2003**, *125*, 4862.
- (7) Fermin, D. J.; Ding, Z.; Duong, H. D.; Brevet, P.-F.; Girault, H. H. *J. Phys. Chem. B* **1998**, *102*, 10334.
- (8) Fermin, D. J.; Duong, H. D.; Ding, Z.; Brevet, P.-F.; Girault, H. H. *J. Am. Chem. Soc.* **1999**, *121*, 10203.
- (9) Fermin, D. J.; Dung Duong, H.; Ding, Z.; Brevet, P. F.; Girault, H. H. *Phys. Chem. Chem. Phys.* **1999**, *1*, 1461.
- (10) Fermin, D. J.; Duong, H. D.; Ding, Z.; Brevet, P. F.; Girault, H. H. *Electrochem. Comm.* **1999**, *1*, 29.
- (11) Jensen, H.; Kakkassery, J. J.; Nagatani, H.; Fermin, D. J.; Girault, H. H. *J. Am. Chem. Soc.* **2000**, *122*, 10943.
- (12) Jensen, H.; Fermin, D. J.; Girault, H. H. *Phys. Chem. Chem. Phys.* **2001**, *3*, 2503.
- (13) Fermin, D. J.; Jensen, H.; Moser, J. E.; Girault, H. H. *ChemPhysChem* **2003**, *4*, 85.
- (14) Jensen, H.; Fermin, D. J.; Moser, J. E.; Girault, H. H. *J. Phys. Chem. B* **2002**, *106*, 10908.
- (15) Bakkers, E. P. A. M.; Marsman, A. W.; Jenneskens, L. W.; Vanmaekelbergh, D. *Angew. Chem. Int. Ed.* **2000**, *39*, 2297.
- (16) Bakkers, E. P. A. M.; Roest, A. L.; Marsman, A. W.; Jenneskens, L. W.; De Jong-Van Steensel, L. I.; Kelly, J. J.; Vanmaekelbergh, D. *J. Phys. Chem. B* **2000**, *104*, 7266.
- (17) Miyake, M.; Torimoto, T.; Nishizawa, M.; Sakata, T.; Mori, H.; Yoneyama, H. *Langmuir* **1999**, *15*, 2714.
- (18) Alivisatos, A. P. *Science* **1996**, *271*, 933.

- (19) Nirmal, M.; Brus, L. *Acc. Chem. Res.* **1999**, *32*, 407.
- (20) Goldman, E. R.; Anderson, G. P.; Tran, P. T.; Mattoussi, H.; Charles, P. T.; Mauro, J. M. *Anal. Chem.* **2002**, *74*, 841.
- (21) Mattoussi, H.; Mauro, J. M.; Goldman, E. R.; Anderson, G. P.; Sundar, V. C.; Mikulec, F. V.; Bawendi, M. G. *J. Am. Chem. Soc.* **2000**, *122*, 12142.
- (22) Coe, S.; Woo, W.-K.; Bawendi, M.; Bulovic, V. *Nature* **2002**, *420*, 800.
- (23) Colvin, V. L.; Schlamp, M. C.; Alivisatos, A. P. *Nature* **1994**, *370*, 354.
- (24) Schlamp, M. C.; Peng, X.; Alivisatos, A. P. *J. Appl. Phys.* **1997**, *82*, 5837.
- (25) Wang, C.; Shim, M.; Guyot-Sionnest, P. *Science* **2001**, *291*, 2390.
- (26) Plass, R.; Pelet, S.; Krueger, J.; Graetzel, M.; Bach, U. *J. Phys. Chem. B* **2002**, *106*, 7578.
- (27) Bruchez, M., Jr.; Moronne, M.; Gin, P.; Weiss, S.; Alivisatos, A. P. *Science* **1998**, *281*, 2013.
- (28) Goldman, E. R.; Balighian, E. D.; Mattoussi, H.; Kuno, M. K.; Mauro, J. M.; Tran, P. T.; Anderson, G. P. *J. Am. Chem. Soc.* **2002**, *124*, 6378.
- (29) Chan, W. C.; Nie, S. *Science* **1998**, *281*, 2016.
- (30) Lingerfelt, B. M.; Mattoussi, H.; Goldman, E. R.; Mauro, J. M.; Anderson, G. P. *Anal. Chem.* **2003**, *75*, 4043.
- (31) Rogach, A. L.; Kornowski, A.; Gao, M.; Eychmueller, A.; Weller, H. *J. Phys. Chem. B* **1999**, *103*, 3065.
- (32) Gao, M.; Richter, B.; Kirstein, S.; Moehwald, H. *J. Phys. Chem. B* **1998**, *102*, 4096.
- (33) Talapin, D. V.; Rogach, A. L.; Mekis, I.; Haubold, S.; Kornowski, A.; Haase, M.; Weller, H. *Collod. Surf. A* **2002**, *202*, 145.
- (34) Gaponik, N.; Talapin, D. V.; Rogach, A. L.; Hoppe, K.; Shevchenko, E. V.; Kornowski, A.; Eychmueller, A.; Weller, H. *J. Phys. Chem. B* **2002**, *106*, 7177.
- (35) Wuister, S. F.; Swart, I.; van Driel, F.; Hickey, S. G.; Donega, C. d. M. *Nano Lett.* **2003**, *3*, 503.
- (36) Wuister, S. F.; De Donega, C.; Meijerink, A. *J. Phys. Chem. B* **2004**, *108*, 17393.
- (37) Natan, M. J.; Thackeray, J. W.; Wrighton, M. S. *J. Phys. Chem.* **1986**, *90*, 4089.
- (38) Aldana, J.; Wang, Y. A.; Peng, X. *J. Am. Chem. Soc.* **2001**, *123*, 8844.
- (39) Fischer, C. H.; Henglein, A. *J. Phys. Chem.* **1989**, *93*, 5578.
- (40) Palik, E. D. *Handbook of Optical Constants II*; Academic Press: Boston, 1991.

- (41) Burda, C.; Green, T. C.; Link, S.; El-Sayed, M. A. *J. Phys. Chem. B* **1999**, *103*, 1783.
- (42) Wuister, S. F.; De Donega, C.; Meijerink, A. *J. Phys. Chem. B* **2004**, *108*, 17393.
- (43) Henglein, A. *Top. Curr. Chem.* **1988**, *143*, 113.
- (44) Wang, Y.; Tang, Z.; Correa-Duarte, M. A.; Pastoriza-Santos, I.; Giersig, M.; Kotov, N. A.; Liz-Marzan, L. M. *J. Phys. Chem. B* **2004**, *108*, 15461.
- (45) Shim, M.; Shilov, S. V.; Braiman, M. S.; Guyot-Sionnest, P. *J. Phys. Chem. B* **2000**, *104*, 1494.
- (46) Samec, Z.; Eugster, N.; Fermin, D. J.; Girault, H. H. *J. Electroanal. Chem.* **2005**, *577*, 323.
- (47) Ding, Z.; Fermin, D. J.; Brevet, P.-F.; Girault, H. H. *J. Electroanal. Chem.* **1998**, *458*, 139.
- (48) Zhang, J.; Unwin, P. R. *Phys. Chem. Chem. Phys.* **2002**, *4*, 3814.



## Chapter 6

# Absolute standard redox potential of monolayer-protected gold nanoclusters

### 6.1 Introduction

Alkanethiolate stabilized gold NPs prepared using the Brust reaction,<sup>1, 2</sup> also called monolayer protected gold nanoclusters (MPCs), have received considerable interest owing to their unique electronic and chemical properties, notably the successive single electron transfer characteristics.<sup>3-6</sup> At ambient temperatures, both freely diffusing and electrode-attached MPCs demonstrate voltammetric responses featuring a series of evenly spaced current peaks on the potential axis.<sup>4</sup> This type of sequential electron transfer reaction is analogous to those observed for fullerene (and derivatives)<sup>7-11</sup> and Pt-carbonyl nanoclusters  $[\text{Pt}_n(\text{CO})_m]$ .<sup>12-14</sup> MPCs are formally equivalent to multivalent redox species, exhibiting equally spaced formal redox potentials.<sup>5</sup>

Given their fascinating properties and reactivity, it is of fundamental interest to understand the factors determining the sequential electron transfer energetics and to relate them to the energy scale of a certain reference system. Weaver *et al.*<sup>15</sup> have developed an electrostatic model to relate the electron-transfer energetics of the metallic clusters to their molecular capacitances in gas and solution-phase systems. On the basis of this work, Chen *et al.*<sup>16</sup> ascribed the occurrence of the successive electron transfer for MPCs to quantized charging of the extremely small (sub-attoFarad) molecular capacitance ( $C_{\text{MPC}}$ ) of the MPC. The capacitance of an MPC with a core size smaller than 2 nm is less than one attofarad, which is so small that a single electron addition to or removal from its core produces a substantial potential change. Accordingly, the sequential electron transfer event involving MPCs has been termed “quantized double layer charging” (QDL). On the other hand, concerning the electrochemistry of the self-assembled MPCs on a metallic electrode surface, there are two interesting phenomena worthy of further investigation. First, in organic media, the successive redox reactions occur with a smaller potential separation as compared to those of freely diffusing MPCs in solutions.<sup>17</sup> Second, in aqueous media, the occurrence of successive electron transfer between MPCs and substrate electrode can be rectified by the supporting electrolyte ions.

In this chapter, we shall introduce an alternative approach to analyze the successive electron transfer properties of MPCs in the solution and self-assembled on the electrode surface. Assuming an MPC as a “giant molecule” and the electron transfers as classical electrochemical reactions, the absolute standard redox potential of MPCs in solutions is theoretically derived. This derivation accounts for the effect of the solvent dielectric constant, which is further experimentally verified by comparing the electrochemical behavior of MPCs in various organic solvents characteristic of different dielectric constants. For MPCs self-assembled on the electrode surface, the electrostatic interaction between MPCs and the electrode is further considered in terms of the classical electrostatic model of image charges. In addition, the redox properties of self-assembled MPCs are also studied in room temperature ionic liquids (RTILs). The rectification of the successive oxidation of self-assembled MPCs by the anionic component of RTILs can be observed.

## 6.2 Absolute standard redox potential of MPCs

Figure 6.1 schematically illustrates an MPC embedded in a dielectric medium. An MPC is here considered as a concentric sphere consisting of a spherical nanometer-sized metallic core of radius  $r_0$  and a coating ligand monolayer that behaves as a dielectric layer of thickness  $d$  with a dielectric constant  $\epsilon_d$ .

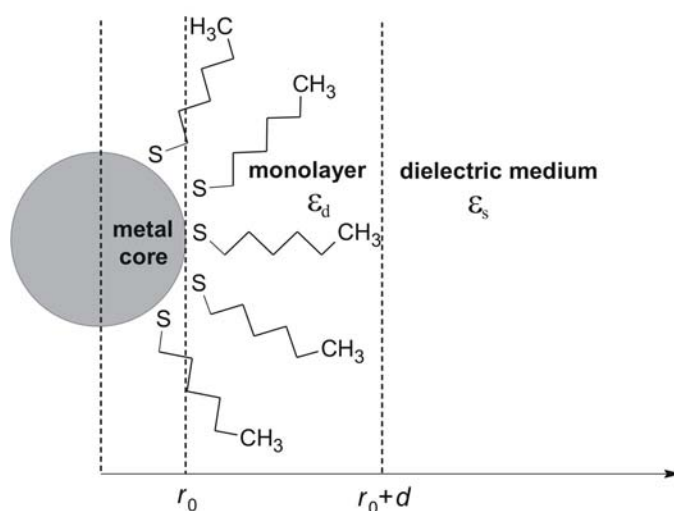


**Figure 6.1** Schematic illustration of the concentric structure of an MPC embedded in a dielectric medium.

### 6.2.1 Molecular capacitance model

For comparison, we first outline briefly the results of the molecular capacitance model proposed by Chen *et al.*<sup>16</sup> In this model, an MPC is considered as an entity consisting of a spherical nanometer-sized metallic core and a coating ligand monolayer, which serves as the dielectric medium of the double layer capacitor. Thus, the MPC molecular capacitance,  $C_{\text{MPC}}$ , can be modeled as a concentric sphere capacitor:

$$C_{\text{MPC}} = 4\pi\epsilon_0\epsilon_d\left(\frac{r_0}{d}\right)(r_0 + d) \quad (6.1)$$

where  $\epsilon_0$  and  $\epsilon_d$  are the dielectric constants of the vacuum and the MPC protecting monolayer, respectively.  $r$  and  $d$  are the radius of the MPC core and the thickness of the protecting monolayer, respectively. Thus, based on simple electrostatic interactions

described by Weaver *et al.*,<sup>15</sup> the formal potential of the successive electron transfer reaction is formulated:

$$E_{z/z-1}^0 = E_{PZC} + \frac{\left(z - \frac{1}{2}\right)e}{C_{MPC}} = E_{PZC} + \frac{\left(z - \frac{1}{2}\right)e}{4\pi\epsilon_0(r_0 + d)} \left(\frac{d}{\epsilon_d r_0}\right) \quad (6.2)$$

where  $E_{z/z-1}^0$  is the formal potential of the  $z/z-1$  charge state “couple” and is given by DPV peak potentials,  $E_{PZC}$  is the MPC potential of zero charge ( $z=0$ ). In terms of eq 6.2, the formal potentials of the serial redox reactions are solely determined by the molecular capacitance of MPC, which can be experimentally estimated from the slope of a linear plot of  $E_{z/z-1}^0$  against MPC charge state. However, the electrochemical properties of MPCs in electrolyte solutions were found to be dependent upon a variety of factors, including the dielectric property of the solvent,<sup>18</sup> the temperature,<sup>19</sup> as well as the solvation and/or penetration of solvent and supporting electrolyte.<sup>18, 20, 21</sup> An additional aspect to which one may pay attention is the charge states of MPCs. On the basis of eq 6.2, the determination of the charge state of a MPC at a given potential largely depends on finding  $E_{PZC}$ , which is however difficult to identify experimentally. Therefore, the molecular capacitance model remains an admittedly crude model.

### 6.2.2 Absolute standard redox potential

Considering the MPC configuration shown in Figure 6.1, the electric field inside the ligand monolayer and outside the sphere are defined, respectively, as:

$$E_1 = -\frac{dV}{dr} = -\frac{q}{4\pi\epsilon_0\epsilon_d r^2} (r_0 \leq r \leq r_0 + d) \quad (6.3)$$

$$E_2 = -\frac{dV}{dr} = -\frac{q}{4\pi\epsilon_0\epsilon_s r^2} (r_0 + d \leq r < \infty) \quad (6.4)$$

where  $r$  is the distance from the center of the metallic core and  $q$  the charge that the MPC carries. Using spherical coordinates and taking the potential equal to zero when  $r \rightarrow \infty$ , the electrostatic potential at the surface of the metallic core corresponds to the sum of the integrals of eqs 6.3 and 6.4:

$$\begin{aligned}
 V(q) &= \int_{r_0}^{r_0+d} E_1 dr + \int_{r_0+d}^{\infty} E_2 dr \\
 &= \frac{q}{4\pi\epsilon_0} \left[ \left( \frac{1}{\epsilon_s} - \frac{1}{\epsilon_d} \right) \left( \frac{1}{r_0+d} \right) + \frac{1}{\epsilon_d r_0} \right]
 \end{aligned} \tag{6.5}$$

When  $d$  is zero, eq 6.5 reduces to the potential at the surface of a bare sphere in a dielectric environment.

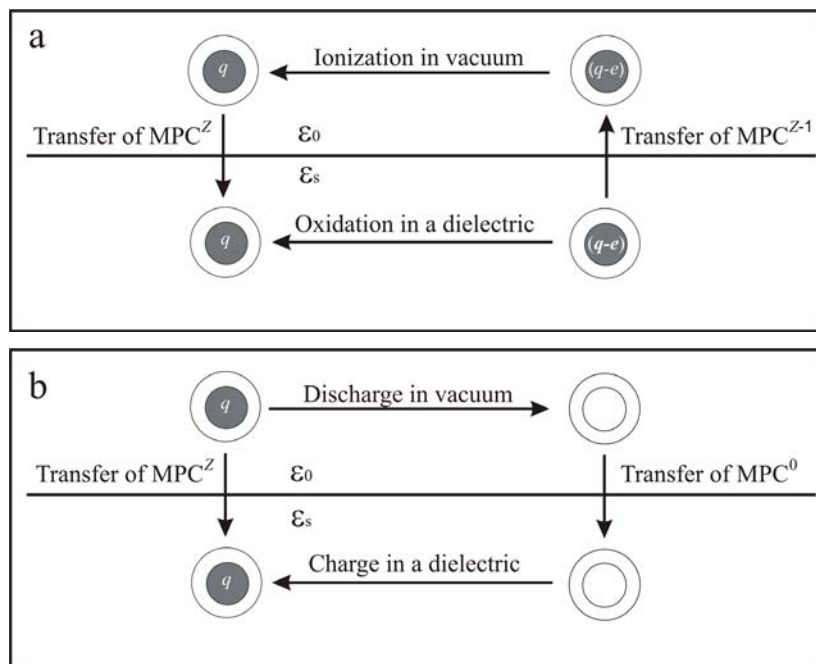


**Figure 6.2** (a) Equivalent thermodynamic cycle for a single electron oxidation process; (b) Born's model of the solvation of  $MPC^Z$ .

Considering MPCs as multivalent redox species, the sequential one-electron transfer process can be generally depicted as an electrochemical reaction at an electrode:



The absolute standard redox potential can be expressed either from the real chemical potentials of the oxidized and reduced species<sup>22</sup> or from a thermodynamic cycle. As shown in Figure 6.2a, the one-electron oxidation reaction can be decomposed to three steps: the transfer of  $MPC^{Z-1}$  from the solvent phase to the gas phase, the ionization of  $MPC^{Z-1}$  to form  $MPC^Z$  in the gas phase, and the transfer of  $MPC^Z$  from the gas phase to the solvent phase. As a first approximation, the work to transfer a charged sphere from the gas phase to a solvent phase can be considered equal to the Gibbs solvation energy of

the charged sphere. Therefore, the absolute standard redox potential,  $\left[ E_{Z/Z-1}^0 \right]_{\text{abs,bulk}}$ , is given by:

$$\begin{aligned} e \left[ E_{Z/Z-1}^0 \right]_{\text{abs,bulk}} &= \alpha_{\text{MPC}^Z}^0 - \alpha_{\text{MPC}^{Z-1}}^0 \\ &= \Delta G_{\text{solv, MPC}^Z}^0 - \Delta G_{\text{solv, MPC}^{Z-1}}^0 + E_{\text{I, Z-1}}^0 \end{aligned} \quad (6.7)$$

where  $e$  is the elementary electronic charge and  $E_{\text{I, Z-1}}^0$  the ionization energy of  $\text{MPC}^{Z-1}$  in the gas phase.  $\alpha_{\text{MPC}^Z}^0$  and  $\alpha_{\text{MPC}^{Z-1}}^0$  are the real chemical potentials of  $\text{MPC}^Z$  and  $\text{MPC}^{Z-1}$ , respectively.  $\Delta G_{\text{solv, MPC}^Z}^0$  and  $\Delta G_{\text{solv, MPC}^{Z-1}}^0$  represent the standard Gibbs solvation energies of  $\text{MPC}^Z$  and  $\text{MPC}^{Z-1}$ .

Evaluation of  $\Delta G_{\text{solv, MPC}^Z}^0$  can be done on the basis of Born's model of ionic solvation, as illustrated in Figure 6.2b. The difference between an  $\text{MPC}^Z$  and a conventional ion is that the  $\text{MPC}^Z$  contains an intrinsic dielectric coating layer. From Figure 6.2b, the work of transferring  $\text{MPC}^Z$  from the gas phase to the solvent phase ( $\Delta G_{\text{solv, MPC}^Z}^0$ ) corresponds to the sum of the work of discharging  $\text{MPC}^Z$  in vacuum to form a neutral sphere of the same size ( $w_{\text{d}}^0$ ), the work of transferring this neutral sphere from the vacuum to the phase ( $w_{\text{n}}$ ), and the work of charging this sphere in the solvent phase ( $w_{\text{c}}^{\text{s}}$ ):

$$\Delta G_{\text{solv, MPC}^Z}^0 = w_{\text{d}}^0 + w_{\text{c}}^{\text{s}} + w_{\text{n}} \quad (6.8)$$

with

$$w_{\text{c}}^{\text{s}} = \int_0^{ze} V(q) dq = \frac{z^2 e^2}{8\pi\epsilon_0} \left[ \left( \frac{1}{\epsilon_{\text{s}}} - \frac{1}{\epsilon_{\text{d}}} \right) \left( \frac{1}{r_0 + d} \right) + \frac{1}{\epsilon_{\text{d}} r_0} \right] \quad (6.9)$$

$$w_{\text{d}}^0 = -\int_0^{ze} V(q) dq = -\frac{z^2 e^2}{8\pi\epsilon_0} \left[ \left( 1 - \frac{1}{\epsilon_{\text{d}}} \right) \left( \frac{1}{r_0 + d} \right) + \frac{1}{\epsilon_{\text{d}} r_0} \right] \quad (6.10)$$

Substituting eqs 6.9 and 6.10 into eq 6.8, we obtain:

$$\Delta G_{\text{solv, MPC}^Z}^0 = \frac{z^2 e^2}{8\pi\epsilon_0} \left( \frac{1}{\epsilon_{\text{s}}} - 1 \right) \left( \frac{1}{r_0 + d} \right) + w_{\text{n}} \quad (6.11)$$

The ionization energy of  $\text{MPC}^{Z-1}$  in vacuum ( $E_{\text{I, Z-1}}^0$ ) can be expressed as:<sup>15, 23</sup>

$$E_{\text{I, Z-1}}^0 = \Phi + w_{\text{c}}^{0, Z-1 \rightarrow Z} \quad (6.12)$$

where  $\Phi$  is the work function of the metal, which is equal to 5.32 eV for bare gold.<sup>22</sup> In the presence of adsorption of alkanethiol monolayers on the surface,  $\Phi$  will be changed due to the formation of a gold-sulfur dipole layer. In the case of 1-hexanethiol, the work function is varied by less than 100 mV for planar Au electrode.<sup>24</sup> For the present MPCs, we can therefore neglect the contribution of the monolayer to the surface potential for simplicity. The second term in eq 6.12,  $w_c^{0,Z-1 \rightarrow Z}$ , is equal to the work of charging an MPC from charged state  $z-1$  to  $z$  in vacuum:

$$w_c^{0,Z-1 \rightarrow Z} = \int_{(z-1)e}^{ze} V(q) dq = \frac{(2z-1)e^2}{8\pi\epsilon_0} \left[ \frac{1}{\epsilon_d} \left( \frac{1}{r_0} - \frac{1}{r_0+d} \right) + \left( \frac{1}{r_0+d} \right) \right] \quad (6.13)$$

From eqs 6.12 and 6.13, we get:

$$E_{1,Z-1}^0 = \Phi + \frac{(2z-1)e^2}{8\pi\epsilon_0} \left[ \frac{1}{\epsilon_d} \left( \frac{1}{r_0} - \frac{1}{r_0+d} \right) + \left( \frac{1}{r_0+d} \right) \right] \quad (6.14)$$

For a given MPC radius, eq 6.14 predicts that the ionization energy linearly increases with  $z$ , reflecting the increasing energy cost of electron loss arising from the electrostatic interactions. Here we must note that an MPC differs with a conventional multivalent redox molecule as the latter possesses discrete electronic energy levels, which correspond to discrete ionization potentials that are not generally equally spaced. MPCs containing < 200 Au atoms are in an intermediate regime between molecular and bulk materials, where electronic band energetics become size and surface confined, and a series of electronic states emerge and distribute in relatively uniform spacing in a certain energetic range.

From eqs 6.7, 6.11 and 6.14, the absolute standard redox potential,  $[E_{Z/Z-1}^0]_{\text{abs}}$ , can then be derived as:

$$[E_{Z/Z-1}^0]_{\text{abs,bulk}} = \frac{\Phi_b}{e} + \frac{\left(z - \frac{1}{2}\right)e}{4\pi\epsilon_0(r_0+d)} \left( \frac{d}{\epsilon_d r_0} + \frac{1}{\epsilon_s} \right) \quad (6.15)$$

Eq 6.15 differs with eq 6.2 as a new term associated with the dielectric constant of the medium appears. However, eq 6.2 gives rise to two concerns. First, the standard redox potential relies on the determination of  $E_{\text{PZC}}$ , which is medium dependent and difficult to measure. This determination has been carried out by impedance measurements of a monolayer attached to a Au electrode.<sup>25</sup> Indeed, the capacitance data measured refer to a

planar electrode covered by a layer of 4, 4'-thiobisbenzenethiol. Even if the capacitance minimum observed is the potential of zero charge, i.e., if we assume the absence of any specific ionic adsorption on the planar gold electrode, it does not necessarily mean that the MPCs are neutral. It just means that the diffuse layer of MPCs and other ions is globally neutral. The  $E_{PZC}$  of a bulk metal in the absolute scale is linked to the work function of the metal by:<sup>22</sup>

$$E_{PZC} = \frac{\Phi}{e} + \Delta_S^M g(\text{dip}) + \chi^S - \chi^M \quad (6.16)$$

where  $\Delta_S^M g(\text{dip})$ ,  $\chi^S$  and  $\chi^M$  represent the dipolar contribution to the metal|solution potential difference, the surface potential of the electrolyte and the surface potential of the bare metal, respectively. Secondly, in eq 6.2 the effect of the surrounding dielectric medium outside the ligand monolayer is also ignored. Indeed, the electron addition to or removal from an MPC core is accompanied by the formation of an ionic space charge layer beyond the ligand monolayer. This space charge layer has recently been found to influence the electron transfer behavior of MPCs under certain conditions.<sup>19-21</sup> In conclusion, eq 6.15 provides a more rigorous definition of the standard redox potential for an MPC.

Figure 6.3a shows a DPV response of 0.02 mM MPCs in 1,2-dichloroethane (DCE) with 0.01 M BTTPATPFB as supporting electrolyte. The DPV trace exhibits a series of well-resolved and evenly spaced current peaks. Figure 6.3b displays the absolute standard redox potential ( $[E_{z/z-1}^0]_{\text{abs}}$ ) at DPV peaks as a function of the MPC charge state change. The linear relation is consistent with the prediction of eq 6.15. The fitting yields a slope of 0.24 V, which is independent on the valence state of MPCs. From the slope of the straight line, the dielectric constant of the coating layer can be estimated to be 6.2 taking  $r = 0.8$  nm and  $d = 0.8$  nm. This value is significantly larger than that of 3.0 previously used,<sup>16</sup> and may indicate that electrolyte ions and solvent molecules ( $\epsilon_s = 10.37$  for DCE) can penetrate into the protecting layer to some extent.<sup>26</sup> Considering 53 hexanethiolate ligands on a surface of a 0.8 nm metallic ball, there exist large voids between the ligands especially at the outer boundary of the coating monolayer. Indeed, Taylor dispersion measurements on the hydrodynamic radii of MPCs have suggested the penetration of solvent into the alkanethiolate monolayer.<sup>26</sup> More recently, the specific solvation and



ionic penetration of the hexanethiolate monolayer has been inferred by investigation of the solvent and supporting electrolyte effects on the electrochemical behavior of MPC.<sup>21</sup>

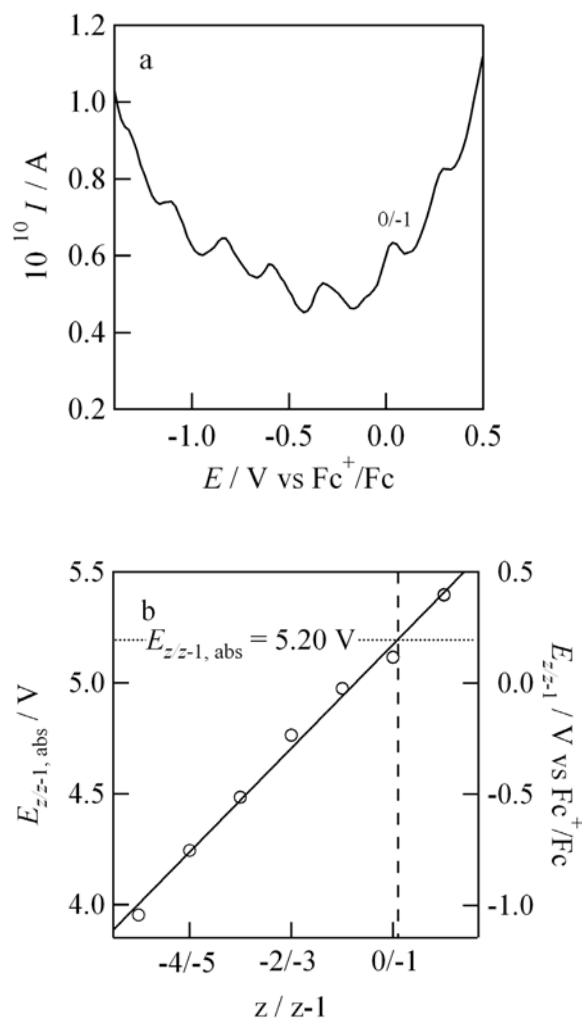


**Figure 6.3** (a) A typical DPV response of MPCs in DCE solution (ca. 0.02 mM MPCs and 0.01 M BTTPATPFB) measured at a 25  $\mu\text{m}$  Pt electrode: scan rate 0.02 V s<sup>-1</sup>, pulse height 0.05 V, pulse width 0.06 s and period 0.2 s. (b) The corresponding Z-plot of  $[E_{z/z-1}^0]_{\text{abs}}$  versus the adjacent valence states.

### 6.2.3 Determination of MPC charge

Eq 6.15 gives the electron transfer energetics of MPCs in an absolute potential scale. However, in solution phase electrochemical systems the electrode potentials are normally expressed with respect to a reference electrode in the same solvent. Hence, it is necessary to correlate these two scales. This was achieved in Figure 6.3b by the addition of ferrocene to the solution at the end of the measurement. The half wave potential of ferrocene can be correlated to the absolute standard redox potential of ferrocene, which is taken equal to 5.01 V. This value was calculated from eqs 6.7 and 6.11 by taking  $r_{\text{Fc}} = r_{\text{Fc}^+} = 0.38 \text{ nm}^{27}$  and  $E_{\text{Fc}}^0 = 6.71 \text{ eV}^{28}$ . It should be also noted that this absolute standard redox potential value is comparable to the value of 5.08 V obtained from adding the formal redox potential of ferrocene in DCE ( $[E_{\text{Fc}^+/\text{Fc}}^{0', \text{DCE}}]_{\text{SHE}} = 0.64 \text{ V})^{29}$  and  $[E_{\text{H}^+/\frac{1}{2}\text{H}_2}^0]_{\text{abs}} = 4.44 \text{ V}$ . The zero value in the potential scale in Figure 6.3a corresponds to an absolute potential of about 5.01 V. According to eq 6.15, the intercept of the straight line for  $z = 0$  should be equal to 5.20 V. Then the peak potential value closest to 5.20 V in the absolute potential scale can be assigned to the redox couple of  $\text{MPC}^0/\text{MPC}^{-1}$ . The corresponding assignment of the valence states of MPCs at the DPV peak potential is illustrated in Figure 6.3b.

On the basis of the above approach, the potential at the minimum of the DPV trace shown in Figure 6.3a corresponds to a mixture of MPCs with  $-2$  and  $-3$  core charges. The estimated values for  $z$  are rather different with those previously determined based on impedance measurements of an MPC monolayer attached to an Au electrode, in which the charged state of MPCs at the minimum of the DPV curve was assigned to be 0 and the neighboring two peaks were assigned to the first oxidation ( $z = +1/0$ ) and reduction ( $z = 0/-1$ ), respectively.<sup>25</sup>

### 6.3 Solvent effect on redox properties of MPCs

The present section is aimed at understanding the solvent effect on the redox properties of MPCs from an experiment point of view. In terms of eq 6.15, the dielectric constant of the solvent has significant effect on the absolute standard redox potentials of MPCs in solution, especially when it is comparable to that of the protecting monolayer of alkanethiolate. The effect can be simply considered from the separation of neighboring absolute standard redox potentials:

$$\Delta V = \frac{e}{4\pi\epsilon_0(r_0 + d)} \left( \frac{d}{\epsilon_d r_0} + \frac{1}{\epsilon_s} \right) \quad (6.17)$$

Eq 6.17 predicts that  $\Delta V$  increases with decreasing the dielectric constant of the medium.

As a matter of fact, both experimental and theoretical investigations of the solvent effect on redox properties of MPCs have been carried out previously. In a very early study, Murray et al. have concluded that the redox properties of MPCs were not sensitive to the solvent dielectric constant. This conclusion was supported by their experimental measurements in various organic solvents or mixed organic solvents with dielectric constants ranging from 14.1 to 5.53, in which the  $\Delta V$  value was reported to be relatively constant. In contrast, the same group has recently reported that the solvent dielectric constant has a strong effect on the redox behavior of MPCs on the basis of electrochemical measurements carried out in mixed organic solvents by varying the ratio of two composing solvents. The effect was ascribed to the complicated specific solvation and penetration of the alkanethiolate monolayer by the less polar solvent and supporting electrolyte ions in the mixed solvents. Apparently, rather divergent and inconsistent results have been reported. However, it should be noted that so far most of the experimental measurements concerning solvent effects have been carried out in mixed solvents. Therefore, comparative analysis of the results obtained would be difficult on account of the indeterminate physicochemical properties of the mixed solvents.

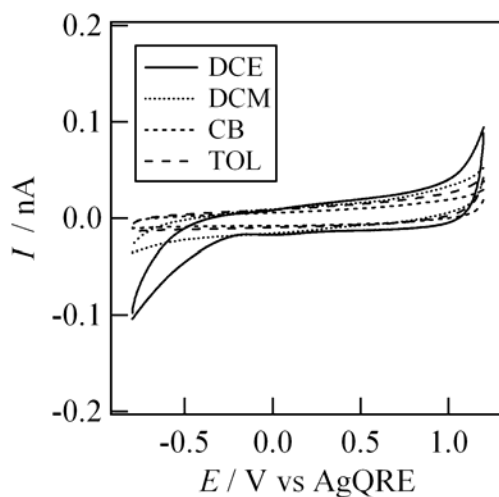
### 6.3.1 Solvents and supporting electrolyte

Table 6.1 lists four types of organic solvents, 1,2-dichloroethane (DCE), dichloromethane (DCM), chlorobenzene (CB) and toluene (TOL), in all of which MPCs have rather good solubility. This set of organic solvents features dielectric constants ranging from 10.37 (DCE) to 2.38 (TOL), which is wide enough to probe the solvent effect on the redox properties of MPCs according to eqs 6.15 and 6.17. The viscosities of the organic solvents are also compared in Table 6.1.

**Table 6.1** *Electrochemical Measurements in Various Solvents<sup>a</sup>*

Solvent	Abbreviated Symbol	Dielectric Constant ( $\epsilon_s$ )	Viscosity (mPa s)	$\Delta V$ (V)
1, 2-Dichloroethane	DCE	10.37	0.779	0.26
1, 2-Dichloromethane	DCM	8.93 <sup>b</sup>	0.413	0.27
Chlorobenzene	CB	5.69	0.753	0.33
Toluene	TOL	2.38 <sup>c</sup>	0.560	0.53

<sup>a</sup> All parameters are referred to 25°C; <sup>b</sup> at 20°C; <sup>c</sup> at 23°C.



**Figure 6.4** *Potential windows obtained on a 25  $\mu\text{m}$  microelectrode in four organic solvents with 0.05 M  $\text{THATf}_2\text{N}$  as supporting electrolytes. The scan rate is 0.1  $\text{V s}^{-1}$  in all cases.*

The choice of solvent for electrochemical measurements is determined by the joint solubility of MPCs and supporting electrolytes employed in the solvent. Tetrahexylammonium bis(trifluoromethylsulfonyl)imide (THATf<sub>2</sub>N), which was prepared as described in section 2.8 of Chapter 2, was used as the common supporting electrolytes in all solvents. It should be mentioned that the electrochemical measurements in single TOL phase has been previously hindered by the lack of supporting electrolyte. Recently, it has been demonstrated that THATf<sub>2</sub>N has excellent solubility in TOL, which provides sufficient conductivity for electrochemical measurements.<sup>30</sup>

Figure 6.4 displays the potential windows obtained on a 25 μm microelectrode with 0.05 M THATf<sub>2</sub>N as the supporting electrolyte. Apparently, a potential window ranging from -0.8 V to 1.2 V could be easily attained in each solvent. The cathodic and anodic current onsets observed at the end of the potential window can be related to the reduction of oxygen and the oxidation of H<sub>2</sub>O, respectively. A potential window with a much more negative limiting potential can be obtained in each organic solvent by degassing the solution with nitrogen or argon stream. Figure 6.4 clearly shows the applicability of THA-Tf<sub>2</sub>N as the common supporting electrolyte in four solvents.

### 6.3.2 Analysis of microelectrode cyclic voltammetric results

Figure 6.5 shows the CVs of 0.08 mM MPCs in four solvents with in the presence of 0.05 M THATf<sub>2</sub>N as the supporting electrolyte. It is obvious that each CV is characteristic of a certain number of well-defined steady-state current-potential waves typically observed on a microelectrode. These waves result from successive redox reactions involving MPCs, which provides clear evidence that MPCs can be considered as multivalent redox species. Most importantly, the solvent effect on the redox properties of MPCs can be clearly observed from Figure 6.5. From DCE to TOL, the number of current-potential waves in the same potential window continuously decreases while  $\Delta V$  increases. This aspect will be further discussed in the next section. Moreover, these current waves are well separated so that we can treat each of them individually.

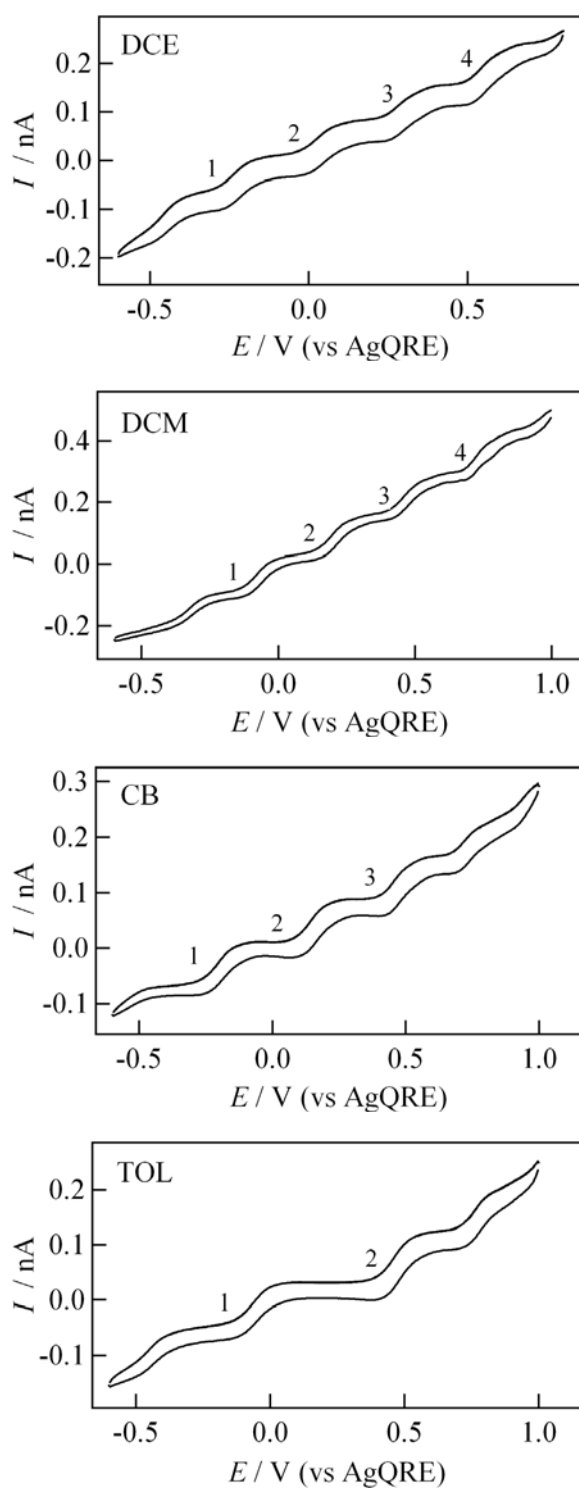


**Figure 6.5** CVs obtained on a 25  $\mu\text{m}$  microelectrode for 0.08 mM MPCs in various solvents with 0.05 M  $\text{THATf}_2\text{N}$  as supporting electrolytes. The scan rate is  $0.1 \text{ V s}^{-1}$  in all cases. The labeled waves were further analyzed.

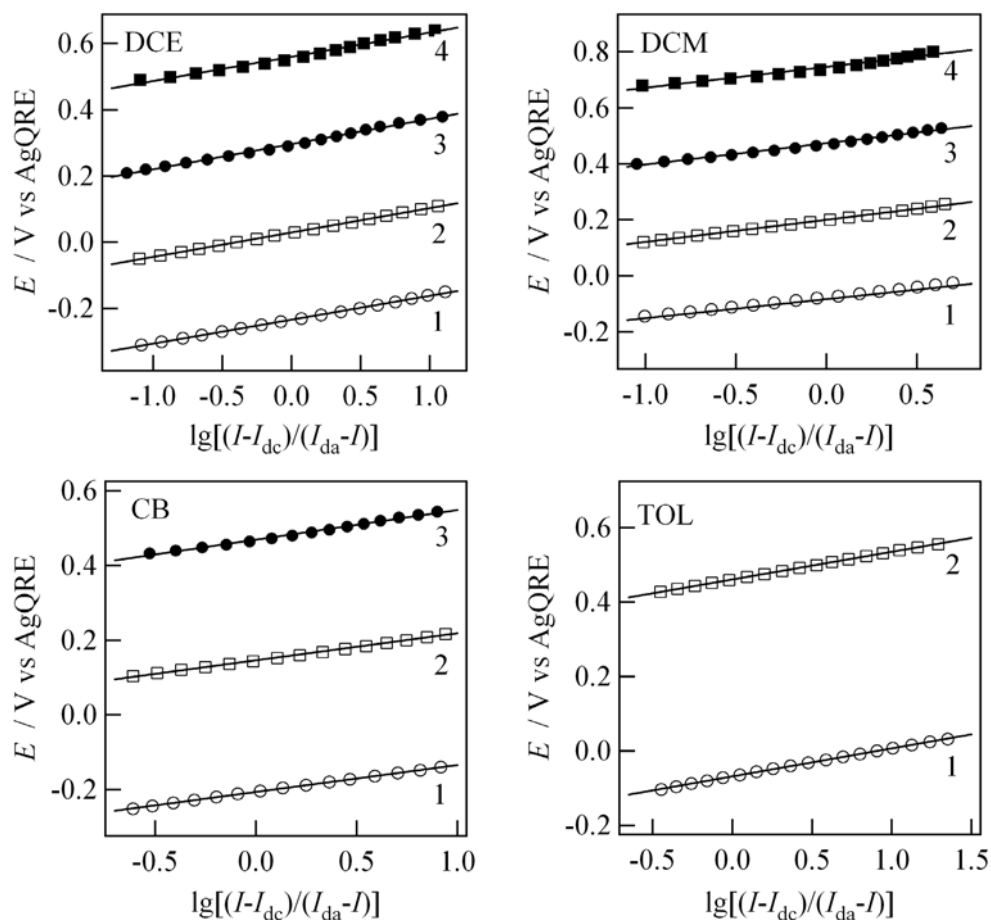


**Figure 6.6** The relation between the applied potential (vs AgQRE) and  $\lg[(I-I_{dc})/(I_{da}-I)]$  for the waves labeled in Figure 6.5.

The reversibility of the successive redox reactions was first analyzed by considering the relation between the current and the electrode potential according to the following equation:<sup>22</sup>

$$E = E'_{O/R} + \frac{2.303RT}{nF} \lg\left(\frac{D_R \delta_R}{D_O \delta_O}\right) + \frac{2.303RT}{nF} \lg\left(\frac{I - I_{dc}}{I_{da} - I}\right) \quad (6.18)$$

where  $E'_{O/R}$  is the formal redox potential,  $D_R$  and  $D_O$  are the diffusion coefficients of the reduced and oxidized species, respectively.  $\delta_R$  and  $\delta_O$  are the thickness of diffuse layers associated with the oxidation and reduction reactions.  $I_{dc}$  and  $I_{da}$  represent the cathodic and anodic limiting currents, respectively. As illustrated in Figure 6.6, the plots of  $E$  versus  $\lg[(I-I_{dc})/(I_{da}-I)]$  for all numbered waves are all straight lines with slopes around 70 mV, indicating that each of these waves corresponds to a reversible one-electron electron transfer reaction. The slight curvature in the plots for the fourth waves

in DCE and DCM is possibly due to the inaccurate determination of experimental data in the post-oxidation portion, where the currents continuously move upward. The slopes of the straight lines are larger than the theoretical value of 59 mV of a one-electron transfer reaction, which may arise from the polydispersity of MPCs in the sample.

**Table 6.2** Diffusion coefficients of MPCs in Various Solvents

Solvent	Wave	$D_e$ ( $\times 10^{-6}$ cm <sup>2</sup> s <sup>-1</sup> )
DCE	1	1.97
	2	1.86
	3	1.91
	4	2.19
DCM	1	3.10
	2	3.46
	3	3.43
	4	3.69
CB	1	2.00
	2	1.99
	3	1.99
TOL	1	2.08
	2	2.36

**Table 6.3** Comparison of calculated and experimental diffusion coefficients of MPCs in Various Solvents

Solvent	$\bar{D}_e$ ( $\times 10^{-6}$ cm <sup>2</sup> s <sup>-1</sup> )	$D_{SE}$ ( $\times 10^{-6}$ cm <sup>2</sup> s <sup>-1</sup> )
DCE	1.98	1.75
DCM	3.42	3.30
CB	1.99	1.81
TOL	2.22	2.44



The limiting currents of steady-state waves were found to be independent on the scan rate ( $\leq 0.2 \text{ V s}^{-1}$ ). These facts indicate that the electron transfer to or from MPCs is kinetically fast and diffusion controlled, regardless of the electronic charge of the MPCs cores. Indeed, it has been reported that the electron transfer involving MPCs at electrode|electrolyte solution interfaces is fast with a rate constant larger than  $0.1 \text{ cm s}^{-1}$ .<sup>31</sup>

For a disc microelectrode, the diffusion-controlled limiting current is proportional to the radius of the microelectrode ( $a$ ), the diffusion coefficient ( $D$ ) and the concentration ( $c$ ) of the redox species:

$$I_s = 4nFDac \quad (6.19)$$

Therefore, the diffusion coefficient of redox species can be derived from the microelectrode voltammograms in terms of eq 6.19. Table 6.2 displays the diffusion coefficients of MPCs derived from the waves observed in various organic solvents. In one solvent, the values of  $D$  do not vary much with the charge states of MPCs, which means that the MPC charge does not materially affect its diffusion rate. In general, the values of  $D$  are within a range of  $2.0$  to  $4.0 \times 10^{-6} \text{ cm}^2 \text{ s}^{-1}$ , which is in well agreement with those reported previously.<sup>32</sup> Considering the average values of diffusion coefficients in DCE, DCM, CB and TOL, a ratio of  $D_{\text{DCE}} : D_{\text{DCM}} : D_{\text{CB}} : D_{\text{TOL}} = 1.0 : 1.7 : 1.0 : 1.1$  can be attained.

In terms of the classical Stokes-Einstein equation, the diffusion coefficient of a spherical object is proportional to the reciprocal of the solvent viscosity:

$$D = \frac{kT}{6\pi\eta r_H} \quad (6.20)$$

where  $k$  is the Boltzmann constant,  $T$  is the temperature,  $\eta$  is the solution viscosity and  $r_H$  the hydrodynamic radius of MPCs. As shown in Table 6.3, the calculated diffusion coefficients of MPCs ( $r_H = 1.6 \text{ nm}$ ) in various solvents were found close to the averaged experimental values.

### 6.3.3 Effect of the solvent dielectric constant

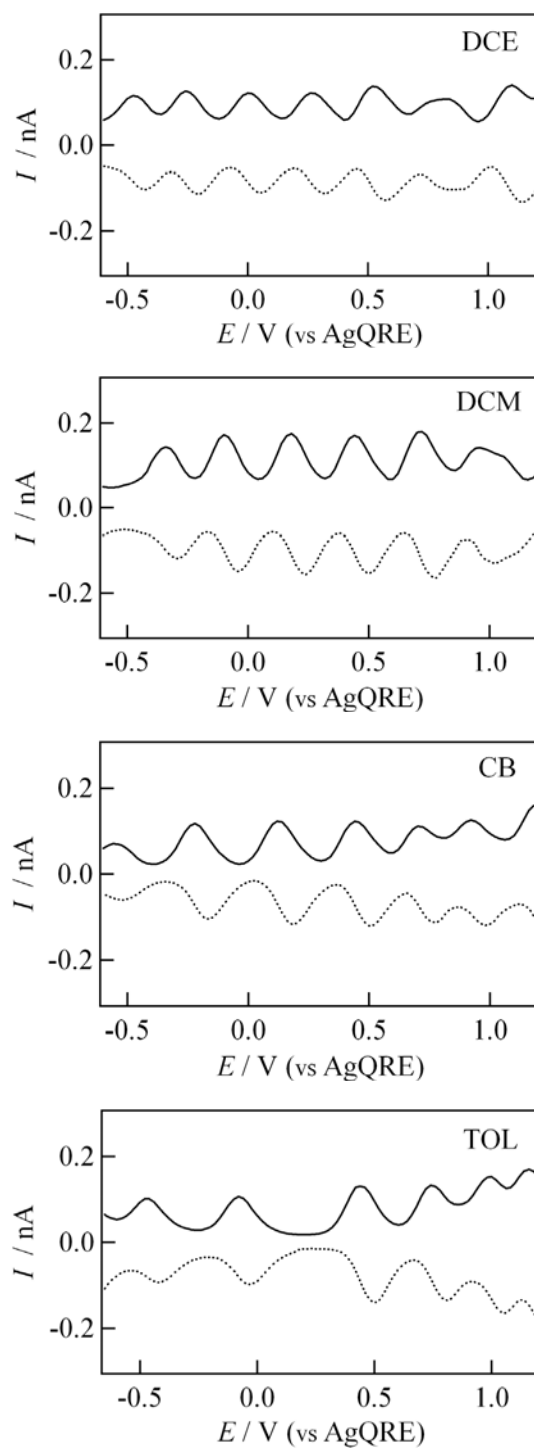


**Figure 6.7** DPVs of 0.08 mM MPCs in various solvents with 0.05 M  $\text{THATf}_2\text{N}$  as the supporting electrolyte: scan rate  $0.02 \text{ V s}^{-1}$ , pulse height 0.1 V, pulse width 0.05 s and period 0.5 s.

One additional phenomenon observed from Figure 6.5 by comparing the microelectrode CVs of MPCs in DCM, CB and TOL is that the number of steady-state waves in the same potential window decreases with decreasing the dielectric constant of the organic solvent. This can be seen much more clearly by DPV measurements. As shown in Figure 6.7, in a potential window ranging from  $-0.5$  V to  $1.2$  V, DPV responses of MPCs in both DCE and DCM are characteristic of 6 and 7 current peaks, respectively, which are very similar and uniformly spaced along the potential axis. No big difference in the average potential separation of the two neighboring current peaks was observed because theoretically it is only about  $10$  mV according to eq 6.17. However, when dissolving MPCs into CB and TOL, one can see that the DPV signals significantly varied with two characteristics: the largely increased potential separation in the low potential range from  $-0.5$  V to  $0.5$  V and the irregular distribution of current peaks in the high potential regime.

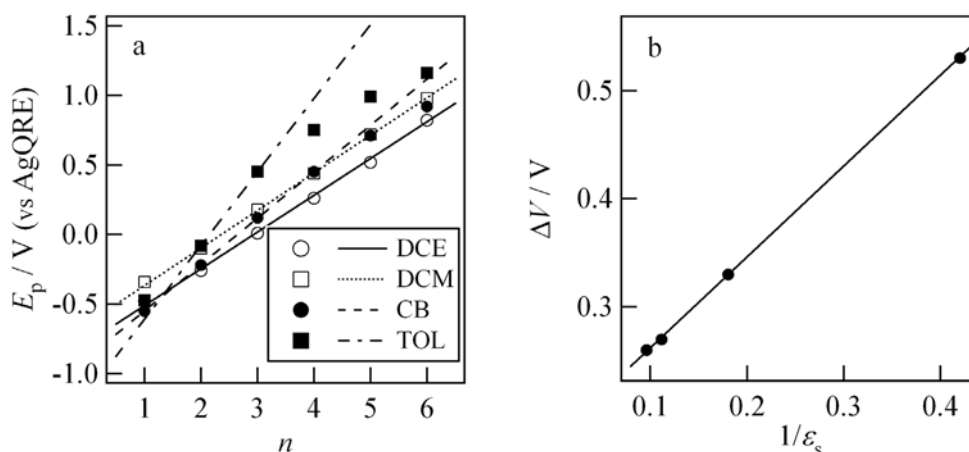


Figure 6.8 (a) Plots of peak potentials versus the number of peaks; (b) The dependence of  $\Delta V$  on the reciprocal of the solvent dielectric constant. The solid line corresponds to a linear fit.

The increase of the potential separation with decreasing dielectric constant of the solvent is in agreement with the prediction of eq 6.17. This tendency can be clearly seen by plotting the peak potential versus the number of the peak (This number starts from 1 and increases from the left to right to represent the current peaks in a DPV. The number is used just for simplicity and has nothing to do with the charge state of MPC), as illustrated in Figure 6.8a. All the six peak potentials in DCE and DCM are linearly increasing with the peak number. In CB, a uniform distribution of the peak potential was

only observed for the first four current-potential waves in the potential range from  $-0.5$  V to  $0.5$  V. However, in TOL, all the peaks potentials are irregularly distributed.  $\Delta V$  declines continuously with the increasing of the applied voltage, with a large separation of  $0.53$  V between the second and the third peaked currents.

As shown in Figure 6.8a, the regular distributed peak potentials were linearly fitted against the peak numbers, respectively, for DPVs in DCE, DCM and CB. The dotted-dashed line corresponds to the straight line passing through the second and third peak potentials in TOL, which was shown for comparison. The slopes of the straight lines essentially reflect the value of  $\Delta V$ . Clearly one can see the increase of the slope when decreasing the dielectric constant of the organic solvent. The relation of the average peak separation versus the reciprocal of the solvent dielectric constant is further plotted, as displayed in Figure 6.8b. A linear correspondence is apparently observed, the agreement of this plot with theoretical prediction of eq 6.17 is excellent. This observation not only verifies that the solvent dielectric demonstrates significant effect on the redox properties of MPCs but also provides concrete evidence that eq 6.15 is a simple and elaborate description of the redox properties of MPCs in solution phase.

Finally, it is apparent from Figure 6.8 that the distribution of  $\Delta V$  in the high potential regime in CB and in the whole potential range in TOL becomes irregular. There are several points possibly accounting for the irregularity. It may be ascribed to the effects of solvent penetration and electrolyte ion binding. Considering the physicochemical properties of the organic solvents from DCE to TOL, they are more and more adaptable to the nonpolar environment the MPC protecting monolayers, which could change the values of  $\epsilon_d$  and  $d$  significantly. The binding of electrolyte ions to MPC sphere can also shift the redox potential of MPCs, if the binding process is considered as a chemical reaction coupled to the MPC redox reaction. On the other hand, It may reflect the real distribution of electronic states within the Au core, which are not regularly distributed as assumed but do appear regularly in a certain dielectric medium.

## 6.4 Redox properties of self-assembled MPCs

MPCs demonstrate redox properties, not only in the electrolyte solutions, but also on the solid electrodes as monolayers or multilayers.<sup>17, 25, 33-36</sup> Freely diffusing MPCs undergo quite fast electron-transfer reactions among MPC cores, and the equilibrium of the MPCs solution can be described in terms of the Nernst equation.<sup>37</sup> Comparatively, the electron-transfer reactions between electrodes and surface-attached MPCs have been reported to occur very slowly in a range of 10-200 s<sup>-1</sup>.<sup>17, 25, 33, 38</sup> The present section will be devoting to the redox properties of self-assembled MPC monolayer on the electrode, a system that has been introduced in section 2.6.3 of Chapter 2, from both theoretical and experimental point of view.

### 6.4.1 Electrochemistry of freely diffusing MPCs

The redox properties of freely diffusing MPCs were first examined to allow further comparison with the self-assembling system. Figure 6.9a shows DPV curves of C<sub>6</sub>Au MPCs in DCE with 0.05 M tetra-*n*-butylammonium perchlorate (TBAClO<sub>4</sub>) as the supporting electrolyte. Figure 6.9b displays the peak potentials as a function of the peak number. The linear relation is consistent with the prediction of eq 6.15. From the slope of the straight line, a value of 0.25 V was obtained for  $\Delta V$ . Taking  $\epsilon_s = 10$  and  $r_0 = d = 0.8$  nm, the contribution of the solvent dielectric constant to  $\Delta V$  can be evaluated to be around 0.09 V, indicating that it is a key parameter contributing to the redox properties of MPCs. On the other hand,  $\epsilon_d$  can also be evaluated to be 5.6, which is much larger than the intrinsic dielectric of the alkanethiolate (3.0). However, the value obtained here is close to the value of 6.2 estimated in section 6.2 using BTPPATPFB as the supporting electrolyte in DCE solvent.<sup>39</sup> These results indicate the effect of the solvent or electrolyte ion on the dielectric property of the MPC protecting monolayer. Indeed, by comparing Figures 6.3, 6.8 and 6.9, we can see small differences in  $\Delta V$  when different supporting electrolyte was employed.

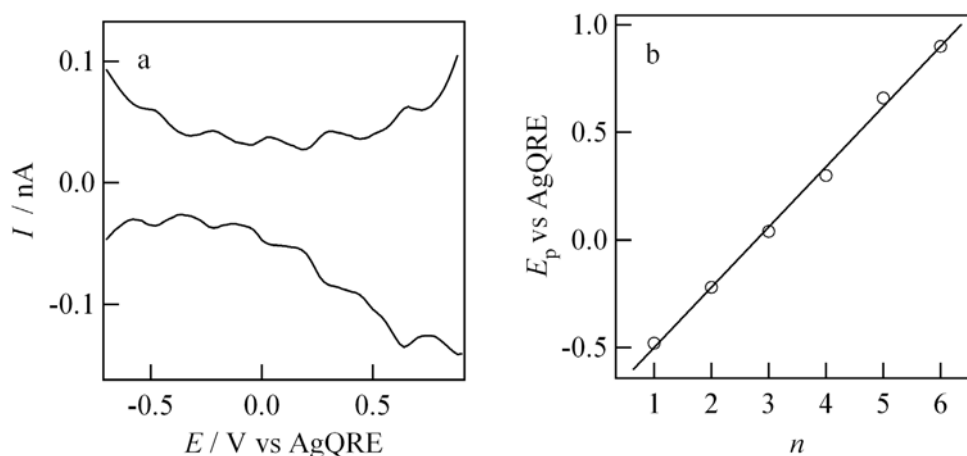


**Figure 6.9** (a) DPV responses obtained on a 25  $\mu\text{m}$  Pt microelectrode for 0.02 M MPCs in DCE with 0.05 M TBAClO<sub>4</sub> as supporting electrolyte: scan rate 0.02 V s<sup>-1</sup>, pulse height 0.05 V, pulse width 0.06 s and period 0.2 s; (b) Linear relation between the peak potentials in (a) and the peak number.

#### 6.4.2 Electrochemistry of self-assembled MPCs

Figure 6.10a and 6.10c show the CVs and DPVs of a self-assembled MPC monolayer on a gold electrode linked by 1,9-nonanedithiol in DCE electrolyte solution. The responses were very consistent with those observed for freely diffusing MPCs in the same solution (Figure 6.9), particularly in the positive potential regime. More current peaks can be obtained by degassing the solution. It was found that the CV peak current grows linearly with increasing the potential scan rate, as shown in Figure 6.10b. This is in agreement with a surface-confined electrochemical process. On the other hand, a large potential separation between the first oxidation and the first reduction potential peaks was observed with a current minimum at around  $-0.30$  V. This phenomenon could be due to the diffuse double layer outside the protecting monolayer.<sup>20</sup>

There is a linear correspondence between the oxidation peak potential and the peak number, as demonstrated in Figure 6.10d. The linear fitting yields a slope of 0.20 V. It is apparent that there is a  $\sim 25\%$  decrease (from 0.25 V to 0.20 V) in  $\Delta V$  when MPCs are anchored onto the electrode compared to that when they are freely diffusive in the same

DCE electrolyte solution. This decrease is consistent with the work of Chen and Pei, where a 25% decrease of the potential spacing took place when the particles were anchored onto the electrode surface.<sup>17</sup> These authors have proposed that the decrease in  $\Delta V$  arises from the preferential assembling of the larger sized particles onto the electrode surface during the self-assembling process.<sup>17</sup> However, there is neither theoretical nor experimental evidence that supports this speculation.

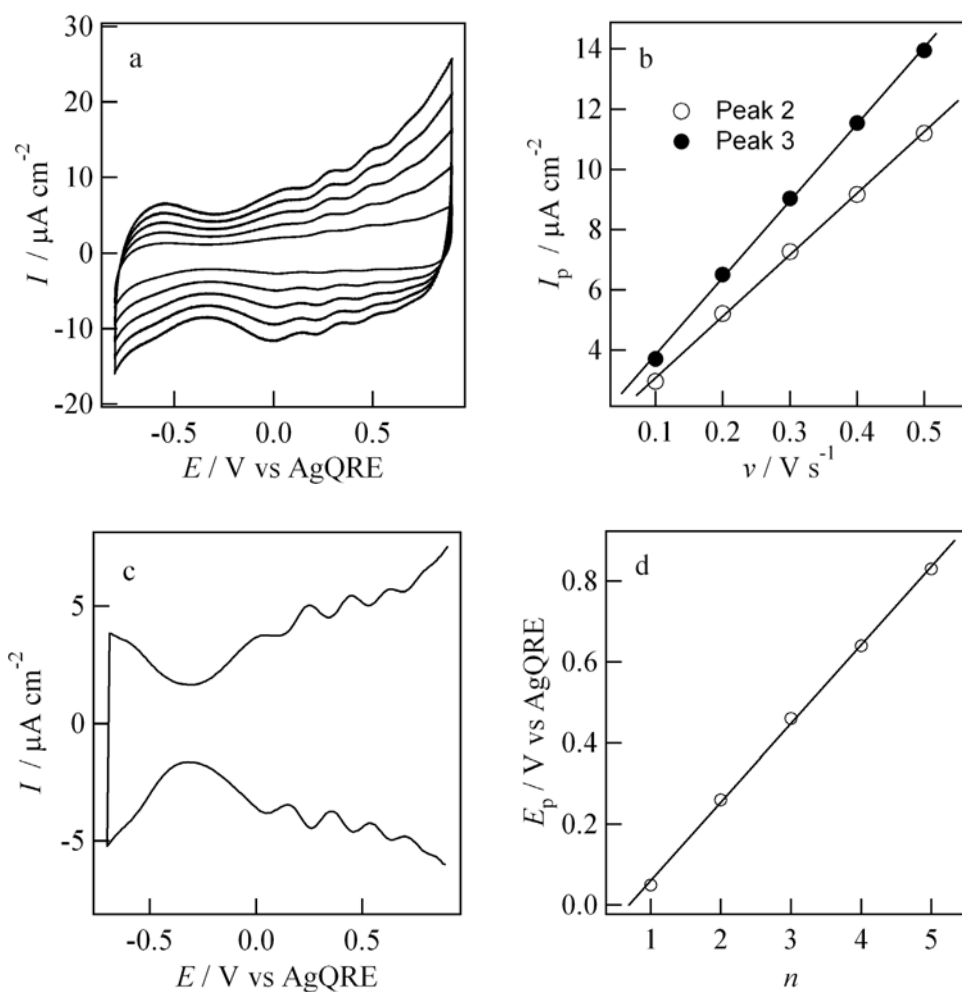


**Figure 6.10** (a) CVs of self-assembled MPCs in DCE with 0.05 M TBAClO<sub>4</sub> as supporting electrolyte at various scan rates: 0.1, 0.2, 0.3, 0.4 and 0.5 V s<sup>-1</sup> from inner to outer; (b) The dependence of the second and third peak currents on the potential scan rate; (c) Typical DPV responses of self-assembled MPCs on a gold electrode in DCE with 0.05 M TBAClO<sub>4</sub> as supporting electrolyte: 0.02 V s<sup>-1</sup>, pulse height 0.05 V, pulse width 0.06 s and period 0.2 s; (d) Linear relation between the peak potentials in (b) and the peak number.

-----

The partial ligand exchange of 1-hexanethiol by 1,9-nonanedithiol results in the increase of the effective thickness of the coating layer, that is, the parameter  $d$  in eq 6.15. In this case, however, a larger  $\Delta V$  is anticipated according to eq 6.15. Indeed, previous experimental work has also demonstrated that  $\Delta V$  regularly increases with the thickness of the protecting monolayer.<sup>18</sup> For example, the voltammetric response of MPCs protected by 1-decanethiolate has a larger peak separation ( $\Delta V = 0.38$ ) than that of MPCs protected by 1-hexanethiolate ( $\Delta V = 0.27$ ), in 2:1 toluene/acetonitrile mixing solution.<sup>18</sup> On the other hand, since the decrease of  $\Delta V$  when transferring freely diffusing MPCs onto the electrode surface was observed in the same electrolyte solution,  $\epsilon_s$  is not expected to change. Therefore, there must be some other factors responsible for the decrease of  $\Delta V$ .

### 6.4.3 Effect of the electrostatic interaction between self-assembled MPCs and substrate electrode

The present system of self-assembling of MPCs on a gold electrode surface is quite similar to a well-known model system in which a redox species, for example ferrocene, is tethered to a metal electrode at a controlled distance via a self-assembled monolayer. In this configuration, the electronic coupling between the redox species and the electrode surface is critically important in determining the kinetics and the pathway of the electron transfer reaction. The electronic coupling factor can be expressed by a matrix element within the framework of the Marcus theory. However, the estimation of this parameter is difficult since it requires knowledge of the nuclear coordinates in the redox species and the electronic structure of the electrode. For the present system, the electronic coupling between MPCs and the gold electrode would contribute to charging work, and therefore to the solvation of the MPC. In the following, we shall estimate the electronic coupling between anchored MPCs and the gold electrode by considering the classical electrostatic model of image charges. As shown in Figure 6.11, an MPC with charge  $q$  is placed at a point  $P$ , which is in the solution side at a distance  $h$  from the electrode|solution interface considered as a plane. An image charge  $q'$  locates at a point  $P'$ , which is in the metal electrode at the same distance from the interface.



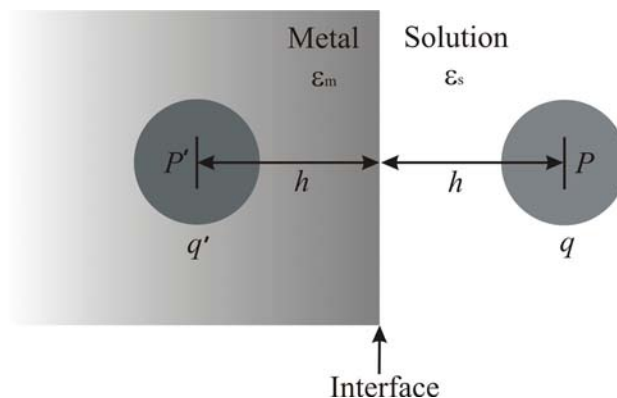


**Figure 6.11** Application of the method of images to an MPC attached to a metal electrode.

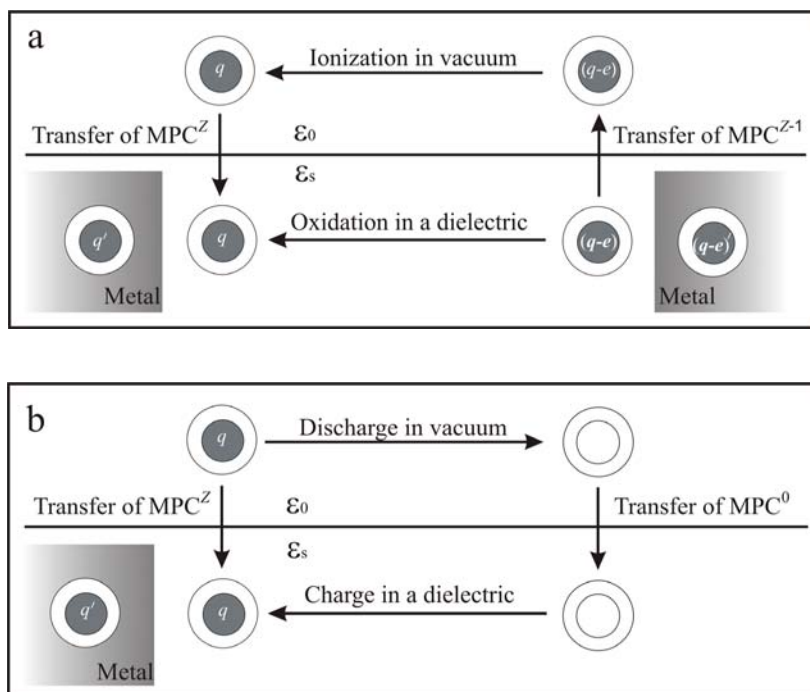


**Figure 6.12** (a) Equivalent thermodynamic cycle for an oxidation process of a surface attached MPC; (b) Born's model of the solvation of a surface attached MPC.

Taking this electrostatic interaction effect into account, the absolute standard redox potential of MPCs attached to an electrode can be derived on the basis of previous works:<sup>39</sup>

$$\left[ E_{Z/Z-1}^0 \right]_{\text{abs, assembly}} = \left[ E_{Z/Z-1}^0 \right]_{\text{abs, bulk}} - \frac{\left( z - \frac{1}{2} \right) e}{8\pi\epsilon_0\epsilon_s h} \quad (6.21)$$

In comparison with eq 6.15, one more term appears in eq 6.21. As a first approximation, this term represents the contribution from the electrostatic interaction between attached MPCs and the substrate electrode. Taking  $\epsilon_s = 10.37$  for DCE and  $h = 1.3$  nm (the approximate chain length of 1,9-nonanedithiol), a decrease of 0.06 V in  $\Delta V$  is expected due to the MPC-electrode interaction. If deducting the possible increase of  $\Delta V$  for the partial ligand exchange, this value falls close to the experimentally observed 0.05 V. This conformity indicates that the electrostatic interaction between MPCs and the substrate electrode is an important factor in dictating the absolute standard redox potential of MPCs assembled on the electrode surface.

The derivation of  $\left[ E_{Z/Z-1}^0 \right]_{\text{abs, bulk}}$  in section 6.2.2 can also be applied to eq 6.21. Indeed,  $\left[ E_{Z/Z-1}^0 \right]_{\text{abs, assembly}}$  is also defined by eq 6.7 and can be equivalent to a thermodynamic cycle, as illustrated in Figure 6.12a. The difference of the present thermodynamic cycle with the one displayed in Figure 6.2a is that in solvent phase the electrostatic interaction will be taken into account in the case of MPCs self-assembled on an electrode. Evaluation of  $\Delta G_{\text{solv, MPC}^z}^0$  is also based on eq 6.8 and the Born's model of ionic solvation as shown in Figure 6.13b. According to the description in Figure 6.12b, the electrostatic interaction between MPCs and the gold electrode only changes  $w_c^s$  but not  $w_d^0$  and  $w_n$ . The work  $w_d^0$  has the same expression as eq 6.10. However, for surface self-assembled MPCs,  $w_c^s$  should be rewritten to include the work associated with the electrostatic interaction between anchored MPCs and the gold electrode ( $w_{c,e}^s$ ):

$$w_c^s = \frac{z^2 e^2}{8\pi\epsilon_0} \left[ \left( \frac{1}{\epsilon_s} - \frac{1}{\epsilon_d} \right) \left( \frac{1}{r_0 + d} \right) + \frac{1}{\epsilon_d r_0} \right] + w_{c,e}^s \quad (6.22)$$

The parameter  $w_{c,e}^s$  will be derived in terms of the classical electrostatic model of image charges. For simplicity, an MPC is considered as a large ion with an effective radius of  $r_0 + d$ . According to Gauss's law, the potential generated by the image charge at  $P$  is:

$$V'(q) = \frac{q'}{4\pi\epsilon_0\epsilon_s \cdot 2h} = \frac{\epsilon_s - \epsilon_m}{\epsilon_s + \epsilon_m} \cdot \frac{q}{4\pi\epsilon_0\epsilon_s \cdot 2h} \quad (6.23)$$

The dielectric constant,  $\epsilon_m$ , can be considered to be very large, and in this case eq 6.23 reduces to:

$$V'(q) = -\frac{q}{4\pi\epsilon_0\epsilon_s \cdot 2h} \quad (6.24)$$

Then the electrostatic interaction energy induced by the image charge,  $w_c^e$ , can be expressed as:

$$w_c^e = \int_0^{ze} V'(q) dq = \frac{z^2 e^2}{8\pi\epsilon_0\epsilon_s \cdot 2h} \quad (6.25)$$

Introducing eq 6.25 to eq 6.22,  $w_c^s$  is obtained:

$$w_c^s = \frac{z^2 e^2}{8\pi\epsilon_0} \left[ \left( \frac{1}{\epsilon_s} - \frac{1}{\epsilon_d} \right) \left( \frac{1}{r_0 + d} \right) + \frac{1}{\epsilon_d r_0} - \frac{1}{2\epsilon_s h} \right] \quad (6.26)$$

Therefore, the standard Gibbs solvation energies of a surface self-assembled MPC<sup>Z</sup>, can be derived from eq 6.7:

$$\Delta G_{\text{sol}, \text{MPC}^Z}^0 = \frac{z^2 e^2}{8\pi\epsilon_0} \left[ \left( \frac{1}{\epsilon_s} - 1 \right) \left( \frac{1}{r_0 + d} \right) - \frac{1}{2\epsilon_s h} \right] + w_n \quad (6.27)$$

The ionization energy of MPC<sup>Z-1</sup> in vacuum ( $E_{1,Z-1}^0$ ) is equal to the sum of the work function of the bulk metal and the work of charging an MPC from charged state  $z-1$  to  $z$  in vacuum.<sup>15, 23</sup> Neither of these two works is affected by the electrostatic interaction. This means that  $E_{1,Z-1}^0$  is the same for a freely diffusing and a surface attached MPC<sup>Z-1</sup> defined by eq 6.14.

Finally, from eqs 6.7, 6.14 and 6.27, the absolute standard redox potential of MPCs attached to electrode surface can be derived as:

$$\left[ E_{Z/Z-1}^0 \right]_{\text{abs., assembly}} = \frac{\Phi_b}{e} + \frac{\left( z - \frac{1}{2} \right) e}{4\pi\epsilon_0 (r_0 + d)} \left[ \frac{d}{\epsilon_d r_0} + \frac{1}{\epsilon_s} - \frac{r_0 + d}{2\epsilon_s h} \right] \quad (6.28)$$

Combining eqs 6.15 and 6.28, we can arrive eq 6.21.

Theoretical considerations based solely on the assumption of the MPC molecular capacitance are not sufficient to describe the redox properties of self-assembled MPCs.<sup>16</sup> According to eq 6.28, there are three contributions to the absolute standard redox potential of self-assembled MPCs, the MPC molecular structure (which can be related to the MPC molecular capacitance), the solvent dielectric constant and the electrostatic interaction. As shown in this section, the occurrence of successive redox reactions with a

smaller  $\Delta V$  for self-assembled MPCs can be ascribed to the effect of electrostatic interactions between MPCs and substrate electrode. However, it should be mentioned that the redox properties of MPCs are controlled by a variety of factors which were not considered in this section. For instance, an even smaller peak-to-peak spacing has been observed in voltammetric responses of self-assembled MPCs in aqueous media.<sup>17</sup> Since  $\epsilon_s$  is very large, the influence of both the solvent dielectric and the electrostatic interaction would be minor. In this case, the much smaller  $\Delta V$  can be ascribed mainly to the increment of  $\epsilon_d$  caused by the penetration of electrolyte ions into the MPC protecting layers. The effect of electrolyte ions on the redox properties of self-assembled MPCs will be further approached in the following section by studying the redox properties of self-assembled MPCs in room temperature ionic liquids (RTILs).

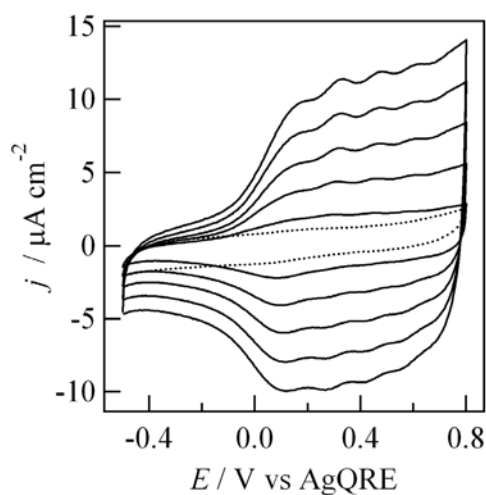
## 6.5 Redox properties of self-assembled MPCs in RTILs

Concerning the self-assembled MPCs, one more interesting phenomenon worthy of further investigation is that in aqueous media they present very different redox behavior with that in organic media.<sup>17, 40</sup> As shown in last two sections, self-assembled MPCs, as well as the freely diffusing MPCs, demonstrate a successive redox feature in the whole potential range. In contrast, in aqueous media self-assembled MPCs only illustrate redox behavior in the positive potential regime, which means that MPCs self-assembled on the electrode surface can only be oxidized. Whereas in the negative potential regime, the current flow through the self-assembled MPCs is depressed in comparison to a naked gold electrode. In this sense the MPC surface assembly behaves like a molecular diode (current rectifier). And furthermore, the oxidation of self-assembled MPCs is controlled by the supporting electrolyte anions present in the aqueous solution but insensitive to the electrolyte cations. For instance, the oxidation occurs in the presence of  $\text{ClO}_4^-$ ,  $\text{PF}_6^-$  and  $\text{BF}_4^-$  but not  $\text{NO}_3^-$ ,  $\text{Cl}^-$  and  $\text{SO}_4^{2-}$ . This phenomenon has been termed “anion-rectification” effect.

It is well known that RTILs are “designer solvent” with structures and properties easily modified by simply changing the ionic components. With this priority, three types of RTILs are prepared as described in section 2.8 of Chapter 2. They have the same cation, 1-*n*-butyl-3-methylimidazolium, but different anions, PF<sub>6</sub><sup>-</sup>, Tf<sub>2</sub>N<sup>-</sup> and BF<sub>4</sub><sup>-</sup>. The comparison of their physicochemical properties can be found in Table 2.1 of Chapter 2. This section will present the preliminary results on redox properties of self-assembled MPCs in these three types of RTILs. The anion rectification effect on the redox behavior of MPCs as those in aqueous media is observed.

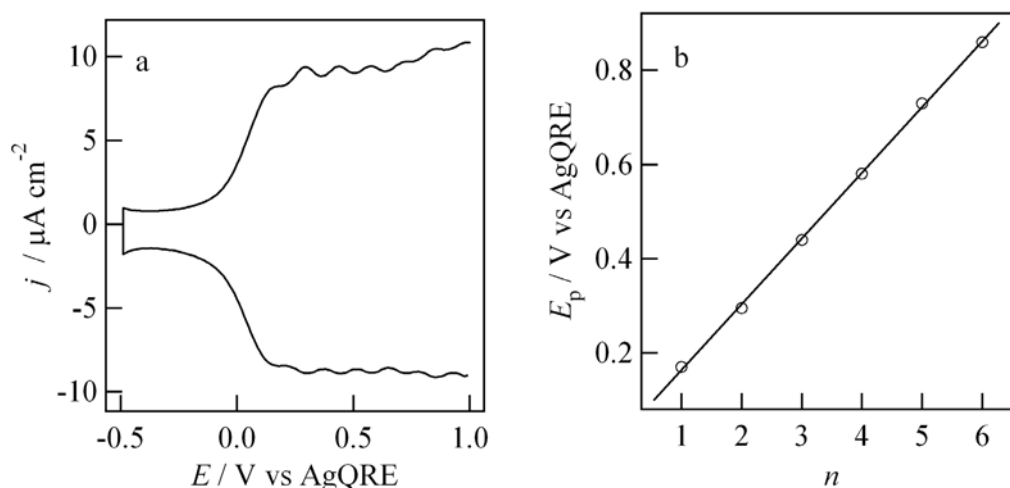
### 6.5.1 In [bmim][PF<sub>6</sub>]

Figure 6.13 shows CVs of MPCs self-assembled on a gold electrode in [bmim][PF<sub>6</sub>] at various scan rates. The corresponding CV of a bare gold electrode is also shown for comparison. In the positive potential regime, self-assembled MPCs display multiple well-defined voltammetric peaks, resulting from the successive electron transfer reactions between MPCs and the gold electrode. These responses are qualitatively similar to those of freely diffusing in electrolyte solutions observed above.



**Figure 6.13** CVs of self-assembled MPCs in [bmim][PF<sub>6</sub>] at various scan rates (solid lines): 0.1, 0.2, 0.3, 0.4 and 0.5 V s<sup>-1</sup> (from inner to outer). The dotted line represents the CV of a naked gold slide at 0.1 V s<sup>-1</sup>.

Figure 6.14a illustrates the corresponding DPV responses of the self-assembled MPCs in [bmim][PF<sub>6</sub>]. A series of current peaks are spaced approximately the same distance apart on the potential axis. There is also a linear correspondence between the peak potential and the MPC charge state, as demonstrated in Figure 6.14b. An average  $\Delta V$  of 0.14 V is obtained from the linear fitting. This value is smaller than those of freely diffusing C<sub>6</sub>Au MPCs and self-assembled (C<sub>6</sub>-C<sub>9</sub>)Au MPCs in DCE electrolyte solutions, as compared in Table 6.4. It is apparent that there is a 30% decrease in  $\Delta V$  (from 0.20 V to 0.14 V) when transferring the self-assembled (C<sub>6</sub>-C<sub>9</sub>)Au MPC monolayer from the DCE electrolyte solution to [bmim][PF<sub>6</sub>]. This phenomenon is similar to that illustrated in a previous work, where a 25-50% decrease in  $\Delta V$  was observed when transferring the self-assembled MPCs from an organic solution to aqueous media.<sup>17</sup>



**Figure 6.14** (a) DPVs of self-assembled MPCs in [bmim][PF<sub>6</sub>]: 0.02 V s<sup>-1</sup>, pulse height 0.05 V, pulse width 0.05 s and period 0.5 s; (b) the relationship between the peak potentials and the peak number.

**Table 6.4** Comparison of the average potential spacing of the successive electron transfer events for MPCs in different conditions.

System	$\Delta V$ (V)
freely diffusing MPCs in DCE (0.05 M TBAClO <sub>4</sub> )	0.25
self-assembled MPCs in DCE (0.05 M TBAClO <sub>4</sub> )	0.20
self-assembled MPCs in [bmim][PF <sub>6</sub> ]	0.14
self-assembled MPCs in [bmim][Tf <sub>2</sub> N]	0.15

In terms of eq 6.28, the additive contributions of solvent dielectric constant and the electrostatic interaction to  $\Delta V$  can be evaluated to be 0.03 V, taking  $\epsilon_{[\text{bmim}][\text{PF}_6]} = 11.4$ <sup>41</sup> and other parameters as previously employed. The remaining 0.11 V is ascribed to the contribution of the MPC molecular structure itself, including the core size, the length and the dielectric constant of the coating layer. Therefore,  $\epsilon_d$  can be estimated to be 8.2, which is significantly larger than 3.0 of the intrinsic alkanethiol chain. This reflects either a strong penetration of ionic liquids into the alkanethiolate monolayer or the specific interactions between the MPC spheres and ionic components in [bmim][PF<sub>6</sub>], both of which could effectively increase the value of  $\epsilon_d$ .

As shown in Figures 6.13 and 14a, voltammetric waves only appear in the positive potential regime, while a featureless response is observed in the negative potential range. This indicates that only the oxidation of self-assembled MPCs occurs. This response differs from those observed in organic media, as shown in section 6.4, where the self-assembled MPCs are redox-active in the whole potential range. Instead, it is similar to those observed in aqueous media in the presence of certain electrolyte anions, such as ClO<sub>4</sub><sup>-</sup>, PF<sub>6</sub><sup>-</sup> and BF<sub>4</sub><sup>-</sup>.<sup>17, 40</sup> This feature was ascribed to the effect of ionic rectification. The rectification mechanism was interpreted on the basis of penetration of electrolyte anions into the MPC protecting monolayers and the ion-pair formation between charged MPCs and anions.

### 6.5.2 In [bmim][Tf<sub>2</sub>N] and [bmim][BF<sub>4</sub>]

The voltammetric responses of self-assembled MPCs in [bmim][Tf<sub>2</sub>N] are displayed in Figure 6.15. Although the purity of [bmim][Tf<sub>2</sub>N] can be questioned due to the presence of an unknown peak on the CV of the anked electrode, the successive oxidation of self-assembled MPCs is clearly observed. The redox behavior of self-assembled MPCs in [bmim][Tf<sub>2</sub>N] resembles that observed in [bmim][PF<sub>6</sub>]. The successive electron transfer occurs only in the positive potential range with an average voltage spacing of 0.15 V. However, in [bmim][BF<sub>4</sub>], the self-assembled MPCs only exhibit featureless voltammetric responses, as illustrated in Figure 6.16. Apparently, the oxidation of self-assembled MPCs in RTILS is rectified by the anionic components as observed previously in aqueous media.

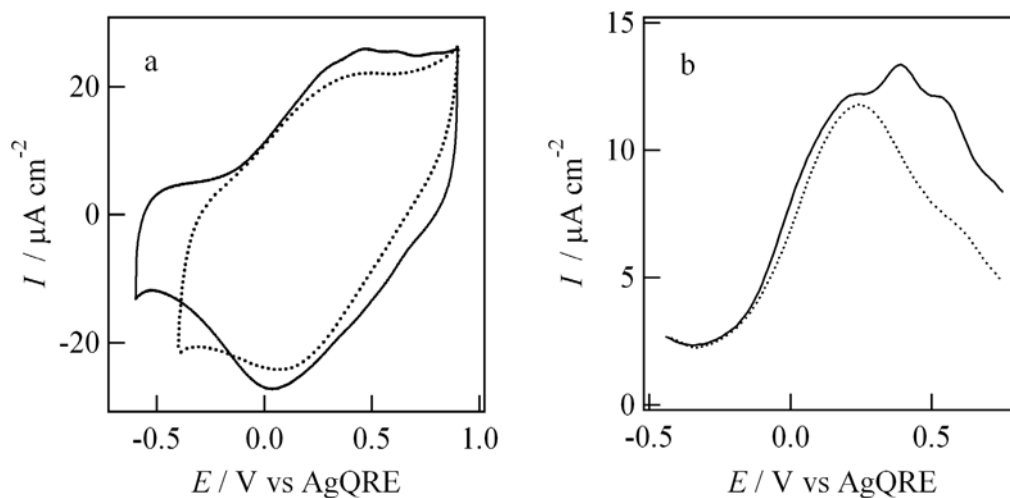


**Figure 6.15** (a) CVs of self-assembled MPCs in [bmim][Tf<sub>2</sub>N] at scan rates of 0.1 V s<sup>-1</sup>; (b) The corresponding DPVs: scan rate of 0.01 V s<sup>-1</sup>, pulse height 0.05 V, pulse width 0.05 s and period 0.2 s V. The responses of a naked gold electrode were also shown with dotted lines for comparison.

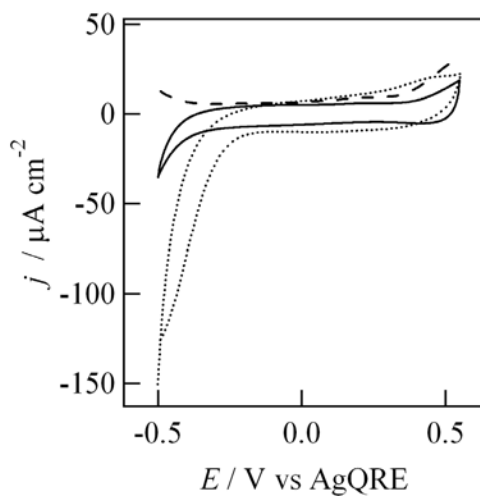


**Figure 6.16** CV (solid line) and DPV (dashed line) of self-assembled MPCs in [bmim][BF<sub>4</sub>]. The dotted line represents the CV response of a naked gold slide electrode. The CVs were recorded at a scan rate of 0.1 V s<sup>-1</sup>. The DPV was obtained at: scan rate of 0.01 V s<sup>-1</sup>, pulse height 0.05 V, pulse width 0.05 s and period 0.2 s V.



### 6.5.3 Analysis of anion rectification effect

The anion rectification effect can be rationalized by considering the interfacial structure of self-assembled MPCs on an electrode surface, the properties of RTILs and the possible interactions involved in the rectification process. With the present protocol for the self-assembled MPCs, the electrode surface is only partially covered by MPCs with large interparticle voids due to the steric hindrance between particles. Since [bmim][PF<sub>6</sub>] and [bmim][Tf<sub>2</sub>N] are hydrophobic, both electrostatic and hydrophobic interactions favor the penetration or binding of the anions into the MPC protecting monolayers, which significantly affect the dielectric environment of the self-assembled MPCs and allow the electron transfer through MPCs. In contrast, [bmim][BF<sub>4</sub>] is hydrophilic, and the penetration or binding of BF<sub>4</sub><sup>-</sup> to MPCs is inhibited. In this case, the self-assembled MPCs act as insulators and the current flows mainly through the naked electrode surface.

## 6.6 Conclusions

In this chapter, the absolute standard redox potential of MPCs in solutions was theoretically derived from electrostatic considerations taking the bulk solvent effect into account. The valence state of MPCs at a given potential can be estimated by employing an internal redox molecular reference, such as ferrocenium/ferrocene.<sup>39</sup> The derivation also indicates that the solvent has significant effect on the redox properties of MPCs. This point was verified experimentally by studies in various organic solvents. In addition, the redox properties of MPCs self-assembled on a gold electrode surface through dithiol linkers were studied in organic electrolyte solutions. The effect of the electrostatic interaction between MPCs and the electrode on the redox behavior of MPCs was theoretically considered in terms of the method of images in classical electrostatics and justified experimentally. Finally, the redox properties of self-assembled MPCs were studied in room temperature RTILs. The rectification of the successive oxidation of self-assembled MPCs by the anionic component of RTILs was observed.

---

## 6.7 References

- (1) Brust, M.; Walker, M.; Bethell, D.; Schiffrin, D. J.; Whyman, R. *J. Chem. Soc. Chem. Commun.* **1994**, 801.
- (2) Brust, M.; Fink, J.; Bethell, D.; Schiffrin, D. J.; Kiely, C. *J. Chem. Soc. Chem. Commun.* **1995**, 1655.
- (3) Ingram, R. S.; Hostetler, M. J.; Murray, R. W.; Schaaff, T. G.; Khoury, J.; Whetten, R. L.; Bigioni, T. P.; Guthrie, D. K.; First, P. N. *J. Am. Chem. Soc.* **1997**, *119*, 9279.
- (4) Chen, S.; Ingrma, R. S.; Hostetler, M. J.; Pietron, J. J.; Murray, R. W.; Schaaff, T. G.; Khoury, J. T.; Alvarez, M. M.; Whetten, R. L. *Science* **1998**, *280*, 2098.
- (5) Chen, S. *J. Electroanal. Chem.* **2004**, *574*, 153.
- (6) Templeton, A. C.; Wuelfing, W. P.; Murray, R. W. *Acc. Chem. Res.* **2000**, *33*, 27.
- (7) Dubois, D.; Kadish, K. M.; Flanagan, S.; Haufler, R. E.; Chibante, L. P. F.; Wilson, L. J. *J. Am. Chem. Soc.* **1991**, *113*, 4364.
- (8) Dubois, D.; Moninot, G.; Kutner, W.; Jones, M. T.; Kadish, K. M. *J. Phys. Chem.* **1992**, *96*, 7137.
- (9) Haufler, R. E.; Conceicao, J.; Chibante, L. P. F.; Chai, Y.; Byrne, N. E.; Flanagan, S.; Haley, M. M.; O'Brien, S. C.; Pan, C.; et al. *J. Phys. Chem.* **1990**, *94*, 8634.
- (10) Koh, W.; Dubois, D.; Kutner, W.; Jones, M. T.; Kadish, K. M. *J. Phys. Chem.* **1992**, *96*, 4163.
- (11) Jehoulet, C.; Bard, A. J.; Wudl, F. *J. Am. Chem. Soc.* **1991**, *113*, 5456.
- (12) Lewis, G. J.; Roth, J. D.; Montag, R. A.; Safford, L. K.; Gao, X.; Chang, S. C.; Dahl, L. F.; Weaver, M. J. *J. Am. Chem. Soc.* **1990**, *112*, 2831.
- (13) Roth, J. D.; Lewis, G. J.; Jiang, X.; Dahl, L. F.; Weaver, M. J. *J. Phys. Chem.* **1992**, *96*, 7219.
- (14) Roth, J. D.; Lewis, G. J.; Safford, L. K.; Jiang, X.; Dahl, L. F.; Weaver, M. J. *J. Am. Chem. Soc.* **1992**, *114*, 6159.
- (15) Weaver, M. J.; Gao, X. *J. Phys. Chem.* **1993**, *97*, 332.
- (16) Chen, S.; Murray, R. W.; Feldberg, S. W. *J. Phys. Chem. B* **1998**, *102*, 9898.
- (17) Chen, S.; Pei, R. *J. Am. Chem. Soc.* **2001**, *123*, 10607.
- (18) Hicks, J. F.; Templeton, A. C.; Chen, S.; Sheran, K. M.; Jasti, R.; Murray, R. W.; Debord, J.; Schaaff, T. G.; Whetten, R. L. *Anal. Chem.* **1999**, *71*, 3703.

- (19) Miles, D. T.; Murray, R. W. *Anal. Chem.* **2003**, *75*, 1251.
- (20) Quinn, B. M.; Liljeroth, P.; Ruiz, V.; Laaksonen, T.; Kontturi, K. *J. Am. Chem. Soc.* **2003**, *125*, 6644.
- (21) Guo, R.; Georganopoulou, D.; Feldberg, S. W.; Donkers, R.; Murray, R. W. *Anal. Chem.* **2005**, *77*, 2662.
- (22) Girault, H. H. *Analytical and Physical Electrochemistry*; EPFL Press: Lausanne, 2004.
- (23) Makov, G.; Nitzan, A.; Brus, L. E. *J. Chem. Phys.* **1988**, *88*, 5076.
- (24) Evans, S. D.; Ulman, A. *Chem. Phys. Lett.* **1990**, *170*, 462.
- (25) Chen, S.; Murray, R. W. *J. Phys. Chem. B* **1999**, *103*, 9996.
- (26) Wuelfing, W. P.; Templeton, A. C.; Hicks, J. F.; Murray, R. W. *Anal. Chem.* **1999**, *71*, 4069.
- (27) Stranks, D. R. *Diss. Faraday Soc.* **1960**, No. 29, 73.
- (28) Linstrom, P. J.; Mallard, W. G. *The NIST WebBook*, 1998.
- (29) Fermin, D. J.; Lahtinen, R. *Surfactant Science Series* **2001**, *95*, 179.
- (30) Zhang, M.; Liu, H.; Hu, H.; Xie, S.; Jing, P.; Li, M.; Gan, L.; Kou, Y.; Shao, Y. *submitted*.
- (31) Quinn, B. M.; Liljeroth, P.; Kontturi, K. *J. Am. Chem. Soc.* **2002**, *124*, 12915.
- (32) Hicks, J. F.; Miles, D. T.; Murray, R. W. *J. Am. Chem. Soc.* **2002**, *124*, 13322.
- (33) Chen, S. *J. Phys. Chem. B* **2000**, *104*, 663.
- (34) Hicks, J. F.; Young, S.-S.; Murray, R. W. *Langmuir* **2002**, *18*, 2288.
- (35) Wuelfing, W. P.; Green, S. J.; Pietron, J. J.; Cliffler, D. E.; Murray, R. W. *J. Am. Chem. Soc.* **2000**, *122*, 11465.
- (36) Zamborini, F. P.; Hicks, J. F.; Murray, R. W. *J. Am. Chem. Soc.* **2000**, *122*, 4514.
- (37) Pietron, J. J.; Hicks, J. F.; Murray, R. W. *J. Am. Chem. Soc.* **1999**, *121*, 5565.
- (38) Hicks, J. F.; Zamborini, F. P.; Murray, R. W. *J. Phys. Chem. B* **2002**, *106*, 7751.
- (39) Su, B.; Girault, H. H. *J. Phys. Chem. B* **2005**, *109*, 11427.
- (40) Chen, S. *J. Am. Chem. Soc.* **2000**, *122*, 7420.
- (41) Wakai, C.; Oleinikova, A.; Ott, M.; Weingaertner, H. *J. Phys. Chem. B* **2005**, *109*, 17028.



## Chapter 7

# Reactivity of monolayer-protected gold nanoclusters at dye-sensitized liquid|liquid interfaces

### 7.1 Introduction

An important property of metallic NPs is their propensity to act as electron donors or acceptors. As shown in last chapter, alkanethiolate monolayer-protected gold nanoclusters (MPCs) are formally equivalent to multivalent redox species which exhibit equally spaced formal redox potentials. The metallic cores of MPCs can both donate and accept electrons in electron transfer reactions. In addition, previous studies have shown that MPCs can be electrochemically charged to the desired valence state in solutions. The charged MPCs are stable and can even be isolated in a solid form. This property enables MPCs to act as tunable and quantitative redox probes in electron transfer chemistry. The redox properties of MPCs have been extensively studied in electrolyte solutions,<sup>1-6</sup> in surface assemblies and films,<sup>7-21</sup> and at the air|water<sup>22</sup> and liquid|liquid<sup>5, 23, 24</sup> interfaces. Photochemical experiments have also demonstrated several examples of excited-state

quenching of surface-bound dyes by the metallic MPC cores through energy transfer<sup>25-27</sup> or electron transfer.<sup>28</sup> The heterogeneous electron transfer reaction between Au<sub>140</sub> MPCs dissolved in DCE and aqueous redox species was first reported by Quinn *et al.* using SECM.<sup>5</sup> They found that that electron transfer reaction was surprisingly slow, which was rationalized in terms of the large size and hydrophobicity of the MPCs resulting in a large separation between the reactants. However, later in another work the electron transfer reaction between organic soluble Au<sub>38</sub> MPCs and aqueous redox species was found to be faster than similar electron transfer reactions between conventional aqueous and organic redox species at the liquid|liquid interface.<sup>23</sup> The dependences of the effective heterogeneous rate constant on the concentration of the aqueous redox mediator and reaction driving force were found to be in agreement with theoretical expectations.

In this chapter, we shall employ MPCs as redox quenchers in heterogeneous photoelectrochemical reactions at the polarized water|DCE interface. Photocurrent responses originating from the heterogeneous quenching of photo-excited water-soluble porphyrin complexes by MPCs present in the organic phase will be investigated.

## 7.2 Photocurrent responses involving MPCs

Figure 7.1 displays the composition of the electrochemical cell. Zinc *meso*-tetrakis(*p*-sulfonatophenyl)porphyrin tetrasodium (Na<sub>4</sub>ZnTPPS) and zinc *meso*-(*N*-methylpyridyl)porphyrin tetratosylate (ZnTMPyP(tosylate)<sub>4</sub>) are co-dissolved in the aqueous phase and MPCs are dispersed in the DCE phase. For simplicity, in this chapter the MPC will be designated MPC<sup>z</sup>, in which *z* indicates the initial valence state.

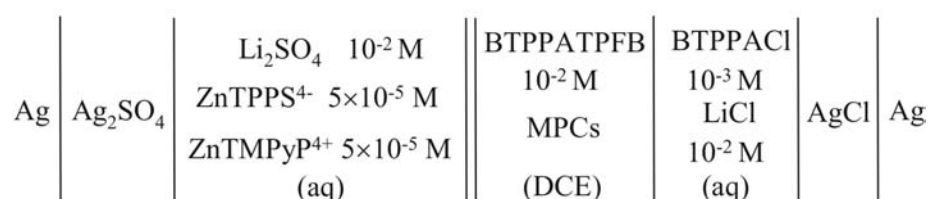


**Figure 7.1** The cell employed for electrochemical and photocurrent measurements.

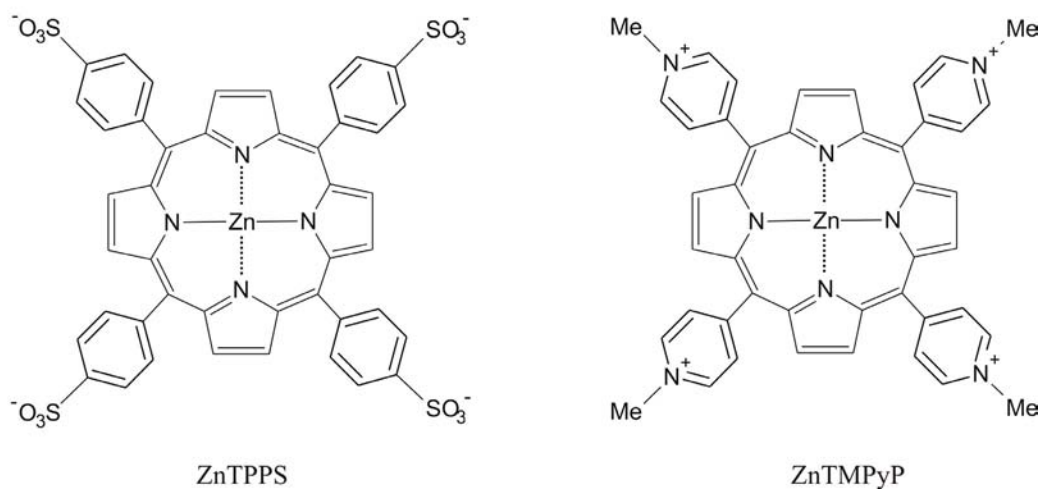


**Figure 7.2** Molecular structures of ZnTPPS and ZnTMPyP.

Figure 7.2 presents the basic molecular structures of ZnTPPS and ZnTMPyP, with four *p*-sulfonatophenyl or *N*-methylpyridyl substituents, respectively, at the *meso* positions of a zinc metalloporphyrin substructure. In the presence of both ZnTPPS and ZnTMPyP in solution, these porphyrins form 1:1 heterodimers by spontaneous electrostatic association with a face-to-face conformation. The co-facial configuration of the heterodimer allows electronic coupling between porphyrin rings. Ultrafast time-resolved spectroscopy reveals that the photoexcitation of the dimer leads to a charge-separated state of the form [ZnTPPS<sup>3-</sup>-ZnTMPyP<sup>3+</sup>] within 40 ps. This charge separated state has a lifetime in the microsecond time scale and can be involved in heterogeneous electron transfer at the water|DCE interface.<sup>29</sup> The photophysical properties of this dimer have been well studied previously.<sup>30</sup>

Figure 7.3a shows the polarizable potential window of the water|DCE interface in the absence and presence of MPC<sup>Z</sup> in DCE phase. The similarity of these two CV curves indicates that MPC<sup>Z</sup> has no substantial effect on the electrochemical behavior of the water|DCE interface. The solid line in Figure 7.3b is the CV in the presence of the ZnTPPS<sup>4-</sup>-ZnTMPyP<sup>4+</sup> complex in aqueous phase. The signals observed close to the ends of the potential window correspond to the transfer and adsorption of porphyrin ions and their counterions.<sup>31</sup> Again, the addition of MPC<sup>Z</sup> to the system did not result in substantial changes in the CV response. This indicates not only that the presence of MPC<sup>Z</sup> has negligible effect on the specific adsorption of the porphyrin complex, but also

that no electron exchange occurs between  $\text{MPC}^Z$  and the ground state of the porphyrin complex. As shown in Figure 7.3b, no faradaic responses are observed between  $-0.15$  V and  $0.10$  V. The Galvani potential difference will be constrained within this potential region in all subsequent photocurrent measurements. In addition, it has been shown that the porphyrin complex exhibits nearly full interfacial coverage of the water|DCE boundary in this potential range.<sup>32</sup>

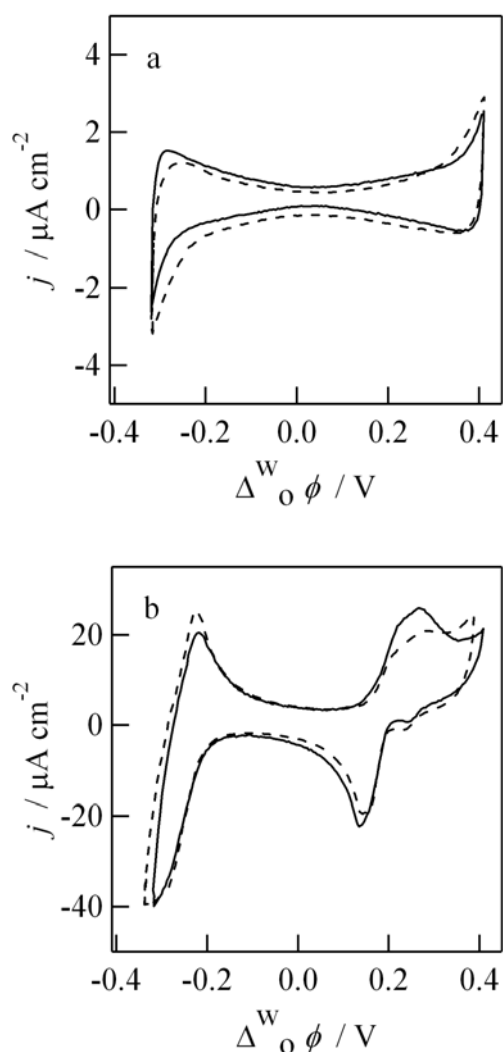


**Figure 7.3** (a) CVs at the water|DCE interface in the absence (solid) and presence (dashed) of ca.  $0.02$  mM Au  $\text{MPC}^Z$  in DCE. (b) CVs of the porphyrin complex at the water|DCE interface in the absence (solid) and presence (dashed) of ca.  $0.02$  mM Au  $\text{MPC}^Z$  in DCE. In all cases, the scan rate is  $50$   $\text{mV s}^{-1}$ .



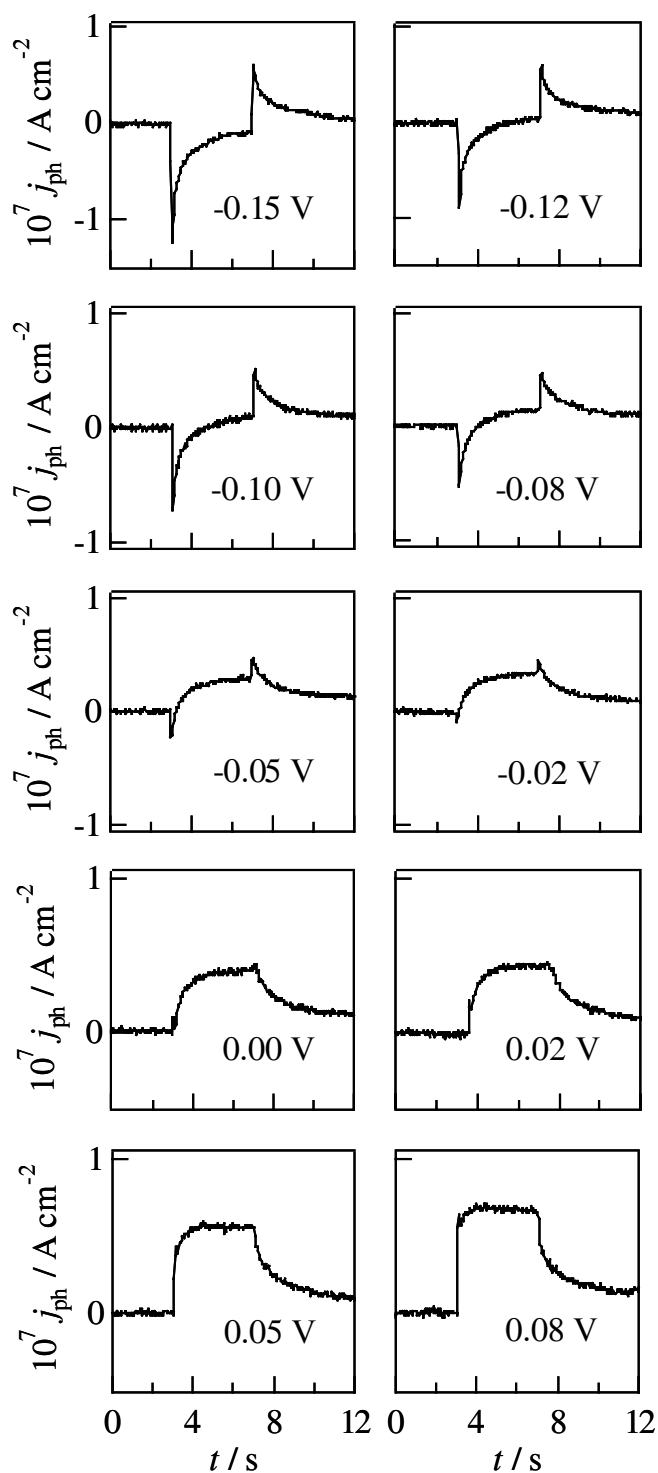


**Figure 7.4** Photocurrent transient responses obtained in the presence of ca. 0.02 mM  $\text{MPC}^{\text{Z}}$  in DCE and 50  $\mu\text{M}$   $\text{ZnTPPS}^+ - \text{ZnTMPyP}^{4+}$  in water at various Galvani potential differences.

Photocurrent responses at various Galvani potential differences in the presence of the porphyrin complex in water and MPC<sup>Z</sup> in DCE are displayed in Figure 7.4. As described in the literature, gold NPs show limited photoactivity under UV-visible light,<sup>28</sup> although photoinduced fusion and fragmentation of nanorods<sup>33-35</sup> and near-IR luminescence of MPCs<sup>36-38</sup> have been observed. The excited electrons in NPs follow fast relaxations via electron-phonon coupling and phonon-phonon interaction of the lattice on the picosecond time scale.<sup>39</sup> On the other hand, as mentioned above photoexcitation of the porphyrin complex leads to a charge separated state with a lifetime in the microsecond time scale.<sup>29</sup> Based on these considerations, we conclude that the photocurrent responses observed in Figure 7.4 arise from the heterogeneous electron transfer between the charge-separated state of the porphyrin complex and the ground state MPC. As demonstrated in Chapter 6, the DPV response of as-prepared MPCs in the DCE electrolyte solution features a series of well-resolved current peaks, which are evenly spaced with a separation about 240 mV. In a formal sense, each peak potential is equivalent to the standard redox potential of an MPC “redox couple” with adjacent valence states. Therefore, an MPC can be regarded as a multivalent redox species exhibiting plentiful standard redox potentials. For simplicity, we shall denote MPCs in the initial state as MPC<sup>Z</sup>, which can be reduced to MPC<sup>Z-1</sup> and oxidized to MPC<sup>Z+1</sup>.

A clear feature of the responses in Figure 7.4 is the evolution of the photocurrent from negative to positive values with increasing the Galvani potential difference. Previous works have shown that the excited porphyrin complex can be heterogeneously quenched by both electron acceptors (such as quinones) and electron donors (such as ferrocene derivatives).<sup>29, 32</sup> As MPCs can function as both electron acceptors and electron donors, the heterogeneous electron transfer across the liquid|liquid interface takes place in both directions:



where S\* corresponds to the photoexcited porphyrin complex in the aqueous phase, and S<sup>+</sup> and S<sup>-</sup> denote the oxidized and reduced states of the porphyrin complex.

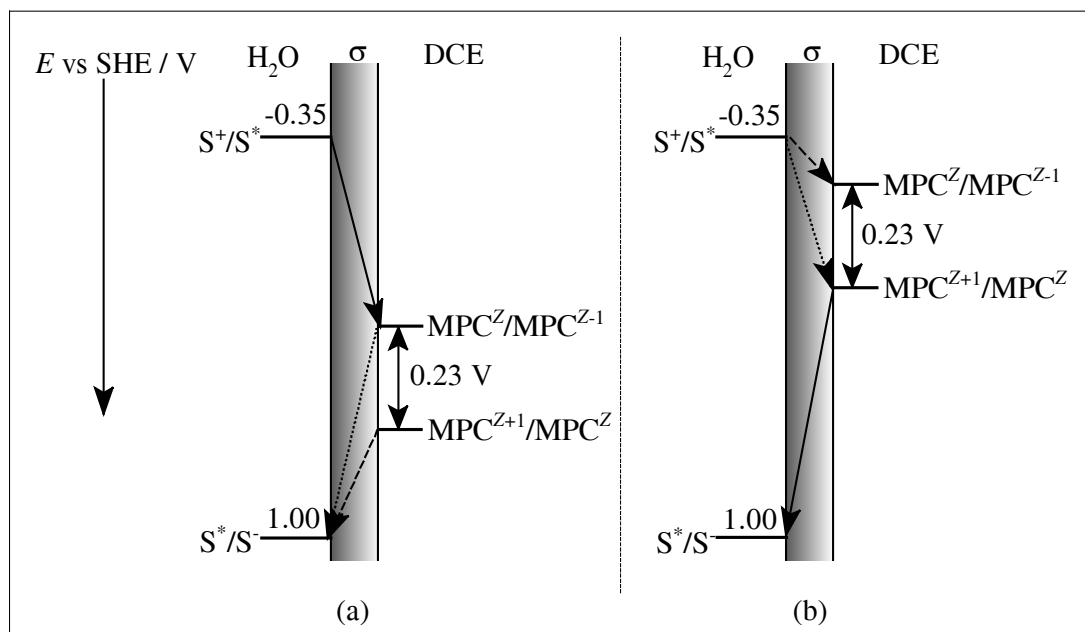


**Figure 7.5** Diagrams of the photoinduced electron transfer reactions: (a) electron injection from the porphyrin complex to  $\text{MPC}^Z$ ; (b) electron injection from  $\text{MPC}^Z$  to the porphyrin complex. The interfacial region is denoted as  $\sigma$ . The solid, dotted and dashed arrows denote the dominant electron transfer reaction, the charge recombination reaction and the opposite electron transfer reaction, respectively.

Under the potentiostatic conditions used in this work, the heterogeneous electron transfer reaction described by eq 7.1 results in a negative current when the interface is illuminated. Similarly to the case of quinone quenchers,<sup>29</sup> this reaction is favored when a negative Galvani potential difference is applied between the aqueous and organic phases. This behavior is reflected in the increase of the photocurrent magnitude when more negative potentials are applied (Figure 7.4). On the other hand, in the case of eq 7.2 the electron transfer manifests itself as positive photocurrents, which are expected to increase when the potential is set to more positive values.

When the Galvani potential difference is tuned from a negative value to more positive values, the negative response decreases while positive photocurrents become dominant. These two separate dependences of the kinetics of reactions 7.1 and 7.2 on the Galvani potential difference are in line with the published data on heterogeneous quenching of porphyrin complex by quinones<sup>29</sup> or ferrocene derivatives.<sup>32</sup> However, in the present case the two reactions occur simultaneously, which results in the convoluted responses observed at intermediate potentials. The magnitude and shape of the photocurrent

transient are determined by the balance between the kinetics of these two reactions. This phenomenon can be rationalized by the scheme in Figure 7.5, which illustrates the electron transfer process for MPC<sup>Z</sup> reduction (a) as well as oxidation (b). The relative difference in redox potential between the porphyrin complex and MPC<sup>Z</sup> depends on the applied potential. For instance, it can be considered that the situation in Figure 7.5a occurs when a negative Galvani potential difference is applied between the two phases, while Figure 7.5b corresponds to the case of positive potentials. The solid arrows show the dominant electron transfer reaction in each case. From the diagrams in Figure 7.5, the formal Gibbs energies for reactions 7.1 and 7.2 can be defined respectively as:

$$\Delta G_{\text{et},1}^{\circ'} = F \left( \left[ E_{\text{S}^+/\text{S}^{\circ'}}^{\circ',\text{w}} \right]_{\text{SHE}} - \left[ E_{\text{MPC}^Z/\text{MPC}^{Z-1}}^{\circ',\text{o}} \right]_{\text{SHE}} + \Delta_{\text{o}}^{\text{w}} \phi \right) = F \left( \Delta_{\text{o}}^{\text{w}} \phi - \Delta_{\text{o}}^{\text{w}} \phi_{\text{et},1}^{\circ'} \right) \quad (7.3)$$

$$\Delta G_{\text{et},2}^{\circ'} = F \left( \left[ E_{\text{MPC}^{Z+1}/\text{MPC}^Z}^{\circ',\text{o}} \right]_{\text{SHE}} - \left[ E_{\text{S}^{\circ'}/\text{S}^{\circ}} \right]_{\text{SHE}} - \Delta_{\text{o}}^{\text{w}} \phi \right) = -F \left( \Delta_{\text{o}}^{\text{w}} \phi - \Delta_{\text{o}}^{\text{w}} \phi_{\text{et},2}^{\circ'} \right) \quad (7.4)$$

where  $\left[ E_{\text{S}^+/\text{S}^{\circ'}}^{\circ',\text{w}} \right]_{\text{SHE}}$ ,  $\left[ E_{\text{S}^{\circ'}/\text{S}^{\circ}} \right]_{\text{SHE}}$  are the formal redox potentials of the excited porphyrin complex in water and  $\left[ E_{\text{MPC}^Z/\text{MPC}^{Z-1}}^{\circ',\text{o}} \right]_{\text{SHE}}$ ,  $\left[ E_{\text{MPC}^{Z+1}/\text{MPC}^Z}^{\circ',\text{o}} \right]_{\text{SHE}}$  those of MPCs in DCE.  $\Delta_{\text{o}}^{\text{w}} \phi_{\text{et},1}^{\circ'}$  and  $\Delta_{\text{o}}^{\text{w}} \phi_{\text{et},2}^{\circ'}$  correspond to the formal electron transfer potentials. When the potential is varied from negative to positive values (i.e., from Figure 7.5a to Figure 7.5b), the redox potential of MPC<sup>Z</sup> shifts to more negative values relative to that of the porphyrin complex in water. Consequently, the Gibbs energy associated with the oxidation of MPC<sup>Z</sup> (eq 7.2) gradually increases while that of eq 7.1 decreases. The dependence of the electron transfer rate constants on the Gibbs energies expressed by eqs 7.3 and 7.4 gives rise to the changes in photocurrent responses observed in Figure 7.4.

The dashed arrows in Figure 7.5 illustrate the opposite processes, which feature slower kinetics due to the lower energy associated with these reactions. The dotted arrows represent charge recombination reactions. Directly after the heterogeneous electron transfer event, the products are expected to remain in close contact as geminate ion pairs  $\{\text{S}^+ \cdots \text{MPC}^{Z-1}\}$  or  $\{\text{S}^{\circ'} \cdots \text{MPC}^{Z+1}\}$  at the interface. As described in the next section, these species are involved in two competing processes: back charge transfer leading to the starting species or separation to the products of reactions 7.1 and 7.2. In the case of molecular quenchers, back charge transfer was observed to proceed as a first order reaction with time constant in the millisecond range.

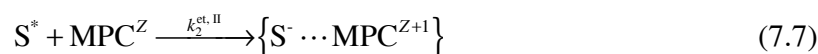
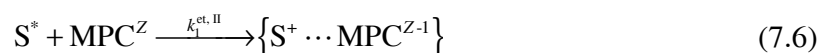
### 7.3 Analysis of the photocurrent transient

According to the scheme in Figure 7.5, the photoinduced electron transfer process can be described by the following set of reactions:

Excitation and relaxation of the porphyrin complex:



Heterogeneous electron transfer reactions:



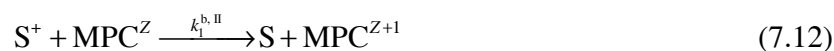
Recombination reactions:



Separation of the products:



Back electron transfer reactions:



On the basis of our previous formulation of photocurrent responses<sup>40</sup> and considering the relatively low magnitude of the signals in Figure 7.5, the concentrations of porphyrin complex and  $MPC^Z$  are taken to be constant. This allows describing the various charge transfer processes as pseudo-first order reactions with rate constants expressed by:

$$k^{et} = k^{et, II} [MPC^Z] \quad (7.14)$$

$$k^b = k^{b, II} [MPC^Z] \quad (7.15)$$

It should be noted that in the case of molecular quenchers such as quinones or ferrocene, reactions 7.12 and 7.13 do not exist. The terms recombination and back electron transfer were used indiscriminately to refer to reactions 7.8 and 7.9. In the present case, however,

these two terms correspond to different mechanisms. Taking the contributions from all the elementary steps, i.e., reactions 7.5-7.13, the photocurrent density as a function of time is obtained (Appendix):

$$j = g_1 F \cdot \left\{ \frac{k_1^{\text{ps}} \exp(-k_1^{\text{b}} t) + (k_1^{\text{rec}} - k_1^{\text{b}}) \exp[-(k_1^{\text{rec}} + k_1^{\text{ps}}) t]}{(k_1^{\text{rec}} + k_1^{\text{ps}} - k_1^{\text{b}})} \right\} + \quad (7.16)$$

$$+ g_2 F \cdot \left\{ \frac{k_2^{\text{ps}} \exp(-k_2^{\text{b}} t) + (k_2^{\text{rec}} - k_2^{\text{b}}) \exp[-(k_2^{\text{rec}} + k_2^{\text{ps}}) t]}{(k_2^{\text{rec}} + k_2^{\text{ps}} - k_2^{\text{b}})} \right\}$$

The parameters  $g_1$  and  $g_2$  correspond to the fluxes of electron injection associated with the electron transfer reactions 7.6 and 7.7:

$$g_1 = I_0 \sigma \Gamma_s \frac{-k_1^{\text{et}}}{k_d + k_1^{\text{et}} + k_2^{\text{et}}} \quad (7.17)$$

$$g_2 = I_0 \sigma \Gamma_s \frac{k_2^{\text{et}}}{k_d + k_1^{\text{et}} + k_2^{\text{et}}} \quad (7.18)$$

where  $I_0$  is the incident photo flux,  $\sigma$  the optical capture cross section,  $\Gamma_s$  the surface excess of porphyrin complex. The parameter  $\Gamma_s$  and  $\sigma$  can be taken as  $4.0 \times 10^{-10}$  mol  $\text{cm}^{-2}$  and  $1.0 \times 10^{-17}$   $\text{cm}^2$ , respectively.<sup>32</sup> Previous studies have shown that  $\Gamma_s$  is effectively potential independent over the range of Galvani potential differences used in Figure 7.4.<sup>30, 32</sup> The incident photon flux,  $I_0$ , is  $6.4 \times 10^{15}$   $\text{cm}^{-2} \text{ s}^{-1}$ . Based on time-resolved EPR spectroscopy and flash photolysis measurements at the water|DCE interface in total internal reflection,  $k_d$  is of the order of  $5.0 \times 10^5$   $\text{s}^{-1}$ . Knowing this, it is possible to extract information on the dependence of  $k_1^{\text{et}}$  and  $k_2^{\text{et}}$  on  $\Delta_o^w \phi$  from the values of the initial photocurrent  $j_0$ . This analysis does not take into account attenuation effects resulting from the uncompensated resistance, which will significantly complicate eq 7.16. As the photocurrent responses in Figure 7.4 appear very sharp, only minimal errors are introduced by this simplification. Considering that a purely negative response is obtained at -0.15 V, a simulation using our previously published model shows an error of less than 5% on the value of  $j_0$ .<sup>40</sup> Finally, it should be mentioned that the formation of other oxidation states of MPCs, such as the photo-oxidation  $\text{MPC}^{\text{Z}+1}$  to  $\text{MPC}^{\text{Z}+2}$ , was not

considered either. Since the successive redox potentials of the MPCs are separated by more than 200 mV, the oxidation of  $\text{MPC}^{\text{Z}+1}$  to  $\text{MPC}^{\text{Z}+2}$  is expected to be slower than that of  $\text{MPC}^{\text{Z}}$  to  $\text{MPC}^{\text{Z}+1}$ . Furthermore, the concentration of  $\text{MPC}^{\text{Z}+1}$  remains much lower than that of  $\text{MPC}^{\text{Z}}$  at realistic illumination levels. Hence, these additional reaction pathways are expected to generate very little current, which is neglected for simplicity.

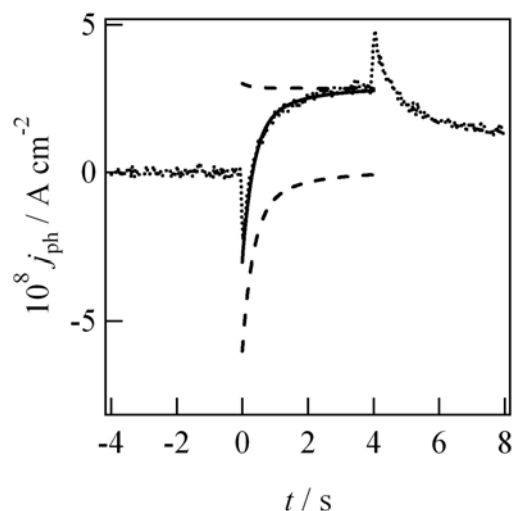


**Figure 7.6** Simulation of the photocurrent transient at 0.05 V. The dotted line corresponds to the experimental trace. The solid line was calculated from eq 7.16 using the following parameters:  $\Gamma_s = 4.0 \times 10^{-10} \text{ mol cm}^{-2}$ ,  $\sigma = 1.0 \times 10^{-17} \text{ cm}^2$ ,  $I_0 = 6.4 \times 10^{15} \text{ cm}^{-2} \text{ s}^{-1}$ ,  $k_d = 5.0 \times 10^5 \text{ s}^{-1}$ ,  $k_1^{\text{et}} = 9.2 \times 10^3 \text{ s}^{-1}$ ,  $k_2^{\text{et}} = 4.6 \times 10^3 \text{ s}^{-1}$ ,  $k_1^{\text{ps}} = 0.5 \text{ s}^{-1}$ ,  $k_2^{\text{ps}} = 3.5 \text{ s}^{-1}$ ,  $k_1^{\text{rec}} = 2.5 \text{ s}^{-1}$ ,  $k_2^{\text{rec}} = 0.2 \text{ s}^{-1}$ ,  $k_1^{\text{b}} = 0.7 \text{ s}^{-1}$ , and  $k_2^{\text{b}} = 0.01 \text{ s}^{-1}$ . The two dashed lines illustrate the positive and negative contributions to the net photocurrent calculated from the second and first term of eq 7.16, respectively.

Figure 7.6 illustrates the deconvolution of the photocurrent transient obtained at  $-0.05 \text{ V}$ . The dotted line is the experimental curve. The dashed lines represent the negative and positive contributions to the photocurrent, which are calculated from the first and second terms of eq 7.16, respectively. The solid line represents the summation of the two dashed lines, corresponding to the net simulated photocurrent response. It can be clearly seen that the experimental curve amounts to the sum of two photocurrent transients related to the electron transfers in two directions. The initial value of the photocurrent, observed directly at the beginning of the illumination, is determined by the sum of the fluxes of electron injection multiplied by Faraday's constant:

$$j_0 = F(g_1 + g_2) = I_0 \sigma \Gamma_s F \frac{k_2^{\text{et}} - k_1^{\text{et}}}{k_d + k_1^{\text{et}} + k_2^{\text{et}}} \quad (7.19)$$

The pseudo-first order electron transfer rate constants  $k_1^{\text{et}} = 9.2 \times 10^3 \text{ s}^{-1}$  and  $k_2^{\text{et}} = 4.6 \times 10^3 \text{ s}^{-1}$  were used to simulate the experimental transient in Figure 7.6. These values confirm that the two processes occur simultaneously with comparable rates. These rate constants remain one or two orders of magnitude lower than the rate of relaxation of the excited state of the porphyrin complex. Clearly, the large number of independent variables contained in eq 7.16 prevents an accurate fitting of the photocurrent transients. The purpose of Figure 7.6 is to illustrate the decomposition of the photocurrent response into two separate contributions. We shall not present an analysis of the dependence of the recombination and back electron transfer rates. Rather, we shall concentrate on the initial photocurrent values to extract information on the kinetics of the photoinduced electron transfer process.

The decay features observed on both the positive and negative contributions to the photocurrent in Figure 7.6 are determined by the rate constants  $k^{\text{ps}}$ ,  $k^{\text{b}}$  and  $k^{\text{rec}}$ . The back electron transfer and charge recombination mechanisms also give rise to the positive overshoot observed in Figure 7.6 after the illumination is stopped. The presence of these two reactions contributing to the photocurrent relaxation gives rise to multi-exponential decays for both the positive and negative contributions.

## 7.4 Kinetic analysis of photoinduced electron transfer

The dependence of the rate constant of heterogeneous electron transfer on the formal Gibbs energy in the case of molecular quenchers was found to follow Marcus theory. However, in the present case the relatively narrow range of  $\Delta G_{\text{et},1}^{\circ'}$  and  $\Delta G_{\text{et},2}^{\circ'}$  values prevent a similar analysis. Rather, we shall consider that a fraction  $\alpha$  of the Galvani potential difference acts to lower the activation barrier for the electron transfer processes. As a first approximation, the same apparent charge transfer coefficient can be taken for reactions 7.6 and 7.7, since both proceed from the same reactants. Within the framework



of Butler-Volmer approximation, the pseudo-first order rate constants for reactions 7.6 and 7.7 are given by:

$$k_1^{\text{et}} = k_1^{\text{et},\circ} \cdot \exp\left(-\frac{\alpha F (\Delta_0^{\text{w}}\phi - \Delta_0^{\text{w}}\phi_{\text{et},1}^{\circ'})}{RT}\right) = k_1^{\text{et},0'} \exp\left(-\frac{\alpha F \Delta_0^{\text{w}}\phi}{RT}\right) \quad (7.20)$$

$$k_2^{\text{et}} = k_2^{\text{et},\circ} \cdot \exp\left(\frac{\alpha F (\Delta_0^{\text{w}}\phi - \Delta_0^{\text{w}}\phi_{\text{et},2}^{\circ'})}{RT}\right) = k_2^{\text{et},0'} \exp\left(\frac{\alpha F \Delta_0^{\text{w}}\phi}{RT}\right) \quad (7.21)$$

where  $k_1^{\text{et},\circ}$  and  $k_2^{\text{et},\circ}$  are the standard rate constants of reactions 7.6 and 7.7, respectively. They are more conveniently referred to the apparent rate constants  $k_1^{\text{et},0'}$  and  $k_2^{\text{et},0'}$  at zero Galvani potential difference ( $\Delta_0^{\text{w}}\phi = 0$ ). Then the following Tafel relations can be obtained:

$$\ln k_1^{\text{et}} = \ln k_1^{\text{et},0'} - \frac{\alpha F \Delta_0^{\text{w}}\phi}{RT} \quad (7.22)$$

$$\ln k_2^{\text{et}} = \ln k_2^{\text{et},0'} + \frac{\alpha F \Delta_0^{\text{w}}\phi}{RT} \quad (7.23)$$

Employing eqs 7.19, 7.22 and 7.23, the initial photocurrent  $j_0$  can be expressed as a function of the Galvani potential difference, the apparent charge transfer coefficient  $\alpha$ , and the apparent rate constants  $k_1^{\text{et},0'}$  and  $k_2^{\text{et},0'}$ . The solid line in Figure 7.7a is a fit of the experimental initial photocurrent as a function of the Galvani potential difference employing this system of equations. This analysis yields apparent rate constants at  $\Delta_0^{\text{w}}\phi = 0$  of  $k_1^{\text{et},0'} = 6000 \text{ s}^{-1}$ ,  $k_2^{\text{et},0'} = 7200 \text{ s}^{-1}$ , and an apparent charge transfer coefficient of  $\alpha = 0.26$ . It can be observed that  $k_d \gg k_1^{\text{et}}, k_2^{\text{et}}$  throughout the potential range. Therefore, the initial photocurrent as described by eq 7.19 appears proportional to  $k_2^{\text{et}} - k_1^{\text{et}}$  with a proportionality constant of  $I_0 \sigma_1 F / k_d$ , and errors in the estimation of these parameters should not affect the trend observed in Figure 7.6a.

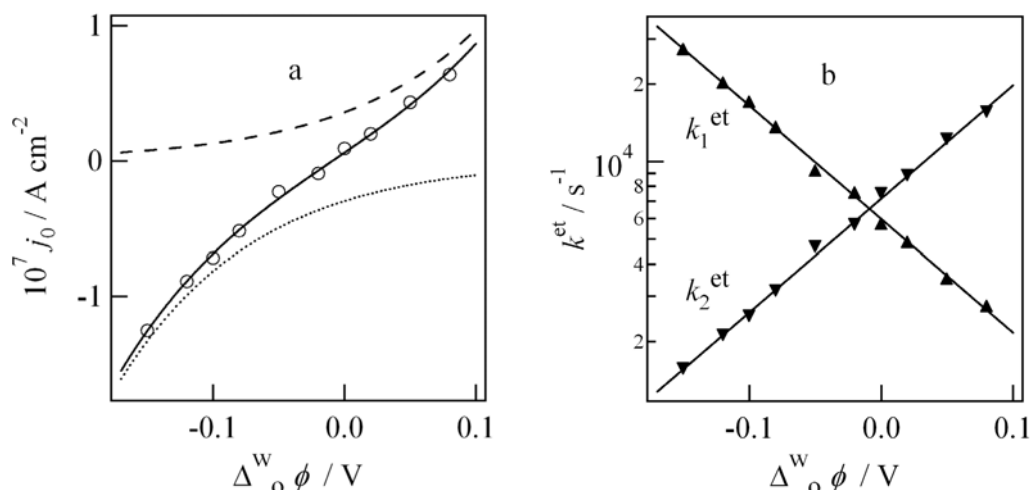


**Figure 7.7** (a) Initial photocurrent  $j_0$  estimated from the data in Figure 7.4 as a function of the Galvani potential difference. The solid line is a fit to eq 7.19 with the rate constants calculated by eqs 7.22 and 7.23. The fitting parameters were  $k_1^{\text{et},0'} = 6.0 \times 10^3 \text{ s}^{-1}$ ,  $k_2^{\text{et},0'} = 7.2 \times 10^3 \text{ s}^{-1}$  and  $\alpha = 0.26$ . The dotted and dashed lines illustrate the positive and negative contributions to  $j_0$ , calculated as  $Fg_2$  and  $Fg_1$ , respectively. (b) Apparent rate constants of the heterogeneous electron transfer reactions as a function of the Galvani potential difference. The solid lines are calculated from eqs 7.22 and 7.23 with the parameters obtained in (a).

The radius of the porphyrin complex is 0.7 nm,<sup>32</sup> and that of  $\text{MPC}^Z$  can be taken as a sum of the metallic core (0.8 nm) and the protecting monolayer thickness of 0.8 nm,<sup>41</sup> which yields a value of 1.6 nm. Therefore, it is reasonable to consider a distance at least 2.3 nm separation the porphyrin complex from the  $\text{MPC}^Z$ . This distance is significantly larger than the thickness of the interfacial layer, which was estimated to be 1 nm by molecular dynamic simulation<sup>42, 43</sup> and spectroscopic techniques.<sup>44, 45</sup> However, the clear dependence of  $k_{\text{et}}$  on the Galvani potential difference indicates that a substantial portion of the Galvani potential difference is developed within the average distance between the porphyrin complex and  $\text{MPC}^Z$ . The obtained value of  $\alpha = 0.26$  suggests that the potential profile across the interface extends over a region much wider than the solvent profile, as predicted previously by the simulations of the ionic distribution based on the Gouy-Chapman<sup>46</sup> and lattice-gas models.<sup>47-49</sup> Further studies could be aimed at controlling the distance separating the redox species by variation of the chain length of the protecting alkanethiolate. By exploring the effect of this parameter on the

heterogeneous electron transfer rate constant, we expect to obtain further insight into the potential distribution at liquid|liquid interfaces.

Figure 7.7b shows the rate constants of heterogeneous electron transfer  $k_1^{\text{et}}$  and  $k_2^{\text{et}}$  as extracted from the data in Figure 7.7a. At  $-0.15$  V,  $k_1^{\text{et}}$  was estimated to be ca.  $2.7 \times 10^4$   $\text{s}^{-1}$ , which corresponds to a heterogeneous pseudo-first order rate constant of  $6.8 \times 10^{-3}$   $\text{cm s}^{-1}$  assuming a characteristic distance of 2.5 nm separating the redox species at the interface. The corresponding value of the apparent bimolecular rate constant is estimated to be  $k_1^{\text{et,II}} = 340$   $\text{M}^{-1} \text{cm s}^{-1}$ . This value is significantly larger than those reported for electron transfer reactions between conventional redox molecules at liquid|liquid interfaces,<sup>50, 51</sup> indicating a fast heterogeneous electron transfer reaction between the porphyrin complex and the MPC. Our present results contradict those reported by Quinn et al. in a recent study,<sup>5</sup> in which the rates of the heterogeneous electron transfer reactions between MPCs and various aqueous redox species were reported to be too slow to measure by scanning electrochemical microscopy (SECM) under feedback operation mode even with the driving force extending over 1.3 V. It should be stressed that the MPCs used in their study are identical to those used in the present work, both containing a sufficiently dominant population of  $\text{Au}_{140}$  cores<sup>3</sup> with a diameter of  $\sim 1.6$  nm. On the other hand, the rate constants obtained here are comparable with that of  $76$   $\text{M}^{-1} \text{cm s}^{-1}$  reported by Georganopoulou et al.<sup>23</sup> for the case of the heterogeneous electron transfer reaction between  $\text{Au}_{38}$  MPC and  $\text{IrCl}_6^{2-}$  at the water|DCE interface employing SECM technique. Indeed, considering a MPC concentration of 0.02 mM and a distance of 2.5 nm between the reactant centers, the bimolecular electron transfer rate constants at  $\Delta_0^{\text{w}}\phi = 0$  can be calculated as  $75$   $\text{M}^{-1} \text{cm s}^{-1}$  and  $90$   $\text{M}^{-1} \text{cm s}^{-1}$  for the reduction and oxidation, respectively. However, it should be noted that the electronic properties of  $\text{Au}_{140}$  and  $\text{Au}_{38}$  MPCs are different. It has been shown that  $\text{Au}_{38}$  is small enough ( $d \sim 1.1$  nm) to exhibit a HOMO-LUMO energy gap, representing molecule-like redox activity.<sup>1,37,52-54</sup> Therefore, in the case of  $\text{Au}_{38}$ , evaluation of the electron transfer rate constant can be carried out using the approach previously developed for electron transfer reactions between traditional redox molecules. Due to the larger size of  $\text{Au}_{140}$  compared with conventional molecules, as well as the possibility of successive electron transfer, bimolecular rate constants obtained with these species should be considered with caution.

---

## 7.5 Conclusions

MPCs were used as redox mediators in heterogeneous photocurrent generation at the polarized water|DCE interface. Photocurrent responses originating from the heterogeneous electron transfer between photo-excited porphyrin complexes and MPCs were studied. As MPCs can function as both electron acceptors and electron donors, heterogeneous electron transfer can take place in either direction. The balance between reduction and oxidation of MPCs can be controlled by tuning the Galvani potential difference across the interface. At intermediate potentials, photoinduced electron transfer in the two directions occurs simultaneously with comparable rates. Analysis of the initial photocurrent values allows addressing the dependence of the rate constants of heterogeneous electron transfer on the Galvani potential difference. The effect of the Galvani potential difference on the photocurrent responses is adequately described by a Butler-Volmer type dependence.

## 7.6 References

- (1) Chen, S.; Ingrma, R. S.; Hostetler, M. J.; Pietron, J. J.; Murray, R. W.; Schaaff, T. G.; Khoury, J. T.; Alvarez, M. M.; Whetten, R. L. *Science* **1998**, *280*, 2098-2101.
- (2) Pietron, J. J.; Hicks, J. F.; Murray, R. W. *J. Am. Chem. Soc.* **1999**, *121*, 5565-5570.
- (3) Hicks, J. F.; Miles, D. T.; Murray, R. W. *J. Am. Chem. Soc.* **2002**, *124*, 13322-13328.
- (4) Hicks, J. F.; Templeton, A. C.; Chen, S.; Sheran, K. M.; Jasti, R.; Murray, R. W.; Debord, J.; Schaaff, T. G.; Whetten, R. L. *Anal. Chem.* **1999**, *71*, 3703-3711.
- (5) Quinn, B. M.; Liljeroth, P.; Kontturi, K. *J. Am. Chem. Soc.* **2002**, *124*, 12915-12921.
- (6) Quinn, B. M.; Liljeroth, P.; Ruiz, V.; Laaksonen, T.; Kontturi, K. *J. Am. Chem. Soc.* **2003**, *125*, 6644-6645.
- (7) Chen, S.; Murray, R. W. *J. Phys. Chem. B* **1999**, *103*, 9996-10000.

- (8) Brennan, J. L.; Branham, M. R.; Hicks, J. F.; Osisek, A. J.; Donkers, R. L.; Georganopoulou, D. G.; Murray, R. W. *Anal. Chem.* **2004**, *76*, 5611-5619.
- (9) Chen, S. *J. Am. Chem. Soc.* **2000**, *122*, 7420-7421.
- (10) Chen, S. *Langmuir* **2001**, *17*, 2878-2884.
- (11) Chen, S. *Langmuir* **2001**, *17*, 6664-6668.
- (12) Chen, S.; Pei, R. *J. Am. Chem. Soc.* **2001**, *123*, 10607-10615.
- (13) Hicks, J. F.; Zamborini, F. P.; Osisek, A. J.; Murray, R. W. *J. Am. Chem. Soc.* **2001**, *123*, 7048-7053.
- (14) Hicks, J. F.; Zamborini, F. P.; Murray, R. W. *J. Phys. Chem. B* **2002**, *106*, 7751-7757.
- (15) Wuelfing, W. P.; Murray, R. W. *J. Phys. Chem. B* **2002**, *106*, 3139-3145.
- (16) Wuelfing, W. P.; Green, S. J.; Pietron, J. J.; Cliffel, D. E.; Murray, R. W. *J. Am. Chem. Soc.* **2000**, *122*, 11465-11472.
- (17) Liljeroth, P.; Quinn, B. M.; Ruiz, V.; Kontturi, K. *Chem. Commun.* **2003**, 1570-1571.
- (18) Liljeroth, P.; Vanmaekelbergh, D.; Ruiz, V.; Kontturi, K.; Jiang, H.; Kauppinen, E.; Quinn, B. M. *J. Am. Chem. Soc.* **2004**, *126*, 7126-7132.
- (19) Zamborini, F. P.; Leopold, M. C.; Hicks, J. F.; Kulesza, P. J.; Malik, M. A.; Murray, R. W. *J. Am. Chem. Soc.* **2002**, *124*, 8958-8964.
- (20) Zamborini, F. P.; Hicks, J. F.; Murray, R. W. *J. Am. Chem. Soc.* **2000**, *122*, 4514-4515.
- (21) Lee, W.-Y.; Hostetler, M. J.; Murray, R. W.; Majda, M. *Isr. J. Chem.* **1997**, *37*, 213-223.
- (22) Yang, Y.; Pradhan, S.; Chen, S. *J. Am. Chem. Soc.* **2004**, *126*, 76-77.
- (23) Georganopoulou, D. G.; Mirkin, M. V.; Murray, R. W. *Nano Lett.* **2004**, *4*, 1763-1767.
- (24) Su, B.; Eugster, N.; Girault, H. H. *J. Am. Chem. Soc.* **2005**, *127*, 10760-10766.
- (25) Templeton, A. C.; Cliffel, D. E.; Murray, R. W. *J. Am. Chem. Soc.* **1999**, *121*, 7081-7089.
- (26) Huang, T.; Murray, R. W. *Langmuir* **2002**, *18*, 7077-7081.
- (27) Aguila, A.; Murray, R. W. *Langmuir* **2000**, *16*, 5949-5954.
- (28) Ipe, B. I.; Thomas, K. G.; Barazzouk, S.; Hotchandani, S.; Kamat, P. V. *J. Phys. Chem. B* **2002**, *106*, 18-21.

- 
- (29) Eugster, N.; Fermin, D. J.; Girault, H. H. *J. Am. Chem. Soc.* **2003**, *125*, 4862-4869.
- (30) Eugster, N. Ph.D Thesis, Ecole Polytechnique Fédérale de Lausanne, Switzerland, Lausanne, Switzerland, 2004.
- (31) Fermin, D. J.; Duong, H. D.; Ding, Z.; Brevet, P.-F.; Girault, H. H. *J. Am. Chem. Soc.* **1999**, *121*, 10203-10210.
- (32) Eugster, N.; Fermin, D. J.; Girault, H. H. *J. Phys. Chem. B* **2002**, *106*, 3428-3433.
- (33) Link, S.; Burda, C.; Mohamed, M. B.; Nikoobakht, B.; El-Sayed, M. A. *J. Phys. Chem. A* **1999**, *103*, 1165-1170.
- (34) Link, S.; Burda, C.; Nikoobakht, B.; El-Sayed, M. A. *J. Phys. Chem. B* **2000**, *104*, 6152-6163.
- (35) Link, S.; El-Sayed, M. A. *J. Chem. Phys.* **2001**, *114*, 2362-2368.
- (36) Huang, T.; Murray, R. W. *J. Phys. Chem. B* **2001**, *105*, 12498-12502.
- (37) Lee, D.; Donkers, R. L.; Wang, G.; Harper, A. S.; Murray, R. W. *J. Am. Chem. Soc.* **2004**, *126*, 6193-6199.
- (38) Wilcoxon, J. P.; Martin, J. E.; Parsapour, F.; Wiedenman, B.; Kelley, D. F. *J. Chem. Phys.* **1998**, *108*, 9137-9143.
- (39) Kamat, P. V. *J. Phys. Chem. B* **2002**, *106*, 7729-7744.
- (40) Samec, Z.; Eugster, N.; Fermin, D. J.; Girault, H. H. *J. Electroanal. Chem.* **2005**, *577*, 323-337.
- (41) Chen, S.; Murray, R. W.; Feldberg, S. W. *J. Phys. Chem. B* **1998**, *102*, 9898-9907.
- (42) Benjamin, I. *Chem. Rev.* **1996**, *96*, 1449-1475.
- (43) Benjamin, I. *Annu. Rev. Phys. Chem.* **1997**, *48*, 407-451.
- (44) Strutwolf, J.; Zhang, J.; Barker, A. L.; Unwin, P. R. *Phys. Chem. Chem. Phys.* **2001**, *3*, 5553-5558.
- (45) Webster, R. D.; Beaglehole, D. *Phys. Chem. Chem. Phys.* **2000**, *2*, 5660-5666.
- (46) Samec, Z. *Chem. Rev.* **1988**, *88*, 617-632.
- (47) Frank, S.; Schmickler, W. *J. Electroanal. Chem.* **2000**, *483*, 18-21.
- (48) Frank, S.; Schmickler, W. *J. Electroanal. Chem.* **2001**, *500*, 491-497.
- (49) Schmickler, W. *J. Electroanal. Chem.* **1997**, *428*, 123-127.
- (50) Tsionsky, M.; Bard, A. J.; Mirkin, M. V. *J. Am. Chem. Soc.* **1997**, *119*, 10785-10792.
- (51) Zhang, J.; Barker, A. L.; Unwin, P. R. *J. Electroanal. Chem.* **2000**, *483*, 95-107.

- (52) Lee, D.; Donkers, R. L.; DeSimone, J. M.; Murray, R. W. *J. Am. Chem. Soc.* **2003**, *125*, 1182-1183.
- (53) Jimenez, V. L.; Georganopoulou, D. G.; White, R. J.; Harper, A. S.; Mills, A. J.; Lee, D.; Murray, R. W. *Langmuir* **2004**, *20*, 6864-6870.
- (54) Yang, Y.; Chen, S. *Nano Lett.* **2003**, *3*, 75-79.

## 7.7 Appendix to eq 7.16

The photocurrent responses involve contributions from the electron transfer reaction, charge recombination and back electron transfer processes, i.e., eqs 7.3-7.11, can be described as:

$$\frac{j}{F} = -k_1^{\text{et}}\Gamma_{S^*} + k_2^{\text{et}}\Gamma_{S^*} + k_1^{\text{rec}}\Gamma_{[S^+ \dots \text{MPC}^{Z-1}]} - k_2^{\text{rec}}\Gamma_{[S^- \dots \text{MPC}^{Z+1}]} + k_1^{\text{b}}\Gamma_{S^+} + k_2^{\text{b}}\Gamma_{S^-} \quad (\text{a7.1})$$

where  $\Gamma_X$  ( $X = S^*$ ,  $[S^+ \dots \text{MPC}^{Z-1}]$ ,  $[S^- \dots \text{MPC}^{Z+1}]$ ,  $[S^+]$  and  $[S^-]$ ) denote surface concentrations.

Eq a7.1 can be expressed in the Laplace plane:

$$\frac{\bar{j}}{F} = -k_1^{\text{et}}\bar{\Gamma}_{S^*} + k_2^{\text{et}}\bar{\Gamma}_{S^*} + k_1^{\text{rec}}\bar{\Gamma}_{[S^+ \dots \text{MPC}^{Z-1}]} - k_2^{\text{rec}}\bar{\Gamma}_{[S^- \dots \text{MPC}^{Z+1}]} + k_1^{\text{b}}\bar{\Gamma}_{S^+} + k_2^{\text{b}}\bar{\Gamma}_{S^-} \quad (\text{a7.2})$$

The differential equations for the concentrations of species involved in the heterogeneous electron transfer process can be written as follows:

$$\frac{d\Gamma_{S^*}}{dt} = I_0\sigma\Gamma_S - k_d\Gamma_{S^*} - k_1^{\text{et}}\Gamma_{S^*} - k_2^{\text{et}}\Gamma_{S^*} = 0 \quad (\text{a7.3})$$

$$\frac{d\Gamma_{[S^+ \dots \text{MPC}^{Z-1}]}}{dt} = k_1^{\text{et}}\Gamma_{S^*} - k_1^{\text{rec}}\Gamma_{[S^+ \dots \text{MPC}^{Z-1}]} - k_1^{\text{ps}}\Gamma_{[S^+ \dots \text{MPC}^{Z-1}]} \quad (\text{a7.4})$$

$$\frac{d\Gamma_{[S^- \dots \text{MPC}^{Z+1}]}}{dt} = k_2^{\text{et}}\Gamma_{S^*} - k_2^{\text{rec}}\Gamma_{[S^- \dots \text{MPC}^{Z+1}]} - k_2^{\text{ps}}\Gamma_{[S^- \dots \text{MPC}^{Z+1}]} \quad (\text{a7.5})$$

$$\frac{d\Gamma_{S^+}}{dt} = k_1^{\text{ps}}\Gamma_{[S^+ \dots \text{MPC}^{Z-1}]} - k_1^{\text{b}}\Gamma_{S^+} \quad (\text{a7.6})$$

$$\frac{d\Gamma_{S^-}}{dt} = k_2^{\text{ps}}\Gamma_{[S^- \dots \text{MPC}^{Z+1}]} - k_2^{\text{b}}\Gamma_{S^-} \quad (\text{a7.7})$$

Laplace transformation of eqs a7.3- a7.7 gives:

$$\bar{\Gamma}_{S^*} = \frac{I_0\sigma\Gamma_S}{s(k_d + k_1^{\text{et}} + k_2^{\text{et}})} \quad (\text{a7.8})$$

$$\bar{\Gamma}_{[S^+ \dots \text{MPC}^{Z-1}]} = \frac{k_1^{\text{et}}\bar{\Gamma}_{S^*}}{s + k_1^{\text{rec}} + k_1^{\text{ps}}} = \frac{I_0\sigma\Gamma_S}{s(k_d + k_1^{\text{et}} + k_2^{\text{et}})} \cdot \frac{k_1^{\text{et}}}{(s + k_1^{\text{rec}} + k_1^{\text{ps}})} \quad (\text{a7.9})$$



$$\overline{\Gamma_{[S^{\dots}MPC^{Z+1}]}} = \frac{k_2^{\text{et}} \overline{\Gamma_{S^*}}}{s + k_2^{\text{rec}} + k_2^{\text{ps}}} = \frac{I_0 \sigma \Gamma_s}{s(k_d + k_1^{\text{et}} + k_2^{\text{et}})} \cdot \frac{k_2^{\text{et}}}{(s + k_2^{\text{rec}} + k_2^{\text{ps}})} \quad (\text{a7.10})$$

$$\overline{\Gamma_{S^+}} = \frac{k_1^{\text{ps}} \overline{\Gamma_{[S^+ \dots MPC^{Z-1}]}}}{s + k_1^{\text{b}}} = \frac{I_0 \sigma \Gamma_s}{s(k_d + k_1^{\text{et}} + k_2^{\text{et}})} \cdot \frac{k_1^{\text{et}}}{(s + k_1^{\text{rec}} + k_1^{\text{ps}})} \frac{k_1^{\text{ps}}}{(s + k_1^{\text{b}})} \quad (\text{a7.11})$$

$$\overline{\Gamma_{S^-}} = \frac{k_2^{\text{ps}} \overline{\Gamma_{[S^{\dots}MPC^{Z+1}]}}}{s + k_2^{\text{b}}} = \frac{I_0 \sigma \Gamma_s}{s(k_d + k_1^{\text{et}} + k_2^{\text{et}})} \cdot \frac{k_2^{\text{et}}}{(s + k_2^{\text{rec}} + k_2^{\text{ps}})} \frac{k_2^{\text{ps}}}{(s + k_2^{\text{b}})} \quad (\text{a7.12})$$

where  $s$  is the Laplace variable.

Introducing eqs a7.8-a7.12 to eq a7.2 yields:

$$\frac{\overline{j}}{F} = \left( -\frac{k_1^{\text{et}} I_0 \sigma \Gamma_s}{k_d + k_1^{\text{et}} + k_2^{\text{et}}} \right) \frac{(s + k_1^{\text{b}} + k_1^{\text{ps}})}{(s + k_1^{\text{rec}} + k_1^{\text{ps}})(s + k_1^{\text{b}})} + \left( \frac{k_2^{\text{et}} I_0 \sigma \Gamma_s}{k_d + k_1^{\text{et}} + k_2^{\text{et}}} \right) \frac{(s + k_2^{\text{b}} + k_2^{\text{ps}})}{(s + k_2^{\text{rec}} + k_2^{\text{ps}})(s + k_2^{\text{b}})} \quad (\text{a7.13})$$

The inverse Laplace transform of eq a7.13 gives **eq 7.16** describing the photocurrent density as a function of time:

$$j = g_1 F \cdot \left\{ \frac{k_1^{\text{ps}} \exp(-k_1^{\text{b}} t) + (k_1^{\text{rec}} - k_1^{\text{b}}) \exp[-(k_1^{\text{rec}} + k_1^{\text{ps}}) t]}{(k_1^{\text{rec}} + k_1^{\text{ps}} - k_1^{\text{b}})} \right\} + \quad (\text{7.16})$$

$$+ g_2 F \cdot \left\{ \frac{k_2^{\text{ps}} \exp(-k_2^{\text{b}} t) + (k_2^{\text{rec}} - k_2^{\text{b}}) \exp[-(k_2^{\text{rec}} + k_2^{\text{ps}}) t]}{(k_2^{\text{rec}} + k_2^{\text{ps}} - k_2^{\text{b}})} \right\}$$



## Chapter 8

### Conclusions and perspective

The results presented in this thesis describe the assembly and reactivity of metallic and semiconducting nanoparticles (NPs) at the liquid|liquid interface, including the voltage-induced assembly of charged NPs, the photoreactivity of semiconducting NPs and the redox properties of alkanethiolate monolayer-protected gold nanoclusters. These studies not only provide the experimental evidence of the assembly and reactivity of NPs at the liquid|liquid interface, but also clearly demonstrate that the liquid|liquid interface can be an alternative medium to approach the electronic and optical properties of NPs.

Chapter 3 was aimed at exploring the effect of the adsorption of ionic species or charged nanoparticles on the charge distribution across the liquid|liquid interface. The adsorption of ions at the interface between two immiscible electrolyte solutions (ITIES) is primarily controlled by the potential distribution across the interface, which in turn is influenced by the adsorption process. We simulated the effect of the adsorption of charged species on

---

the charge distribution at the ITIES based on the classical description of the interface employing the Gouy-Chapman model. The inner layer was considered as a charged plane, where the ionic adsorption takes place. The potential at this plane is determined by the electroneutrality condition. Various adsorption isotherms were considered, including potential independent, Langmuir and Frumkin adsorption models. The potential distribution and the charge density profile across the interface were derived by solving the Poisson-Boltzmann equation numerically. We showed in all cases that the charge distribution in the interfacial region is significantly affected by the adsorption of ionic species. Under certain conditions, the adsorption results in a nonmonotonic potential distribution with a potential trap at the interface.

The voltage induced assembly of mercaptosuccinic acid (MSA) stabilized gold NPs of  $1.5 \pm 0.4$  nm in diameter was investigated at the polarizable water|1,2-dichloroethane (DCE) interface. Cyclic voltammograms, admittance measurements and quasi-elastic laser scattering (QELS) studies revealed that the surface concentration of the gold NPs at the liquid|liquid boundary can be reversibly controlled by the applied bias potential. The electrochemical and optical measurements provide no evidence of irreversible aggregation or deposition of the particles at the interface. Analysis of the electrocapillary curves constructed from the dependence of the frequency of the capillary waves on the applied potential and bulk particle concentration indicated that the maximum particle surface density is  $3.8 \times 10^{13} \text{ cm}^{-2}$ , which corresponds to 67% of a square closed-pack arrangement. This approach has the unique advantage of effectively allowing control the number of particles at the interface by tuning the Galvani potential difference. In conjunction with surface spectroscopic techniques, this method allows studying single vs. collective properties of metal and semiconductor NPs.

Water-soluble MSA protected cadmium selenide (CdSe) NPs can also be reversibly adsorbed at the polarizable water|DCE interface. Within the potential range where the NPs are adsorbed, illumination of the interface leads to heterogeneous electron transfer from CdSe NPs to electron acceptors located in the organic phase. The interfacial Galvani potential difference plays an important role in these phenomena, as it affects the interfacial density of the NPs, as well as the driving force for the electron transfer. The photocurrent efficiency also strongly depends on the formal redox potential of the

electron acceptor, indicating that the heterogeneous photoreaction is kinetically controlled. No photocurrents were observed in the presence of electron donors in the organic phase, suggesting that the photogenerated holes are swiftly captured by species present in the aqueous phase. From a phenomenological point of view, the photoelectrochemical behavior of MSA stabilized CdSe NPs can be compared to a self-assembled ultrathin p-type semiconductor photoelectrode. In contrast, photocurrent responses can be observed in both directions with citrate protected CdSe NPs, that is, both photoexcited electrons and holes are available for heterogeneous electron transfer reactions. These results reveal the important role of the surface modification on the optical and electronic properties of CdSe NPs.

The alkanethiolate monolayer-protected gold nanoclusters (MPCs) demonstrate fascinating electronic properties and can be formally equivalent to multivalent redox species. Their redox properties have been studied at both solid|liquid and liquid|liquid interfaces. First, taking the bulk solvent effect into account, we derived the absolute standard redox potential of hexanethiolate monolayer-protected gold nanoclusters (MPCs) in solutions from electrostatic considerations. In terms of this derivation, the valence state of MPCs at a given potential can be estimated by employing an internal redox molecular reference, such as ferrocenium/ferrocene. Importantly, the significant effect of the solvent on the redox properties of MPCs was verified experimentally by studies in various organic solvents, which provides concrete evidence that the theoretical description based solely on the assumption of the MPC molecular capacitance is not sufficient to explain its redox behavior. Second, the redox properties of MPCs self-assembled on the gold electrode surface through dithiol linkers were studied in organic electrolyte solutions and room temperature ionic liquids (RTILs). The effect of the electrostatic interaction between MPCs and substrate electrode on the redox behavior of MPCs was theoretically considered in terms of the method of images in classical electrostatics and verified experimentally. In RTILs, the rectification of the successive oxidation of self-assembled MPCs by the anionic component of RTILs was also observed. However, the mechanism of the rectification remains worthy of further studies.

MPCs were also used as redox quenchers at the polarizable water|DCE interface. Photocurrent responses originating from the heterogeneous quenching of photoexcited porphyrin species by MPCs dissolved in the DCE phase were observed. As MPCs can

function as both electron acceptors and electron donors, the photocurrent results from the superposition of two simultaneous processes, which correspond to the oxidation and reduction of MPCs. The magnitude of the net photocurrent is essentially determined by the balance of the kinetics of these two processes, which can be controlled by tuning the Galvani potential difference between the two phases. We show that, within the available potential window, the apparent electron transfer rate constants follow classical Butler-Volmer dependence on the applied potential difference. The rate of the electron transfer reaction was found to be faster than those previously reported in the case of conventional redox molecules at liquid|liquid interfaces.

# Curriculum Vitae

## Personal

---

Name: Bin SU

Birth: 17<sup>th</sup> October 1976, Heilongjiang, China

Nationality: Chinese

## Education

---

- Sept. 2002 - 2006: Ph. D student  
Laboratoire d'Electrochimie Physique et Analytique, EPFL, Switzerland  
Thesis: Assembly and Reactivity of Nanoparticles at Liquid|Liquid Interfaces  
Advisor: Prof. Hubert Girault
- Sept. 1999 – July 2002: Master of Science  
Changchun Institute of Applied Chemistry, Chinese Academy of Sciences, China  
Thesis: Facilitated Ion Transfer across the Micro-Liquid/Liquid Interfaces  
Advisor: Prof. Yuanhua Shao
- Sept. 1995 – July 1999: Bachelor of Engineering  
Jilin University, China  
Thesis: Synthesis of 1, 2-Diacetoxy-1, 2-di-2-Furanylethylene with Furfural  
Advisor: Prof. Dawei Gao

## Publications

---

- [1] Bin Su, Sheng Zhang, Yi Yuan, Jidong Guo, Liangbing Gan, Yuanhua Shao, Investigation of Ion Transfer across the Micro-Water/Nitrobenzene Interface Facilitated by a Fullerene Derivative, *Anal. Chem.*, 2002, **74**, 373-378.
- [2] Zhiquan Zhang, Yi Yuan, Peng Sun, Bin Su, Jidong Guo, Yuanhua Shao, Hubert H. Girault, Study of Electron Transfer Reactions across an Externally Polarized Water/1,2-Dichloroethane Interface by Scanning Electrochemical Microscopy, *J. Phys. Chem. B*, 2002, **106**, 6713-6717.
- [3] Bin Su, Yuanhua Shao, Mechanisms of Sodium and Potassium Ions Transfer Facilitated by Dibenzo-15-crown-5 across the Water/1,2-Dichloroethane Interface using micropipette, *Chinese Science Bulletin*, 2002, **47**, 1325-1329.

- [4] Bin Su, Jean-Pierre Abid, David J. Fermin, Hubert H. Girault, Hana Hoffmannova, Petr Krtil, Zdenek Samec, Voltage Induced Assembly of Au Nanoparticles at Liquid|Liquid Interfaces, *J. Am. Chem. Soc.*, 2004, **126**, 915-919.
- [5] Bin Su, Nicolas Eugster, Hubert H. Girault, Simulations of the Adsorption of Ionic Species at Polarizable Liquid|Liquid Interfaces, *J. Electroanal. Chem.*, 2005, **577**, 187-196.
- [6] Bin Su, David J. Fermin, Jean-Pierre Abid, Nicolas Eugster, Hubert H. Girault, Adsorption and Photoreactivity of CdSe Nanoparticles at Liquid|Liquid Interfaces, *J. Electroanal. Chem.*, 2005, **583**, 241-247.
- [7] Bin Su, Hubert H. Girault, Absolute Standard Redox Potential of Monolayer Protected Gold Nanoclusters, *J. Phys. Chem. B*, 2005, **109**, 11427-11431.
- [8] Bin Su, Nicolas Eugster, Hubert H. Girault, Reactivity of Monolayer Protected Gold Nanoclusters at Dye-Sensitized Liquid|Liquid Interfaces, *J. Am. Chem. Soc.*, 2005, **127**, 10760-10765.
- [9] Bin Su, Hubert H. Girault, Redox Properties of Self-assembled Gold Nanoclusters, *J. Phys. Chem. B*, 2005, **109**, 23925-23929.
- [10] Nicolas Eugster, Koliyat P. Sreenivasan, Bin Su, Hubert H. Girault, 2-Dimensional Porphyrin Self-assemblies at Molecular Interfaces, *Langmuir*, 2006, **22**, 1112-1120.
- [11] Bin Su, Meiqin Zhang, Yuanhua Shao, Hubert H. Girault, Solvent Effect on the Redox Properties of Gold Nanoclusters, *revised*.
- [12] Mohamad Hojeij, Nicolas Eugster, Bin Su, Hubert H. Girault, CdSe Sensitized Thin Aqueous Films: Probing the Potential Distribution inside Multilayer Assemblies, *submitted*.
- [13] Shuxin Tan, Mohamad Hojeij, Bin Su, Guillaume Meriguet, Nicolas Eugster and Hubert H. Girault, Dye-sensitized thin aqueous layer on reticulated vitreous carbon, *in preparation*.

## Presentation and Posters

---

- Organization and Reactivity of CdSe Nanoparticles at the Water|1, 2-Dichloroethane Interface  
The 9<sup>th</sup> International Seminar on Electroanalytical Chemistry,  
Changchun, China, Oct. 10 - 13, 2003
- Simulations of the Adsorption of Charged Species at Liquid|Liquid Interfaces  
37<sup>th</sup> Heyrovsky Discussion "Electrochemistry on Liquid|Liquid Interfaces"  
Prague, Czech Republic, 2004.